



Fatigue crack initiation (in 304L steel) : influence of the microstructure and variable amplitude loading

Yan Li

► To cite this version:

Yan Li. Fatigue crack initiation (in 304L steel) : influence of the microstructure and variable amplitude loading. Other. Ecole Centrale Paris, 2012. English. NNT : 2012ECAP0015 . tel-00697002

HAL Id: tel-00697002

<https://theses.hal.science/tel-00697002>

Submitted on 14 May 2012

HAL is a multi-disciplinary open access archive for the deposit and dissemination of scientific research documents, whether they are published or not. The documents may come from teaching and research institutions in France or abroad, or from public or private research centers.

L'archive ouverte pluridisciplinaire **HAL**, est destinée au dépôt et à la diffusion de documents scientifiques de niveau recherche, publiés ou non, émanant des établissements d'enseignement et de recherche français ou étrangers, des laboratoires publics ou privés.



**ÉCOLE CENTRALE DES ARTS
ET MANUFACTURES**

« ÉCOLE CENTRALE PARIS »

THÈSE

présentée par

Yan LI

pour l'obtention du

GRADE DE DOCTEUR

Spécialité : Mécanique & Matériaux

Laboratoire d'accueil : MSSMat (CNRS UMR 8579)

SUJET :

Amorçage de fissures en fatigue dans un acier 304L: influence de la microstructure et d'un chargement d'amplitude variable

soutenue le : 10 Février 2012

devant un jury composé de :

**M. Benoit DEVINCRE
M. François HILD
M. Franck MOREL
Mme. Véronique FAVIER
M. Eric CHARKALUK
M. Philippe BOMPARD
Mme. Véronique AUBIN**

**Président
Rapporteur
Rapporteur
Examineur
Examineur
Directeur de thèse
Co-directrice de thèse**

2012ECAP0015

Acknowledgements

This dissertation is the result of three and a half years of work whereby I have been accompanied, supported and tremendously helped by many people. It is really a pleasant aspect that I have now the opportunity to express my gratitude to all of them.

First of all, I would like to thank Dr. Benoit Devincere who has done me the honor of being the president of the jury of my thesis. I would like to thank Dr. Francois Hild and Dr. Franck Morel, my two examiners of thesis, for their well-directed support and meticulous reading of my dissertation. I am really touched and thankful for their time and patience in reading carefully my dissertation and improving my writing. I will keep all those details in mind. I would like to give my sincere thanks to Dr. Veronique Favier and Dr. Eric Charkaluk, my other committee members, for their time and their valuable advices.

My deepest thanks go to my supervisor Dr. Philippe Bompard for providing an opportunity to study at ECP and for his excellent supervision, guidance, patience, and encouragement on this dissertation. Over these years, Dr. Philippe Bompard has taught me so much, and made such a difference in my life, that just saying “Thanks” is woefully inadequate. From him, I learnt not only the science knowledge but also how to fight against the failures. He always shared his time and enthusiasm to try to improve my knowledge of the French language and culture. He gave me so much support in my daily life during the stay in France.

My sincere thanks go to my co-supervisor Dr. Veronique Aubin, for her valuable supervision, guidance and suggestions to improve the dissertation. This work would not have been possible without her precious help, advice and support. I can never forget her exceptional support during the time of my manuscripts and thesis preparation.

I owe a huge debt of gratitude to all the members in MSSMat laboratory: Francoise Garnier, Sylviane Bourgeois, Sokona Konate, Nicolas Roubier, Eric Perrin and Thomas Reiss who taught me so much in experiments such as specimen preparation, fatigue test, SEM observation and EBSD measurement. I also want to thank Dr. Colette Rey for helping with learning of polycrystalline plasticity and UMAT code for numerical simulation.

Of course, I want to thank my labmates in MSSMat for their continuous support and making my stay a happy and memorable experience: Julien Colombeau, Julien De Jaeger, Samuel Hemery, Morgan Chabanon, Haidong Wang, Saeid Rezaee.

Thanks to my master's thesis supervisor Dr. Binjun Fei and Dr. Rui Bao in Beihang university (BUAA) who recommended me to pursue my PhD in France.

This research was supported financially by Carnot C3S in France and CSC in China. A special thanks goes to them. Thanks to EDF research center in France for supplying the materials studied in this work.

Thanks to all my other friends both in France and in China who are always supporting me all these years.

Lastly and most importantly, I would like to thank my wonderful parents and parents-in-law for their loving support and encouragement during this years of my study in France, and my sweetheart, confidant, closest friend and dear wife — Ye, for her love, patience, and help. I don't know how I ever got lucky enough to marry her, but it was without a doubt the smartest thing I've ever done. To them, I owe the greatest debt of gratitude.

Yan Li

Paris, France, February 2012

Table of contents

TABLE OF CONTENTS.....	I
LIST OF FIGURES	V
LIST OF TABLES	XV
INTRODUCTION	1
1 LITERATURE REVIEW OF FATIGUE	5
1.1 HISTORICAL OVERVIEW.....	7
1.2 HIGH CYCLE FATIGUE AND LOW CYCLE FATIGUE.....	9
1.2.1 <i>High cycle fatigue</i>	9
1.2.2 <i>Low cycle fatigue</i>	9
1.3 APPROACHES TO FATIGUE ANALYSIS	9
1.4 CYCLIC DEFORMATION.....	10
1.4.1 <i>Cyclic stress – strain response</i>	10
1.4.2 <i>Evolution of dislocation microstructure during cyclic loading</i>	13
1.5 FATIGUE CRACK INITIATION AND PROPAGATION	19
1.5.1 <i>Fatigue crack initiation</i>	19
1.5.2 <i>Fatigue crack propagation</i>	25
1.5.3 <i>Transition from the crack initiation to propagation stage</i>	25
1.6 CRACK OBSERVATION TECHNIQUES	28
1.7 FATIGUE UNDER VARIABLE-AMPLITUDE LOADING	31
1.8 SUMMARY	34
2 MATERIAL CHARACTERISTICS OF AUSTENITIC STAINLESS STEEL 304L	35
2.1 OVERVIEW.....	37
2.2 CHEMICAL COMPOSITION.....	37
2.3 MICROSTRUCTURAL CHARACTERIZATION.....	38
2.3.1 <i>Preparation</i>	38
2.3.2 <i>Surface observation</i>	39
2.4 DEFORMATION MECHANISMS	40
2.5 MECHANICAL PROPERTIES	41
2.6 SUMMARY	43

3 MODELING OF THE CYCLIC HARDENING/SOFTENING BEHAVIOR.....	45
3.1 DESCRIPTION OF THE SELECTED MODELING METHOD.....	47
3.1.1 <i>Representative volume element</i>	47
3.1.2 <i>Microstructure generation and representation</i>	48
3.1.3 <i>Three dimensional modeling method</i>	50
3.2 MATERIAL CONSTITUTIVE LAWS.....	51
3.2.1 <i>Crystalline elasticity</i>	51
3.2.2 <i>Crystal plasticity for FCC structure</i>	54
• Plastic flow mechanism.....	54
• Flow rule in modeling.....	59
• Isotropic and kinematic hardening	59
• Softening rules	60
3.3 IDENTIFICATION OF THE PARAMETERS	64
3.3.1 <i>Identification results</i>	65
3.4 RESULT DISCUSSION	70
3.4.1 <i>Stress evolution during fatigue</i>	70
3.4.2 <i>Stress-strain loop curves evolution during fatigue</i>	74
3.4.3 <i>Comparison with results obtained not considering cyclic softening</i>	77
3.5 CONCLUSIONS	80
 4 EVALUATION AND COMPARISON OF FATIGUE CRITERIA FOR PREDICTION OF THE CRACK	
INITIATION SITES	81
4.1 EXPERIMENTAL PROCEDURE.....	85
4.1.1 <i>Fatigue testing machine</i>	85
4.1.2 <i>Specimen</i>	85
4.1.3 <i>Loading</i>	87
4.1.4 <i>Interruption</i>	88
4.1.5 <i>Observation</i>	89
4.2 EXPERIMENTAL OBSERVATION RESULTS	90
4.2.1 <i>Crack initiation at inclusions</i>	91
4.2.2 <i>Crack Initiation on grain boundaries (GBs)</i>	93
4.2.3 <i>Crack initiation on slip lines (SLs)</i>	97
4.2.4 <i>Crack Initiation at GB-SLs intersection</i>	100
4.2.5 <i>Summary for crack initiation observation</i>	105
4.3 PREDICTION OF THE CRACK INITIATION SITES	106
4.3.1 <i>Review of fatigue criteria</i>	106
4.3.1.1 <i>Classical macroscopic fatigue criteria</i>	106

• Manson–Coffin criterion	107
• Smith–Watson–Topper criterion	108
• Walker criterion	109
• Ostergren criterion	109
4.3.1.2 Fatigue criteria based on micromechanical approaches	109
• Energy dissipation criterion	110
• LMS criterion	111
• Fatemi-Socie criterion	111
• Critical plane criterion	112
• Depres criterion	113
• Dang Van criterion	113
4.3.2 <i>Simulation procedure</i>	116
4.3.3 <i>Simulation results</i>	122
4.3.3.1 Macroscopic crack initiation indicators	122
• Maximum local stress and strain	122
4.3.3.2 Microscopic crack initiation indicators	124
• Maximum shear strain amplitude and normal stress	124
• Fatemi-Socie criterion	126
• Microscopic dissipated energy	127
• LMS criterion	128
4.4 CONCLUSIONS	129
 5 VARIABLE AMPLITUDE LOADING EFFECTS ON CYCLIC PLASTICITY AND MICROCRACK	
INITIATION	131
5.1 INTRODUCTION	133
5.2 DISTRIBUTION CLOUDS CORRESPONDING TO LOCAL STRESS AND STRAIN	133
5.3 OVERLOAD EFFECTS	136
5.3.1 <i>Strain-controlled</i>	136
5.3.1.1 Experimental procedure	137
• Specimen	137
• Loading	137
• Interruptions for observation	138
• Observation	138
5.3.1.2 Experimental results	139
5.3.1.3 Simulation results	141
5.3.2 <i>Load-controlled</i>	148
5.3.2.1 Experimental results	148
5.3.2.2 Simulation results	149
5.4 CONCLUSIONS	159

Table of contents

CONCLUSIONS AND PERSPECTIVES.....	161
REFERENCES.....	167
RÉSUMÉ / ABSTRACT	182

List of figures

Figure 1 (a) Cyclic hardening/softening curves for 304L steel [Le-Pecheur 2008] (b) Evolution of stress-strain loops under controlled strain cycling amplitude ± 0.005 , a progressive decrease in stress amplitude is observed with increasing cycles, final instability is due to macrocrack propagation.....	11
Figure 2 Cyclic hardening/softening curves for 304L steel (a) 316L-VZ steel (b)316L-TH steel [Polak, Obrtlik and Hajek 1994]	12
Figure 3 Temperature effect on the fatigue behavior of 304L (a) Evolution of minimum and maximum with increase of the number of cycles (b) Stress/ strain curves at mid-life under 90, 165 and 320 ° C, total strain amplitude equal to $\pm 0.2\%$, $f = 1$ Hz [Haddar 2003]	12
Figure 4 Cyclic stress response at various strain amplitudes for austenitic stainless steel AISI 316L with two different grain sizes of 90 and 139 μm [Basu, Das, Bhattacharjee and Chakraborti 2007].....	13
Figure 5 Schematic diagram showing different regimes of the saturation stress-strain curve [Suresh 1991].....	14
Figure 6 Amplitude of the resolved saturation shear stress $\Delta\tau_s/2$ versus the plastic strain amplitude $\Delta\gamma_{pl}/2$ for 316L steel [Obrtlik, Kruml and Polak 1994; Polak, Obrtlik and Hajek 1994]	15
Figure 7 Dislocation structure of a 316L specimen cycled with a plastic strain amplitude of 5×10^{-4} (a) $N=2.2 \times 10^6$ cycles (at mid-life) (b) $N= 5.3 \times 10^6$ cycles (at failure) [Obrtlik, Kruml and Polak 1994]	16
Figure 8 Schematic representation of the dislocation arrangements in (a) a matrix structure and (b) a persistent slip band (redrawn from [Suresh 1991]).....	17
Figure 9 Matrix structure with PSB structure in the 316L specimens cycled in the plateau regime (a) with a plastic strain amplitude of 2×10^{-4} , $N=1.3 \times 10^6$ cycles (at failure) (b) a plastic strain amplitude of 1×10^{-3} , $N=9 \times 10^4$ cycles [Obrtlik, Kruml and Polak 1994].....	17
Figure 10 PSB structures in specimens of 316L steel cycled with plastic strain amplitude of 5×10^{-3} , $N_f=2800$ (a) cell structure with a PSB (b) PSBs with wall structure	18
Figure 11 Microstructures observed in 304L at 300°C [Garcia 2006] (a) Planar dislocation structure (b) channels and veins (c) PSB structure.....	19
Figure 12 Different stages of crack propagation under push–pull loading conditions [Kunkler, Duber, Koster, Krupp, Fritzen and Christ 2008].....	20

List of figures

Figure 13 A rough surface consisting of extrusions and intrusions produced by cyclic plastic strain (redrawn from [Suresh 1991]).....	21
Figure 14 (a) Development of cyclic slip bands and a microcrack in a pure copper specimen, $S_m=0$, $S_a=77.5$ MPa, $N_f=2\times 10^6$ cycles (a1) Slip lines are clearly visible (a2) Same as in (a1) but plastically strained (5%) which opens a microcrack, see arrow [Bullen, Head and Wood 1953] (b) Intrusion and extrusion [Forsyth and Stubbington 1955].....	22
Figure 15 Grain boundary effect on crack propagation rate in an Al-alloy [Blom, Hedlund, Zhao, Fathalla, Weiss and Stickler 1985]. The crack length was measured along the material surface.	23
Figure 16 Typical cracks and slip lines on the specimen surface in 304L at the $N = 15000$ cycles under total strain controlled amplitude of $\pm 0.3\%$ ($N/N_f = 50\%$)	24
Figure 17 Crack distribution during fatigue test in 304L under total strain controlled amplitude of $\pm 0.3\%$, $N_f=25000$ cycles [Lehericy and Mendez 2006].....	24
Figure 18 Various stages of the fatigue life redrawn from [Schijve 2009].....	26
Figure 19 Schematic of Kitakawa-Takahashi diagram showing the relationship between stress range and crack length (from [Stephens, Fatemi, Stephens and Fuchs 2000])	27
Figure 20 Different scenarios of fatigue crack propagation (redrawn from [Schijve 2009]).	28
Figure 21 MFM observation results in 304L stainless steel: (a) near an stress corrosion crack, (b) about 5 mm apart from a stress corrosion crack [Takaya and Miya 2005].....	29
Figure 22 In situ EAFM image of early stage grain boundary attack on sensitized 304 SS in 1% oxalic acid, showing exposed chromium carbide precipitates. (b) 21 minutes later, showing dissolution of carbide precipitates [Williford, Windisch Jr and Jones 2000].....	29
Figure 23 (a) SEM observation of a crack with a length of about 200 μm in 304L (b) The same one observed in optical microscope (this 304L specimen is from LMT, ENSC, observed at ECP)	30
Figure 24 EBSD map in the same surface zone in Figure 23.....	30
Figure 25 (a) 2D slice observation with cracks in 302 steel (b) Reconstructed 3D crack surface obtained by manual segmentation with X-ray microtomography technique (c) Combination of a and b [Babout, Marrow, Engelberg and Withers 2006]	31
Figure 26 (a) and (b): Optical microscopy of 304L steel	39
Figure 27 (a) One example of EBSD mapping (b) Distribution of area fraction vs. grain sizes (c) Distribution of grain number vs. grain sizes	39

Figure 28 (a) A cracked inclusion in 304L observed in SEM (b) chemical composition obtained with energy-dispersive (EDS) detector integrated in the SEM.....	40
Figure 29 Tensile curves at room temperature, 150 °C and 300 °C for stainless steel 304L [Haddar 2003].....	41
Figure 30 A hundred-grain polycrystal generated by Voronoi tessellation method [Quey, Dawson and Barbe 2011].	49
Figure 31 Results of EBSD mapping measurements [Le-Pecheur 2008] (a) EBSD on the surface layer (b) reconstruction of EBSD maps of 4 layers	50
Figure 32 (a) Numerical aggregate of 304L steel including actual grain orientation from EBSD (b) Boundary conditions applied to the aggregate during the simulation.	51
Figure 33 Simplified picture showing the inhomogeneous stress distribution from grain to grain due to elastic anisotropy (hypothesis of a homogeneous average stress in each single grain)......	54
Figure 34 Slip Planes and directions in FCC single crystal structure	55
Figure 35 Slip direction and slip plane of the definition of Schmid factor	56
Figure 36 Movement of the dislocation and crossing valleys of Peierls	57
Figure 37 Dislocation forest obstacles	58
Figure 38 A Frank-Read source for the multiple initiation of dislocation loops.....	59
Figure 39 Dislocation structure in a specimen of 304L steel cycled to fracture with a total strain amplitude of 5×10^{-3} [Le-Pecheur 2008].....	61
Figure 40 The description in the modeling for hardening/softening accommodation behavior	61
Figure 41 Dislocation structure in a specimen of 316L steel cycled to fracture with the plastic strain amplitude of (a) 5×10^{-5} (b) 2×10^{-4} (c) 5×10^{-3} [Polak, Obrtlík and Hajek 1994].....	64
Figure 42 Mid-life hysteresis loops for 304L subjected to fully reversed tension-compression cyclic deformation with increasing values of total strain amplitude. The numerical simulated results are examined and compared to fatigue experiments [Le-Pecheur 2008].....	66
Figure 43 (a) Amplitude of the resolved saturation shear stress $\Delta\tau_s/2$ vs. the plastic strain amplitude $\Delta\gamma_{pl}/2$ for 316L steel [Obrtlík, Kruml and Polak 1994; Polak, Obrtlík and Hajek 1994]. (b) Simplified relation of the volume fraction of channels with the cyclic plastic strain amplitude.....	67

List of figures

Figure 44 The stress evolution curves obtained with various K values (cycled with a strain amplitude of $\pm 5 \times 10^{-3}$).....	69
Figure 45 The stress evolution curves obtained with various H values (cycled with a strain amplitude of $\pm 5 \times 10^{-3}$) (a) K=1 (b) K=2	69
Figure 46 Stress/strain hysteresis loops obtained with different H values (cycled with a strain amplitude of $\pm 5 \times 10^{-3}$).....	70
Figure 47 Comparison of hardening and softening curves for a uniaxial low-cycle fatigue test with a total strain amplitude $\pm 0.5\%$ for 304L steel and the stress-strain curves in different phases during fatigue.	71
Figure 48 Comparison of hardening and softening curves for a uniaxial low-cycle fatigue test with a total strain amplitude $\pm 0.3\%$ for 304L steel and the stress-strain curves in different phases during fatigue.	72
Figure 49 Acceleration factors: simulation cycles compared with the experiment cycles	73
Figure 50 Different K and H factor values used for simulating the cyclic hardening and softening under total strain amplitude of 0.3% and 0.5%	74
Figure 51 Numerical simulation of stress-strain loops in comparison with experiments (a) total strain amplitude: 0.3% (b) total strain amplitude: 0.5%	75
Figure 52 Evolution of the stress-strain loop curves during fatigue under total strain amplitude of 0.5% compared with experiments	76
Figure 53 Comparison of stress amplitude evolutions with number of simulated cycles between the old and new enriched CristalECP codes, under the total strain amplitude of $\pm 0.5\%$ (1st cycle = $\frac{1}{4}$ cycle).....	77
Figure 54 Comparison of stress-strain loops at stabilized cycle between the old and new enriched CristalECP codes	78
Figure 55 Distributions of some mechanical factors at tension peak in the stabilized cycle obtained with the old and new enriched CristalECP codes: (a) maximum plastic strain amplitude on the 12 slip systems (b) normal stress on the corresponding plane with maximum plastic strain amplitude (c) local uniaxial strain in loading direction (d) local uniaxial stress in loading direction.....	79
Figure 56 (a) MTS 810 servo-hydraulic system used for fatigue tests (b) Specimen mounted in the grips	85
Figure 57 The plate specimen geometry size for fatigue test under load-controlled	86
Figure 58 In-situ crack observation in SEM (a)(c) zero loading (b)(d) in tension of 1200N (about 200MPa).....	86

Figure 59 The microscope observation zone (1.5mm x 3mm) on the surface	89
Figure 60 Distribution of various crack initiation sites observed on the surfaces.....	91
Figure 61 Cracks initiated from an inclusion (specimen A2) after 7000 cycles under stress amplitude of 260 MPa (a) near slip lines (b) near a grain boundary	92
Figure 62 A crack initiated from an inclusion observed in SEM after 9500cycles under stress amplitude of 260 MPa (specimen A1) (a) at 500x magnification (b) at 1000x magnification (c) at 5000x magnification	92
Figure 63 A crack initiated from an inclusion near the grain boundary observed in SEM after 11500cycles under stress amplitude of 260 MPa (specimen A1) (a) at 2000x magnification (b) at 5000x magnification. (In order to open the crack, the specimen was loaded at about 200 MPa on a in-situ micro machine in SEM).....	93
Figure 64 A crack initiated from an inclusion observed (a) after 30000cycles with an optical microscope LEICA, (b) after 35000 cycles with a digital optical microscope ALICONA, under stress amplitude of 220 MPa (specimen A7).....	93
Figure 65 (a) (b) and (c): Cracks initiate on GB after 20000 cycles under stress amplitude of 220 MPa (specimen A3), observed by SEM	94
Figure 66 Cracks initiated on GB under stress amplitude of 260 MPa after 5000 cycles (specimen A2), observed by SEM.....	95
Figure 67 Cracks initiated on GBs and propagated cross or along slip lines the under stress amplitude of 260 MPa after 5000 cycles (specimen A2), observed by SEM.....	95
Figure 68 Angle α between cracked GB and the loading axis	96
Figure 69 Distribution of the orientations of cracks initiated in grain boundaries with respect to angle α	97
Figure 70 (a) A crack initiated on slip lines, under stress amplitude of 220 MPa after 30000 cycles (specimen A7), observed with an optical microscope LEICA (b) the crack propagates in the lateral direction, this image is taken after 35000 cycles with an optical microscope ALICONA.....	98
Figure 71 Cracks initiated on slip lines after 20000 cycles under stress amplitude of 220 MPa (specimen A3), observed in the SEM.	98
Figure 72 Angle β between cracked slip lines and the loading axis	99
Figure 73 Distribution of the orientations of cracks initiated on slip lines with respect to angle β	99
Figure 74 Cracks initiated at intersection of grain boundaries and slip lines, under stress amplitude of 260 MPa after 11500 cycles (specimen A1) (a) observed in an optical	

List of figures

microscope Alicona (b) observed in the SEM on same zone of a (c) first crack indicated in b (d) second crack indicated in b (e) third crack indicated in b	100
Figure 75 The same crack initiation as shown in Figure 74 (a) and (b) crystallographic orientations obtained from EBSD (c) observed in SEM	101
Figure 76 Crack initiation (Specimen A1) observed in SEM after 9500 cycles under stress amplitude of 260 MPa (a) observed by an optical microscope Alicona (b) observed in the SEM at 1000x magnification (c) at 5000x magnification (d) at 10000x magnification (e) at 30000x magnification	102
Figure 77 (a) A crack observed with an optical microscope LEICA after 30000cycles under stress amplitude of 220 MPa, the crack initiates along the grain boundary (b) The crack propagates first along the slip line and then in the lateral direction, this image was taken after 35000 cycles with an optical microscope ALICONA	103
Figure 78 Angle α' between GB and the loading axis; angle β' between corresponding SL and the loading axis for the cracks initiated at GB-SL	103
Figure 79 Distribution of crack initiations at GB-SLs with various α' and β' angles observed on the surfaces of eight specimens under different load spectra	105
Figure 80 Typical Strain-Life Curve	108
Figure 81 Dissipated energy for one stabilized cycle	110
Figure 82 (a) Simulation of extrusions on the surface by dislocation dynamics (b) Depth of the SL hg and grain size Dg [Depres 2004]	113
Figure 83 (a) Surface observation with an optical microscope ALICONA after 35000 cycles under 220 MPa stress amplitude (specimen A7); three zones with cracks chosen to make the numerical aggregates (b) zone 1 (c) zone 2 (d) zone 3	117
Figure 84 Different kinds of cracks indicated in Figure 83, observed after 35000 cycles under 220 MPa stress amplitude with an optical microscope Alicona (a) Crack No. 1 in zone 2 (b) Crack No. 2 in zone 2 (c) Crack No. 3 in zone1 (d) Crack No. 4 in zone 1 (b) Crack No. 6 in zone 3	118
Figure 85 Surface observation combined with EBSD maps on the three considered zones (a) zone 1 (b) zone 2 (c) zone 3 (cracks are indicated with arrows)	119
Figure 86 Microhardness marks proformed for location-setting and measuring the polished-out thickness	120
Figure 87 Vickers pyramid diamond indenter indentation	120
Figure 88 (a) EBSD maps on four successive layers in zone 1 (b) the 3D meshed aggregate	121

Figure 89 (a) Numerical aggregate of zone 1 performed based on EBSD measurement results (b) boundary conditions applied to the aggregate during the simulation.....	122
Figure 90 (a) Surface observation combined with EBSD maps of zone 1 with an optical microscopy after 35000 cycles under 220 MPa stress amplitude (b) strain ϵ_{22} field after 5 cycles at strain peak (c) stress σ_{22} field after 5 cycles at strain peak.....	123
Figure 91 (a) Surface observation combined with EBSD maps of zone 2 with an optical microscopy after 35000 cycles under 220 MPa stress amplitude (b) strain ϵ_{22} field after 5 cycles at strain peak (c) stress σ_{22} field after 5 cycles at strain peak.....	123
Figure 92 (a) Surface observation combined with EBSD maps of zone 3 with an optical microscopy after 35000 cycles under 220 MPa stress amplitude (b) strain ϵ_{22} field after 5 cycles at strain peak (c) stress σ_{22} field after 5 cycles at strain peak.....	124
Figure 93 (a) Surface observation of zone 1 with an optical microscopy after 35000 cycles under 220 MPa stress amplitude (b) $\Delta\gamma_{max}$ field after 5 cycles at strain peak (c) σ_n field after 5 cycles at strain peak.....	125
Figure 94 (a) Surface observation of zone 2 with an optical microscopy after 35000 cycles under 220 MPa stress amplitude (b) $\Delta\gamma_{max}$ field after 5 cycles at strain peak (c) σ_n field after 5 cycles at strain peak.....	125
Figure 95 (a) Surface observation of zone 3 with an optical microscopy after 35000 cycles under 220 MPa stress amplitude (b) $\Delta\gamma_{max}$ field after 5 cycles at strain peak (c) σ_n field after 5 cycles at strain peak.....	125
Figure 96 FS criterion function fields compared with the surface crack observation.....	126
Figure 97 Plastic strain energy fields compared with the surface crack observation.....	127
Figure 98 LMS criterion function fields compared with the surface crack observation .	128
Figure 99 (a) Simulation results of stabilized hysteresis loops subjected to fully reversed tension-compression cyclic deformation ($R = -1$) with increasing values of total strain amplitude at stabilized cycles. (b) and (c) The distribution clouds of points corresponding to local stress-strain within each element on the surface in peak tension.	135
Figure 100 (a) Distribution of the strain ϵ_{22} of the surface layer at the stabilized cycle; (b) Distribution of the stress σ_{22} of the surface layer at the stabilized cycle.....	136
Figure 101 (a) The specimen geometry for fatigue tests under strain control (b) shape of the notches	137
Figure 102 Load spectra for total strain-controlled fatigue tests.....	138
Figure 103 Microscope observation zone (2mm x 2mm) on the surface	138

List of figures

Figure 104 Comparison of hardening and softening curves obtained under constant strain amplitude of 0.3% and under variable strain amplitude of 0.3-0.7-0.3% for 304L steel, the test under strain amplitude of 0.3% without interruption is from [Le-Pecheur 2008] on the same material.....	139
Figure 105 Stress/strain hysteresis loops during fatigue under total strain-controlled loading, comparison between constant total strain amplitude of $\pm 0.3\%$ and variable strain amplitude of $\pm 0.3-0.7-0.3\%$ (a) after 2000 cycles (b) after 5000 cycles (c) after 9000 cycles (d) after 15000 cycles	140
Figure 106 The relationship between the number of cracks on 4 mm ² observation area of the specimen surface and number of loading cycles under strain-controlled amplitude loading.	141
Figure 107 Cyclic stress-strain curves and surface local stress-strain distributions in tension peak under variable amplitude load spectrum, (a) from 0.3% to 0.7%, (b) from 0.7% to 0.3%.....	142
Figure 108 Distributions of the strain ε_{22} and stress σ_{22} in the surface layer elements before and after the overload when the overload block ends in tension	142
Figure 109 Distributions of the maximum shear strain amplitude on the 12 slip systems and of the normal stress on the slip plane with maximum shear strain amplitude in the surface layer elements before and after the overload when overload block ends in tension	143
Figure 110 Cyclic stress-strain curves and surface local stress-strain distributions in tension peak under variable amplitude load spectrum, (a) $\Delta\varepsilon_t/2$ from 0.1% to 0.5%, (b) $\Delta\varepsilon_t/2$ from 0.5% to 0.1%	144
Figure 111 Stress-strain curves and surface local stress-strain distributions in tension peak while loading amplitude changing from 0.5% to 0.1% (a) overload block ends in tension (b) overload block ends in compression.....	145
Figure 112 Distributions of local strain ε_{22} and stress σ_{22} in the surface layer elements before and after the overload when overload block ends in tension	145
Figure 113 Distribution of local strain ε_{22} and stress σ_{22} on the surface layer elements before and after the overload when overload block ends in compression.....	146
Figure 114 Comparison of the distribution of maximum shear on the 12 slip systems $\Delta\gamma_{max}$ and normal stress on the relevant slip plane σ_n in the surface layer elements before and after an overload when the overload block ends in tension.....	146
Figure 115 Comparison of the distribution of maximum shear on the 12 slip systems $\Delta\gamma_{max}$ and normal stress on the relevant slip plane σ_n in the surface layer elements before and after an overload when the overload block ends in compression	147

Figure 116 Comparison of distribution of function value of SF criterion in the surface layer elements before and after the overload when overload block ends (a) in tension and (b) in compression	148
Figure 117 The relationship between the number of cracks on 4.5 mm ² observation area of the specimen surface and the number of loading cycles under load-controlled amplitude loading.	149
Figure 118 Stress/strain curves simulated under four different loading paths	151
Figure 119 Distributions of strain ε_{22} and stress σ_{22} in the surface layer elements at peaks before and after the overload, loading path 1: overload block starts in compression and ends in tension.	152
Figure 120 Distributions of strain ε_{22} and stress σ_{22} in the surface layer elements at peaks before and after the overload, loading path 2: overload block starts in tension and ends in compression.	153
Figure 121 Distributions of strain ε_{22} and stress σ_{22} in the surface layer elements at peaks before and after the overload, loading path 3: overload block starts and ends both in compression.	153
Figure 122 Distributions of strain ε_{22} and stress σ_{22} in the surface layer elements at peaks before and after the overload, loading path 4: overload block starts and ends both in tension.	154
Figure 123 Field results of strain ε_{22} in the surface layer elements at peak before and after the overload, analysis of the four loading paths.	155
Figure 124 Field results of strain σ_{22} in the surface layer elements at peak before and after the overload, analysis of the four loading paths (same color scale).	156
Figure 125 Field results of strain amplitude of $\Delta\varepsilon_{22}/2$ in the surface layer elements before and after the overload, analysis of the four loading paths (same color scale).	157
Figure 126 Maximum shear strain amplitude fields before and after the overload with four different loading paths (same color scale).	158
Figure 127 Fields results of normal stress on corresponding plane before and after the overload with four different loading paths (same color scale)	158

List of tables

Table 1 Comparison of chemical composition of austenitic stainless steels 304 and 316 (wt%) [Cunat 2003]	37
Table 2 Chemical composition of 304L steel used in this study (wt. %) [Le-Pecheur 2008]	38
Table 3 Mechanical properties of austenitic stainless steels 304L at room temperature [Farahmand, Bockrath and Glassco 1997; Haddar 2003; Le-Pecheur 2008]	42
Table 4 Some parameters in the elastic stiffness matrices and anisotropy coefficients of several common materials	53
Table 5 Schmid and Boas notation of slip systems in FCC	55
Table 6 The parameters of the crystalline constitutive law identified for 304L steel	68
Table 7 Fatigue load spectra used under constant load-controlled amplitude.....	87
Table 8 Fatigue load spectra considered under variable load-controlled amplitude	88
Table 9 Interruption and observation cycles during fatigue tests.....	89
Table 10 Number of cracks at various crack initiation sites, from 8 fatigue tests under load-controlled loading.....	90
Table 11 Distribution of the orientations of cracks initiated in grain boundaries with respect to angle α	96
Table 12 Distribution of the orientations of cracks initiated on slip lines with respect to angle β	99
Table 13 Distribution of the orientations of cracks initiated GB-SLs with respect to angle α'	104
Table 14 Distribution of the orientations of cracks initiated GB-SLs with respect to angle β'	104
Table 15 $\Phi(x)$ fonction in the fatigue criteria.....	115
Table 16 Analysis of distribution clouds in the stabilized state: σ_{22} - ε_{22} in peak tension	135
Table 17 Values of the local stress and strain in all the elements at free surface before and after the overload.....	154

Introduction

Thermal fatigue in high or low cycle regime is a relatively new phenomenon in the nuclear energy field. Nevertheless, the components of the cooling circuits of PWR (Pressurized Water Reactor) are subjected to thermal fluctuation that may lead to fatigue cracks which can propagate up to failure. This was the reason of the incident that occurred in the cooling circuit of the reactor of the Civaux nuclear power station in 1998 [Maillot, Degallaix, Degallaix and Fissolo 2006; Le-Pecheur 2008; Osterstock 2008]. This problem highlighted the risk of thermal fatigue damage zones on pipes where turbulent fluids having different temperatures mix.

The available rules of fatigue design codes for PWR components are based on load-controlled fatigue tests. Features observed in the temperature mixing zones allowed engineers to conclude that these design rules could not be tailored to this new phenomenon. For structures subjected to thermal fatigue with variable amplitude loading cycles in service, the fatigue problem becomes rather complex. One purpose of this study is to contribute to the elaboration of a more suitable fatigue criterion under variable amplitude loading.

In order to understand and predict the damage and fatigue life of a component in the temperature mixing zone mentioned above, it is important to understand the cyclic deformation behavior of material and its loading history effects. Different models have been proposed to represent the effects of variable amplitude loadings, and some rules have also been developed for mean stress effects [Suresh 1991; Shin and Hsu 1993; Hamam, Pommier and Bumbieler 2007; Harmain 2009; Fatemi and Colin 2010]. However, these criteria are generally proposed from the macroscopic point of view and are thus not linked to the microstructure properties. Therefore, in order to understand the mechanisms of the damage occurring in materials, it is essential to take into account the microstructural mechanisms of cyclic plastic strain within grains.

Many studies have been conducted in this domain for years, and significant progress has been made in understanding the mechanisms of fatigue damage [Suresh 1991; Stephens, Fatemi, Stephens and Fuchs 2000; Krupp 2007; Schijve 2009]. These advances are mainly due to the confluence of high performance computing, advanced experimental methods for in situ and ex situ measurement and observation of evolving microstructure at various length scales under cyclic loading, leading to deeper understanding of cyclic deformation mechanisms and relevant modeling in fatigue. These various elements have introduced new possibilities to consider the role of the microstructure in the initiation and growth of small cracks in fatigue.

The purpose of this work is to study the influence of the microstructure on cyclic plasticity and crack initiation in 304L austenitic stainless steel (used in temperature mixing zones mentioned above) under constant amplitude and variable amplitude loading. For this purpose, numerical simulations of cyclic plasticity and fatigue crack initiation,

based on crystal plasticity theory, were performed and compared to experimental observations under the same loading condition. Thus the influence of local values of mechanical factors, used in both macroscopic and microscopic fatigue criteria, on crack initiation in the grains was evaluated through the comparison between experimental surface observation and numerical simulation from 3D aggregates with realistic crystallographic orientations. Strain-controlled and load-controlled fatigue tests were conducted and the specimen surfaces were intermittently observed using 3D optical microscope or SEM during the fatigue tests to observe and analyze the slip lines distribution and crack initiation sites. EBSD was used to obtain the crystallographic orientations on the surface to help identifying crack initiation sites. In addition, cross sectioning EBSD maps were also used to provide realistic crystallographic orientations of the 304L specimen in order to construct the finite element aggregates for comparison purposes.

This thesis includes five chapters:

- The first chapter is a part of literature review. Some key points in fatigue theory are reviewed in particular for 304L. Some experimental results of macroscopic cyclic stress-strain response and evolution of dislocation microstructure during cyclic loading are presented. Then several new experimental crack observation techniques are reviewed. Lastly, the literature review of overload effects on the long crack propagation is presented.
- The second chapter is a literature study of the material properties of stainless austenitic steel 304L. It includes its chemical composition, deformation mechanisms and mechanical properties.
- The third chapter describes the development of the crystal plastic code CristalECP. The enriched model is able to better simulate the cyclic hardening and softening behavior based on polycrystal deformation theory. Cyclic hardening and stabilization are considered to relate to the dislocation density increase and saturation. The softening behavior is described as the result of the formation of persistent slip bands and corresponding evolution of dislocation microstructure (walls and channels). The results show that local strain amplitude distribution is enlarged if considering the cyclic hardening/softening behavior.
- The fourth chapter presents the studies about prediction of crack initiation sites based on the polycrystal numerical simulation results under constant strain amplitude loading. The first half of this chapter gives some experimental observations of the microcracks in fatigue experiments and indicates the microcrack types classified by their initiation sites. In the second part, some fatigue criteria based on both macro- and micro-approach in literature are reviewed. The last part presents the numerical simulations and mechanical field results which are compared with the experimental surface observations. These results allow us to evaluate the efficiency of the mechanical factors issued from fatigue criteria that control the crack initiation in the grains. These parameters can give useful contributions to predict the crack initiation location and severity in

order to eventually propose a new more adapted fatigue crack initiation criterion based on mechanical parameters which actually control the crack initiation.

- Lastly, the fifth chapter deals with the variable amplitude loading effects on cyclic plasticity and microcrack initiation. Firstly, the simulation results of distribution clouds corresponding to local stress and strain under five constant strain amplitudes loading are analyzed, and compared with experimental results. Next, this chapter presents the historical loading effects on cyclic plasticity and microcrack initiation under both load-controlled and strain-controlled loading conditions. The results show that “microscopic” parameter maximum plastic shear strain amplitude on the 12 slip systems $\Delta\gamma_{max}$ used in Socie-Fatemi criterion is more likely to give good predictive results for variable amplitude loading condition.

Chapter 1

Literature review of fatigue

Table of contents

CHAPTER 1 LITERATURE REVIEW OF FATIGUE	5
1.1 HISTORICAL OVERVIEW.....	7
1.2 HIGH CYCLE FATIGUE AND LOW CYCLE FATIGUE.....	9
1.2.1 <i>High cycle fatigue</i>	9
1.2.2 <i>Low cycle fatigue</i>	9
1.3 APPROACHES TO FATIGUE ANALYSIS	9
1.4 CYCLIC DEFORMATION.....	10
1.4.1 <i>Cyclic stress – strain response</i>	10
1.4.2 <i>Evolution of dislocation microstructure during cyclic loading</i>	13
1.5 FATIGUE CRACK INITIATION AND PROPAGATION.....	19
1.5.1 <i>Fatigue crack initiation</i>	19
1.5.2 <i>Fatigue crack propagation</i>	25
1.5.3 <i>Transition from the crack initiation to propagation stage</i>	25
1.6 CRACK OBSERVATION TECHNIQUES	28
1.7 FATIGUE UNDER VARIABLE-AMPLITUDE LOADING	31
1.8 SUMMARY	34

1.1 Historical overview

Fatigue is the localized and progressive structural damage that occurs when a material is subjected to cyclic loading. The maximum stress values are less than the ultimate tensile strength, and may be below the yield stress of the material. Fatigue has been a problem for engineers since the earliest days of industrial revolution. The first study of metal fatigue was conducted by a German mining engineer, W.A.J. Albert, who performed repeated proof load tests on iron mine-hoist chains around 1829. Since then, significant progress has been made in the study of fatigue [Suresh 1991; Krupp 2007; Schijve 2009].

Over the years, fatigue has been a widely accepted term in engineering field to describe damage and failure of materials under cyclic loading. In general, there are several common types of fatigue: mechanical, creep, thermo mechanical, sliding, rolling, fretting and corrosion fatigue [Suresh 1991]. Mechanical fatigue is due to fluctuations in applied stresses or strains. Cyclic loading in association with high temperatures, results in creep-fatigue while a combination of cyclic loading and thermal high-low temperature fluctuation causes thermomechanical fatigue. Repeated applications of load in conjunction with sliding and rolling contact between material surfaces produce sliding and rolling contact fatigue respectively, while fretting fatigue occurs as a result of pulsating stresses along with oscillatory relative motion and frictional sliding between surfaces. Corrosion fatigue is caused by fluctuating load in the presence of corrosive environments.

The first detailed research into fatigue was initiated in 1842 following the Versailles railway accident in France [Suresh 1991]. An early explanation for fatigue was the ‘crystallization theory’, which postulated that the cause of fatigue failure in materials resulted from microstructural crystallization due to the very fine and smooth appearance of fatigue crack. This theory remained unchallenged for several decades until the work of Ewing and Humphrey in 1903 showed the development of slip bands and subsequent fatigue cracks in polycrystalline materials [Ewing and Humphrey 1903]. They tested specimens of Swedish iron in rotating bend at stress levels above their fatigue limit, the specimen surface being polished and etched. They observed few slip lines initially and new slip lines formed close to existing ones, producing slip bands. Although these bands grew wider and denser, there were areas between the bands where no slip was observed. Successive workers using other ductile polycrystals and more sophisticated metallographic techniques have added more detail which, in general, has confirmed the sequence of events described by Ewing and Humphrey. For example, some decades later, Thompson [Thompson, Wadsworth and Louat 1956] tested annealed electropolished, polycrystalline high-purity copper specimen in reversed direct stress (zero mean load), the specimen being removed from the fatigue machine and examined metallurgically. Slip bands appeared early in the test and became more numerous as the test progressed. Electropolishing removed the roughness associated with slip bands, and most of them became invisible. A few, however, became accentuated and were termed persistent slip bands; fatigue cracks grew eventually from these bands. If the electropolishing was continued until the persistent bands were removed, it was found that the slip bands reformed and again became persistent. In many cases the pattern of the new bands

reproduced in some detail that which had been removed, implying that slip was still active on the same planes. Because no new markings were ever uncovered in internal structure of material during the electropolishing, this shows that the origin of cracking was associated with the free surface.

One of the earliest systematic investigations of fatigue failure, worked by A. Wöhler from 1852-1869, was full scale fatigue testing in torsion, bend and axial loading of railway axles [Suresh 1991]. His work contributed to the characterization of fatigue behavior in terms of stress amplitude-life (S-N) curves and also to the introduction of the concept of fatigue endurance limit. Some engineers in the second half of the nineteenth century, such as Gerber (1874) and Goodman (1899) began developing methods for fatigue design and formulated ways to account for mean stresses. Bauschinger (1886) first observed the differences in the elastic limit for materials subjected to reverse loading, and later in 1910, the changes in stress-strain response during cycling were investigated by Bairstow, and he subsequently identified cyclic softening and hardening behavior in metals [Suresh 1991; Krupp 2007; Schijve 2009] .

Basquin in 1910 first proposed equations for the characterization of S-N curves and it was later refined by Coffin and Manson (1954) for strain-based characterization of fatigue [Manson 1954]. Investigations into damage accumulation models for fatigue were performed by Palmgren (1924) and Miner (1945) [Miner 1945]. Neuber, in 1946, studied the effects of notch on monotonic and cyclic deformation, while Langer (1937) pioneered the work in variable amplitude fatigue.

In 1961, a power law was proposed by Paris, Gomez and Anderson which characterized the crack propagation rate in terms of stress intensity factor amplitude, ΔK . This later became known as Paris' Law. The next important contribution came in 1970, when Elber showed that fatigue cracks could remain closed even when subjected to cyclic tensile loads. From this, the concept of crack closure was born. Since then, Ritchie, and Suresh, amongst many others, have intensified research in crack closure and its effects on fatigue crack propagation. Today, crack closure and its associated effects form the basis for any mechanistic study of fatigue crack propagation.

More recently, significant interest in fatigue research has centered on short or small fatigue crack propagation. This problem was first identified by Pearson in 1975, who observed that crack propagation rates for short cracks are higher than those observed for long cracks at the same stress intensity range. Crack propagation, even at stress intensity ranges below the threshold for long cracks has also been detected. Such anomalous behavior contradicts conventional LEFM theory and thus far, significant progress has been made in characterizing the types of short cracks and explaining this unique behavior [Kitagawa and Takahashi 1976].

The past decade has witnessed a confluence of high performance computing, advanced experimental methods for in situ and ex situ measurement of evolving microstructure at various length scales under cyclic loading, and substantial advances in understanding deformation mechanisms, material degradation, and relevant modeling concepts in fatigue. Together, these various elements have introduced new possibilities to consider the role of

the microstructure on the initiation and propagation of small cracks in fatigue. Microstructure-sensitive computational methods for fatigue crack formation in polycrystalline microstructures over the past few decades were developed rapidly [Barbe, Decker, Jeulin and Cailletaud 2001; Barbe, Forest and Cailletaud 2001; Devincere, Kubin and Hoc 2006; Zeghad, Forest, Gourgues and Bouaziz 2007; Zeghad, N'Guyen, Forest, Gourgues and Bouaziz 2007; McDowell and Dunne 2010; Saai, Louche, Tabourot and Chang 2010; Schwartz, Fandeur and Rey 2010]. Such approaches can be pursued to explore effects of microstructure attributes that give rise to extreme value fatigue responses which are associated with the tails of probability distributions of potential surface and subsurface fatigue crack formation sites, including transitions between modes of crack formation, surface to subsurface transitions, and so forth.

1.2 High cycle fatigue and low cycle fatigue

1.2.1 High cycle fatigue

High-cycle fatigue is considered when the cyclic loadings induce stresses close to but below the engineering yield stress so that the number of cycles to initiate a microcrack is high, which typically is larger than 10^5 . The plastic strain is usually not measurable on a mesoscale but dissipation exists on a microscale to induce the phenomenon of damage [Lemaitre and Desmorat 2005].

1.2.2 Low cycle fatigue

Low cycle fatigue failures may occur when structures are subjected to heavy cyclic loadings which induce irreversible strains on small or large scale, giving rise to damage up to crack initiation and propagation [Lemaitre and Desmorat 2005].

The number of cycles to rupture can be on the order of 10 to 100 for aerospace rockets. It can be on the order of 100 to 1000 for nuclear or thermal power plants, chemical plants, and many domestic apparatus as the butt hinges of polymeric boxes. The state of stress is somewhat higher than the yield stress σ_y . For aircraft engines or car engines where, on some parts, the number of cycles to rupture can be on the order of 1000 to 10000, the state of stress induces plastic strain on the order of the elastic strain. For $10^4 < N_R < 10^5$, low- or high-cycle fatigue may be considered depend on the case and, moreover, on the degree of accuracy needed [Lemaitre and Desmorat 2005]. Low cycle fatigue is mainly governed by the local strain at meso-level and it is essentially encountered in metals.

1.3 Approaches to fatigue analysis

Generally there are three main approaches (stress, strain and “damage” approach or fracture mechanics) to fatigue analysis [Ravichandran, Ritchie and Murakami 1999; Stephens, Fatemi, Stephens and Fuchs 2000; Krupp 2007; Schijve 2009].

Under stress-based approach, the stress-life (S-N) curves (magnitude of a cyclic stress (S) against the number of cycles to failure (N)) are used primarily for fatigue life prediction. A main feature commonly found in S-N curves is the fatigue or endurance limit, σ_D , which defines the maximum stress amplitude possible for a defect-free specimen to have infinite life when mean stress is zero. The endurance limit for metallic materials is typically listed at 10^7 cycles. Stress-based approach to fatigue is used primarily for long life, high cycle fatigue, and elastic and unconstrained deformation problems [Suresh 1991; Schijve 2009].

Strain-based approaches over the stress-based approach can handle local plasticity effects with greater detail than the latter and take into account both elastic and inelastic deformation under constrained conditions. Contrary to the stress-based approach, load levels are high and usually exceed the yield stress of the material. The result of this is considerable cumulative plastic deformation and hence, plastic strain is much larger than elastic strain and fatigue life is controlled by ductility [Suresh 1991; Schijve 2009].

Early fatigue investigations were carried out using predominantly stress-based approaches. However, since the introduction of servo-hydraulic testing machines, strain-based approaches have become increasingly popular in their use to analyze fatigue problems. Both approaches represent extremes of completely unconstrained or stress-cycling conditions and completely constrained or strain-cycling conditions. However, fatigue under conditions of controlled strain is more favorable since most high performance engineering components are subjected to a certain degree of structural constraint, reminiscent of strain-control. Furthermore, fracture mechanics has proved efficient in facilitating the understanding of crack propagation mechanisms and characterizing crack propagation rates. Stress or strain-based approaches may provide total life data for smooth samples subjected to complex loading histories [Stephens, Fatemi, Stephens and Fuchs 2000; Schijve 2009].

The 304L or 316L steel structures, for example, used in the nuclear industry are particularly subjected to low-cycle fatigue. LCF analysis needs to handle local plasticity effects and takes into account both elastic and inelastic deformation under constrained conditions. However, according to fatigue tests of 304L, it was found that even when 304L steel is subjected to a small level strain amplitude loading, it shows cyclic plastic behavior as well [Le-Pecher 2008]. In particular, the stress-based, strain-based, energy-based and mixed approach can all commonly be used for the fatigue analysis of structures in 304L or 316L [Curtit 2007].

1.4 Cyclic deformation

1.4.1 Cyclic stress – strain response

When a metal is subjected to cyclic loading, characteristic stress-strain response curves are observed depend on the material type, initial condition (annealed or work hardened) and loading conditions (stress or strain controlled, loading amplitude and so on). Under strain-controlled fatigue, cyclic hardening means stress amplitudes increases with

increasing number of cycles. The opposite occurs for cyclic softening, where the stress amplitudes of hysteresis loops decreases with increasing number of cycling. In general, the rate of hardening progressively diminishes and reaches the maximum stress amplitude then cyclic softening occurs. And with continued cyclic loading, a quasi-steady state of stress-strain cycle (cyclic saturation) will be reached. It is common for cyclic saturation to be reached within half-life in most cases of fatigue loading. As a result, the calculation of fatigue parameters are usually based on mid-life hysteresis loop data [Sandor 1972; Stephens, Fatemi, Stephens and Fuchs 2000; Schijve 2009].

For 304L steel, generally the fatigue behavior consists of three phases during fatigue under cyclic constant strain amplitude loading. There is first a consolidation phase with a primary hardening during the first cycles. This phase is followed by a cyclic softening phase, and then it reaches a stabilization phase. However, the stabilization is not observed for all tests, it depends on the imposed strain amplitude. Figure 1a gives the change of stress for different strain amplitudes during the total strain controlled fatigue test for 304L with the different strain amplitudes from 0.15% to 1% [Le-Pecher 2008]. It can be found that cyclic hardening and softening behavior is significant. However, in the lower domain of plastic strain amplitude (less than 0.01%), the pronounced initial growth of the stress amplitude is followed by saturation (see Figure 2). The saturated stress amplitude is constant up to 3×10^6 - 5×10^6 cycles [Polak, Obrtlík and Hajek 1994]. Furthermore, in the higher plastic amplitude domain (greater than 1%) due to the early fracture, the softening is only transient or absent and the stress amplitude increases during most of the fatigue life.

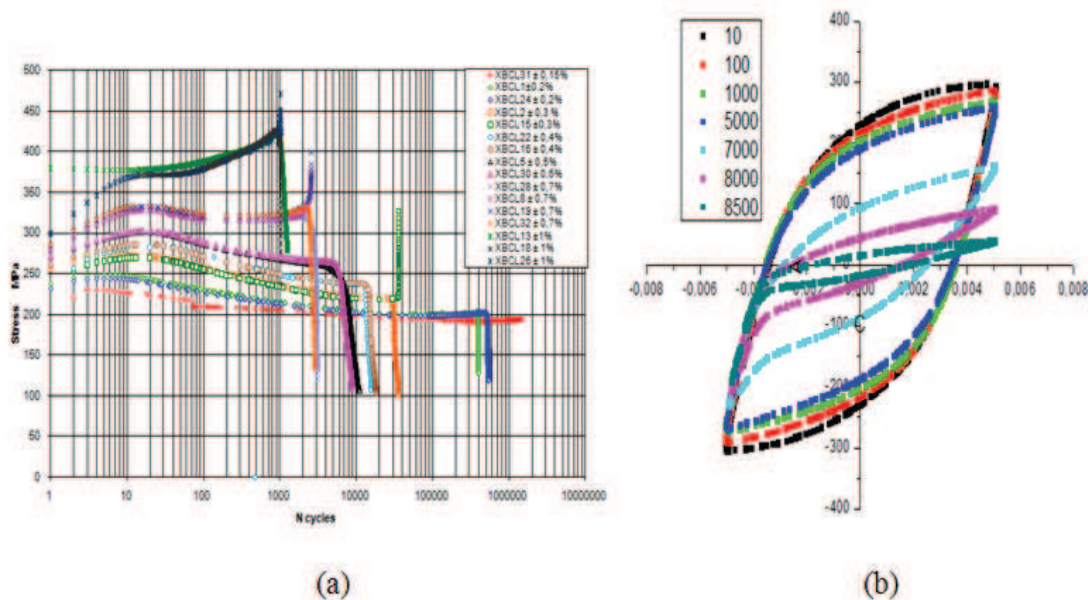


Figure 1 (a) Cyclic hardening/softening curves for 304L steel [Le-Pecher 2008] (b) Evolution of stress-strain loops under controlled strain cycling amplitude ± 0.005 , a progressive decrease in stress amplitude is observed with increasing cycles, final instability is due to macrocrack propagation

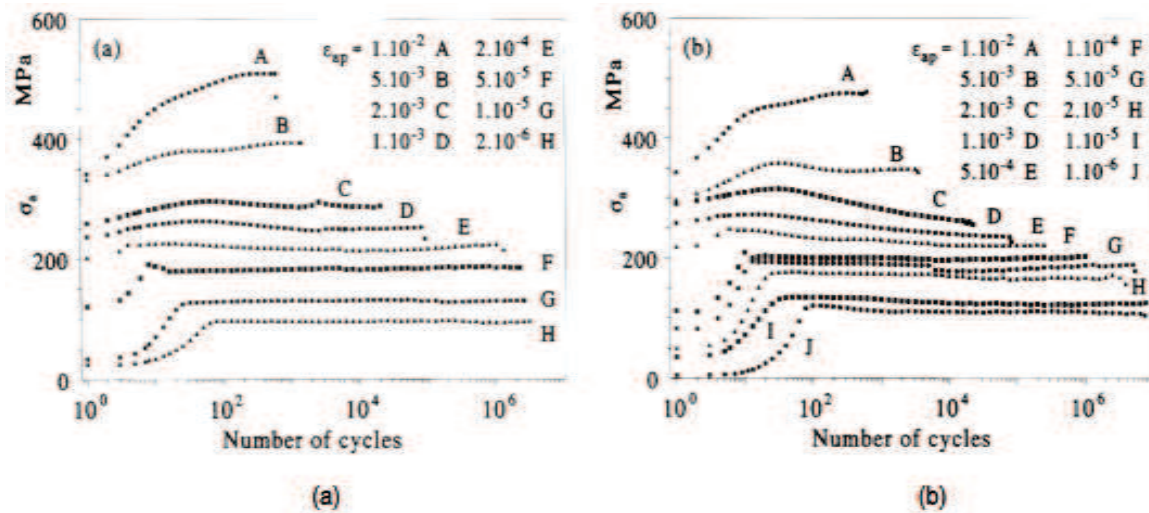


Figure 2 Cyclic hardening/softening curves for 304L steel (a) 316L-VZ steel (b) 316L-TH steel [Polak, Obrtlík and Hajek 1994]

Other research work showed that, for 304L or 316L steel hardening/softening behavior, the stress/strain curve at mid-life and the crack initiation life are both strongly influenced by temperature [Ravichandran, Ritchie and Murakami 1999; Hull and Bacon 2001; Haddar 2003] (see Figure 3). The evolution of maximum and minimum stress at the same total strain amplitude shows that the material has a higher tensile stress and a higher fatigue life at 90°C than at other higher temperature levels.

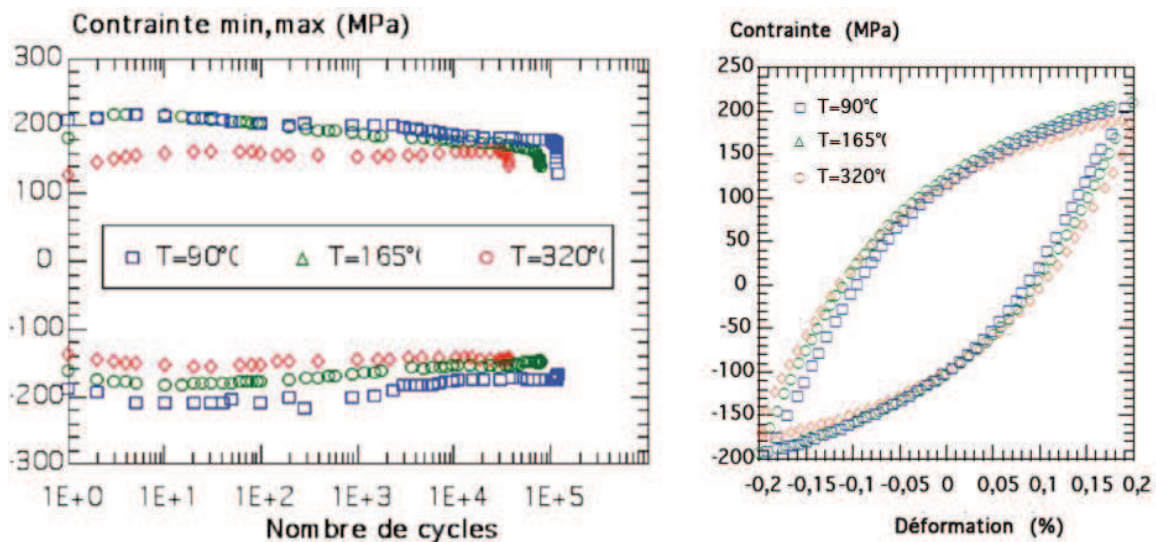


Figure 3 Temperature effect on the fatigue behavior of 304L (a) Evolution of minimum and maximum with increase of the number of cycles (b) Stress/ strain curves at mid-life under 90, 165 and 320 °C, total strain amplitude equal to $\pm 0.2\%$, $f = 1$ Hz [Haddar 2003]

Cyclic stress-strain response and fatigue lives have also been found to be highly dependent on grain size [Rao, Valsan, Sandhya, Mannan and Rodriguez 1991; Kobayashi,

Yamaguchi, Hayakawa and Kimura 2005; Song, Lee and Kim 2005; Zhang and Jiang 2006; Basu, Das, Bhattacharjee and Chakraborti 2007]. K. Basu et.al investigated at room temperature low cycle fatigue (LCF) behavior of solution annealed austenitic stainless steel AISI 316L with two different grain sizes of 90 and 139 μm developed by solution annealing treatment at 1050 and 1150 $^{\circ}\text{C}$ respectively and at six strain amplitudes ranging between 0.375% and 1.0% [Basu, Das, Bhattacharjee and Chakraborti 2007]. The results show that grain size has a major influence on determining the LCF life in such a manner that coarser grain size results in higher cyclic life above 0.5% strain amplitude within the experimental domain. The differences of cyclic life increase with the increasing strain amplitude for strain amplitude greater than 0.5%. In addition, cyclic hardening occurs both in these AISI 316LN steels with two grain sizes, the degree of hardening being higher with fine grain sized steel [Basu, Das, Bhattacharjee and Chakraborti 2007] (see Figure 4).

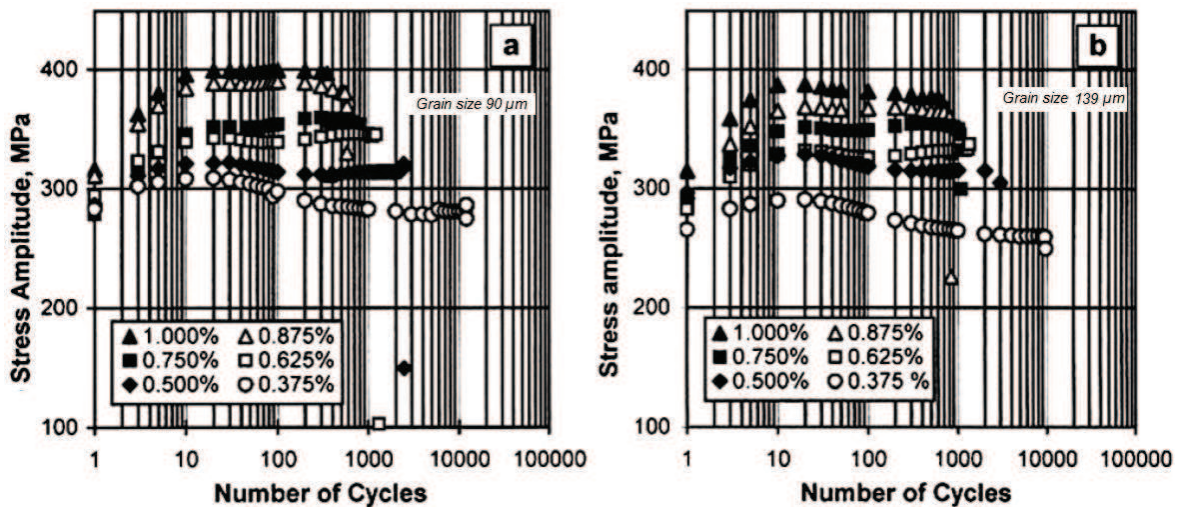


Figure 4 Cyclic stress response at various strain amplitudes for austenitic stainless steel AISI 316L with two different grain sizes of 90 and 139 μm [Basu, Das, Bhattacharjee and Chakraborti 2007]

1.4.2 Evolution of dislocation microstructure during cyclic loading

It is important to explain the stress-strain response of fatigue loading on the basis of microstructure because microstructural processes underlie and influence the examination, interpretation, and understanding of macroscopic behavior. The basic mechanism for cyclic deformation involves irreversible dislocation movement within the microstructure.

Experiments of fully reversed fatigue under constant amplitudes of resolved plastic shear strain point to the existence of a saturation stress after initial cyclic hardening. A plot of peak resolved shear stress at saturation as a function of plastic shear strain amplitude provides the cyclic stress-strain curve for a copper single crystal, which was first experimentally measured by Mughrabi [Mughrabi 1978]. Figure 5 shows schematically a diagram for FCC single crystals oriented for single slip.

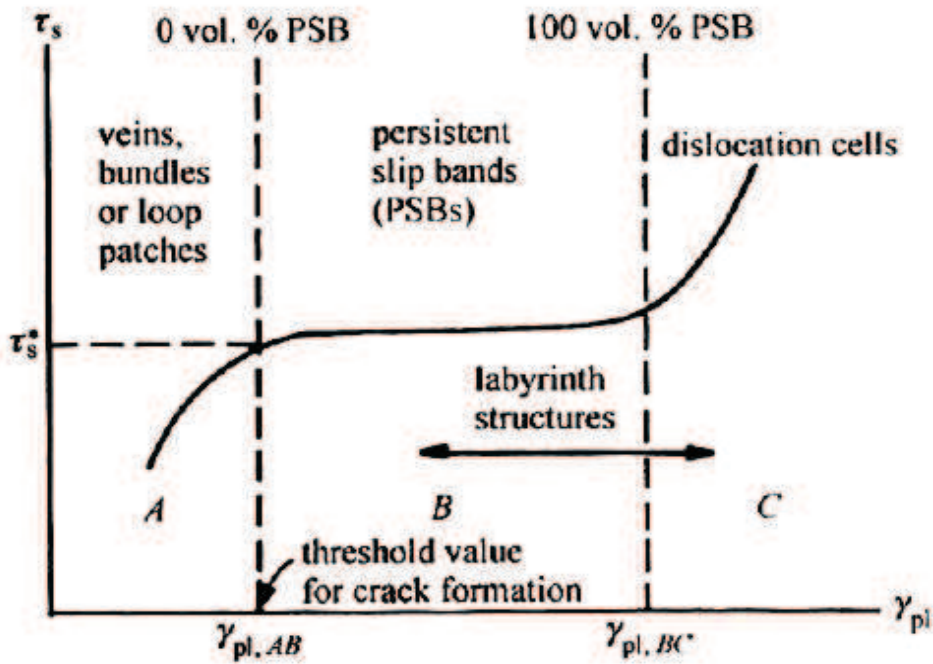


Figure 5 Schematic diagram showing different regimes of the saturation stress-strain curve [Suresh 1991]

The microstructural processes that take place in polycrystals are basically the same as those studied for single crystals: at low amplitudes, loose veins are formed; in an intermediate range, veins with PSBs are formed and at high amplitudes, cells are formed. Even when cyclic saturation is reached, minor changes to dislocation structures have been found. It is important to realize that dislocation arrangement and cell size are determined primarily by the plastic strain amplitude and not the flow stress [Suresh 1991; Polak, Degallaix and Degallaix 1993; Obrtlik, Kruml and Polak 1994; Polak, Obrtlik and Hajek 1994; Schijve 2009]. For 316L or 304L steel, there are also three similar regimes considered to describe the microstructure evolution as shown in Figure 6 [Obrtlik, Kruml and Polak 1994; Polak, Obrtlik and Hajek 1994]. The dislocation arrangement for slip systems during cyclic loading is highly dependent on the loading amplitude and number of cycles during fatigue [Polak, Degallaix and Degallaix 1993; Obrtlik, Kruml and Polak 1994; Polak, Obrtlik and Hajek 1994].

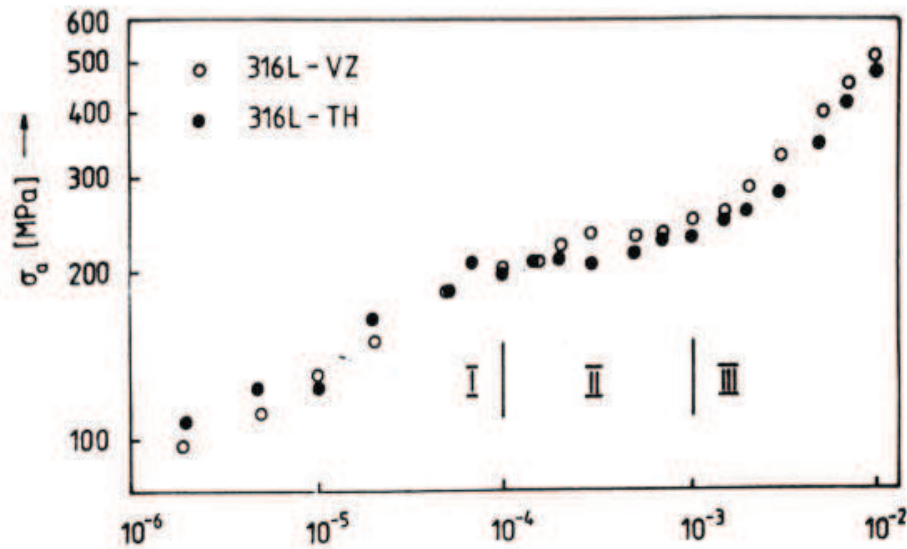


Figure 6 Amplitude of the resolved saturation shear stress $\Delta\tau^s/2$ versus the plastic strain amplitude $\Delta\gamma_{pl}/2$ for 316L steel [Obrtlík, Kruml and Polak 1994; Polak, Obrtlík and Hajek 1994]

Cyclic loading in small plastic amplitudes yields arrangements of edge dislocation dipoles caused by single slip. Dislocations often agglomerate into bundles or veins which are separated by regions of low dislocation density. At low plastic amplitudes in region A (in Figure 5), cyclic hardening is due almost entirely to the accumulation of primary edge dislocations. During the initial phases of cycling, dislocations are produced which accumulate on the primary glide plane [Suresh 1991]. Fully reversed cyclic strain produces approximately equal amounts of positive and negative edge dislocations which are attracted over small distances to form dislocation dipoles. This process of positive and negative dislocation attraction can also be termed trapping. Only edge dislocations are likely to form dipoles since screw dislocations have a tendency of cross slipping, which is promoted in materials with high stacking fault energies, mutually annihilating each other in the process. Figure 7 shows the dislocation structures of a 316L specimen cycled with rather low plastic strain amplitude of 5×10^{-4} at middle life and at failure [Obrtlík, Kruml and Polak 1994].

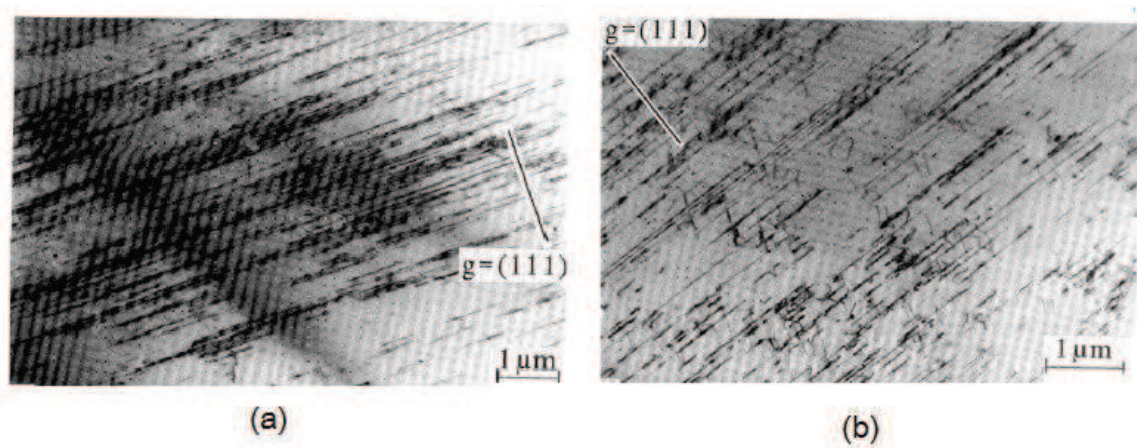


Figure 7 Dislocation structure of a 316L specimen cycled with a plastic strain amplitude of 5×10^{-4} (a) $N=2.2 \times 10^6$ cycles (at mid-life) (b) $N= 5.3 \times 10^6$ cycles (at failure) [Obrtlík, Kruml and Polak 1994]

After cycling under a little higher plastic strain amplitude from regime A to B, the accumulation of dislocations occurs predominantly in the form of mutually trapped edge dislocations, typically called veins, bundles or loop patches, making up approximately 50% by volume of the matrix shown in Figure 8a. Dislocation veins contribute to the cyclic hardening during the initial stages of fatigue by partially impeding dislocation motion on the primary slip system. Matrix veins are known to accommodate only small plastic strains of the order of 10^{-4} and undergo microyielding [Suresh 1991]. One of the most visible features of cyclic saturation is the localization of slip along bands. This process is formed at strain amplitudes corresponding to the beginning of region B and is intensified as the applied plastic strain is increased as shown in Figure 9. These slip lines were termed persistent slip bands firstly by the group of Thompson [Thompson, Wadsworth and Louat 1956]. They found that in Ni and Cu, the bands persistently reappeared at the same sites during continued cycling even after a thin layer of the surface containing these bands was removed by electropolishing. Some studies of microhardness measurements on fatigue-induced slip bands revealed that the PSBs are much softer than the matrix [Helgeland 1965]. These results imply that during saturation in the plateau region of the cyclic stress-strain curve, essentially the entire deformation is carried by PSBs. In fact, the formation of the PSBs appears to be closely related to the occurrence of the plateau. The increase in the volume of the crystal covered by the PSBs is due to the increase in plastic strain amplitude [Suresh 1991]. From Figure 9, it is clearly shown matrix structure with PSB structure in the 316L specimens cycled at beginning of the plateau regime which is also in accordance with the descriptions of those in single crystal [Obrtlík, Kruml and Polak 1994].

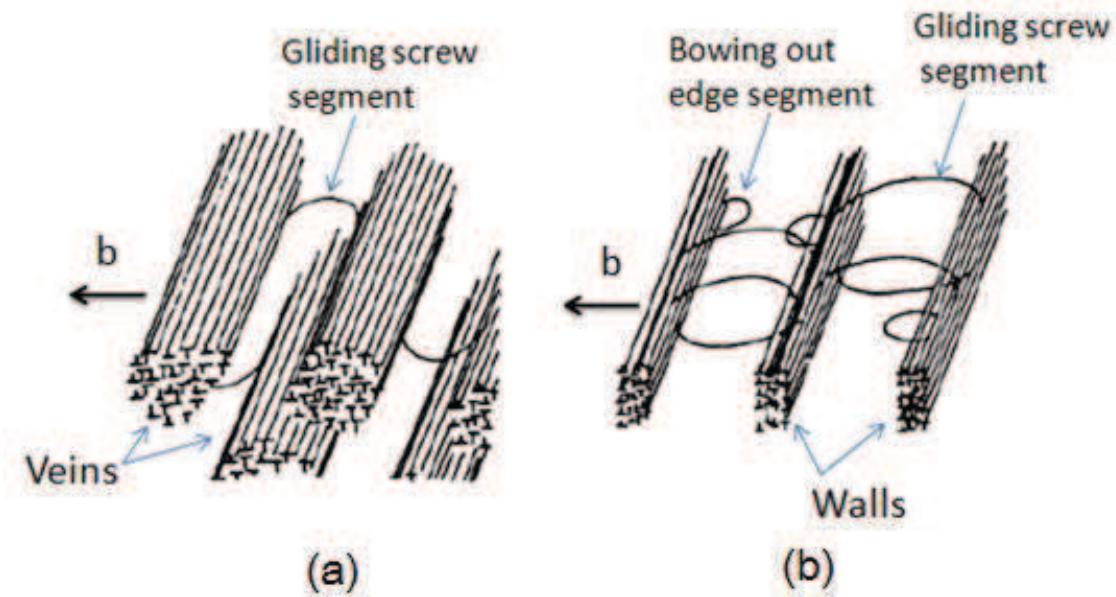


Figure 8 Schematic representation of the dislocation arrangements in (a) a matrix structure and (b) a persistent slip band (redrawn from [Suresh 1991])

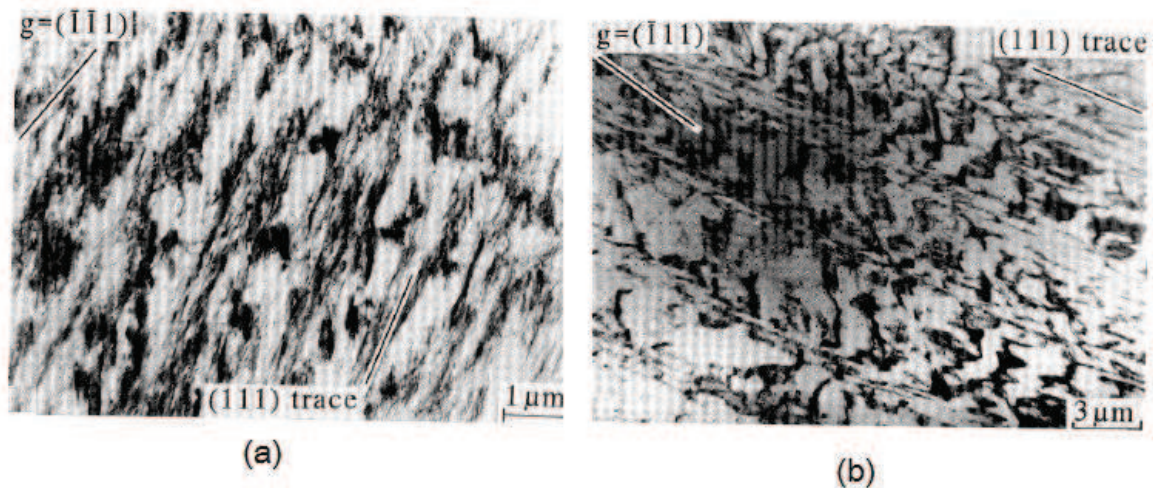


Figure 9 Matrix structure with PSB structure in the 316L specimens cycled in the plateau regime (a) with a plastic strain amplitude of 2×10^{-4} , $N = 1.3 \times 10^6$ cycles (at failure) (b) a plastic strain amplitude of 1×10^{-3} , $N = 9 \times 10^4$ cycles [Obrtlík, Kruml and Polak 1994]

The dislocation structures in PSBs are considerably different to that observed in a matrix. It consists of dislocation veins that only occupy 10% of volume and are arranged into wall-like configurations (Figure 8b) [Suresh 1991]. PSBs can support high plastic shear strains of the order of 0.01 and undergo macroyielding. A dynamic equilibrium between dislocation multiplication and annihilation has been identified as the saturation mechanism for fatigue involving intermediate degrees of plastic straining and PSB formation. Dislocation walls (veins) and dislocation channels take part in plastic deformation by macroyielding of PSB. Edge dislocations bow out from walls, traverse the

channels, and penetrate partially into the opposite wall leading to the existence of screw dislocation segments that glide along the channels. During cyclic deformation, edge dislocations will glide between walls with constant renewal of dislocations caused by a dynamic process of dislocation formation and annihilation. Annihilation occurs by climbing of edge dislocations of opposite signs in the wall structures of PSBs or by cross slip between screw dislocations. Therefore, bundles and walls consist primarily of edge dislocations [Suresh 1991].

At higher loading amplitudes, secondary slip occurs and the multiple slip contributes to the formation of labyrinth and cell-like dislocation structures (region C in Figure 5). Figure 10 shows PSBs structures in specimens of 316L steel cycled with plastic strain amplitude of 5×10^{-3} at failure.

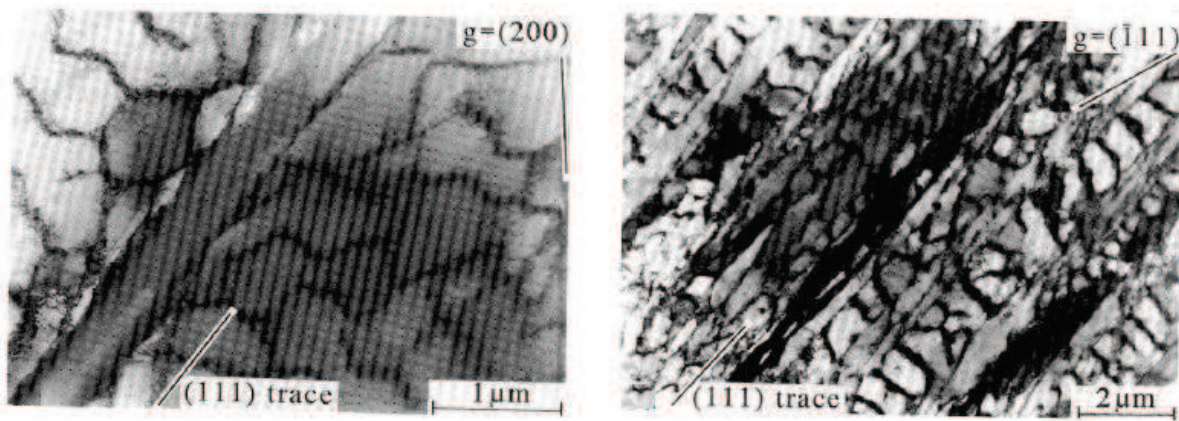


Figure 10 PSB structures in specimens of 316L steel cycled with plastic strain amplitude of 5×10^{-3} , $N_f = 2800$ (a) cell structure with a PSB (b) PSBs with wall structure

Cell size has been reported to decrease with increasing plastic strain amplitude and saturation. For material with high stacking fault energy, cell size is independent of the initial condition of the material (i.e. cell structures during cyclic saturation are the same for annealed or cold worked materials). It was also revealed that cell size increases as the test temperature increases. [McEvily, Gonzalez and Hallen 1996; Yokoyama, Umezawa, Nagai, Suzuki and Kokubo 2000; Heino and Karlsson 2001; Robertson, Fivel and Fissolo 2001; Yang, Li, Li, Ma and Li 2001; Huang 2003; Jia and Fernandes 2003]

It was observed that microstructures in 304L under two levels of plastic strain amplitude 0.15% and 1% in high-temperature environment at 300°C as shown in Figure 11. The results show that the temperature has no effect on the microstructures type changes [Garcia 2006].

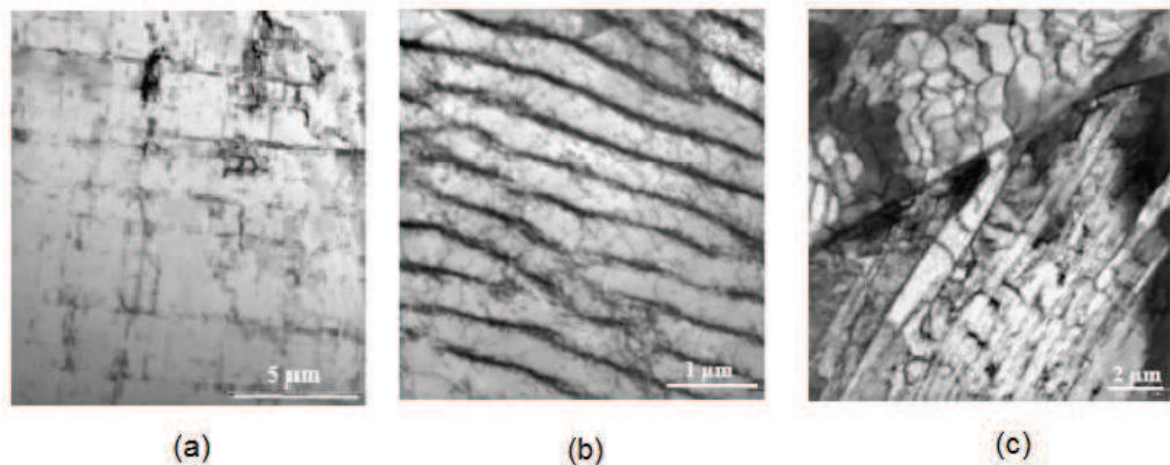


Figure 11 Microstructures observed in 304L at 300°C [Garcia 2006] (a) Planar dislocation structure (b) channels and veins (c) PSB structure

Furthermore, as for cyclic softening observed in Figure 1 and Figure 2, two ways of physical explanations to this macro behavior can be found. On one hand, cyclic softening can result from a decrease in dislocation density through dislocation annihilation and change in dislocation structure [Armas, Petersen, Schmitt, Avalos and Alvarez-Armas 2002; Marmy and Kruml 2008]. On the other hand, cyclic softening can also be explained by using the concept of ‘dislocation starvation’ proposed by Li and Laird [Li and Laird 1994; Li and Laird 1994]. According to Li and Laird, cyclic softening occurs for polycrystals due to ‘dislocation starvation’ - i.e. the inability or difficulty in generating dislocations to carry the applied strain in the first few cycles. The initial stress applied is high in order to generate enough dislocations to carry the imposed strain. Dislocations are required to carry strain – the more mobile the dislocations, the better they can carry the applied strain. As a result, cyclic softening can occur due to difficult dislocation generation in the early stage, or through dislocation annihilation where reduced dislocation density reduces the resistance to dislocation movement.

1.5 Fatigue crack initiation and propagation

1.5.1 Fatigue crack initiation

The development of a fatigue crack is traditionally classified into two main phases: 1) crack initiation and microcrack propagation 2) stable crack propagation and fracture. The definition of crack “initiation” has evolved with the advancement of crack detection methods. This limit of crack detection has improved over the years from several millimeters to the order of 1 μm or less. Since a fatigue crack must be of a certain length before it can be observed, some microcrack propagation will always occur before the measured cycles to crack “initiation” is detected [Krupp 2007; Schijve 2009].

It should be noted that surface micro-notches, inclusions or inherent microscopic defects, all provide avenues for immediate crack propagation. Henceforth, the term fatigue crack

“initiation” will be quoted in inverted commas to remind that such a phase though often quoted in textbooks and in literature, may not actually exist in reality. References to the term “initiation” are still made throughout the context of this thesis to facilitate the understanding of general concepts of fatigue crack propagation. It should be reminded that the word “initiation” is a loosely coined term used simply to refer to the onset of a detectable crack and not the very beginning of crack propagation.

In 1903, Ewing first demonstrated the microcracks occur as a result of cyclic deformation leading to strain localization. This strain localization is caused by irreversible dislocation movement (slip along crystallographic planes when stress is applied) and with time, the dislocations agglomerate into bundles at critical stress or strain levels causing strain localization to occur, thus forming thin lamellae of persistent slip bands also known as PSBs [Peralta, Laird, Ramamurty, Suresh, Campbell, King and Mitchell 1999; Huang and Ho 2000; Schijve 2009]. The PSBs at free surface is usually the preferred area for the “initiation” of fatigue cracks [Li 1996; Peralta, Laird, Ramamurty, Suresh, Campbell, King and Mitchell 1999; Ravichandran, Ritchie and Murakami 1999; Shiozawa, Nishino, Ohtani and Mizuno 1999; Huang and Ho 2000]. The following early crack propagation in stage I on single crystallographic slip bands inclined by about 45° to the applied stress (Figure 12) is determined by cyclic shear displacement at the crack tip [Suresh 1991; Schijve 2009].

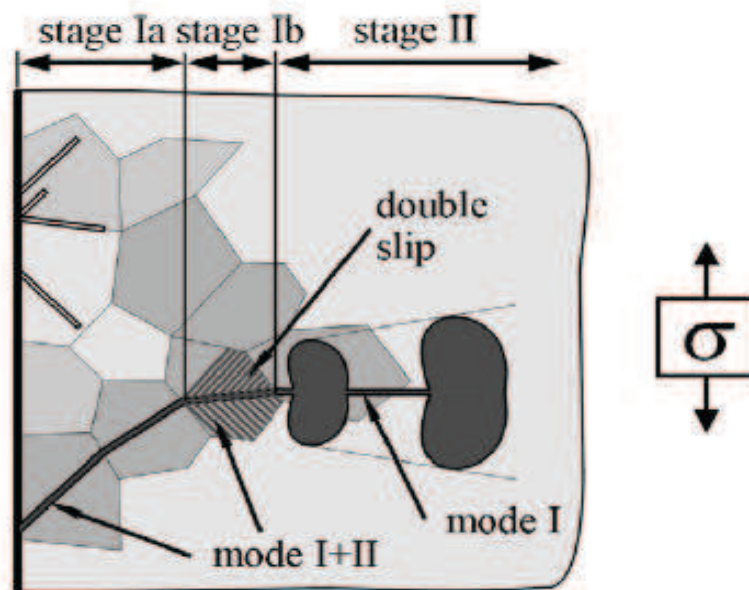


Figure 12 Different stages of crack propagation under push–pull loading conditions [Kunkler, Duber, Koster, Krupp, Fritzen and Christ 2008]

This initial crack propagation is identified as stage I crack propagation and usually penetrates only a few tenths of one millimeter (i.e. one or a few grains) into the specimen. Fatigue crack “initiation” and crack propagation during stage I, occurs by slip plane cracking. Stage I crack propagation is observed both in high cycle fatigue and in low

cycle fatigue in 304L, and is strongly affected by environments and microstructures that tend to concentrate slip and enhance slip reversibility [Haddad 2003].

The cyclic shear stress is required to form cyclic slips. On the microscale, the shear stress is not homogeneously distributed through the material. The shear stress on crystallographic slip planes differs from one grain to the others, depend on the size and shape of the grains, on the crystallographic orientation of the grains, and on the elastic anisotropy of the material. In some grains at the material surface, these conditions are more favorable for cyclic slip than in other surface grains. If slip occurs in a grain, a slip step will be created at the material surface. A slip step implies that a new surface of the material will be exposed to the environment. The fresh surface material will be immediately covered by an oxide layer in most environments, at least for most structural materials. Such monolayer strongly adheres to the material surface and is not easily removed. Another significant aspect is that slip during the increase of the load also implies some strain hardening in the slip band. As a consequence, upon unloading, a larger shear stress will be present on the same slip band, but now in the reversed direction. It is clear that the oxide monolayer cannot simply be removed from the slip step and that strain hardening in the slip band is also not fully reversible. As a consequence, reversed slip, although occurring in the same slip band, will occur on adjacent parallel slip planes [Suresh 1991; Schijve 2009]. Figure 13 schematically describes in extrusions and intrusions produced by cyclic plastic strain on the surface.

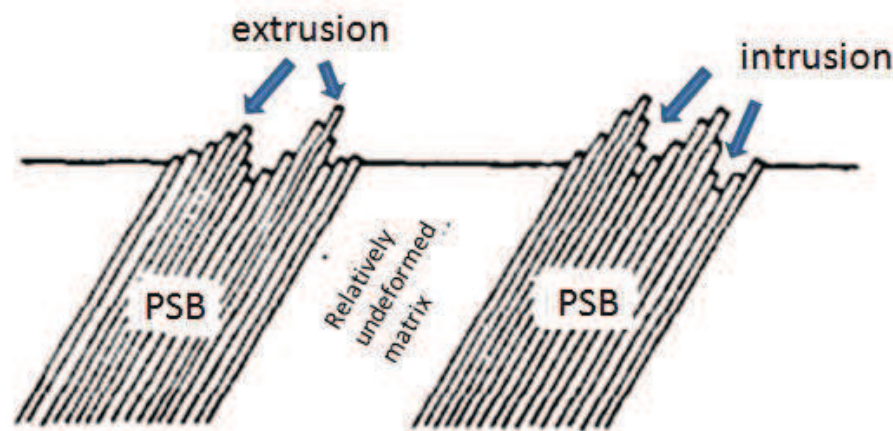


Figure 13 A rough surface consisting of extrusions and intrusions produced by cyclic plastic strain (redrawn from [Suresh 1991])

Figure 14 shows the formation and development of cyclic slip bands and a microcrack in a pure copper specimen [Bullen, Head and Wood 1953; Forsyth and Stubbington 1955].

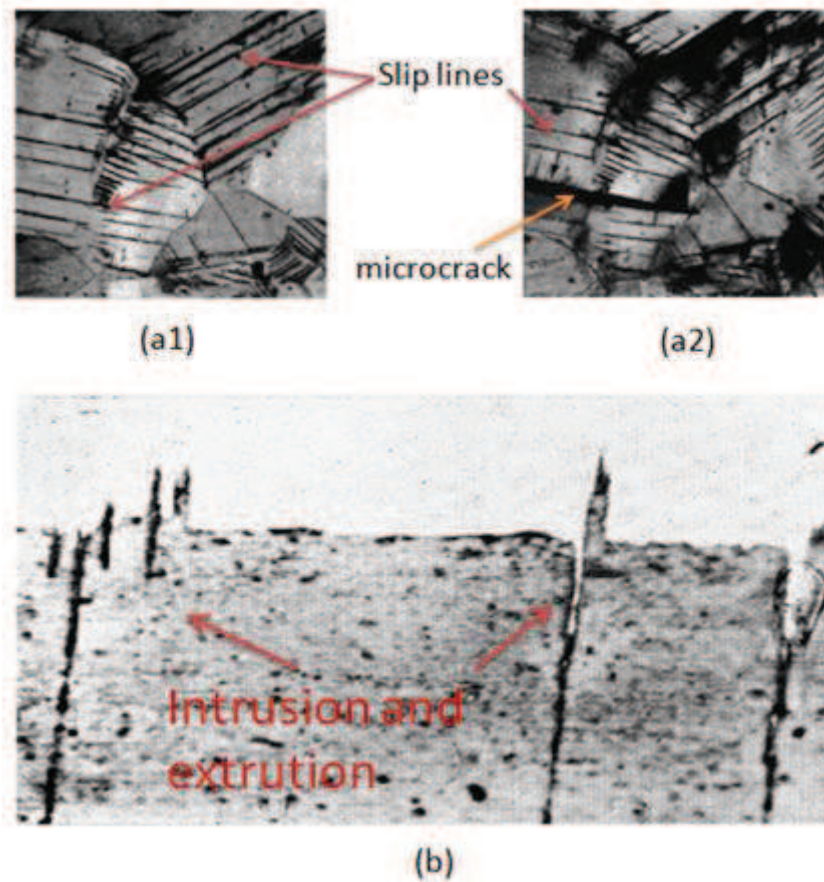


Figure 14 (a) Development of cyclic slip bands and a microcrack in a pure copper specimen, $S_m=0$, $S_a=77.5$ MPa, $N_f=2\times 10^6$ cycles (a1) Slip lines are clearly visible (a2) Same as in (a1) but plastically strained (5%) which opens a microcrack, see arrow [Bullen, Head and Wood 1953] (b) Intrusion and extrusion [Forsyth and Stubbington 1955]

The lower restraint on cyclic slip at the material surface has been considered as a favorable condition for crack initiation at the free surface. However, more arguments for crack initiation at the material surface in polished specimens are present [Suresh 1991; Stephens, Fatemi, Stephens and Fuchs 2000; Lemaitre and Desmorat 2005; Krupp 2007; Schijve 2009]. A very practical reason is the inhomogeneous stress distribution due to a notch effect of a hole, an inclusion, grain boundaries or some other geometric discontinuity. Because of an inhomogeneous stress distribution, a peak stress occurs on the surface (stress concentration). Furthermore, surface roughness also promotes crack initiation at the material surface. Other surface conditions with a similar effect are corrosion pits and fretting fatigue damage both occurring at the material surface.

As long as the size of the microcrack is still on the order of the grain size, the microcrack is obviously present in an anisotropic material with a crystalline structure and a number of definite slip systems. The microcrack contributes to a more inhomogeneous local stress distribution, with a stress concentration at the tip of the microcrack. As a result, more than one slip system may be activated. Moreover, if the crack is growing into some adjacent

grains, the constraint on slip displacements will increase due to the presence of the neighboring grains. Similarly, it will become increasingly difficult to accommodate the slip displacements by slip on one slip system only. Several slip systems will thus be activated. The microcrack propagation direction will then deviate from the initial slip band orientation. Because microcrack propagation depends on crystallography, microstructural barriers to slip can imply an obstacle for crack propagation. As the illustrative results presented in [Blom, Hedlund, Zhao, Fathalla, Weiss and Stickler 1985] (see Figure 15), the crack propagation rate measured as the crack length increment per cycle decreased when the crack tip approached the first grain boundary. After penetrating through the grain boundary the crack propagation rate increased during growth into the next grain, but it decreased again when approaching the second grain boundary. After passing that grain boundary, the microcrack continued to grow with a steadily increasing rate.

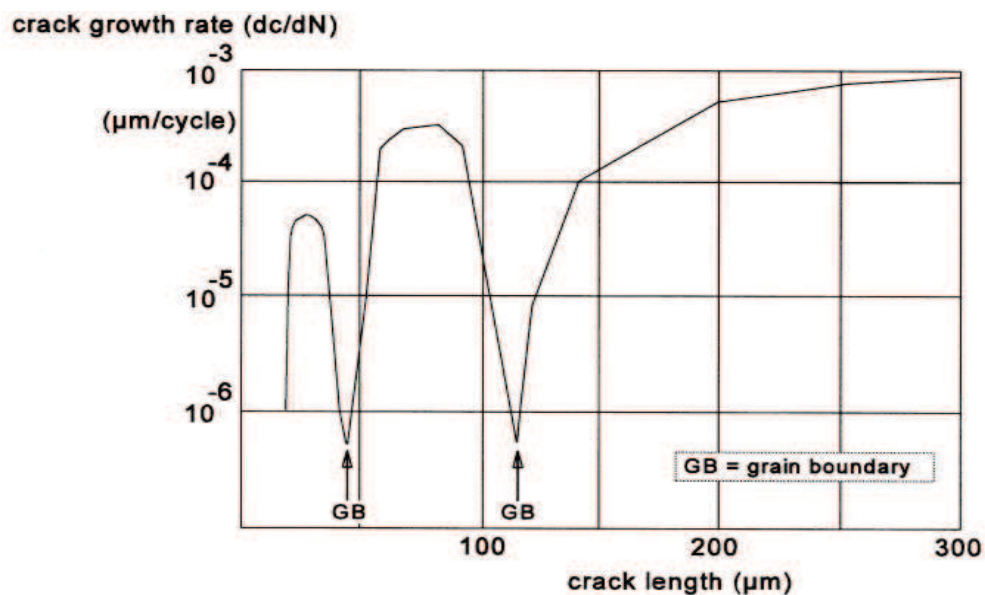


Figure 15 Grain boundary effect on crack propagation rate in an Al-alloy [Blom, Hedlund, Zhao, Fathalla, Weiss and Stickler 1985]. The crack length was measured along the material surface.

During these phases, microcrack propagation is strongly affected by the microstructure of the material and crack advance is dominated by local plasticity. This aspect is especially important for the materials for which a substantial part of the total life is spent during short fatigue crack propagation. For example, cyclically loaded components in structural applications often undergo stress amplitude that is close to the fatigue limit of the material used. Under such conditions, the stages of crack initiation and short crack propagation are considered to play an important role for the lifetime. Thus a way of analytically quantifying this stage is a question of great concern [Swenson 1969; Li 1996; Ostash, Panasyuk and Kostyk 1998; Huang and Ho 2000]. For 304L steel, the crack initiation life (in our work it is defined as the number of cycles before maximum crack size is greater than 200μm) accounts for about 50% of total fatigue life under strain controlled amplitude of $\pm 0.3\%$. Figure 16 shows the surface observation of the short cracks with the

size about 100 to 200 μm . This point was also confirmed by the work of [Lehericy and Mendez 2006], crack distribution during fatigue test also showed that the sizes of cracks were mainly found in the range from 20 to 120 μm .

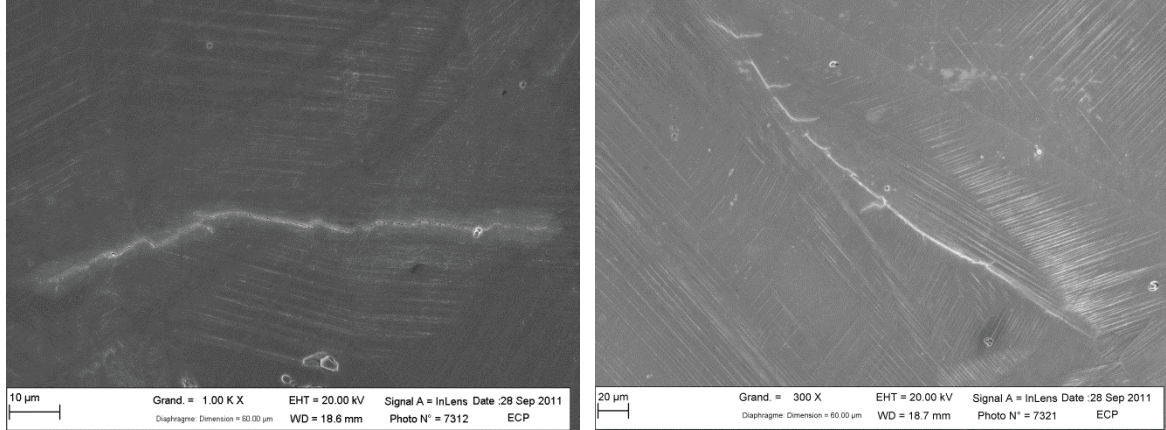


Figure 16 Typical cracks and slip lines on the specimen surface in 304L at the $N = 15000$ cycles under total strain controlled amplitude of $\pm 0.3\%$ ($N/N_f = 50\%$)

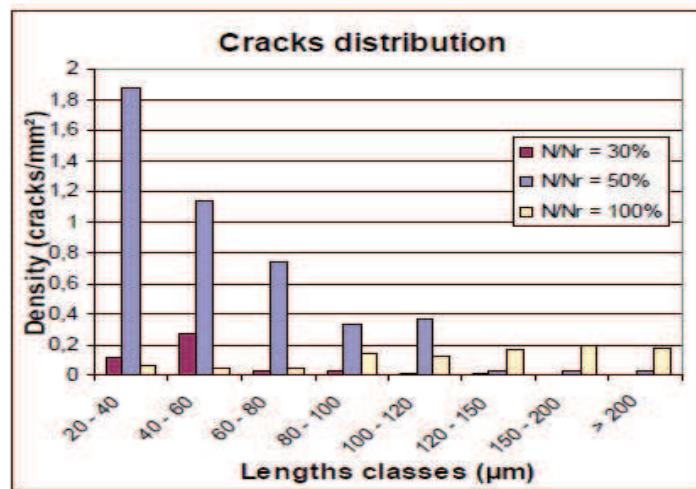


Figure 17 Crack distribution during fatigue test in 304L under total strain controlled amplitude of $\pm 0.3\%$, $N_f = 25000$ cycles [Lehericy and Mendez 2006]

Furthermore, concerning numerical simulation some studies about the initiation and propagation of the stage I cracks can be found in literature. Some models of short crack fatigue growth have been proposed [Bjerken and Melin 2003; Kunkler, Duber, Koster, Krupp, Fritzen and Christ 2008]. Brinckman and Van der Giessen used computational framework that ties together dislocation dynamics, the fields due to crystallographic surface steps and cohesive surfaces to model near-atomic separation leading to fracture [Brinckman and Van der Giessen 2007]. Crack tip shielding by dislocations is an essential feature of the modeling of initiation and propagation of the cracks. Some researchers

considered that crack tip shielding by dislocation can cause a reduction in fatigue growth rate [Weertman 2007] and several multiscale simulation of crack tip shielding by dislocation has been worked out for confirming these conclusions [Tanguy, Razafindrazaka and Delafosse 2008].

When the crack propagates long enough and out of the stage I, the influence of the microstructure can become negligible. It is well established that the part of life of a component spent in the Paris' regime [Paris 1965], can readily be estimated.

1.5.2 Fatigue crack propagation

When the crack is long then the microstructure no longer affects the crack propagation. At this moment, the rate at which a long crack grows has considerable importance in determining the life of a material. The crack growth rate depends on the stress level applied. In the 1960's, Paris examined a number of alloys and realized that crack growth rate against range of stress intensity factor gave the relation as [Paris 1965]:

$$\frac{da}{dN} = C(\Delta K)^n \quad (1)$$

where the parameters C and n are properties of the material, da is the change in crack length, and dN is the change in the number of cycles, ΔK is the change in the stress intensity factor which is dependent on stress and crack length. As a result, the relation of the number of cycles of failure N_f , to the size of the initial default length a_0 , and the critical crack length a_c can be written as:

$$N_f = \int_0^{N_f} dN = \int_{a_0}^{a_c} \frac{da}{C(\Delta\sqrt{\pi a})^n} = \frac{1}{C\pi^{\frac{n}{2}}(\Delta\sigma)^n} \int_{a_0}^{a_c} \frac{da}{a^{\frac{n}{2}}} \quad (2)$$

where N_f is an estimate of the number of cycles to failure, and $\Delta K = \Delta\sqrt{\pi a}$.

It must be noted that Paris law, for the first time, made it possible to make a quantitative prediction of residual life for a crack of a certain size. Now it is well known that N_f also depends on several other factors such as stress ratio, loading frequency, loading sequence, and environment conditions. In the last few decades, it has been modified to take into account more other factors to use in the special loading conditions such as Walker's equation, Forman's equation and Elber's equation [Suresh 1991; Ravichandran, Ritchie and Murakami 1999; Stephens, Fatemi, Stephens and Fuchs 2000; Krupp 2007; Schijve 2009].

1.5.3 Transition from the crack initiation to propagation stage

As mentioned above, the fatigue life was described as consisting of a crack initiation stage and propagation stage (Figure 18). The definition of transition from the initiation stage to the crack propagation is difficult even cannot really be given in quantitative terms. According to Schijve [Schijve 2009], the definition is that the first initiation stage is over when microcrack propagation is no longer depend on the material microstructure, or

surface conditions for a polished specimen. The sizes of the microcrack at the transition from the initiation stage to the crack propagation stage differ significantly with the types of materials. The transition depends on microstructural barriers to be overcome by a growing microcrack, and these barriers are not the same in all materials. The transition also implies the change from microstructurally short crack to short crack (about 200 μm -1mm) which is no longer sensitive to microstructure, but the crack is still short and influenced by full opening and closing at the bottom of the cycle. Figure 19 provides a schematic comparison between stress range and crack length, on a log-log scale as first presented by Kitagawa and Takahashi [Kitagawa and Takahashi 1976], in which a_1 is a size comparable to the scale of some microstructural dimension, for example the grain size and a_2 is typically between 200 μm to 1 or 2mm [Stephens, Fatemi, Stephens and Fuchs 2000; Schijve 2009] and [ASTM Standard E647].

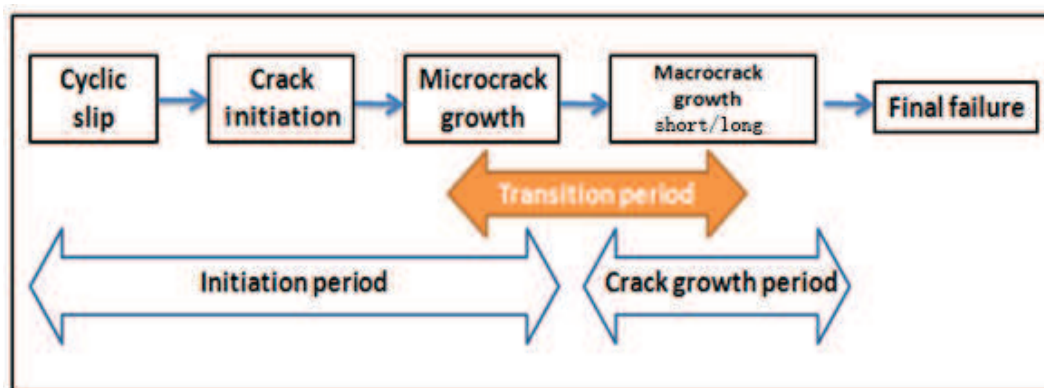


Figure 18 Various stages of the fatigue life redrawn from [Schijve 2009]

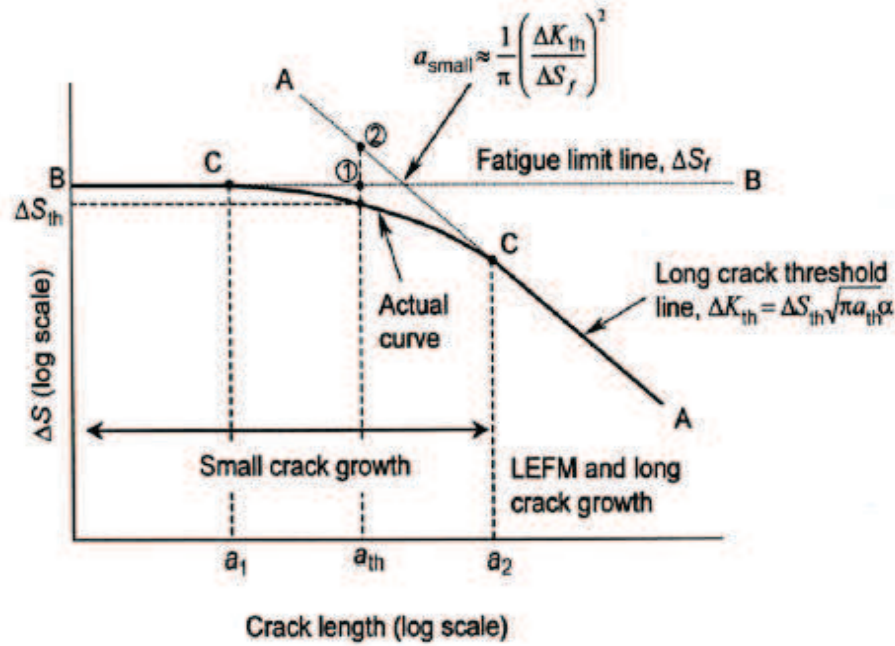


Figure 19 Schematic of Kitakawa-Takahashi diagram showing the relationship between stress range and crack length (from [Stephens, Fatemi, Stephens and Fuchs 2000])

The crack initiation stage includes the initial microcrack propagation. Because the growth rate is still low, the initiation stage may cover a significant part of the fatigue life. This is illustrated by the generalized picture of crack propagation curves presented in Figure 20 which schematically shows the crack propagation development as a function of the percentage of the fatigue life consumed [Schijve 2009]. There are three curves in Figure 20, all of them in agreement with crack initiation in the very beginning of the fatigue life, however, with different values of the initial crack length. The lower curve corresponds to microcrack initiation at a perfect surface of the material; the middle curve represents crack initiation from an inclusion; the upper curve is associated with a crack starting from a material defect which should not have been present, such as defects in a welded joint.

From Figure 20, it is clear that only cracks starting from macro defects can have a detectable macrocrack length immediately. The two lower crack propagation curves illustrate that the major part of the fatigue life is spent with a crack size below 1 mm, i.e. with a practically invisible to bare eyes crack size. It is also possible that cracks do not always grow until failure as shown with dotted lines in Figure 20. It implies that there must have been microstructural barriers in the material which stopped crack propagation.

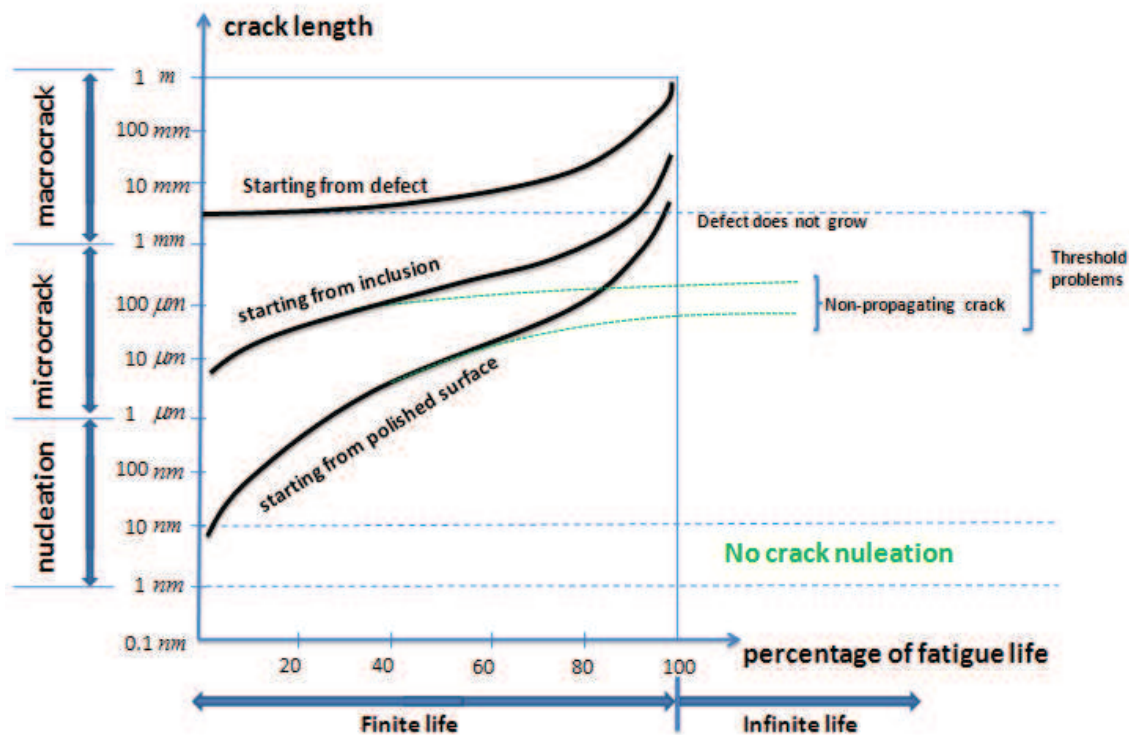


Figure 20 Different scenarios of fatigue crack propagation (redrawn from [Schijve 2009]).

1.6 Crack observation techniques

Since the definitions of crack initiation and propagation stages evolved with the advancement of crack detection methods and as it is important to know the underlying mechanism of the crack initiation, recently a wide range of microscopy techniques have been applied to characterize crack initiation and propagation. In this section, some crack observation techniques in austenitic stainless steels are summarized as follows. First, magnetic force microscopy (MFM) has been used to detect Cr depletion, the early stages of stress corrosion crack (as shown in Figure 21) [Takaya, Suzuki, Matsumoto, Demachi and Uesaka 2004; Takaya and Miya 2005].

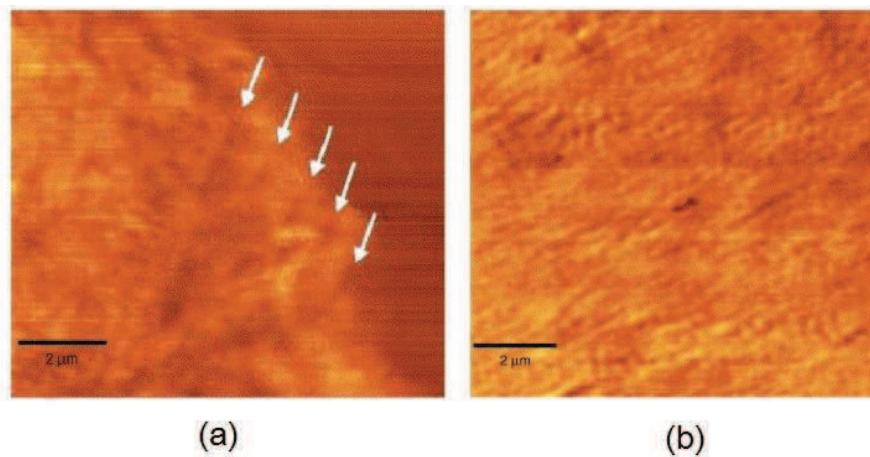


Figure 21 MFM observation results in 304L stainless steel: (a) near a stress corrosion crack, (b) about 5 mm apart from a stress corrosion crack [Takaya and Miya 2005].

Intergranular corrosion in 304 steel also have been studied by electromechanical atomic force microscopy (EAFM) [Williford, Windisch Jr and Jones 2000] as shown in Figure 22. Optical or scanning electron microscopy (SEM) observations (Figure 23); electron backscatter diffraction (EBSD) and orientation image mapping (OIM) (Figure 24) have been applied to observe the crack initiation sites and propagation path with the slip bands or grain boundary. All these techniques provide two-dimensional (2D) information.

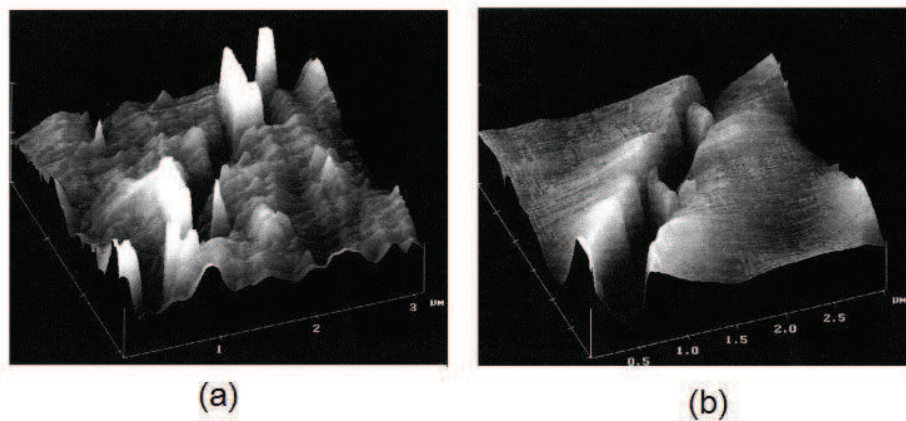


Figure 22 In situ EAFM image of early stage grain boundary attack on sensitized 304 SS in 1% oxalic acid, showing exposed chromium carbide precipitates. (b) 21 minutes later, showing dissolution of carbide precipitates [Williford, Windisch Jr and Jones 2000]

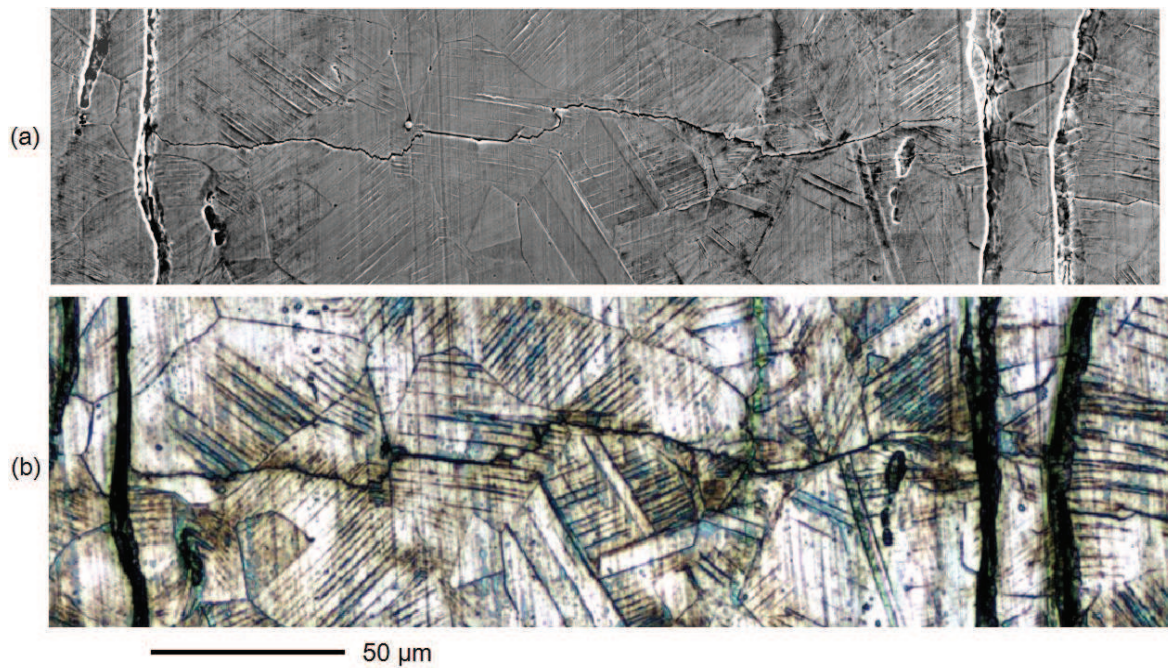


Figure 23 (a) SEM observation of a crack with a length of about 200 μm in 304L (b) The same one observed in optical microscope (this 304L specimen is from LMT, ENSC, observed at ECP)



Figure 24 EBSD map in the same surface zone in Figure 23

Since fatigue cracking is a three-dimensional (3D) phenomenon and with development of the micro computed tomography ($\mu\text{-CT}$) technique, recently 3D crack observation method was used and developed [Marrow, Buffiere, Withers, Johnson and Engelberg 2004; Ferrie, Buffiere and Ludwig 2005; Ferrie, Buffiere, Ludwig, Gravouil and Edwards 2006; Herbig, King, Reischig, Proudhon, Lauridsen, Marrow, Buffiere and Ludwig 2011; Limodin, Rethore, Buffiere, Hild, Ludwig, Rannou and Roux 2011]. X-ray microtomography is a non-destructive technique to visualize the internal structure of materials. The general

concept of X-ray tomography is an extension of classical X-ray radiography, and is based on the attenuation of the X-ray beam through the specimen. X-ray radiography provides only a projection of the sample volume on one single plane. X-ray tomography overcomes this disadvantage by combining the information from a series of many radiographs, each being recorded with different orientation of the sample in front of the detector. The variation of X-ray attenuation in the volume of the sample can be reconstructed by combining a sufficient number of radiographs with an appropriate algorithm [Limodin, Rethore, Buffiere, Hild, Ludwig, Rannou and Roux 2011]. As shown in Figure 25, X-ray microtomography was used to observe and analyze the intergranular stress corrosion cracking (IGSCC) of austenitic stainless steels.

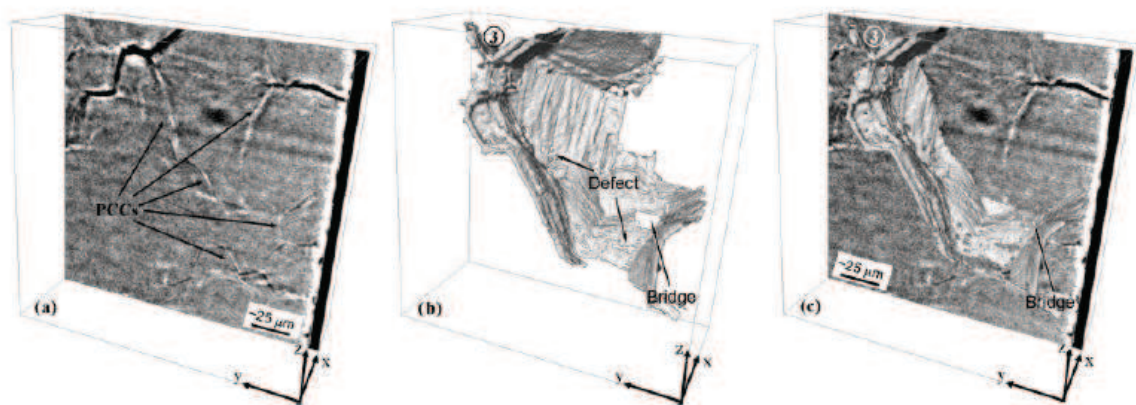


Figure 25 (a) 2D slice observation with cracks in 302 steel (b) Reconstructed 3D crack surface obtained by manual segmentation with X-ray microtomography technique (c) Combination of a and b [Babout, Marrow, Engelberg and Withers 2006]

1.7 Fatigue under variable-amplitude loading

Constant-amplitude (CA) fatigue loading is defined as fatigue under cyclic loading with constant amplitude and a constant mean load. However, it was well known that various structures in service such as in airplanes and in pressurized water reactors are in practice subjected to variable-amplitude (VA) loading, which can be a rather complex load-time history [Suresh 1991; Stephens, Fatemi, Stephens and Fuchs 2000].

Fatigue behavior of metallic materials under variable amplitude loading has been addressed in many papers over the last decades [Shin and Hsu 1993; Shimojo, Chujo, Higo and Nunomura 1998; Wei, Li and Ke 1998; Hussain, Tauqir, Ul Haq and Khan 1999; Kelestemur and Chaki 2001; Lagoda 2001; Lagoda 2001; Wei, de los Rios and James 2002; Moreno, Zapatero and Dominguez 2003; Pommier 2003; Zapatero, Moreno, Gonzalez-Herrera and Dominguez 2005; Ahmadi and Zenner 2006; Kim, Tadjiev and Yang 2006; Hamam, Pommier and Bumbleler 2007; Walther and Elfler 2007; Fomichev 2008; Daneshpour, Kocak, Langlade and Horstmann 2009]. Some of them pay special attention to the simulation of representative load histories of defined random loading processes. Others analyzed the effect of overloads and their distribution throughout the

load history of the crack propagation life. There are also many articles that present numerical or analytical models to simulate the crack propagation under this type of loading. However, all these current damage accumulation rules proposed are based on phenomenological approaches. So fatigue behavior under VA loading remains an open problem and fatigue life prediction is obviously more complex than that under CA loading.

At first, in order to calculate the fatigue life of a part under variable amplitude loading using constant amplitude fatigue life data, Miner popularized a rule [Miner 1945] that had first been proposed by Palmgren [Palmgren 1924]. The rule states that where there are k different stress magnitudes in a spectrum, S_i ($1 \leq i \leq k$), each contributing $n_i(S_i)$ cycles, then if $N_i(S_i)$ is the number of cycles to failure of a constant reversal stress S_i , failure occurs when

$$\sum_{i=1}^k \frac{n_i}{N_i} = D$$

D is originally proposed to be 1 and experimentally found to be between 0.7 and 2.2 . Usually for design purposes, D is still assumed to be 1. This can be thought of as assessing what proportion of life is consumed by reversal stress at each magnitude then forming a linear combination of their contribution.

Though Miner's rule is a useful approximation in many circumstances, some results of VA fatigue tests clearly indicated that Miner's rule does not give accurate and reliable predictions on fatigue lives. The shortcomings can be understood. The most important one is that it does not consider the effect of overload or high level stress/strain amplitude on crack initiation and propagation.

Conventional knowledge in crack growth behavior shows that in metallic materials it is expected a decrease in crack growth rate immediately after the overloading. This idea, stemming from Elber's model, was the first to employ the concept of crack closure to explain retardation in fatigue crack growth following overloading [Elber 1970]. It was discovered that overloading produced compressive residual stresses, which acted on fatigue crack surfaces causing crack closure. As a result, subsequent tensile loading will see a portion of this tensile load consumed in overcoming the crack closure caused by residual compressive stresses ahead of the crack tip and crack growth retardation is achieved assuming that crack growth would not take place when a crack is closed. It was also suggested that the primary mechanisms of closure are reasoned to be associated with the wedging crack face asperities (roughness induced closure) and more importantly closure induced by cyclic plasticity in the crack wake [Suresh 1991; Stephens, Fatemi, Stephens and Fuchs 2000; Schijve 2009].

So up to now, from the macroscopic point of view, it is well recognized that the occurrence of positive overloads or the alternance of high to low load sequences had a strong effect on the crack propagation behavior leading to favorable crack propagation

retardation in certain cases [Shin and Hsu 1993; Shimojo, Chujo, Higo and Nunomura 1998; Wei, Li and Ke 1998; Hussain, Tauqir, Ul Haq and Khan 1999; Kelestemur and Chaki 2001; Daneshpour, Kocak, Langlade and Horstmann 2009]. However, whether the overload cycles before the initiation of a microcrack are also beneficial for the fatigue crack initiation life is not yet well understood.

1.8 Summary

In this chapter, some key points in fatigue theory in literature were reviewed in particular for 304L. Some experimental results of macroscopic cyclic stress-strain response and evolution of dislocation microstructure during cyclic loading were presented. The microstructural processes that take place in polycrystals are basically the same as that studied for single crystals: at low amplitudes, loose veins are formed; in an intermediate range, veins with PSBs are formed and at high amplitudes, cells are formed. Even when cyclic saturation is reached, minor changes to dislocation structures can be found. For 316L or 304L steel, the dislocation arrangement for slip systems during cyclic loading is highly dependent on the loading amplitude and number of cycles during fatigue.

As a result of cyclic deformation leading to strain localization, microcracks may occur. The development of a fatigue crack is traditionally classified into two main phases: 1) crack initiation and microcrack propagation 2) stable crack propagation and propagation. Stage I crack propagation is observed both in high cycle fatigue in 304L and in low cycle fatigue and is strongly affected by microstructures and environments that tend to concentrate slip and influence slip reversibility. When the crack propagates long sufficiently and comes out of the stage I, the influence of the microstructure is negligible.

In addition, because the definitions of crack initiation and propagation stages were evolved with the advancement of crack detection methods and as it is important to know the underlying mechanism of crack initiation, a wide range of microscopy techniques applied to characterize crack initiation and propagation have been reviewed and compared.

Last, research status of one of the open problems, namely, fatigue behavior under variable amplitude loading was reviewed and discussed. All current damage accumulation rules proposed in the literature are based on phenomenological approaches. In terms of crack propagation, it is well recognized now that the occurrence of positive overloads or the alternance of high to low load sequences leads to favorable crack propagation retardation in certain cases. However, whether the overload cycles before the initiation of a microcrack are also beneficial for the fatigue crack initiation life is not yet well understood. In order to study the effect of overload on crack initiation and microcrack propagation, microstructure of the material must be taken into account.

Chapter 2

Material characteristics of austenitic stainless steel 304L

Table of contents

CHAPTER 2 MATERIAL CHARACTERISTICS OF AUSTENITIC STAINLESS STEEL 304L	35
2.1 OVERVIEW	37
2.2 CHEMICAL COMPOSITION.....	37
2.3 MICROSTRUCTURAL CHARACTERIZATION.....	38
2.3.1 Preparation	38
2.3.2 Surface observation	39
2.4 DEFORMATION MECHANISMS	40
2.5 MECHANICAL PROPERTIES	41
2.6 SUMMARY	43

This chapter presents some main properties of austenitic stainless steel type 304L and 316L including chemical composition, microstructural characterization and mechanical properties.

2.1 Overview

304 and 316 stainless steels are the most frequently used alloys in the austenitic family. These alloys may be considered for a wide variety of applications where one or more of the following properties are important:

- Resistance to corrosion
- Resistance to oxidation
- Excellent formability
- High tensile strength and toughness
- Good strength and toughness at cryogenic temperatures

This combination of properties is the reason for the extensive use of these alloys which represent nearly one half of the total stainless steel production. Alloys 304, 304L, 304H, 316, 316L and 316H are available in a wide range of product forms including sheet, strip, and plate. Alloy 304L is used for welded products which might be exposed to conditions which could cause intergranular corrosion in service. Alloy 304H is a modification of alloy 304 in which the carbon content is controlled to a range of 0.04 to 0.10 to provide improved high temperature strength to parts exposed to temperatures above 400 °C [Mcguire 2008].

2.2 Chemical composition

Austenitic type Iron-Chromium-Nickel alloys are widely used and are characterized by a range of nuance with grades of between 17 and 20% chromium, between 9 and 14% nickel and optionally contain between 2 and 4.5% molybdenum by weight as given in Table 1 [Cunat 2003].

Table 1 Comparison of chemical composition of austenitic stainless steels 304 and 316 (wt%) [Cunat 2003]

Type	Cr	Ni	Cmax	Mo
304	17-20	9-12	0.080	-
304L	17-20	9-12	0.030	-
316	16-19	10-14	0.080	2.25-2.75
316L	16-19	10-14	0.030	2.25-2.75

Their face-centered cubic crystallographic structure confers extreme ductility and toughness. They have good corrosion resistance and good formability. They do not show ductile/brittle transition and can be used at low temperatures. The basic element, chromium, provides good resistance to corrosion and oxidation at high temperature. Nickel can stabilize austenite not only at room temperature but also at lower temperature.

The other alloying elements contained in these steels can improve their properties. For example, molybdenum improves resistance to corrosion in virtually any environment. The carbon can stabilize a bit more austenite during cold deformation. The low carbon content prevents from intergranular corrosion. The nitrogen content is targeted to offset the loss of strength due to reducing the carbon content while avoiding the possible formation of nitrides [Rousseau 1973; Lacombe, Baroux and Béranger 1990].

These materials are very sensitive to thermal fatigue because of their low thermal conductivity combined with very high coefficients of thermal expansion, which leads to significant stress gradient under thermal cyclic loadings. The thermal conductivity of steels is generally lower than that of ferrite [Mcguire 2008]. Detailed chemical composition for 304L used in this study is shown in Table 2 [Le-Pecheur 2008].

Table 2 Chemical composition of 304L steel used in this study (wt. %) [Le-Pecheur 2008]

C	Mn	Si	S	P	Ni	Cr	Mo	Cu	N ₂
0.029	1.86	0.37	0.004	0.029	10.00	18.00	0.04	0.02	0.056

2.3 Microstructural characterization

2.3.1 Preparation

The EBSD maps were made using a field emission scanning electron microscope (FESEM) LEO 1530 equipped with an EBSD analysis (Electron Back Scattered Diffraction). The first step in collecting OIM data is preparing the specimen so that high quality EBSD patterns are observed and obtained with the imaging system. The near-incident energy backscattered electrons form the EBSD patterns. Backscattered electrons that have experienced inelastic events inside the bulk of the specimen do not contribute to the pattern. This fact, combined with the high tilt angle of the specimen (70 degrees), results in a diffraction region that forms within the top 10-50 nanometers of the specimen. The crystal lattice in this region should be strain-free and clean from contamination or oxide layers for diffraction to occur. If these conditions are not met the resulting EBSD patterns will be of poor quality or will not be visible at all. In our work, for the material of 304L steel, polishing is done by manual polishing with grit paper roughness between 14 μm and 5 μm . It is then refined by felt polishing with diamond powder until 3 and 1 μm roughness.

To improve pattern quality, an electro-polishing step is performed to reveal its microstructure. Electro-polishing allows removing surface material by electrolytic action. This method removes the residual deformation layers and surface irregularities. For electro-polish purposes, the specimen is made an anode in an electrolytic cell. There are some variables that affect the anodic film, and consequently the polishing rate. They are the specimen material, the electrolyte solution used, operating voltage, specimen size, solution temperature, the time of the solution, the flow rate of the solution. The detailed information about electro-polishing in this work can be found in section 4.1.2 and 5.3.1.1.

2.3.2 Surface observation

The austenitic stainless steel (AISI 304L) has an FCC structure. The steel used here does not show any residual delta ferrite (less than 3% in volume) as observed on optical microscopy (Figure 26). The twins are observed following the thermal annealing treatment.

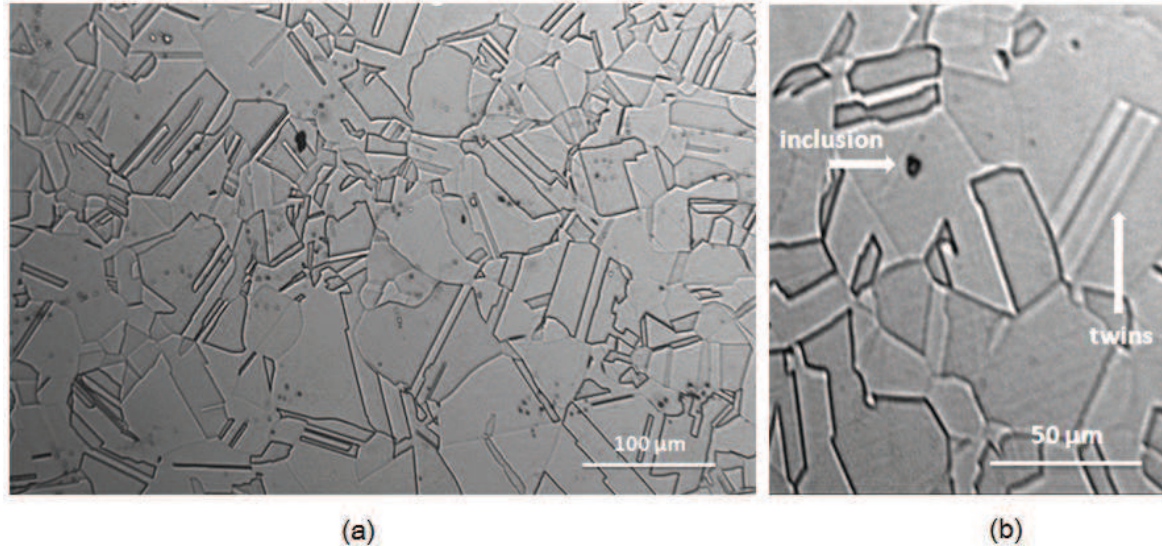


Figure 26 (a) and (b): Optical microscopy of 304L steel

The grain size distribution was measured by EBSD (Figure 27) and no significant difference was found between the longitudinal (direction parallel to axis Z in the model) and transverse direction (perpendicular to axis Z in the model). The grain size varies from 5 to 300 μm with a majority between 30 and 100 μm . However, these data tend to overestimate the percentage of grains of small sizes. In addition, the twins are taken into account in the grain size distribution. Using several maps, the average grain size is 40 μm with a standard deviation of 28 μm .

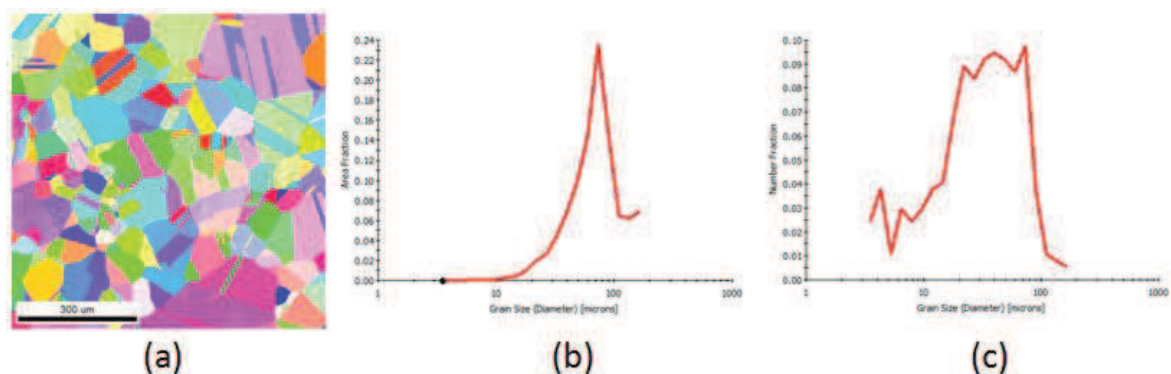


Figure 27 (a) One example of EBSD mapping (b) Distribution of area fraction vs. grain sizes (c) Distribution of grain number vs. grain sizes

A few inclusions were observed on the surface. Figure 28 shows the SEM observations taken in the area near an inclusion on the surface of a fatigued specimen and this inclusion was split into two parts. The EDS chemical analysis results show that only one type of inclusions was found. All inclusions show a core which is mainly composed of aluminum, manganese, titanium and oxygen. Around the core, the material consists of sulfur and manganese.

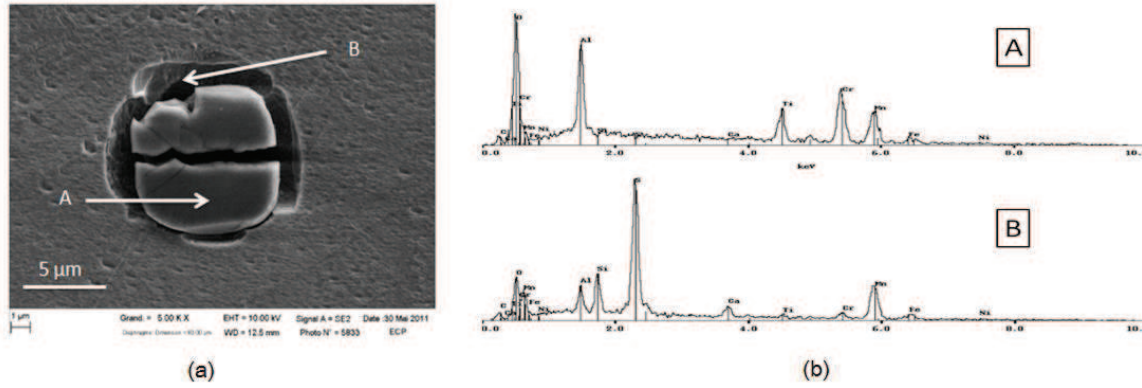


Figure 28 (a) A cracked inclusion in 304L observed in SEM (b) chemical composition obtained with energy-dispersive (EDS) detector integrated in the SEM

2.4 Deformation mechanisms

The deformation mechanisms of face-centered cubic alloys mainly depend on the stacking fault energy called SFE [Lacombe, Baroux and Béranger 1990]. The value of the SFE determines the deformation modes of austenite. Its influence on the arrangement of dislocations, the sensitivity to the martensitic transformation and the twinning ability has been reported [Breedis and Robertson 1962; Reed 1962; Rousseau 1973; Maxwell, Goldberg and Shyne 1974; Hennessy, Steckel and Altstetter 1976; Pickering 1984; Baffie, Stolarz and Magin 2000; Lebedev and Kosarchuk 2000; Chevalier, Calloch, Hild and Marco 2001]

For austenitic stainless steels, SFE is low at room temperature of about 20MJ/M². It can be calculated using the following relationship [Pickering 1984]:

$$SFE(MJ/m^2) = 25.7 + 2(\%Ni) + 410(\%C) - 0.9(\%Cr) - 77(\%N) - 13(\%Si) - 1.2(\%Mn) \quad (3)$$

It increases almost linearly with increasing temperature and depends on the content of various alloying elements. The following relationship of the SFE with temperature range between -200 and 100 °C was proposed by Pineau [Lecroisey and Pineau 1972]:

$$(SFE)_T = (SFE)_{T_0} + A(T - T_0) \quad (4)$$

where A is a parameter depend on the chemical composition of the steel.

For low stacking fault energy, the deviated slip becomes difficult, dislocations dissociate readily into partial dislocations of Shockley type (i.e. dislocations having a Burgers vector which is not a vector of the network). Between the two Shockley half-dislocations, a fault plane is formed whose structure is close to a bcc arrangement. These stacking faults appear at the beginning of plasticity and thus form deformation bands consisting of a mixture of ϵ martensitic phase in the form of platelets and γ austenite.

2.5 Mechanical Properties

The austenitic stainless steel 304L yield stress $Rp_{0.2\%}$ is about 250 MPa; the failure strength is less than 600 MPa and the elongation to rupture is about 60% at room temperature [Le-Pecher 2008]. These mechanical properties are strongly influenced by temperature. Figure 29 shows tensile curves at room temperature, 150 °C and 300 °C for stainless steel 304L [Haddar 2003].

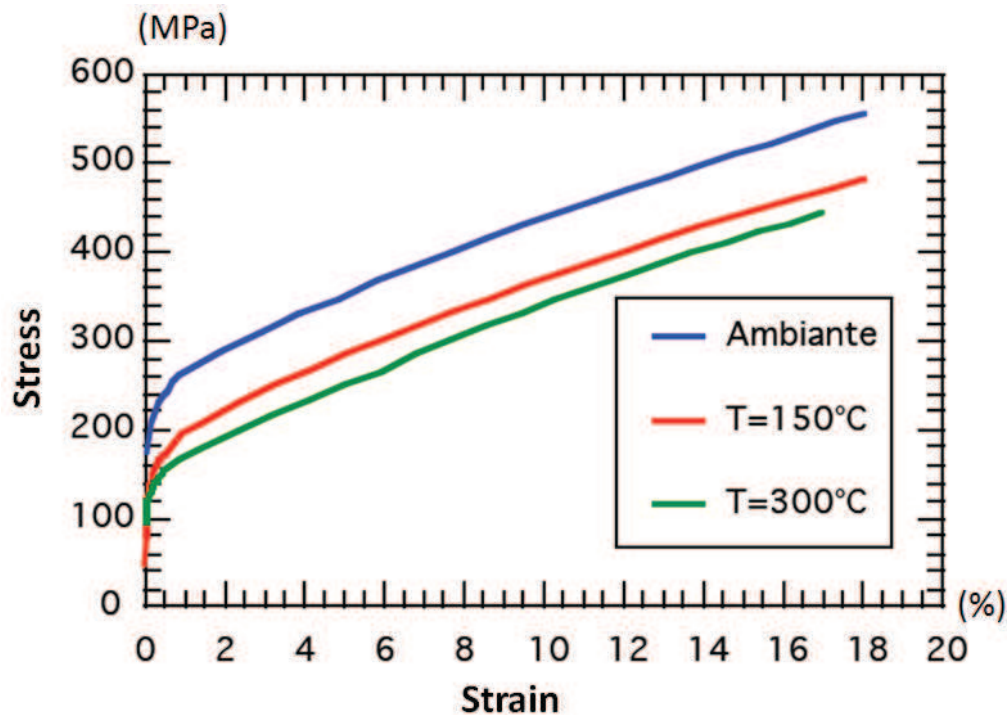


Figure 29 Tensile curves at room temperature, 150 °C and 300 °C for stainless steel 304L [Haddar 2003]

Table 3 gives some mechanical properties of austenitic stainless steels 304L at room temperature [Farahmand, Bockrath and Glassco 1997; Haddar 2003; Le-Pecher 2008]. To improve the mechanical properties, several types of hardening are possible: solid solution hardening, strain hardening or precipitation hardening. For example, a strain hardening (such as rolling) can increase the tensile strength to 1500 MPa. However, this improvement is at the expense of ductility.

Table 3 Mechanical properties of austenitic stainless steels 304L at room temperature [Farahmand, Bockrath and Glassco 1997; Haddar 2003; Le-Pecheur 2008]

Property	Values
Yield Strength	250 MPa (0.2%), 294 MPa (1%)
Failure strength	≈ 550 MPa
Elongation to rupture	60%
Critical stress intensity factor	$> 220 \text{ MPa}\sqrt{m}$

2.6 Summary

In this chapter, the properties of austenitic 304L and 316L stainless steel were reviewed and presented. The chemical composition and microstructural characterization of 304L studied in this work were presented in details. In addition, the chemical composition of the inclusions on the surface was studied. Then austenite instability and martensitic transformation in 304L were briefly introduced. Last, the mechanical properties of austenitic stainless steels 304L are summed up which are dependent on environmental conditions such as temperature.

Chapter 3

Modeling of the cyclic hardening/softening behavior

Table of contents

CHAPTER 3 MODELING OF THE CYCLIC HARDENING/SOFTENING BEHAVIOR	45
3.1 DESCRIPTION OF THE SELECTED MODELING METHOD	47
3.1.1 <i>Representative volume element</i>	47
3.1.2 <i>Microstructure generation and representation</i>	48
3.1.3 <i>Three dimensional modeling method</i>	50
3.2 MATERIAL CONSTITUTIVE LAWS	51
3.2.1 <i>Crystalline elasticity</i>	51
3.2.2 <i>Crystal plasticity for FCC structure</i>	54
• Plastic flow mechanism	54
• Flow rule in modeling	59
• Isotropic and kinematic hardening	59
• Softening rules.....	60
3.3 IDENTIFICATION OF THE PARAMETERS.....	64
3.3.1 <i>Identification results</i>	65
3.4 RESULT DISCUSSION.....	70
3.4.1 <i>Stress evolution during fatigue</i>	70
3.4.2 <i>Stress-strain loop curves evolution during fatigue</i>	74
3.4.3 <i>Comparison with results obtained not considering softening</i>	77
3.5 CONCLUSIONS	80

Typically, the cyclic response of most engineering alloys exhibits a cyclic hardening then softening until stabilization behavior near mid-life. In low-cycle fatigue analysis, the cyclic stress-strain relationship should be set up first. The traditional method [Coffin 1954], was built by the amplitudes of stress and plastic strain in the stable state which is generally considered at $N_f/2$. All the cyclic processes were neglected which included the effect of cyclic hardening or softening. It is obviously correct for stable cyclic materials, but for most engineering metallic materials including 304L, cyclic hardening and softening property can be observed obviously in the fatigue tests [Broom and Ham 1957; Turner 1975; Choe and Lee 1995]. For predicting cyclic plasticity, fatigue crack initiation and failure life more accurately by numerical simulation, the fatigue cyclic hardening and softening of materials should be studied and the cyclic process must be described in the code.

This chapter focuses on modeling cyclic hardening and softening. The FE model CristaIECP [Erieau and Rey 2004; Cedat, Libert, Flem, Fandeur, Rey, Clavel and Schmitt 2009; Le Pecheur, Clavel, Curtit, Rey, Stephan and Bompard 2011] was enriched to take account of fatigue cyclic hardening and softening. It is based on crystalline cyclic plasticity and strain localization and can take into account dislocation densities on the 12 slip systems, crystal orientation, elastic anisotropy, and kinematic hardening. The identification of parameters used in the crystalline constitutive law for 304L steel is based on the previous work of Anne Le Pecheur [Le-Pecheur 2008]. Some parameters were directly measured from experimental results [Bayoumi and Ellatif 1995; Alain, Violan and Mendez 1997; Gerland, Alain, Saadi and Mendez 1997; Mayama and Sasaki 2006], or obtained from the literature. The others were identified through an inverse identification procedure. Cyclic hardening and stabilization can be limited to dislocation density increase and saturation. Meanwhile the softening behavior is the result of the evolution of the microstructure (persistent slip bands, cells...), because of the elimination or weakening of the obstacles to dislocation movements, showing different dislocation arrangements and densities.

3.1 Description of the selected modeling method

3.1.1 Representative volume element

The simulation of the behavior of a representative volume element (RVE) of the microstructure of the material is a basic method in continuum micromechanics. All the important information about the statistical properties of the microstructure should be contained in the volume element. Furthermore, the RVE size should be large enough in order that the average properties of this volume element are independent of its size and position in the material. The required computer time to solve the problem increases with the size of the RVE, and it is necessary and important to define clearly the meaning of RVE and also to determine its critical size.

Two different methods were proposed by Drugan and Willis to define the RVE [Drugan and Willis 1996]. The first one defines the RVE as the smallest material volume statistically representative of the microstructure. This definition is based on the statistical

nature of the material microstructure. The second definition is more pragmatic. It defines the RVE just for a given material property or behavior. In this case, the RVE is the smallest volume of the heterogeneous material whose behavior accurately represents the actual macroscopic behavior. Accuracy is determined by the maximum allowed error between the exact value and that obtained from the RVE. The basic strategy is to compute the desired macroscopic property in RVEs with increasing sizes until the results converge to the actual value of an infinite size RVE.

In polycrystals, plastic mechanisms on different scales are not same. Generally speaking, it is considered that the material is not homogeneous because each grain is characterized by its crystal orientation. In this way, the grain is considered as the characteristic inhomogeneity for a single phase alloy. So the polycrystalline modeling requires taking account in the crystallographic structure with a large number of grains in the material. Then, one of difficulties is to set the size of RVE which means the number of grains, their respective volume fractions and the distribution of their crystal orientations. As for the distribution of crystallographic orientations, the local EBSD method, or global X-ray diffraction can be used to characterize the crystallographic texture of the material. Moreover, it is generally considered that about 500 to 2000 random grains can represent accurately an isotropic material. And several authors have proved that in the case of non-textured materials of isotropic distributions, 48 grains or even 40 chosen grains are sufficient to achieve a representative macroscopic behavior [Cailletaud 1992; Abdul-Latif 2004].

3.1.2 Microstructure generation and representation

In order to obtain the actual properties of the material, it is also important to ensure that the grain and phase (in the studied 304L, there is only one phase) arrangement within the RVE reproduces faithfully the microstructure of the material. In general, many approaches have been used to obtain the spatial distribution of the microstructure in the RVE.

The first option is simply to construct random polycrystal RVEs through the experimental statistical data provided by two- or three-dimensional microstructural characterization techniques such as Voronoi polyhedral method [Barbe, Decker, Jeulin and Cailletaud 2001; Barbe, Forest and Cailletaud 2001; Tewari, Gokhale, Spowart and Miracle 2004; Zeghad, N'Guyen, Forest, Gourgues and Bouaziz 2007; Quey, Dawson and Barbe 2011]. But Voronoi tessellations are sometimes considered as coarse models of microstructures [Dobrich, Rau and Krill 2004] because they quite significantly underestimate the variability in grain size and overestimate the number of grain neighbors. Nevertheless, Voronoi tessellations can still show important variabilities in grain size and shape which are representative of real polycrystal morphologies (see Figure 30), but that it particularly needs challengingly mesh with rather good-quality elements [Quey, Dawson and Barbe 2011]. The statistical information, although it is not identical to the original material, can be used to reconstruct microstructures. It shows similar features as defined by the statistical correlation functions. The simulation of the properties of the generated microstructures is very useful to establish a direct link between microstructural statistical

parameters which define the spatial arrangement of the grains and the macroscopic behavior. However, at last, it should be noted that this method has a serious limit that the available reconstruction algorithms do not always give a satisfying representation of the original microstructure, which can lead to inaccurate simulation results.

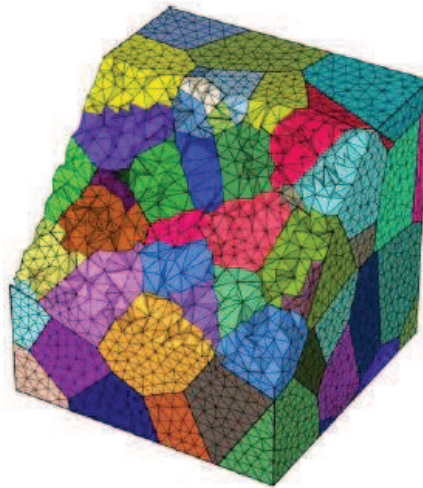


Figure 30 A hundred-grain polycrystal generated by Voronoi tessellation method [Quey, Dawson and Barbe 2011].

The second method is to generate realistic RVEs with three-dimensional microstructure. Non-destructive X-ray diffraction contrast tomography (DCT) and serial sectioning technology are two practicable solutions up to now. X-ray diffraction contrast tomography is an emerging tool for non-destructive 3D characterization of microtexture in polycrystalline materials. It can be used in in-situ investigation of microtexture evolution in the bulk of polycrystalline materials during plastic deformation or grain coarsening processes without material destruction. However, to use this method, it is necessary the material exhibit low intra-grain orientation spreads. A practical lower grain size limit of about 10 μm is also required by DCT. In addition, the size of the specimen should be small enough and number of the grains should be smaller than about 1000 [Dobrich, Rau and Krill 2004; King, Herbig, Ludwig, Reischig, Lauridsen and Marrow 2009].

Serial sectioning works by taking optical or electronic micrographs after successive polishing cycles, from which a layer of material of controlled thickness is removed. The micrographs are analyzed and segmented to the images with a certain size, while retaining the true grain morphology in the microstructure. The segmented serial sections are then stacked, and the three dimensional microstructure is reconstructed. In order to get realistic microstructures, several experimental measurement method were used and developed such as X-ray and EBSD. X-ray computed micro tomography is based on X-ray radiography and provides detailed information at the micron level in three dimensions of the spatial arrangement of the phases within the material [Dobrich, Rau and Krill 2004]. EBSD is a microstructural-crystallographic technique used to examine the crystallographic orientation of many materials, which can be used to determine the texture

to generate the realistic 3D aggregate [Erieau and Rey 2004; Heripre, Dexet, Crepin, Gelebart, Roos, Bornert and Caldemaison 2007; Cedat, Libert, Flem, Fandeur, Rey, Clavel and Schmitt 2009; Schwartz, Fandeur and Rey 2010; Le Pecheur, Clavel, Curtit, Rey, Stephan and Bompard 2011; Li, Aubin, Rey and Bompard 2011]. These methods to generate RVEs can provide rather realistic microstructures, only a negligible disadvantage is that they are not adequate for all types of materials and usually require a lot of time to complete the very expensive experiments. This serial sectioning method is used in our work.

3.1.3 Three dimensional modeling method

As mentioned above, in order to generate RVEs providing quite realistic microstructures and to simulate the realistic intergranular and intragranular stress-strain heterogeneities under cyclic loadings, in our work, a 3D numerical aggregate was used from [Le-Pecheur 2008].

This aggregate was constructed from 4 electron backscattered diffraction (EBSD) maps performed on successive cross-section polishing on the same area from a sample of 304L steel. The microstructure of the aggregate was extruded from each layer through the third direction. The EBSD maps were acquired with a resolution of $1\mu\text{m}$ on a $300\mu\text{m}$ by $300\mu\text{m}$ area and the distance between successive polished sections is $24\mu\text{m}$ thick, which is about $\frac{1}{2}$ average grain size for 304L.

Three other aggregates with an area of $500\mu\text{m}$ by $500\mu\text{m}$ from one fatigue specimen were constructed. The detailed method and procedure to obtain the aggregates (including position-setting for each layer and measurement of polish thickness between two layers) will be presented in chapter 4.

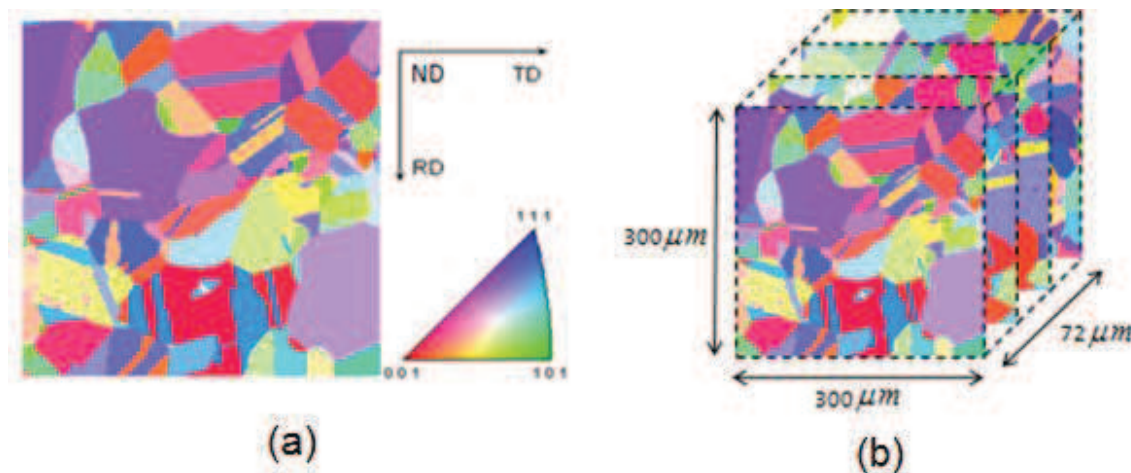


Figure 31 Results of EBSD mapping measurements [Le-Pecheur 2008] (a) EBSD on the surface layer (b) reconstruction of EBSD maps of 4 layers

Figure 31 shows the results of EBSD mapping measurements. These EBSD maps give the local crystallographic orientations within the specimen and allow for the construction of

the numerical aggregate. The actual crystallographic orientation information was written into the Abaqus program in order to get a fixed cubic meshed numerical aggregate including grain orientation as shown in Figure 32a. The meshing is composed of C3D8R element (eight-node brick element with reduced integration) with the size of $4\mu\text{m} \times 4\mu\text{m} \times 8\mu\text{m}$. Every 16 EBSD points (4×4) are assigned to one element. Each meshed element has a corresponding spatial position, orientation and initial crystallographic constitutive properties obtained from EBSD. No particular element is taken into account for the grain boundaries.

The boundary conditions were chosen to approximate those of an aggregate placed on the surface of a specimen. As shown in Figure 32b, the displacements of all the nodes on the surface 2 are fixed to zero in direction 2; the displacements of all the nodes on the surface 1 are fixed to zero in direction 3; the displacements of all the nodes on the surface 3 are fixed to zero in direction 1 and surface 4 keeps parallel to surface 3 during cyclic loading. The last two surfaces are loading surface and free surface ($\sigma_3 = 0$), respectively.

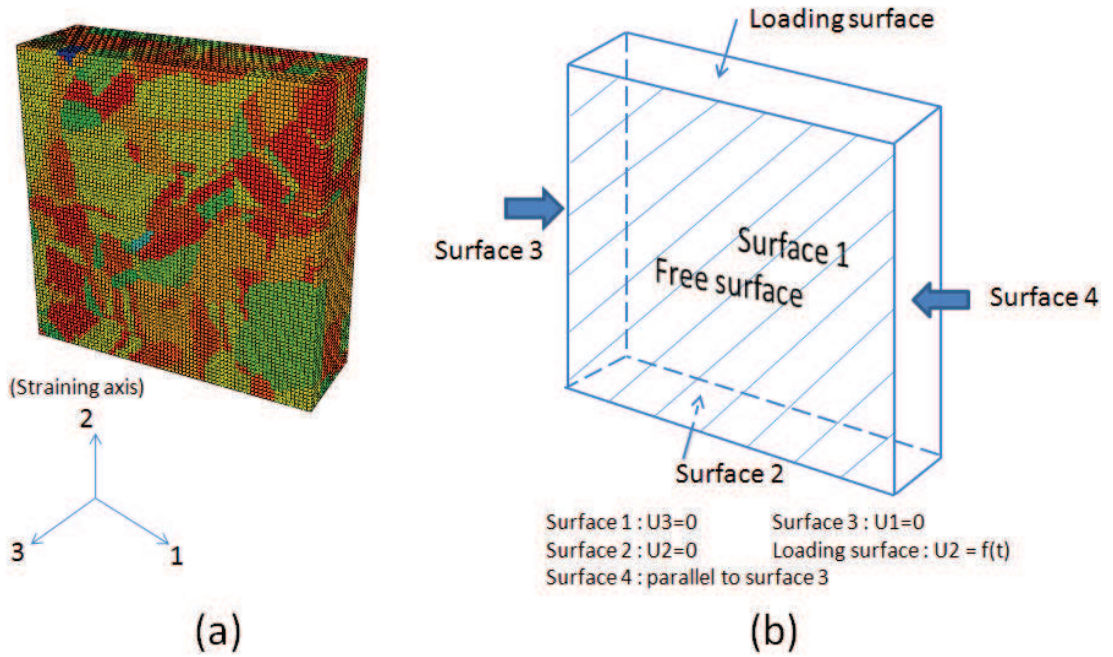


Figure 32 (a) Numerical aggregate of 304L steel including actual grain orientation from EBSD (b) Boundary conditions applied to the aggregate during the simulation.

3.2 Material constitutive laws

3.2.1 Crystalline elasticity

The crystal anisotropic elastic behavior can be described through a stiffness tensor that links elastic stress and strain tensors: $\sigma = C : \varepsilon$ in which C is a 4th order tensor containing 81 elastic coefficients. Due to the symmetry of the stress tensor, strain tensor, and stiffness tensor, only 21 elastic coefficients are independent.

In the case of linear isotropic elasticity, 2 independent coefficients are necessary to define C: the Young's modulus E and Poisson's ratio ν .

$$\mathbf{C} = \begin{pmatrix} C_{11} & C_{12} & C_{12} & 0 & 0 & 0 \\ C_{12} & C_{11} & C_{12} & 0 & 0 & 0 \\ C_{12} & C_{12} & C_{11} & 0 & 0 & 0 \\ 0 & 0 & 0 & C_{44} & 0 & 0 \\ 0 & 0 & 0 & 0 & C_{44} & 0 \\ 0 & 0 & 0 & 0 & 0 & C_{44} \end{pmatrix} \quad (5)$$

where

$$C_{11} = \lambda + \mu \quad (6)$$

$$C_{12} = \lambda = \frac{\nu E}{(1+\nu)(1-2\nu)} \quad (7)$$

$$C_{44} = \mu = \frac{E}{2(1+\nu)} \quad (8)$$

Anisotropic linear elasticity (general case) can be subdivided into several cases depend on their anisotropy. In the case of orthotropic linear elasticity, the crystal has 3 planes of symmetry and 9 independent coefficients. The material studied in this work, an austenitic stainless steel of type AISI 304L, has an FCC structure and shows cubic symmetries. In this case, 3 independent coefficients are sufficient to describe the stiffness tensor: C_{11} , C_{12} and C_{44} . In the crystal coordinate ($\langle 100 \rangle$, $\langle 010 \rangle$, $\langle 001 \rangle$), the elastic constitutive law can be written as:

$$\begin{pmatrix} \sigma_{11} \\ \sigma_{22} \\ \sigma_{33} \\ \sigma_{31} \\ \sigma_{32} \\ \sigma_{21} \end{pmatrix} = \begin{pmatrix} C_{11} & C_{12} & C_{12} & 0 & 0 & 0 \\ C_{12} & C_{11} & C_{12} & 0 & 0 & 0 \\ C_{12} & C_{12} & C_{11} & 0 & 0 & 0 \\ 0 & 0 & 0 & C_{44} & 0 & 0 \\ 0 & 0 & 0 & 0 & C_{44} & 0 \\ 0 & 0 & 0 & 0 & 0 & C_{44} \end{pmatrix} \begin{pmatrix} \varepsilon_{11} \\ \varepsilon_{22} \\ \varepsilon_{33} \\ \varepsilon_{31} \\ \varepsilon_{32} \\ \varepsilon_{21} \end{pmatrix} \quad (9)$$

The anisotropy of a given material is characterized by comparison to the isotropic case by an anisotropy coefficient:

$$\chi = \frac{C_{11} - C_{12}}{2C_{44}} \quad (10)$$

An isotropic elastic material has an anisotropy coefficient $\chi = 1$. On the contrary, if the material is anisotropic, this value will deviate from 1. Table 4 shows some coefficients in the elastic stiffness tensor and anisotropy coefficients of several common materials [Huntington 1958]. The anisotropy is quite large for Cu and fairly small for Al, with Ni at an intermediate position. The austenitic (Fey) is highly anisotropic with an anisotropy coefficient $\chi = 3.4$ (see Table 4).

Table 4 Some parameters in the elastic stiffness matrices and anisotropy coefficients of several common materials

Material	C_{11}	C_{12}	C_{44}	χ	$\frac{E_{\max}}{E_{\min}}$
Isotropic	$\lambda + \mu$	$\lambda = \frac{\nu E}{(1 + \nu)(1 - 2\nu)}$	$\mu = \frac{E}{2(1 + \nu)}$	1	1
Fey	197.5	125	122	3.36	2.96
Cu	170	124	75	3.26	3.0
Al	107	60.8	28.3	1.2	1.17
Fex	247.7	144.6	118	2.5	2.5
Ni	246.5	147.3	124.7	1.51	2.22

When the material is subjected to external loading, and as a result of elastic anisotropy, the stress distribution from grain to grain should be inhomogeneous as schematically indicated in Figure 33. It suggests a homogeneous average stress in each single grain, which is an approximation. According to anisotropy coefficients listed in Table 4, one conclusion is that the inhomogeneity of the stress distribution from grain to grain is small for Al-alloys and much larger for steels. In other words, in Al-alloys most grains will be subjected to similar stress levels, whereas for steel and other materials the stress level can vary significantly from grain to grain due to elastic anisotropy. Once the material such as steels is subjected to cyclic loading, some “hard” grains may show larger stress than average level while crystal plastic slip and accumulated plastic strain occur in some “soft” grains. This may lead to stress and strain concentration in grain or at grain boundaries, which is considered as one of the reasons for crack initiation. So fatigue damage can occur even at low average stress levels without macroplastic deformation.

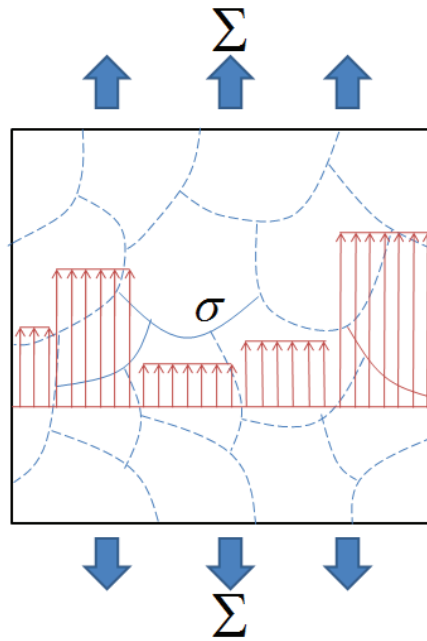


Figure 33 Simplified picture showing the inhomogeneous stress distribution from grain to grain due to elastic anisotropy (hypothesis of a homogeneous average stress in each single grain).

3.2.2 Crystal plasticity for FCC structure

- ***Plastic flow mechanism***

In 1934, Orowan, Polanyi and Taylor, roughly simultaneously, showed that plastic deformation could be explained in terms of the theory of dislocations [Hull and Bacon 2001]. As revealed in more detail in some publications such as [Hull and Bacon 1965], the initiation of plastic deformation can, in most instances, be traced to the onset of dislocation motion. That is to say slip is the process by which plastic deformation is produced by a dislocation motion. At room temperature, it is a major cause of the inelastic material behavior. By an external force, parts of the crystal lattice glide along each other, resulting in a changed geometry of the material. Slip in FCC (face centered cubic) crystals occurs along the close packed planes and in close packed directions. Specifically, such as shown in the Figure 34, the specific slip planes and the three directions are type (111) and $[-1\ 1\ 0]$, $[0\ -1\ 1]$, $[1\ 0\ -1]$, respectively. Given the symmetric permutations of the slip plane types and direction types, FCC crystals have 12 slip systems.

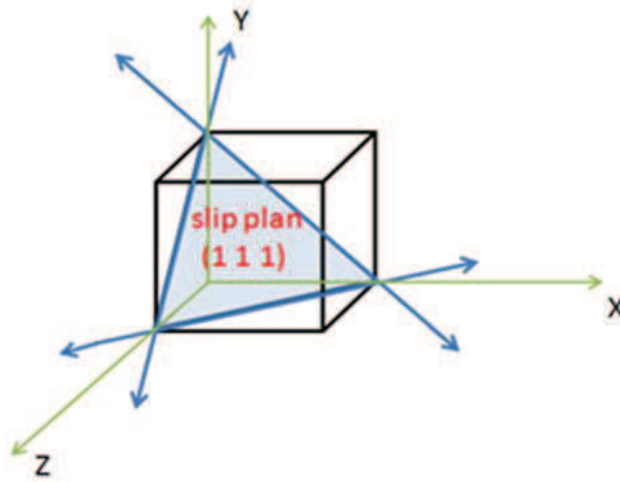


Figure 34 Slip Planes and directions in FCC single crystal structure

In order to discuss the different slip-systems properties, we adopt the following notation for slip systems proposed earlier by Schmid and Boas [Schmid and Boas 1935], in which letters and numbers are given with respect to planes and slip directions, respectively. Table 5 gives Schmid and Boas notation of slip systems in FCC crystals.

Table 5 Schmid and Boas notation of slip systems in FCC

Normal to slip plane			Slip direction			Potential slip system						
A ($\bar{1}$ 1 1) B (1 1 1) C ($\bar{1}$ $\bar{1}$ 1) D (1 $\bar{1}$ 1)			1 [0 1 1]			A2 A3 and A6 B2 B4 and B5 C1 C3 and C5 D1 D4 and D6						
			2 [0 $\bar{1}$ 1]									
			3 [1 0 1]									
			4 [$\bar{1}$ 0 1]									
			5 [$\bar{1}$ 1 0]									
			6 [1 1 0]									
A2 A3 A6		B2 B4 B5		C1 C3 C5		D1 D4 D6						
Plane	($\bar{1}$ 1 1)		(1 1 1)			($\bar{1}$ $\bar{1}$ 1)			(1 $\bar{1}$ 1)			
\vec{b}	[0 $\bar{1}$ 1]	[1 0 1]	[1 1 0]	[0 $\bar{1}$ 1]	[$\bar{1}$ 0 1]	[$\bar{1}$ 1 0]	[0 1 1]	[1 0 1]	[$\bar{1}$ 1 0]	[0 1 1]	[$\bar{1}$ 0 1]	[1 1 0]
No.	1	2	3	4	5	6	7	8	9	10	11	12

Schmid's law gives the general condition to flow on a system of sliding and it is well verified in the case of FCC crystals at ambient temperature. As shown in Figure 35, when the applied stress along the tensile axis is σ and if slip occurs on the slip plane, with plane normal n , then the slip direction will lie in this plane and the shear stress on the slip plane parallel to the slip direction is therefore given by:

$$\tau = \sigma \cos \lambda \cos \phi \quad (11)$$

The quantity $\cos \lambda \cos \phi$ is called Schmid's factor. Imagine that a series of slip systems which we will label with s and that a slip system refers to a particular slip plane characterized by a normal \vec{n}^s and an allied slip direction characterized by the unit vector \vec{m}^s . Activation of a given slip system means that plastic strain (i.e. a relative displacement across particular planes) has begun on that slip system. The motivation for introducing such strong kinematic assumptions is revealed already at the level of the optical

microscope in which a plastically deformed material is seen to have surface steps that run along certain preferred directions corresponding to the end of the slip planes at the crystal surface. The resolved shear stress due to external loading on each system increases until eventually a critical shear stress τ_c^s is reached on one system. The crystal begins to plastically deform by dislocation move and slip on this system, known as the primary slip system:

$$|\tau^s| - \tau_c^s = 0 \quad (12)$$

τ^s can be framed in tensor language as:

$$\tau^s = \sigma(\vec{m}^s \otimes \vec{n}^s) \quad (13)$$

where σ is the stress tensor, \vec{m}^s and \vec{n}^s as related slip direction and slip plane normal.

From Schmid's Law, it is apparent that the primary slip system will be the system with the greatest Schmid factor. It is possible to calculate the values of $\cos \lambda \cos \phi$ for every slip system.

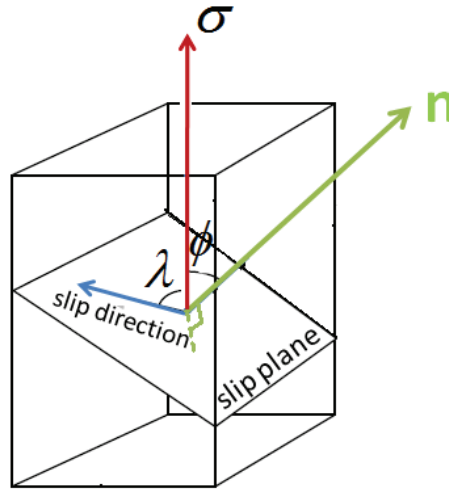


Figure 35 Slip direction and slip plane of the definition of Schmid factor

The value of the critical shear stress τ_c^s is determined by the stress required to overcome obstacles preventing the movement of dislocations. The main obstacles to movements of dislocations are described below:

- *Peierls-Nabarro stress*. The applied resolved shear stress required to make a dislocation glide in an otherwise perfect crystal is called the Peierls (Peierls-Nabarro) “friction” stress (see Figure 36). It arises as a direct consequence of the periodic structure of the crystal lattice and depends significantly on the form of the force-distance relationship between individual atoms, i.e. on the nature of the interatomic bonding. For FCC structures, the depth of the Peierls valleys is low. At room temperature, the dislocations glide almost without friction. If there are no other

barriers to movement of dislocations, the material deforms easily without need of a high stress level. On the contrary, for low temperatures, friction is the predominant mechanism controlling the plastic flow of CFC structure.

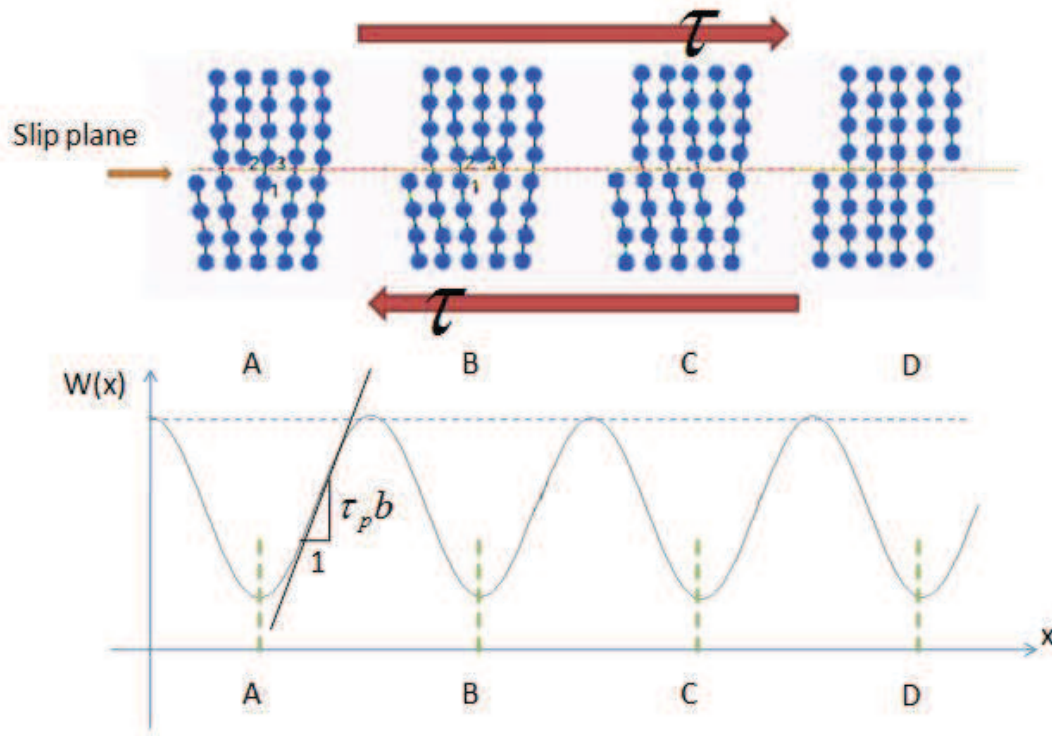


Figure 36 Movement of the dislocation and crossing valleys of Peierls

- *Latent hardening.* When a dislocation is moving, it may encounter dislocations from other systems that break its sliding barriers and become its progression. The crossing of these barriers is sensitive to thermal activation. Dislocations piercing the slip plane dislocations are called "forest" (Figure 37). In CFC structures, the forest of dislocations is the dominant obstacle for dislocations moving.
- *Other obstacles.* Precipitates, defects and grain boundaries are also other obstacles to the movement of dislocations.

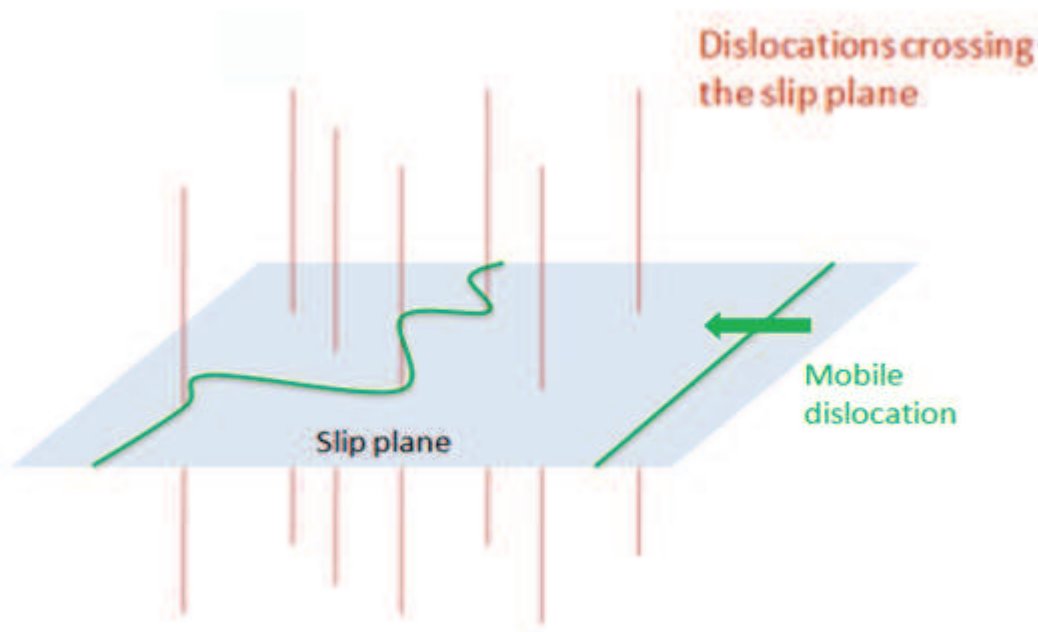


Figure 37 Dislocation forest obstacles

The interaction of dislocations, the dislocation forest, the precipitates and so on limit their movement and are responsible for the increase of critical shear stress, i.e. the hardening of the material. During the hardening, different phenomena such as multiplication or annihilation of dislocations are also highlighted. These mechanisms are more or less depend on the crystal structure, the temperature or the deformation level. Some points are mentioned here aiming at making better reading and understanding of polycrystal constitutive models.

One of the predominant mechanisms in the CFC type structures, determined by Frank and Read, is the production and multiplication dislocations when a crystal is subjected to a certain stress level. Frank-Read sources occur when a dislocation is pinned at two points within the crystal lattice. The dislocation may be pinned by impurities or it may be a dislocation loop that lies obliquely to the basal plane and so is immobile. In the latter case, the section intersecting the basal plane can be considered as a line dislocation pinned at its ends by the immobile sections that are oblique to the basal plane (see Figure 38). When a small stress is applied to the lattice the pinned dislocation bows. With increasing stress the bow becomes unstable and grows to form the shape illustrated in Figure 38d. The dislocation becomes unstable if the shear stress is larger than the critical shear stress level which can be written as:

$$\tau = G b / 2R \quad (14)$$

where G is the shear modulus, b the Burgers vector, and $2R$ is the distance between the pinning sites. With continued stress the loop grows and eventually curls onto itself. This mechanism is shown in Figure 38 and is activated if the shear stress applied on the

dislocation segment reaches a threshold inversely proportional to the radius of curvature R of the dislocation.

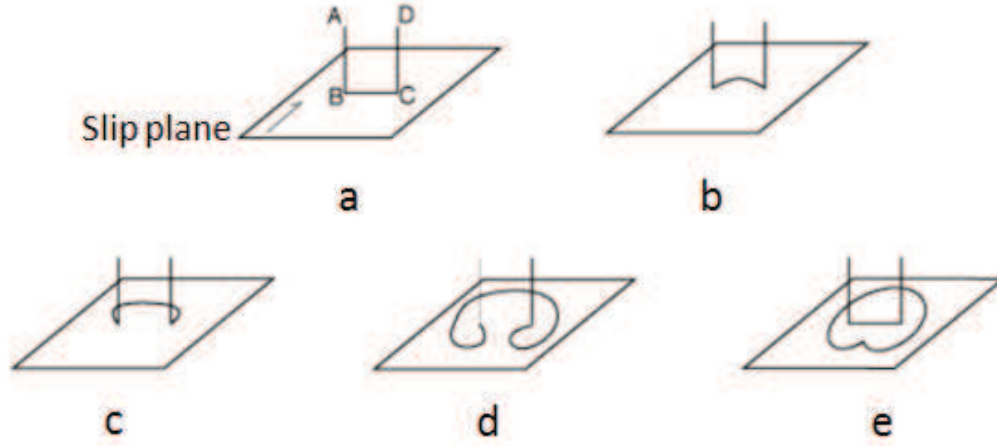


Figure 38 A Frank-Read source for the multiple initiation of dislocation loops.

• Flow rule in modeling

In our CristaleCP model [Erieau and Rey 2004], the flow rule is a viscoplastic one written on each slip system. The resolved shear stress τ^s applied determines the rate of deformation $\dot{\gamma}^s$. τ_c^s is the critical shear stress on the system (s), n determines the sensitivity to the rate of deformation:

$$\dot{\gamma}^s = \begin{cases} \dot{\gamma}^0 \left(\frac{|\tau^s - x^s|}{\tau_c^s} \right)^n \times \text{sign}(\tau^s - x^s) , & \text{if } \frac{|\tau^s - x^s|}{\tau_c^s} \geq 1 \\ 0 & , \text{if } \frac{|\tau^s - x^s|}{\tau_c^s} < 1 \end{cases} \quad (15)$$

where x^s is called the back stress, and expresses the hardening of the material.

By considering the possible hardening of various slip systems, increasing dislocation density on one slip system will harden other systems, through the mechanism of the forest hardening. The critical shear stress on each system will then take the form as:

$$\dot{\tau}_c^s = \sum_u h^{su} |\dot{\gamma}^u| \quad (16)$$

where h^{su} is called hardening matrix giving interaction between slip systems (s) and (u). $|\dot{\gamma}^u|$ is the accumulation rate of the plastic strain on slip system (u).

• Isotropic and kinematic hardening

The critical shear stress on slip system (s) is given by:

$$\tau_c^s = \tau_0 + \mu b \sqrt{\sum_{t=1}^{12} a^{st} \rho^t} \quad (17)$$

The evolution of the density of dislocations can occur in each slip system, and the rate is written as:

$$\dot{\rho}^s = \frac{|\dot{\gamma}^s|}{b} \left(\frac{1}{\lambda^s} - 2g_c \rho^s \right) \quad (18)$$

It results from a combination of two mechanisms: the production of new dislocations controlled by parameter $\lambda^s = \frac{L}{\sqrt{\sum_{t \neq s} \rho^t}}$ which describes the free path on the slip system(s), and the annihilation of dislocation controlled by annihilation distance g_c . L is a material parameter controlling the dislocation production.

This hardening rule (equations (17) and (18)) takes into account all interactions between dislocations through the hardening matrix a^{st} . Nevertheless this hardening rule makes no difference between short range forest and long-range interactions. Therefore, in spite of a partial kinematic effect resulting from long range grain strain incompatibilities, these equations are not sufficient to precisely describe the cyclic plasticity and the Bauschinger effect. In addition, kinematic hardening exists even in only one grain as shown by DD simulations [Depres, Fivel and Tabourot 2008]. Therefore, it has been shown in this steel that the introduction of long range interactions through a long range kinematic back stress x^s is necessary. It was also reported recently that kinematic hardening can also be described by geometrically necessary dislocation accumulation but this needs a very fine meshing of the aggregate [Evers, Parks, Brekelmans and Geers 2002; Schwartz, Fandeur and Rey 2010]. In our case, the nonlinear kinematic hardening rule initially proposed by Armstrong and Frederick [Armstrong and Frederick 1966] was chosen:

$$\dot{x}^s = C\dot{\gamma}^s - D|\dot{\gamma}^s|x^s \quad (19)$$

where C , D are material parameters. They are fitted from the macroscopic cyclic stress-strain curve at midlife under 0.5% strain amplitude.

• *Softening rules*

As mentioned in the first chapter, for 304L, fatigue test under total strain controlled amplitude ranging from 0.15% to 1% all showed obvious cyclic softening behavior after cyclic hardening, especially from 0.15% to 0.5%. The stress amplitudes fell down about 10% to 25% when the strain amplitude was stabilized. Cyclic softening in single phase CFC alloys is due to the microstructure evolution, i.e. decrease in dislocation density through dislocation annihilation and changes in dislocation structure [Armas, Petersen, Schmitt, Avalos and Alvarez-Armas 2002; Marmy and Kruml 2008].

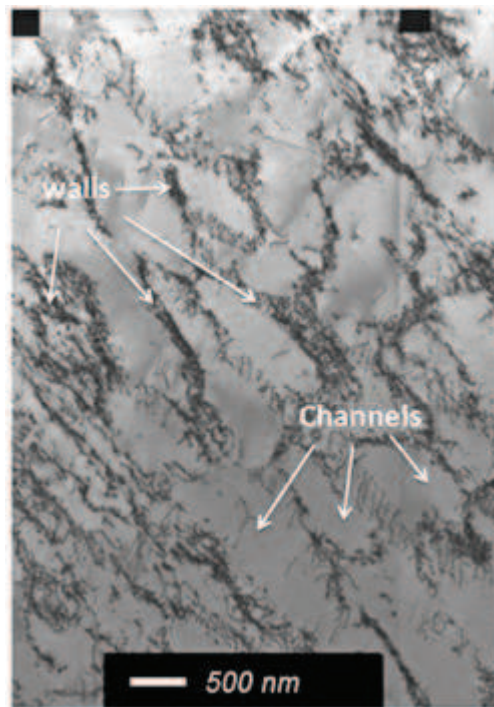


Figure 39 Dislocation structure in a specimen of 304L steel cycled to fracture with a total strain amplitude of 5×10^{-3} [Le-Pecheur 2008]

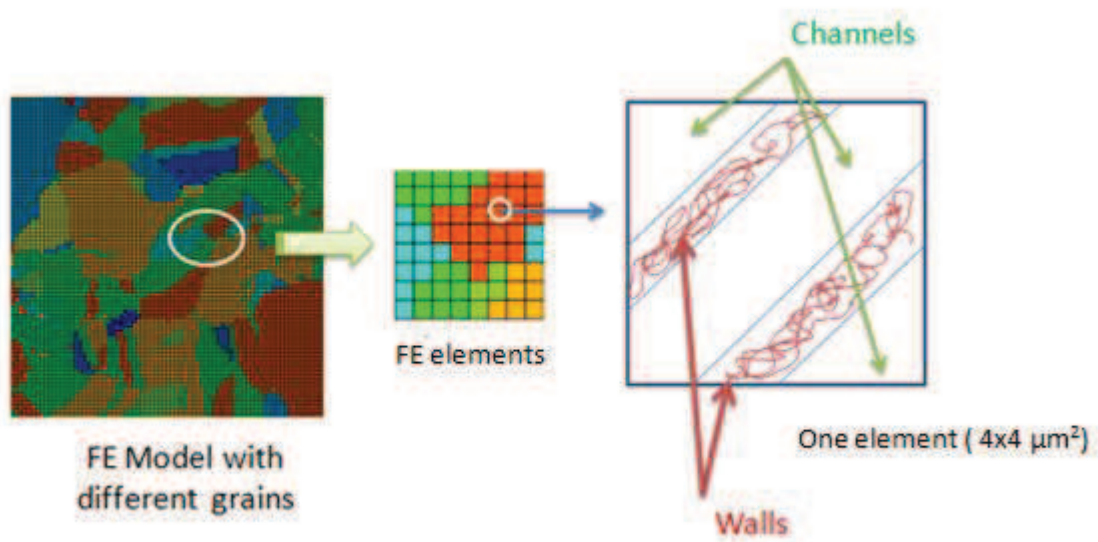


Figure 40 The description in the modeling for hardening/softening accommodation behavior

As observed by TEM (Figure 39), 304L steel subjected to cyclic loading presents a microstructure composed of dislocation walls which are barriers to the movement of dislocations and channels where the mobility of dislocations is easy. In the present model, it is considered that the cyclic softening is due to the occurrence of heterogeneous

microstructure of dislocations composed of alternating wide channels with low dislocation density and thin walls with high dislocation density [Polak, Degallaix and Degallaix 1993; Obrlik, Kruml and Polak 1994; Mayama and Sasaki 2006; Evrard, Alvarez-Armas, Aubin and Degallaix 2010]. According to heterogeneous dislocation structures observed in low-cycle fatigue, Mughrabi proposed a composite model [Mughrabi 1983] in which the grain contains simultaneously walls and channels (Figure 40). Both are based on the evolution of dislocation densities and the forest hardening. The rearrangement of dislocations is taken into account through the volume fraction of channels, which increases during the cyclic straining. This composite model was written at the slip system scale in an austenitic stainless steel [Evrard, Aubin, Degallaix and Kondo 2008] and in an austenitic-ferritic stainless steel [Evrard, Alvarez-Armas, Aubin and Degallaix 2010]. It is assumed that the total strain is the same in the walls and channels within a given FE element. The resolved shear stress τ^s is given by [Suresh 1991]:

$$\tau^s = f_w^s \tau_w^s + f_{ch}^s \tau_{ch}^s \quad (20)$$

where τ_w^s and τ_{ch}^s are the resolved shear stresses in walls and in channels on the slip system (s) and f_w^s and f_{ch}^s are the volume fraction of walls and channels, respectively.

As other authors [Estrin 1998], it is considered that the shear strain rate is the same in walls and channels:

$$\dot{\gamma}^s = \dot{\gamma}_{ch}^s = \dot{\gamma}_w^s \quad (21)$$

where $\dot{\gamma}_{ch}^s$ and $\dot{\gamma}_w^s$ are shear strain rate in channels and walls, respectively. Consequently, as in the proposed crystalECP law, the critical shear stress on slip system (s) τ_c^s , now includes the critical shear stresses of walls and channels via a mixture law is written as [Evrard, Aubin, Degallaix and Kondo 2008]:

$$\tau_c^s = f_w^s \tau_{c,w}^s + f_{ch}^s \tau_{c,ch}^s \quad (22)$$

where $\tau_{c,w}^s$ and $\tau_{c,ch}^s$ are the critical shear stresses of walls and channels.

It is supposed that the wall and channel structure evolution on the slip system (s) is described by the channel volume fraction. Using the relationship $f_w^s + f_{ch}^s = 1$, the equation (22) is modified as:

$$\tau^s = (1 - f_{ch}^s) \tau_w^s + f_{ch}^s \tau_{ch}^s \quad (23)$$

$$\tau_c^s = (1 - f_{ch}^s) \tau_{c,w}^s + f_{ch}^s \tau_{c,ch}^s \quad (24)$$

Two hardening laws are considered: one for walls and another for channels. In walls, the classical hardening law is kept. According to the work of Evrard, the following formula for the critical shear stress of walls $\tau_{c,w}^s$ is taken [Evrard, Aubin, Degallaix and Kondo 2008]:

$$\tau_{c,w}^s = \tau_0 + \mu b \sqrt{\sum_{12} a_{st} \rho_w^s} \quad (25)$$

where ρ_w^s is the dislocation density in walls on the slip system (s) and its evolution rate is given by:

$$\dot{\rho}_w^s = K \left(\frac{\sqrt{\sum_{12} \rho_w^u - \rho_w^s}}{L_w} + \frac{1}{D} - g_{c,w} \rho_w^s \right) \frac{|\dot{\gamma}_w^s|}{b} \quad (26)$$

where L_w and $g_{c,w}$ are material parameters controlling the dislocation production and annihilation distance in walls, respectively. K is a factor controlling the evolution rate of ρ_w^s which has to be fitted to the shape of the hardening/softening curve for one strain amplitude level.

In channels, only few dislocations intercept an active slip system. The critical shear stress of channels $\tau_{c,ch}^s$ is described as [Evrard, Aubin, Degallaix and Kondo 2008]:

$$\tau_{c,ch}^s = \tau_0 + \mu b \sqrt{a_{ss} \rho_{ch}^s} \quad (27)$$

where a_{ss} is a self hardening coefficient. This parameter was set to 1 in the work of Evrard [Evrard, Aubin, Degallaix and Kondo 2008]. However, it was found that the stress amplitude level decreased slightly after several calculation cycles, which is not in good agreement with fatigue experimental results in 304L. So the value of a_{ss} was taken as 0.045 here, the same value as a_0 , and ρ_{ch}^s in equation (27) is the dislocation density in channels on the slip system (s) and its rate is described as:

$$\dot{\rho}_{ch}^s = \left(\frac{\sqrt{\rho_{ch}^s}}{L_c} + \frac{1}{D} - g_{c,ch} \rho_{ch}^s \right) \frac{|\dot{\gamma}_{ch}^s|}{b} \quad (28)$$

where L_c and $g_{c,ch}$ are material parameters controlling the dislocation production and annihilation distance in channels, respectively.

According to Estrin and Evrard, the modification of channel volume fraction on each slip system can be defined by a phenomenological law [Estrin 1998; Evrard, Aubin, Degallaix and Kondo 2008]:

$$\dot{f}_{ch}^s = H \left(1 - \frac{1}{f_{\infty}^s} f_{ch}^s \right) |\dot{\gamma}^s| \quad (29)$$

where f_{∞}^s is the asymptotic volume fraction of channels. Contrary to the work of Evrard [Evrard, Aubin, Degallaix and Kondo 2008], in the present study, f_{∞}^s is not a fixed constant but depends on the cyclic shear amplitude according to experimental observations carried out on 316L steel which is similar to 304L (Figure 41). It is observed that when the imposed plastic strain amplitude increases, the dislocation density increases in the walls, and the channel width and wall thickness evolve [Polak, Degallaix and Degallaix 1993; Obrtlík, Kruml and Polak 1994]. H is a factor controlling the f_{ch}^s

evolution rate which has to be fitted on the shape of the hardening-softening curve for one strain amplitude.

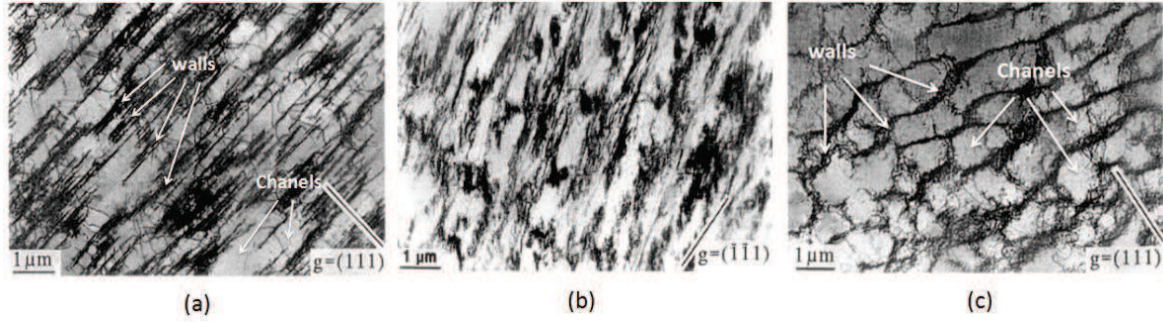


Figure 41 Dislocation structure in a specimen of 316L steel cycled to fracture with the plastic strain amplitude of (a) 5×10^{-5} (b) 2×10^{-4} (c) 5×10^{-3} [Polak, Obrtlik and Hajek 1994]

In order to avoid the accumulation of volume fraction of channels during $\frac{1}{4}$ cycle of the monotonic straining and to allow for a monotonic strain to be considered with the same model, $\left(1 - \frac{|\gamma^s|}{\Gamma^s}\right)$ was involved:

$$\dot{f}_{ch}^s = H \left(1 - \frac{1}{f_{\infty}^s} f_{ch}^s\right) |\dot{\gamma}^s| \left(1 - \frac{|\gamma^s|}{\Gamma^s}\right) \quad (30)$$

where γ^s is the value of slip shear on the slip system (s) and Γ^s is the accumulated absolute value of slip, which can be written as respectively:

$$\gamma^s = \int_0^t \dot{\gamma}^s dt \quad (31)$$

$$\Gamma^s = \int_0^t |\dot{\gamma}^s| dt \quad (32)$$

In the case of a monotonic straining, $|\gamma^s| = \Gamma^s$ then $\dot{f}_{ch}^s = 0$; and for pure cyclic straining $|\gamma^s| = 0$ then $\dot{f}_{ch}^s = H \left(1 - \frac{1}{f_{\infty}^s} f_{ch}^s\right) |\dot{\gamma}^s|$.

3.3 Identification of the parameters

The character of such model is generally presented, but the determination of coefficients in the models for particular 304L steels presents some problems. It is tried to keep a physical meaning for each parameter. The identification of parameters used in the crystalline constitutive law for steel 304L is based on the previous work of Anne Le Pecheur [Le-Pecheur 2008]. Some parameters were directly measured from experimental results, or obtained from the literature. The others were identified through an inverse identification. Elastic constants C_{11} , C_{12} and C_{44} were adopted from the work of Sauzay [Sauzay 2006]. The initial dislocation density is low, and we set $\rho_0 = 1.10^{12}/m^2$. The mean free path of dislocations λ^s was chosen as the average size of the cells observed at the stabilized cycle. It is approximately equal to $1 \mu m$. So the related mean free path constant,

L , can be calculated by $L = \lambda^s \sqrt{\sum_{t \neq s} \rho^t}$ and is equal to 1. The interaction matrix coefficients, the reference shear rate, $\dot{\gamma}_0$, and the rate exponent, n , were set from the values identified in the literature from dislocation dynamics simulation for an initial dislocation density equal to $10^{12} /m^2$, which is close to our observation [Devincre, Kubin and Hoc 2006]. The distance of annihilation, g_c , the material parameters in nonlinear kinematic hardening rule C , D and the microscopic yield stress τ_0 were identified through an inverse procedure, in which the simulation of a polycrystalline aggregate was compared to the macroscopic experimental stress-strain behavior measured during the stabilized cycle at midlife with a strain amplitude of 0.5% (Figure 42).

3.3.1 Identification results

As shown in Figure 42, experiment and simulation results were compared. The simulated stabilized hysteresis loops are compared with experimental mid-life results under five different total strain amplitudes of 0.2%, 0.3%, 0.5%, 0.7%, and 1.0%,. Here the 0.5% strain amplitude data were used to identify material parameters τ_0, g_c, C, D . The curves under strain amplitudes of 0.2%, 0.3%, 0.7% and 1.0% are predictive results [Le-Pecheur 2008].

It should be noted that even for the case of low strain amplitude the plastic part is important and cannot be neglected. This is an important feature of the cyclic behavior of 304L. It is also necessary to take notice that the loops show a strong Bauschinger effect that means the yield stress in compression is much lower than that obtained in tension. The center of the elastic domain is thus strongly shifted towards positive stresses. The origin of the Bauschinger effect observed at the macroscopic level is the heterogeneity of plastic deformation within the material at the microscopic level. This heterogeneity may be the consequence of different orientations of grains thus varying the flow stress.

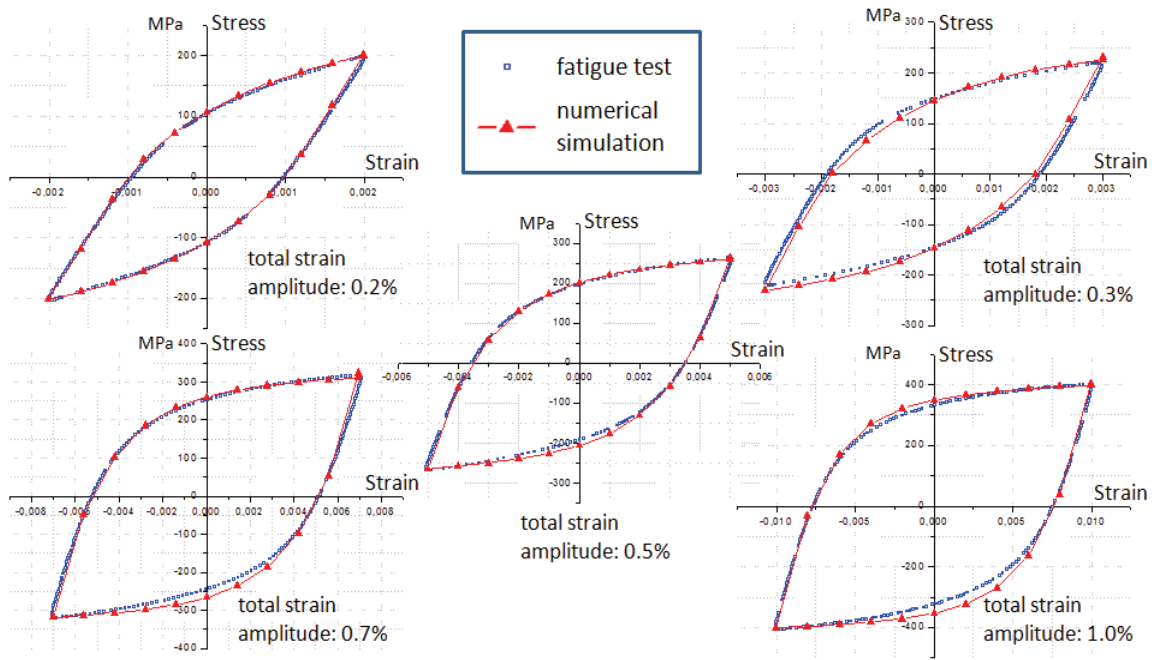


Figure 42 Mid-life hysteresis loops for 304L subjected to fully reversed tension-compression cyclic deformation with increasing values of total strain amplitude. The numerical simulated results are examined and compared to fatigue experiments [Le-Pecheur 2008].

The asymptotic volume fraction of channels f_{∞}^s must lie in the range $[0, 1]$. However, as both walls and channels are visible in a very large range of plastic strain amplitude, it was proposed that at least 10% of the volume is occupied by either walls or channels in the material. For sake of simplicity, it is considered that the asymptotic volume fraction of channels is a linear function of the cyclic plastic strain amplitude between 10^{-4} and 2×10^{-3} (Figure 43b). According to the dislocation measurement (Figure 41), the volume fraction of the channel is rather low when the material is subjected to small plastic strain amplitude loading (see Figure 41a). According to [Obtlik, Kruml and Polak 1994; Polak, Obtlik and Hajek 1994; Krupp 2007], at low levels of plastic shear amplitude (less than 10^{-4}), denoted region I in Figure 43a, the work hardening is almost entirely due to the accumulation of primary dislocations. Under these conditions, the specimen could withstand a very high number of fatigue cycles because the cyclic plastic strain amplitude is too low to form PSBs. So the level of plastic shear amplitude 10^{-4} can be considered as the threshold of PSBs formation. The asymptotic volume fraction of channels f_{∞}^s is set as a small value, here 0.1, as long as plastic shear amplitude is less than 10^{-4} (Figure 43b).

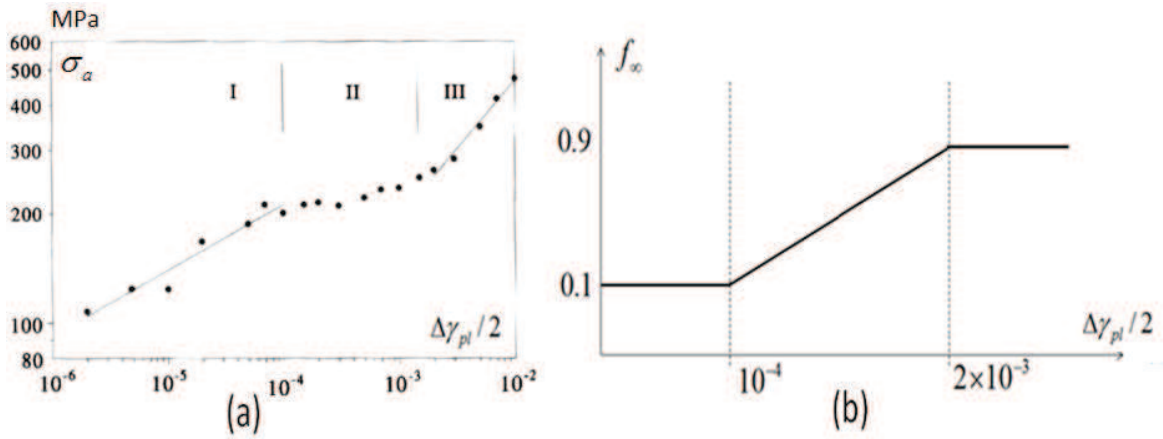


Figure 43 (a) Amplitude of the resolved saturation shear stress $\Delta\tau^s/2$ vs. the plastic strain amplitude $\Delta\gamma_{pl}/2$ for 316L steel [Obtlik, Kruml and Polak 1994; Polak, Obtlik and Hajek 1994]. (b) Simplified relation of the volume fraction of channels with the cyclic plastic strain amplitude

In Figure 43a, when the plastic shear amplitude increases until 2×10^{-3} , the resolved shear stress is plateaued, which is called region II in this figure. In this region, the dislocation arrangement shows the mixture of the matrix structure (Figure 41b). A further increase in plastic shear amplitude results in an increase in the peak resolved shear stress at saturation, called region III as shown in Figure 43a. Under these conditions of plastic shear amplitude greater than 2×10^{-3} , the dislocation structure showed the channels were densely distributed around the walls (Figure 41b). At this stage, f_∞^s has been chosen as 0.9 according to experimental observation (Figure 41c).

Overall, the asymptotic volume fraction of channels f_∞^s can be calculated as:

$$f_\infty^s = \begin{cases} 0.1 & \Delta\gamma^s < 10^{-4} \\ \frac{8000}{19} \cdot \frac{\Delta\gamma^s}{2} + \frac{11}{190} & 10^{-4} \leq \Delta\gamma^s \leq 2 \times 10^{-3} \\ 0.9 & \Delta\gamma^s \geq 2 \times 10^{-3} \end{cases}$$

Table 6 summarizes the model parameter values obtained for the studied 304L steel material.

Table 6 The parameters of the crystalline constitutive law identified for 304L steel

C_{11} MPa	C_{12} MPa	C_{44} MPa	μ MPa	τ_0 MPa	$\dot{\gamma}_0$ /s	n	a_0	a_1
197500	125000	122000	61000	10	10^{-5}	49	0.045	0.625
a_2	a_3	a_{ss}	ρ_0 /m ²	b nm	L	g_c nm	C	D
0.137	0.122	0.045	10^{12}	0.254	1	150	15300	430

As mentioned in section 3.2.2, K and H are two factors controlling the ρ_w^s and f_{ch}^s evolution rates that have to be fitted on the shape of the hardening-softening curve for a given amplitude level. Under strain controlled amplitude loading, the stabilized stress amplitude should reach the same level no matter what K and H values were used. In order to confirm this point, the tests on a monocrystal with 1000 elements were simulated under strain amplitude of $\pm 5 \times 10^{-3}$. Figure 44 shows the stress evolution curves obtained with four different K values 0.005, 0.05, 0.2 and 1. The results show that the stabilized stress amplitudes reach the almost the same value (difference less than 3MPa). Figure 45 shows the stress evolution curves obtained with different four H are 5, 10, 50 and 100 in 100 simulation cycles in the cases when K=1 and K=2. It can be seen that when K is taken as a large value 2, the stress reaches maximum value in only one cycle then softening appears. On the contrary, when K is taken as 1, the maximum stress was delayed after 2 or 3 cycles. So it can be said that if smaller values of the K are taken then more details about cyclic hardening can be obtained. The behavior, for H, is similar as if it is taken to a larger one, fewer cycles are needed to reach the stabilization. Furthermore, Figure 46 shows that stabilized stress/strain hysteresis loops obtained with these five H values are also similar. After 100 cycles the peak stress difference for these different H values is less than 0.4 MPa.

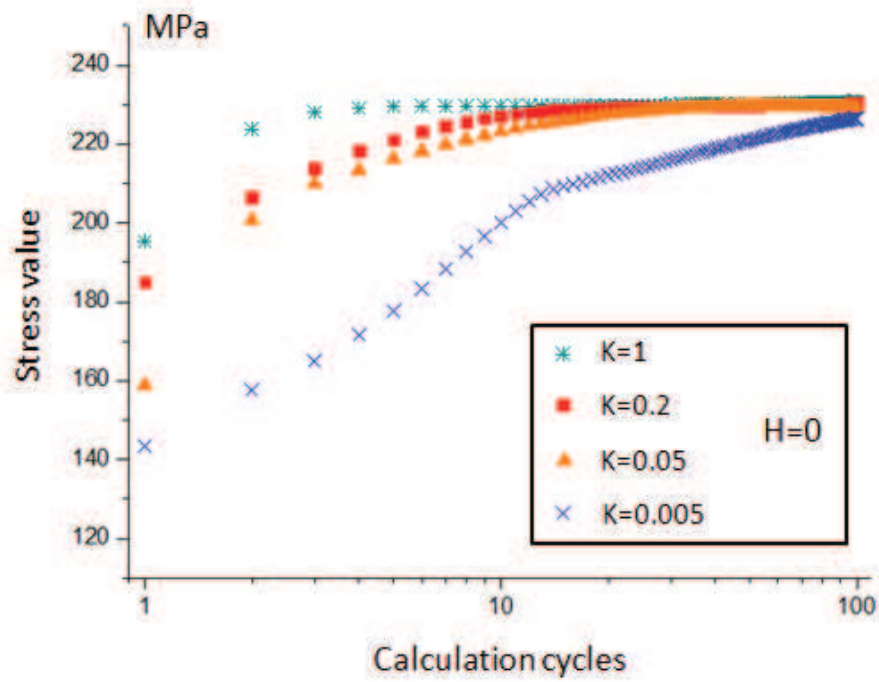


Figure 44 The stress evolution curves obtained with various K values (cycled with a strain amplitude of $\pm 5 \times 10^{-3}$)

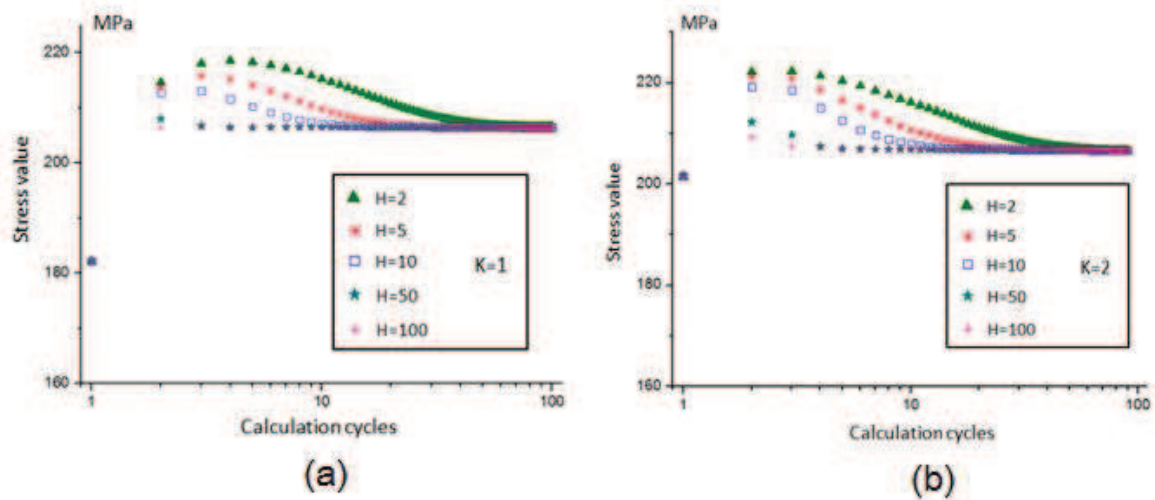


Figure 45 The stress evolution curves obtained with various H values (cycled with a strain amplitude of $\pm 5 \times 10^{-3}$) (a) $K=1$ (b) $K=2$

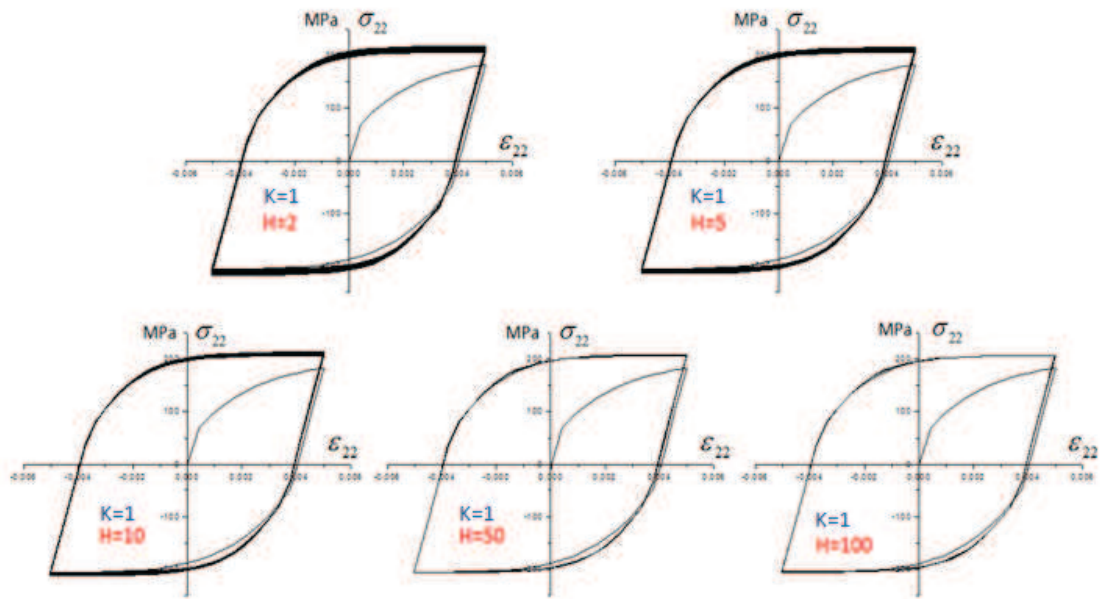


Figure 46 Stress/strain hysteresis loops obtained with different H values (cycled with a strain amplitude of $\pm 5 \times 10^{-3}$)

3.4 Result discussion

3.4.1 Stress evolution during fatigue

Two reversed low-cycle fatigue tests were conducted under total strain control at two levels $\pm 0.3\%$ and $\pm 0.5\%$. The simulation results of cyclic hardening/softening curves under two levels of the strain amplitude are respectively given in Figure 47 and Figure 48 and compared with experimental results. The results show that the model based on crystalline plasticity is able to account for the cyclic mechanical behavior which includes a hardening followed by a softening and then a stabilized phase.

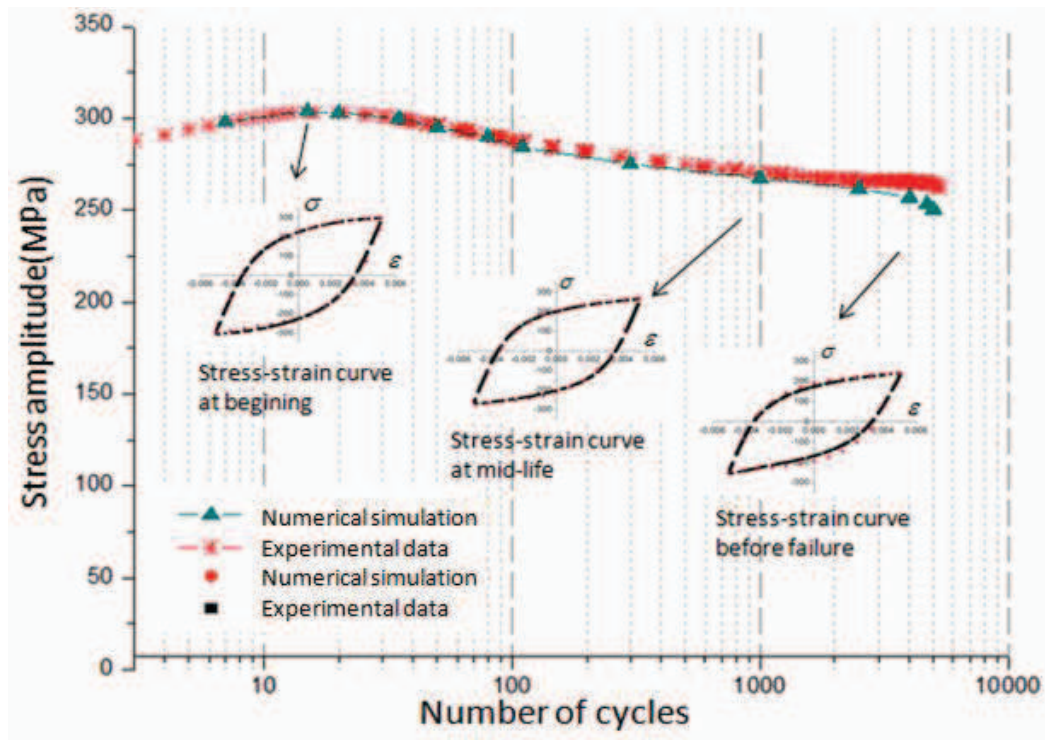


Figure 47 Comparison of hardening and softening curves for a uniaxial low-cycle fatigue test with a total strain amplitude $\pm 0.5\%$ for 304L steel and the stress-strain curves in different phases during fatigue.

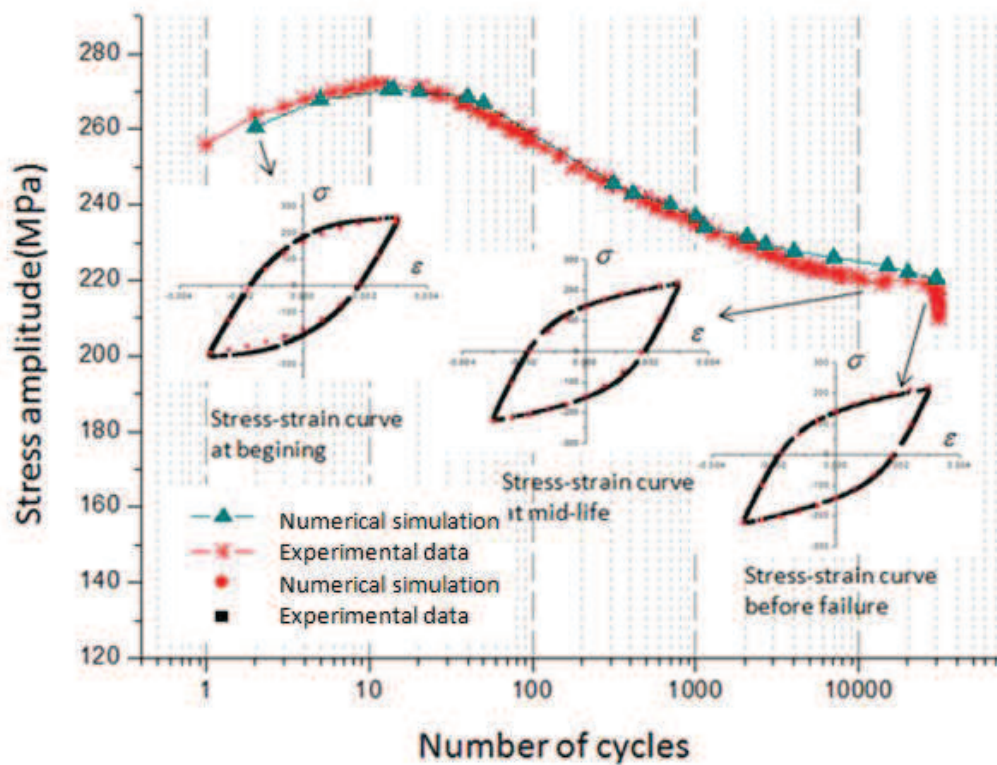


Figure 48 Comparison of hardening and softening curves for a uniaxial low-cycle fatigue test with a total strain amplitude $\pm 0.3\%$ for 304L steel and the stress-strain curves in different phases during fatigue.

It is worth noting that the final stress decrease shown by numerical simulation in Figure 47 and Figure 48 is linked to an increase of plastic localization but does not feature the crack growth as it can be observed in a real specimen.

Furthermore, as discussed in section 3.3, K and H are two important parameters which control the dislocation density and channel fraction evolution rates, respectively. As the results shown in Figure 44, Figure 45 and Figure 46, if H , the coefficient of controlling channel fraction evolution rate, is taken to a larger one, fewer cycles are needed to reach the stabilization. Computing time can be reduced but the detailed softening will be lost. On the contrary, if H is set to a smaller value, more details of softening evolution can be obtained. Meanwhile in order to simulate the detailed hardening cycles, K should be taken a smaller value. Of course, this needs more time to get to the stabilized cycle.

It should be noted that the values of K and H are difficult to set. The values of H under different imposed strain amplitude levels cannot be the same because the acceleration factors are not the same one under different strain amplitudes. As shown in Figure 49, in the case of the simulation under strain amplitude of 0.5% , the acceleration factor is 400 and in the other case of that under strain amplitude of 0.3% , the acceleration factor is 1500. It is clear that H should be larger when the imposed strain amplitude is larger. Because our simulation cycles are still limited by the computing and storage capacity and generally are almost 15-20 cycles. So the value of H can be taken according to the fatigue

life under each level of strain amplitude loading. Following the Coffin-Manson fatigue criteria, strain-life could be modeled using a power relationship: $\frac{\Delta \epsilon_p}{2} = c(N_f)^m$. According to the fatigue studies of [Raman and Padmanabhan 1995; Lehericy and Mendez 2006], the 304L Coffin-Manson parameter m is equal to -0.494. So it means 304L fatigue life is approximatively proportional to $\left(\frac{\Delta \epsilon_p}{2}\right)^{-2}$, then H can be expected to be proportional to $\left(\frac{\Delta \epsilon_p}{2}\right)^{-2}$. In the simulation shown in Figure 47 and Figure 48, the values of K and H are chosen as given in Figure 50.

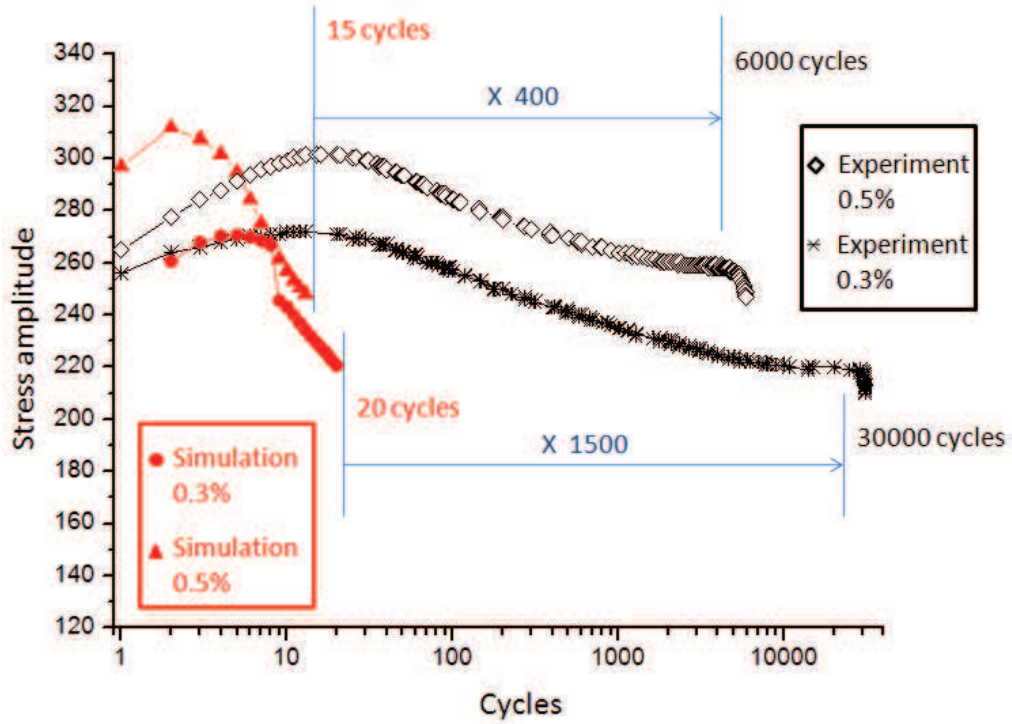


Figure 49 Acceleration factors: simulation cycles compared with the experiment cycles

So here, according to this relationship between H and imposed strain amplitude, H in the first cyclic hardening stage is considered to take a value around $\left(\frac{\sqrt{2}}{100\Delta \epsilon_t}\right)^2$ and K is chosen as 0.2, where $\frac{\Delta \epsilon_t}{2}$ is the total strain amplitude. In order to observe the hardening hysteresis loop characteristics, the first stage needs to correspond to at least 7 or 8 cycles. After these first few cycles, in order to quickly get the stabilized cycle, H is set to 2 to 5 times of the original value.

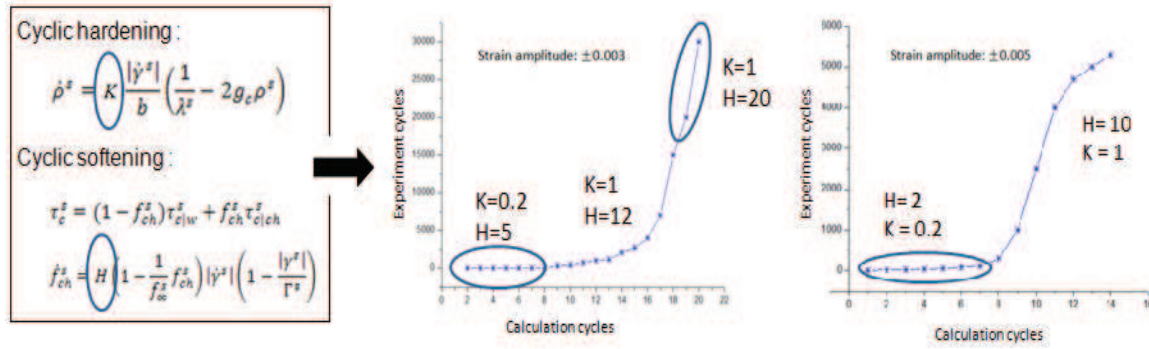


Figure 50 Different K and H factor values used for simulating the cyclic hardening and softening under total strain amplitude of 0.3% and 0.5%

3.4.2 Stress-strain loop curves evolution during fatigue

As seen in Figure 47 and Figure 48, the stress-strain loop curves change during fatigue. The results of the evolution of the stress-strain loop curves are respectively compared to the experimental data. Figure 51 shows the numerical simulation of stress-strain loops in early 20 cycles in comparison with that of early 31000 cycles in experiment under the strain amplitude of $\pm 0.3\%$. Figure 51b gives simulated stress-strain loops in early 15 cycles in comparison with that of early 6100 cycles in experiment under the strain amplitude of $\pm 0.5\%$.

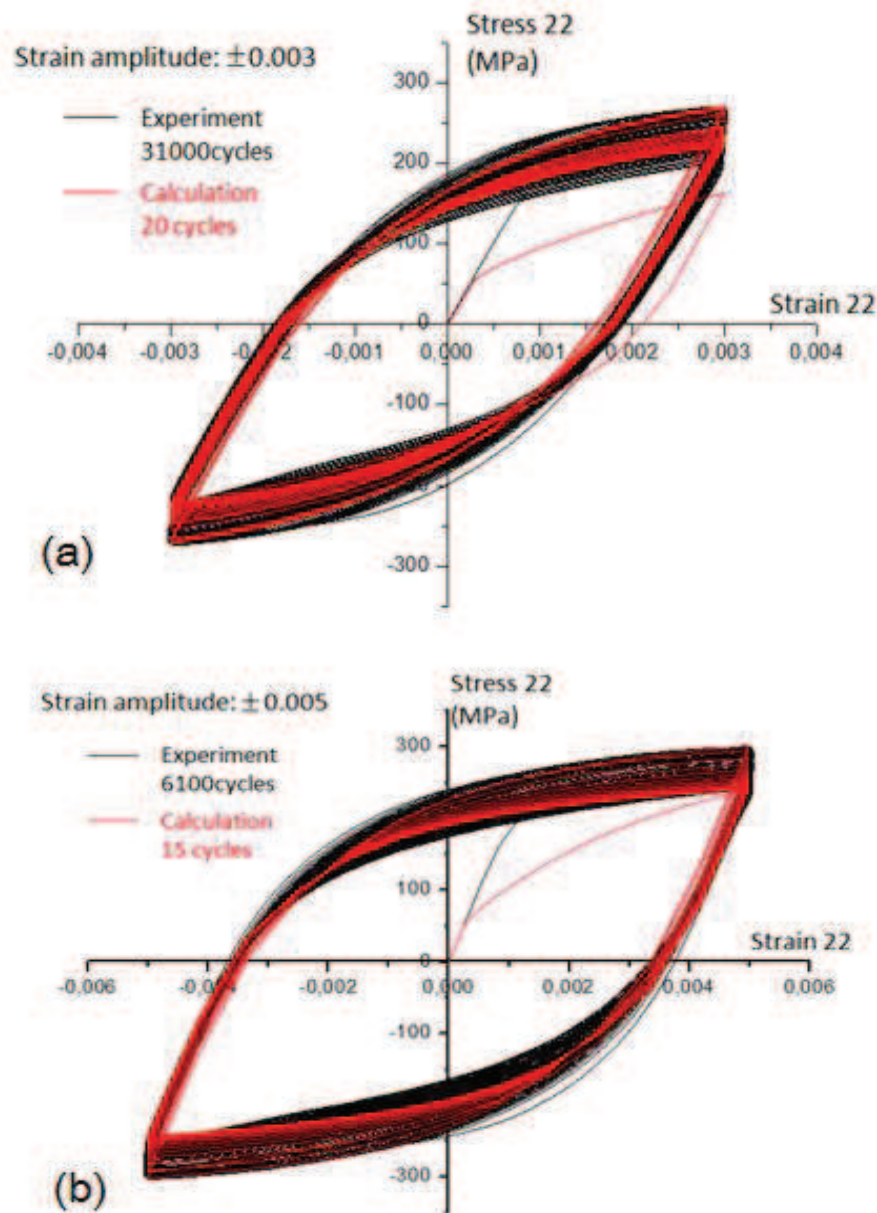


Figure 51 Numerical simulation of stress-strain loops in comparison with experiments (a) total strain amplitude: 0.3% (b) total strain amplitude: 0.5%

Figure 52 shows the stress- strain loops evolution under strain controlled amplitude of 0.5%. By comparing to numerical simulation, it can be found that the simulation results are satisfactory with the experimental results except for the final cycles. As mentioned in section 3.4.1, the reason is that the simulation of softening in this model is based on plastic localization but does not take into account the crack growth as observed from the fatigue experiments.

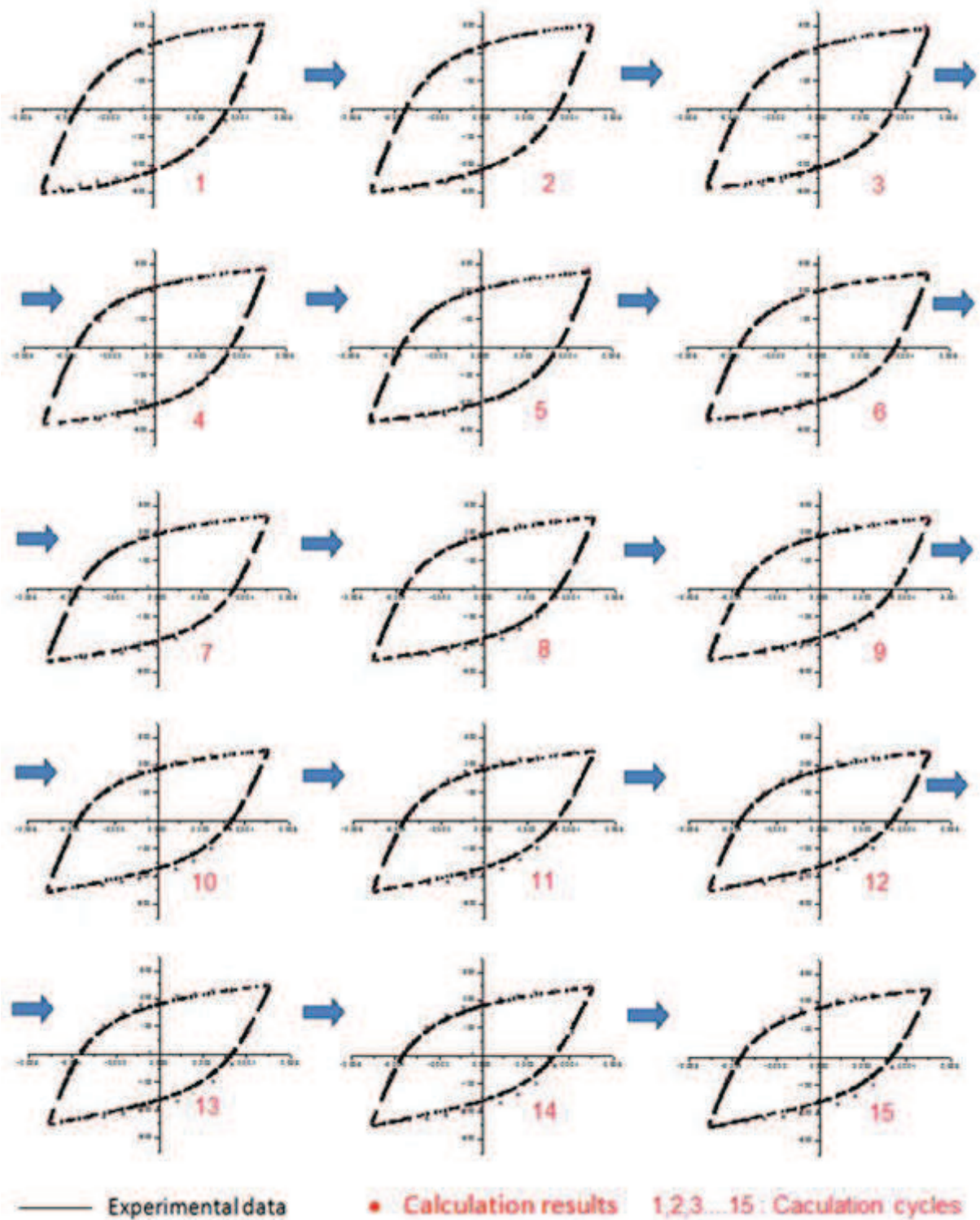


Figure 52 Evolution of the stress-strain loop curves during fatigue under total strain amplitude of 0.5% compared with experiments

3.4.3 Comparison with results obtained not considering cyclic softening

The cyclic hardening/softening simulation results obtained with the new enriched CristalECP code have shown that at the grain scale, polycrystalline numerical simulation of cyclic hardening/softening behavior is possible and can better describe macroscopic cyclic processes occurring during fatigue than with the previous version in which only cyclic hardening was considered. Figure 53 shows the stress amplitude evolutions with the number of simulated cycles under the total strain amplitude of $\pm 0.5\%$ as calculated by previous and new enriched CristalECP codes.

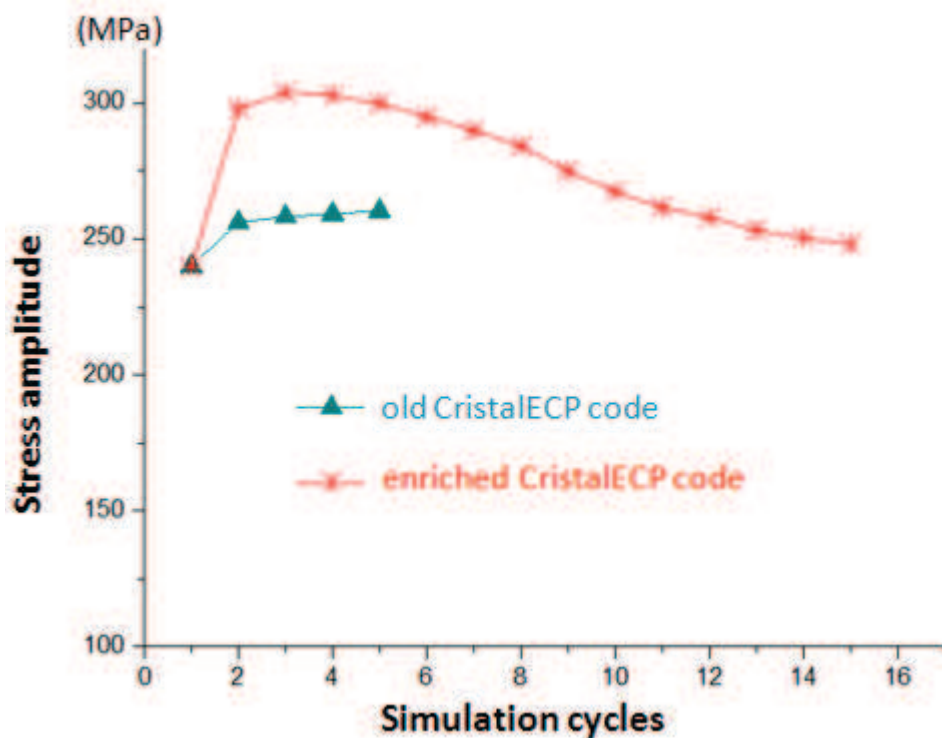


Figure 53 Comparison of stress amplitude evolutions with number of simulated cycles between the old and new enriched CristalECP codes, under the total strain amplitude of $\pm 0.5\%$ (1st cycle = $\frac{1}{4}$ cycle)

However, as shown in Figure 54, from a macroscopic point of view, the stress-strain loops of stabilized cycle simulated by previous CristalECP code and enriched CristalECP code do not show great difference. They are both in good agreement with experiments.

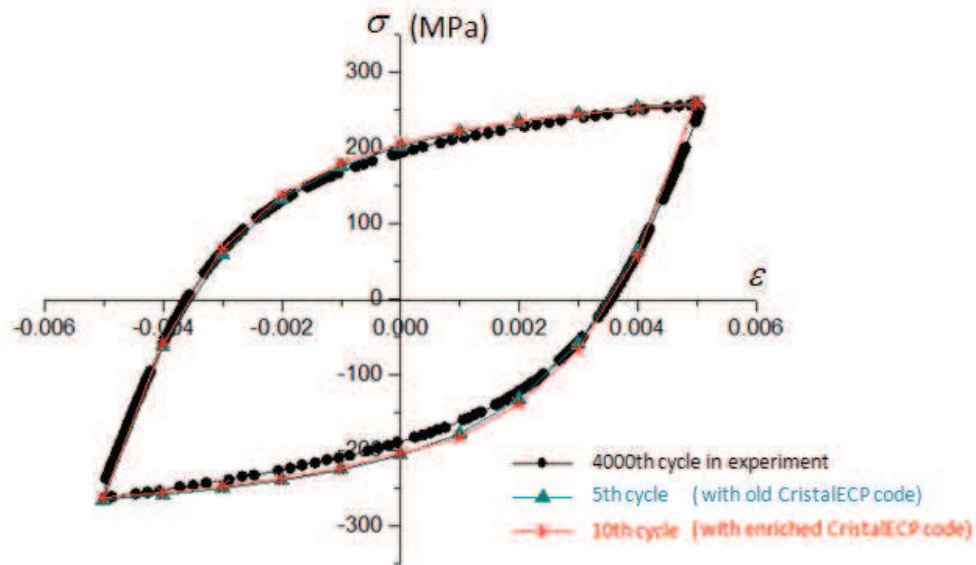


Figure 54 Comparison of stress-strain loops at stabilized cycle between the old and new enriched CristalECP codes

Figure 55 gives the distributions of some mechanical factors at tension peak of the stabilized cycle obtained with the two codes. The values were worked out within all 67500 elements in the aggregate. It can be found that the distributions of maximum plastic strain amplitude on the 12 slip systems and local uniaxial strain obtained with enriched CristalECP code are significantly different from those obtained with the model not considering cyclic softening. However, concerning the normal stress on the corresponding plane with maximum plastic strain amplitude and local uniaxial stress in loading direction, results obtained with new enriched CristalECP have almost the same distributions as those obtained from previous CristalECP.

It is well known that the distribution tail controls the maximum values experienced by the material, and then indicates the place where a crack may occur, especially for low amplitude fatigue. As shown in Figure 55, the maximum plastic strain amplitude values and local uniaxial strains in certain grains obtained with new enriched code are much higher than those obtained with previous code (see the right sides of the curves in Figure 55(a) and (c)). This means that although the model not considering cyclic hardening/softening behavior gives good predictive results of macroscopic stress-strain loops at stabilized cycle, it cannot simulate accurately the peak mechanical values within certain grains and will give nonconservative predictive results of crack initiation life. This shows the importance of taking into account the real stress-strain history to accurately predict local strain heterogeneities and strain life.

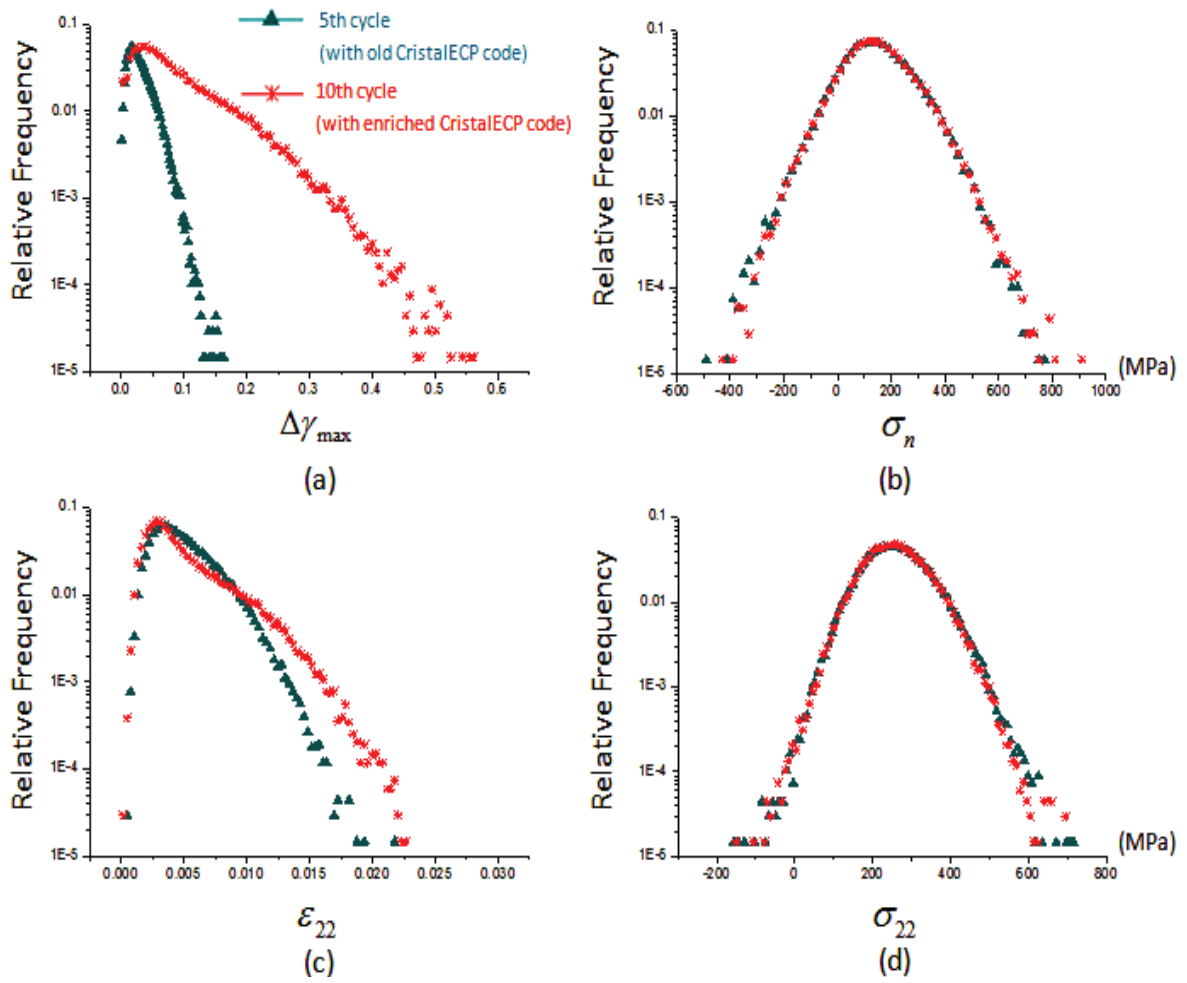


Figure 55 Distributions of some mechanical factors at tension peak in the stabilized cycle obtained with the old and new enriched CristalECP codes: (a) maximum plastic strain amplitude on the 12 slip systems (b) normal stress on the corresponding plane with maximum plastic strain amplitude (c) local uniaxial strain in loading direction (d) local uniaxial stress in loading direction

3.5 Conclusions

The cyclic hardening and softening behavior of materials is a complex phenomenon which is observed in 304L steel subjected to low cycle fatigue. In this chapter, a polycrystal FE model was enriched in order to describe the cyclic hardening/softening based on formation of PSB and the evolution of dislocation densities on slip systems. It was used to describe the mechanical behavior of the austenitic stainless steel 304L using a numerical aggregate obtained from real EBSD measurements. Two different methods to define the RVE were reviewed and compared. The material parameters were obtained through experimental measurements, from the literature or were identified through an inverse procedure. The simulation results of stress and strain curves are in good agreement with experiments under two strain amplitudes loading of 0.3% and 0.5%. They show that at the grain scale, polycrystalline numerical simulation of cyclic hardening and softening behavior is feasible. The obvious advantage of the model is that a relatively small number of cycles is required to be calculated.

Through comparison with results obtained not considering cyclic softening, it shows that the model not considering cyclic hardening/softening behavior can give good predictive results of macroscopic stress-strain loops at stabilized cycle, but it cannot simulate accurately the peak mechanical values within certain grains and will give nonconservative predictive results of crack initiation life. This shows the importance of taking into account the real stress-strain history to accurately predict local strain heterogeneities and strain life.

Because of the good macromechanical prediction accuracy, expressed by presented results, this model could be used in many polycrystal metals in engineering applications. Furthermore, this model can give some field results at grain scale which are required as indicators for predicting the location of crack initiation (this will be discussed in the next chapter). The field results at midlife, reflecting the macromechanical behavior, can be used in fatigue life predictions. It is also possible to analyze the variable amplitude loading effects on cyclic plasticity and crack initiation (this will be presented in chapter 5).

Chapter 4

Evaluation and comparison of fatigue criteria for prediction of the crack initiation sites

Table of contents

CHAPTER 4 EVALUATION AND COMPARISON OF FATIGUE CRITERIA FOR PREDICTION OF THE CRACK INITIATION SITES.....	81
4.1 EXPERIMENTAL PROCEDURE	85
4.1.1 <i>Fatigue test machine</i>	85
4.1.2 <i>Specimen</i>	85
4.1.3 <i>Loading</i>	87
4.1.4 <i>Interruption</i>	88
4.1.5 <i>Observation</i>	89
4.2 EXPERIMENTAL OBSERVATION RESULTS	90
4.2.1 <i>Crack initiation at inclusions</i>	91
4.2.2 <i>Crack Initiation at grain boundaries (GBs)</i>	93
4.2.3 <i>Crack initiation in slip lines (SLs)</i>	97
4.2.4 <i>Crack Initiation at GB-SLs intersection</i>	100
4.2.5 <i>Summary for crack initiation observation</i>	105
4.3 PREDICTION OF THE CRACK INITIATION SITES.....	106
4.3.1 <i>Review of fatigue criteria</i>	106
4.3.1.1 Classical macroscopic fatigue criteria	106
• Manson–Coffin criterion	107
• Smith–Watson–Topper criterion.....	108
• Walker criterion	109

• Ostergren criterion	109
4.3.1.2 Fatigue criteria based on micromechanical approach	109
• Energy dissipation criterion	110
• LMS criterion.....	111
• Fatemi-Socie criterion.....	111
• Critical plane criterion	112
• Depres criterion	113
• Dang Van criterion	113
4.3.2 <i>Simulation procedure</i>	116
4.3.3 <i>Simulation results</i>	122
4.3.3.1 Macroscopic crack initiation indicators	122
• Maximum local stress and strain	122
4.3.3.2 Microscopic crack initiation indicators	124
• Maximum shear strain amplitude and normal stress	124
• Fatemi-Socie criterion.....	126
• Microscopic plastic strain energy	127
• LMS criterion.....	128
4.4 CONCLUSIONS	129

Because the phase of fatigue crack initiation and the propagation of microstructurally short cracks represents most of the high-cycle fatigue life of some industrial components made of high-strength materials, the study of crack initiation has attracted increasing attention recently, in contrast to the conventional research approaches where fatigue crack initiation and microcrack propagation path were ignored and only the number of cycles to failure of the specimen was studied [Demulsant and Mendez 1995; Shiozawa, Tohda and Sun 1997; Akahori, Niinomi and Ozeki 1998; Mutoh, Moriya, Zhu and Mizuhara 1998; Peralta, Laird, Ramamurty, Suresh, Campbell, King and Mitchell 1999; Lin, Liu and Liang 2003; Depres, Robertson and Fivel 2004; Komano, Ishihara, McEvily and Shibata 2007].

In classical fatigue life criteria, the material is considered to be elastically and plastically isotropic and with a homogeneous structure. However, for studying the crack initiation and microcrack propagation, it is necessary to study at grain scale to consider the effect of microstructure. The reason is that, in reality, most structural alloys show polycrystalline structure and large amounts of small grains with various orientations. When polycrystalline material is subject to external loading, the stress/strain distribution from grain to grain should be inhomogeneous because of the elastic and plastic anisotropy. Some “hard” grains may show larger stress than average level while crystal plastic slip and accumulated plastic strain occur in some “soft” grains. This may lead to stress and strain concentrations in grains or at grain boundaries, which is considered as one of the reasons for crack initiation [Suresh 1991; Schijve 2009]. After crack initiation, as the microcrack size is smaller than or comparable with the grain size, the inhomogeneous microstructure strongly affects the microcrack initiation and propagation behavior.

In the literature, there are also many factors influencing the fatigue crack initiation such as material microstructure (grain size, microscopic flaws at grain boundaries, twin boundaries and inclusions) and loading conditions such as sequence and path effects (multiaxial fatigue, variable amplitude problem) and so on [McDowell 1996; Van der Giessen, Deshpande, Cleveringa and Needleman 2001; Bjerken and Melin 2004; Krupp 2007; Weertman 2007; Mastorakos and Zbib 2008; Osterstock 2008; McDowell and Dunne 2010]. Although the principal mechanisms leading to fatigue crack initiation were well studied and identified, the effect of microstructure and local stress / strain distribution on crack initiation remain unclear.

The classic measurements of load and strain obtained from macroscopic domain cannot be used to analyze the local conditions near the microcrack or the location where the cracks initiate because these measurements result in an average over a certain volume. As for surface deformation measurement, in the past few decades, 2D/3D digital image correlation (DIC) has been improved by many researchers and developed into an effective and flexible optical technique at the macroscopic scale. However, for observing and quantitatively measuring microscale deformation at reduced size, the DIC combined with a high-spatial-resolution imaging device (especially, SEM and AFM) has just begun and is still an open problem [El Bartali, Aubin and Degallaix 2008; Efstathiou, Sehitoglu and Lambros 2010; Saai, Louche, Tabourot and Chang 2010]. For the measurement of microscopic stress or the intergranular stress, the X-ray, synchrotron X-ray and neutron

diffraction methods have been studied over the past decades, and are still at a preliminary stages [Mochizuki, Hayashi and Hattori 2000; Goudeau, Villain, Tamura and Padmore 2003; Takago, Yasui, Awazu, Sasaki, Hirose and Sakurai 2006; Woo, Feng, Wang, An, Hubbard, David and Choo 2006]. The residual stress determined using X-ray diffraction is limited by the arithmetic average stress in a volume of material defined by the irradiated area, which may vary from square centimeters to less than a square millimeter, and the depth of penetration of the X-ray beam. Recently, infrared image processing technique was studied for observing and quantitatively analyzing the dissipative effects that accompany localized plastic deformation band propagation. But it is still rather difficult to take microstructural information into account [Bodelot, Sabatier and Charkaluk 2009]. Until now the experimental measurements of micromechanical quantities such as the local strain and stress fields in grains are still quite difficult.

With the development of the high performance computing, numerical analysis at microscopic scale can now take advantage of sophisticated constitutive laws taking into account for instance the grain orientations, and appropriate internal variables (e.g. dislocation densities) that reflect the physical properties of the material [McDowell and Dunne 2010]. In the literature, several numerical approaches have been proposed such as polycrystalline aggregate modeling [Barbe, Decker, Jeulin and Cailletaud 2001; Barbe, Forest and Cailletaud 2001; Eriean and Rey 2004; Heripre, Dexet, Crepin, Gelebart, Roos, Bornert and Caldemaison 2007; Zeghad, Forest, Gourgues and Bouaziz 2007; Zeghad, N'Guyen, Forest, Gourgues and Bouaziz 2007; McDowell and Dunne 2010; Schwartz, Fandeur and Rey 2010] and dislocation dynamics (DD) method [Devincre and Kubin 1997; Deshpande, Needleman and Van-Der-Giessen 2003]. The polycrystalline aggregate modeling enables to simulate stress and strain fields in a 3D polycrystal through the Finite Element Method. Local crystalline behavior laws are based on physical mechanisms of plastic deformation and need slip systems description. In addition, they make it possible to simulate a dozen to a thousand loading cycles. On the contrary, dislocation dynamics simulates interactions between thousands individual dislocations. Because of the high number of interactions between dislocation segments, it is up to now limited to the simulation of one grain submitted to small strain amplitudes during a few cycles.

In this section, the aim is to simulate micromechanical behavior of 304L steel and to study the microstructure effect on fatigue crack initiation and to evaluate the crack initiation predictive capabilities of some factors in fatigue criteria.

The main experimental work focuses on observing the microscopic sites of fatigue crack initiation at grain size scale to compare with numerical results. With the help of optical microscope and scanning electron microscope (SEM), surface states at interrupted points were observed. The actual strikingly clear images allow us to better observe and be sure that if there are really cracks.

For numerical simulation, in order to get the numerical mechanical field results near the cracks to study the microstructure effect on fatigue crack initiation, three numerical aggregates are built from one fatigue specimen of 304L steel. There are one or two cracks on each aggregate. This finite element model of polycrystal plasticity with details of realistic grain orientations was modeled in Abaqus. The numerical results were compared

with the experimental observation on the same zones. The numerical mechanical fields of local strain, stress, maximum shear strain amplitude on the 12 slip systems and normal stress on the slip plane with maximum shear strain amplitude, the function value of Socie-Fatemi criterion, plastic strain energy were considered. These results give useful contributions to establish new fatigue crack initiation criterion based on the micromechanical factors controlling the crack initiation and to predict the crack initiation sites.

4.1 Experimental procedure

In this work, both load-controlled and strain-controlled fatigue tests were conducted. Load-controlled fatigue tests will be introduced in this section and strain-controlled fatigue tests will be presented in Chapter 5. Load-controlled fatigue tests were performed under both CA and VA loading. The results of VA fatigue tests will also be analyzed in Chapter 5.

4.1.1 Fatigue testing machine

The mechanical fatigue tests were investigated experimentally with an MTS 810 servo-hydraulic testing machine with a maximum applying force capacity of 100 kN (Figure 56).

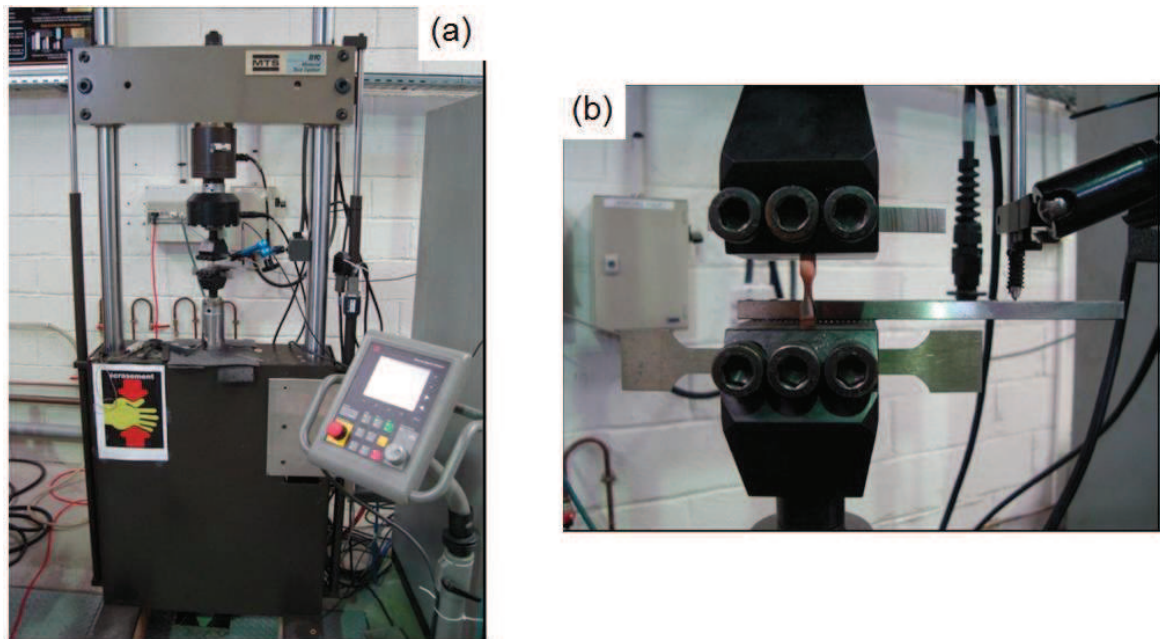


Figure 56 (a) MTS 810 servo-hydraulic system used for fatigue tests (b) Specimen mounted in the grips

4.1.2 Specimen

In order to locate the crack initiation site as well as to make observation and measurement easier and to avoid the crack occur due to stress concentration at sharp corners, a smooth

circular notch (10.88mm in radius) was chosen and machined. The geometry size is also designed according to required parameters of an in-situ machine used in SEM with a total length of 44mm (Figure 57).

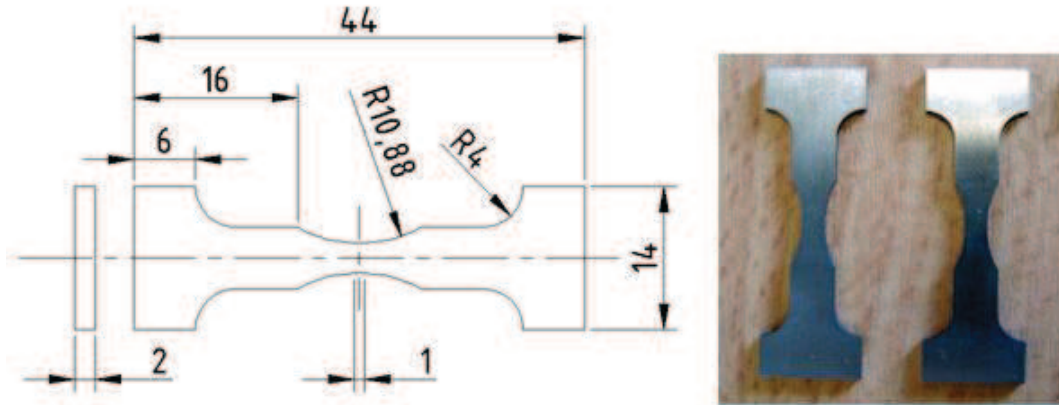


Figure 57 The plate specimen geometry size for fatigue test under load-controlled

The original purpose was to open a small crack in tension with the help of in-situ machine in SEM. However, it is required to take a lot of time to prepare this in-situ test every time and no significant difference was observed when there was a certain tension load imposed. So in-situ machine was not used in the subsequent tests.

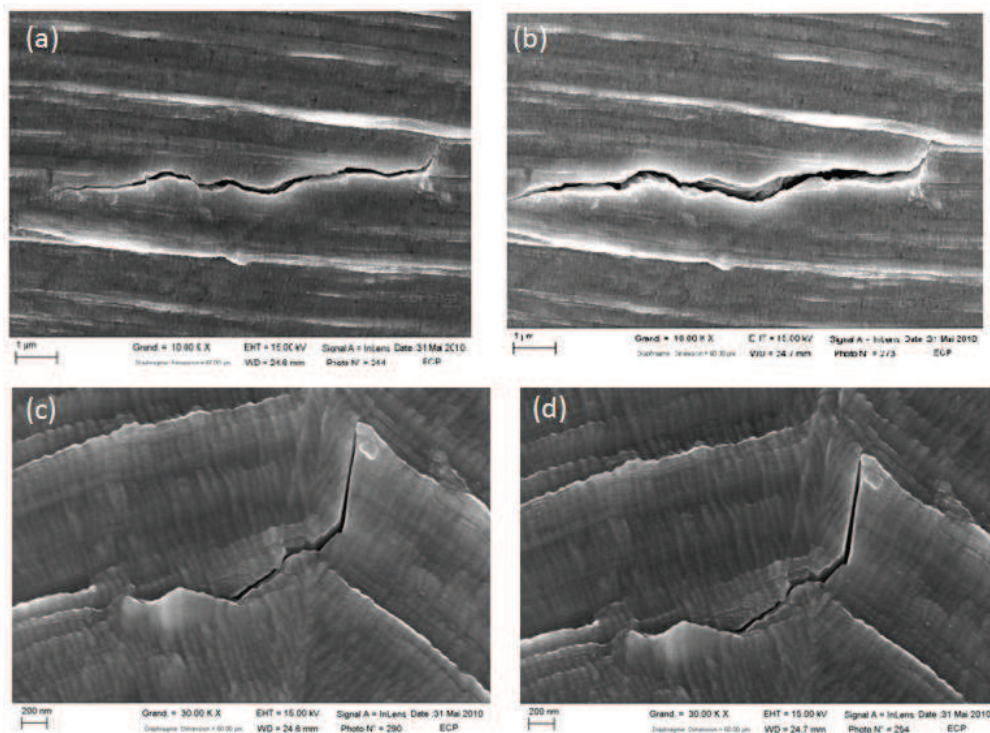


Figure 58 In-situ crack observation in SEM (a)(c) zero loading (b)(d) in tension of 1200N (about 200MPa)

For these fatigue specimens, no pre-cracking was performed and cracks appeared naturally. All specimens were mechanically polished before fatigue tests by manual polishing with SiC grit paper roughness between 14 μ m and 5 μ m. It is then refined by polishing with diamond powder from 3 to 1 μ m roughness in order to satisfy the surface requirement for electron backscattered diffraction test (EBSD) and simultaneously improve optical measurements. Because the surface residual stresses influence both the initiation and propagation of small fatigue cracks, and they appear to be produced by standard machining processes, it was tried to keep the same manual polishing procedures (pressure load, polish time...) for all these specimens although their surface residual stresses were not measured. It is well known that electropolishing is the only viable means of removing material without inducing residual stresses. Then in order to reveal its microstructure an electro-polishing was used for the 304L steel in a bath of 10% oxalic acid at 20 °C with a voltage of 10V for 60 seconds.

However, it should be noted that all four specimen surfaces (front, back, left and right) were polished except A2 and A3 on which left and right surfaces were not polished. This led to shorter crack initiation life. Lots of the cracks initiated from the left and right side were observed.

4.1.3 Loading

Eight fatigue tests were conducted under load-controlled amplitude. Two specimens were subjected to constant amplitude of 220 MPa as well as two specimens were subjected to 260 MPa; the other four tests were performed under variable amplitude loading of 220 MPa-320 MPa-220 MPa. The detailed load spectra are shown in Table 7 and Table 8.

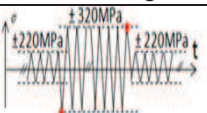
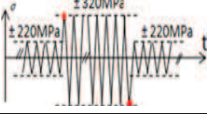
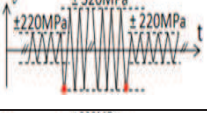
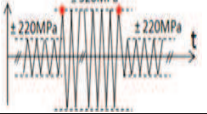
Table 7 Fatigue load spectra used under constant load-controlled amplitude

Specimen number	Amplitude	Frequency	Surface condition
A1	260 MPa	1Hz	4 surface polished
A2	260 MPa	1Hz	2 surface polished
A3	220 MPa	2Hz	2 surface polished
A7	220 MPa	2Hz	4 surface polished

For the tests under variable amplitude loading of 220 MPa-320 MPa-220 MPa, four different loading paths were considered in order to evaluate the influence of the sign of beginning and end in the overload block on cyclic plasticity and crack initiation. The detailed load spectra information is listed in Table 8. The first loading block with an amplitude of 220 MPa was always performed during 1000 cycles, and next the specimen was subjected to the loading with an amplitude of 320 MPa during 20 cycles. After these 1020 cycles, there is no crack found on the surfaces for all these specimens. Then stress amplitude goes back to 220 MPa until the cracks propagate enough to leave out the first stage of crack initiation.

4 Evaluation and comparison of fatigue criteria for prediction of the crack initiation sites

Table 8 Fatigue load spectra considered under variable load-controlled amplitude

Specimen number	Loading Path	Frequency	Surface condition	Overload block start	Overload block end	Schematic diagram
A4	Path 1	2Hz	4 surface polished	compression	tension	
A5	Path 2	2Hz	4 surface polished	tension	compression	
A8	Path 3	2Hz	4 surface polished	compression	compression	
A9	Path 4	2Hz	4 surface polished	tension	tension	

4.1.4 Interruption

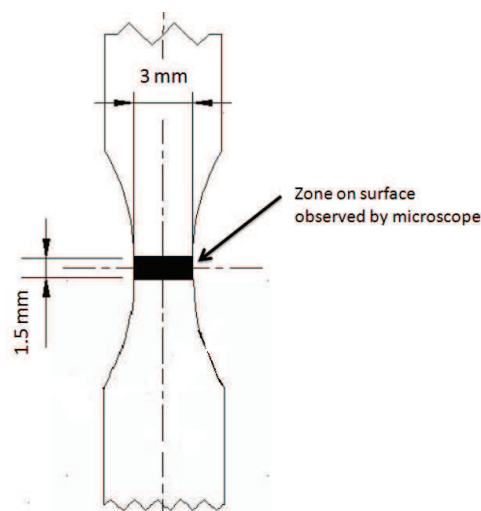
The fatigue tests were interrupted for a given number of cycles (dependent on the level of the stress imposed). The specimen was dismantled and its surfaces were observed with microscopes (with Alicona infinite-focus, Leica microscope and SEM). Then the specimen was carefully mounted again and the fatigue test continued to be performed a given number of loading cycles then the next observation was performed. Such work was repeated until the crack is long enough leaving out of the crack initiation stage (in our work it is defined as the maximum length from 150 to 200 μm). The interruption and observation cycles for all specimens are given in Table 9.

Table 9 Interruption and observation cycles during fatigue tests

Specimen number	Interruption and observation cycles								
A1	1500	2500	3500	4500	5500	6500	7500	8500	9500
	10500	11500	12500	14500	16500	18500	20000	30000	/
A2	3000	5000	7000	/					
A3	5000	10000	15000	20000	/				
A7	1000	4000	10000	15000	20000	25000	30000	35000	/
A4	1020	4020	10000	15000	20000	25000	30000	35000	40000
	50000	60000	70000	90000	140000	/			
A5	1020	4020	10000	15000	20000	25000	30000	40000	50000
	60000	70000	90000	140000	/				
A8	10000	20000	50000	90000	120000	/			
A9	10000	20000	50000	90000	/				

4.1.5 Observation

For all 8 specimens, the central zone with a surface of 4.5 mm^2 (as shown in Figure 59) was observed at every interruption. Though microcracks even with a length of 10 nm can be observed with a high resolution SEM, it requires a special preparation which would take a relatively long time. In addition, it is quite difficult to find and observe the microcracks in the rather large zone of 4.5 mm^2 . Leica optical microscope can show a good performance to observe the microcracks longer than $5\text{-}10 \mu\text{m}$. Alicona digital infinite-focus optical microscope also shows a good performance to observe the microcracks longer than $10 \mu\text{m}$, it can capture large area images by recording an array of images which are aligned in a rectangular area and then merged into one image automatically. However, due to the amount of data that has to be handled this is a time and memory consuming process. In summary, for microcrack observation in a large zone of 4.5 mm^2 in this work, Alicona microscope is advantageous over the others and is chosen as the main observation tool for counting the crack on the specimen surface.

**Figure 59 The microscope observation zone (1.5mm x 3mm) on the surface**

Before fatigue tests, EBSD measurements in observation zone (about 1.5mm x 3mm) were performed for A1, A4, A5 and A7 to get the crystallographic orientation in order to help identifying the crack sites (in grain or at the grain boundary...) on the surface.

4.2 Experimental observation results

According to the observations on the surfaces of the specimens mentioned above, four kinds of the crack initiation sites were sorted out: inclusions, grain boundaries (GB), slip lines (SLs) and at the location with the interaction of GB and SLs. The number of the cracks at various initiation sites is given in Table 10 and Figure 60.

Table 10 Number of load-controlled loading cracks at various crack initiation sites, from 8 fatigue tests under

Specimen NO.	Loading type	Number of cracks at various initiation sites			
		Inclusion	SL	GB	SL-GB
A1	±260 MPa	3	12	9	6
A2	±260 MPa	1	10	18	10
total :69 cracks		4 (6%)	22 (32%)	27 (39%)	16 (23%)
A3	±220 MPa	1	9	9	7
A7	±220 MPa	1	1	2	2
total :32 cracks		2 (6%)	10 (32%)	11 (34%)	9 (28%)
A4	220-320-220 MPa-CT	0	0	1	1
A5	220-320-220 MPa-TC	0	0	2	2
A8	220-320-220 MPa-CC	1	2	4	2
A9	220-320-220 MPa-TT	0	4	2	1
total:22 cracks		1 (5%)	6 (27%)	9 (41%)	6 (27%)
Total:123 cracks		7 (6%)	38 (31%)	47 (38%)	31 (25%)

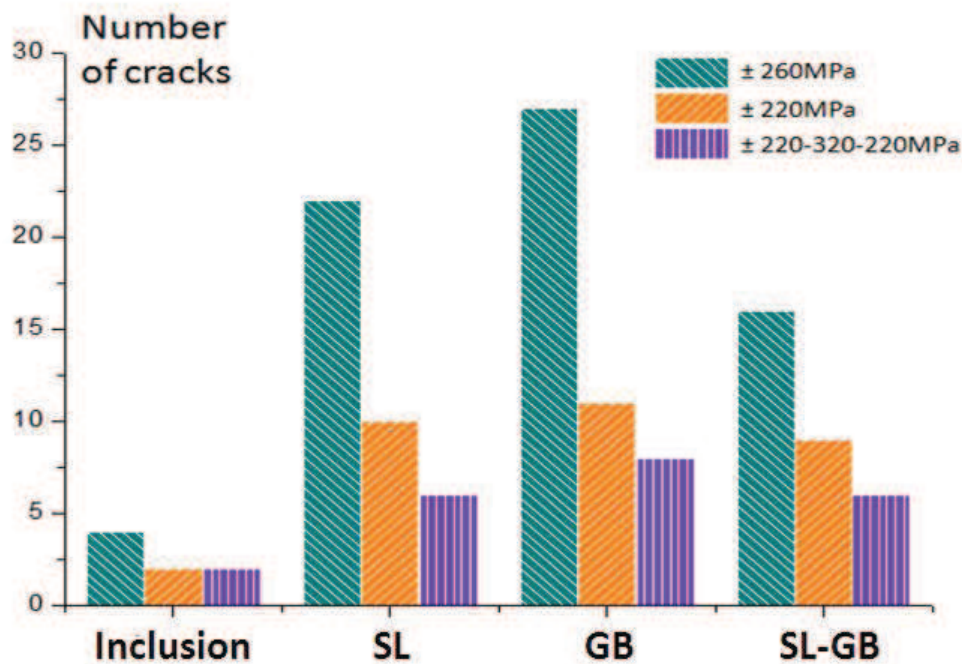


Figure 60 Distribution of various crack initiation sites observed on the surfaces

From Table 10 and Figure 60, it seems that these three types of the load spectra have only little influence on the crack initiation sites distribution.

4.2.1 Crack initiation at inclusions

Inclusions are common sites for fatigue crack initiation and are known to be particularly deleterious in high strength steels [Krupp 2007]. During the fatigue tests, only 8 fatigue cracks among 123 cracks initiated from inclusions. This kind of crack initiation only accounts for seven percent of the total observed cracks. The cracks that initiate from inclusions can be observed in fatigue tests. In most cases, the cracks that initiate from inclusions formed earlier than the ones initiating in other locations. For example, in specimen A1, a crack initiated from an inclusion was found after 9500 cycles but the other cracks, which were of other types, initiated after 11500 cycles. For A7, a crack initiated from an inclusion was observed after 20000 cycles but the other type of cracks initiated after 30000 cycles.

It should be noted that only few inclusions on the surface lead to crack initiation for 304L. It was generally observed that large inclusions with a diameter greater than $5\text{ }\mu\text{m}$ where crack initiated were located near a grain boundary or near the slip line, as shown in Figure 61- Figure 64. No crack was found that initiated from an inclusion located in the center of a large grain.

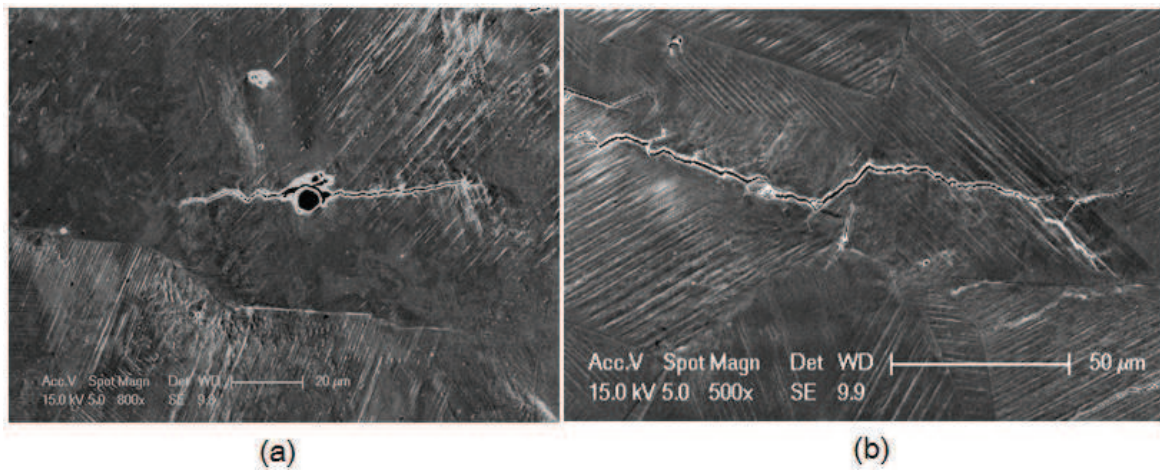


Figure 61 Cracks initiated from an inclusion (specimen A2) after 7000 cycles under stress amplitude of 260 MPa (a) near slip lines (b) near a grain boundary

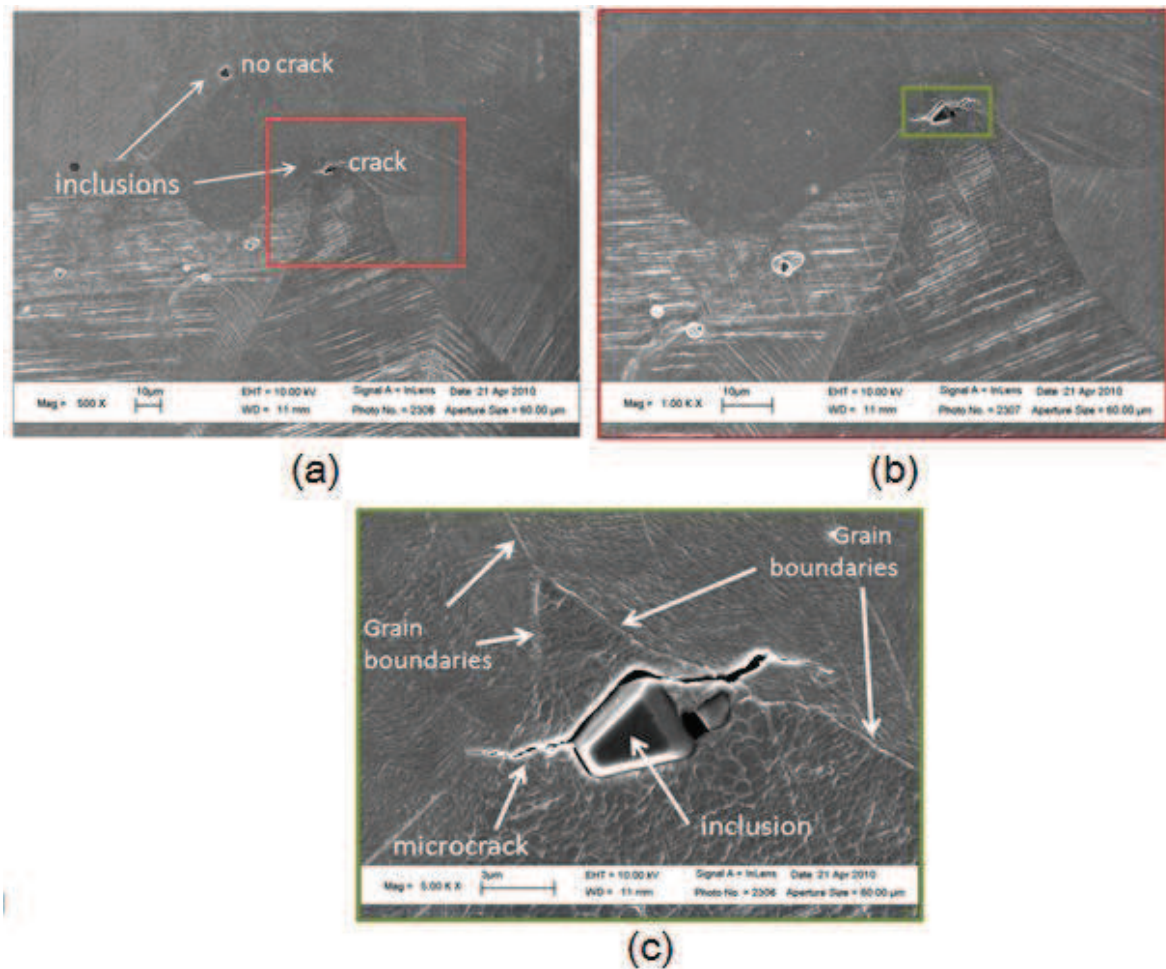


Figure 62 A crack initiated from an inclusion observed in SEM after 9500cycles under stress amplitude of 260 MPa (specimen A1) (a) at 500x magnification (b) at 1000x magnification (c) at 5000x magnification

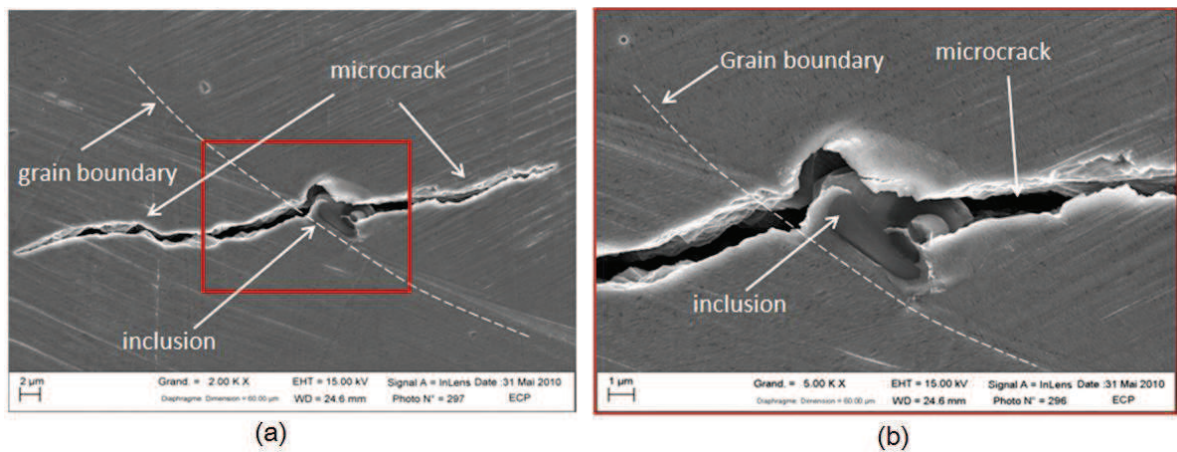


Figure 63 A crack initiated from an inclusion near the grain boundary observed in SEM after 11500cycles under stress amplitude of 260 MPa (specimen A1) (a) at 2000x magnification (b) at 5000x magnification. (In order to open the crack, the specimen was loaded at about 200 MPa on a in-situ micro machine in SEM)

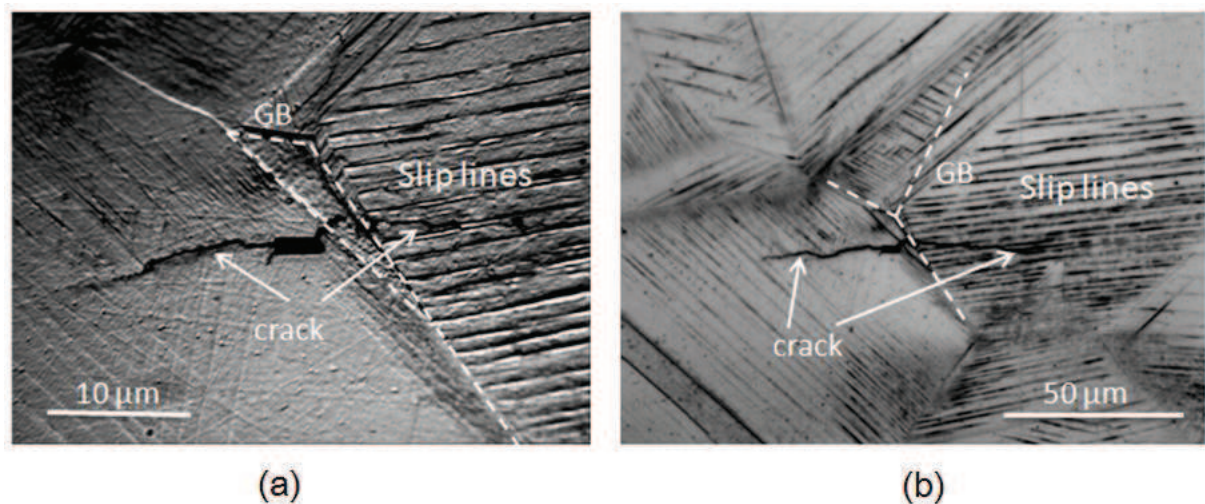


Figure 64 A crack initiated from an inclusion observed (a) after 30000cycles with an optical microscope LEICA, (b) after 35000 cycles with a digital optical microscope ALICONA, under stress amplitude of 220 MPa (specimen A7)

4.2.2 Crack Initiation on grain boundaries (GBs)

Up to now it has been generally considered that differences in crystallographic orientation of the grains cause stress peaks at the grain boundaries and triple lines that may exceed locally the yield strength. When plastic strain occurs in neighboring grains under fatigue loading, the grain boundary becomes incompatible. Once the stress concentration reaches a certain point, a grain boundary crack initiates [Suresh 1991; Ravichandran, Ritchie and Murakami 1999; Stephens, Fatemi, Stephens and Fuchs 2000; Krupp 2007; Schijve 2009].

From our observations of crack initiation during fatigue tests, grain boundaries (GBs) were the most favorable locations for crack initiation (shown in Figure 65- Figure 67). It has been observed that cracks initiate preferentially on grain boundaries parallel to slip lines in neighboring grains, as the crack can easily propagate along the slip lines. By contrast, crossing slip lines as well as grain boundaries are obstacles for crack propagation. In the case of a propagating crack crossing the slip lines or grain boundaries, propagation paths may be changed and it may branch.

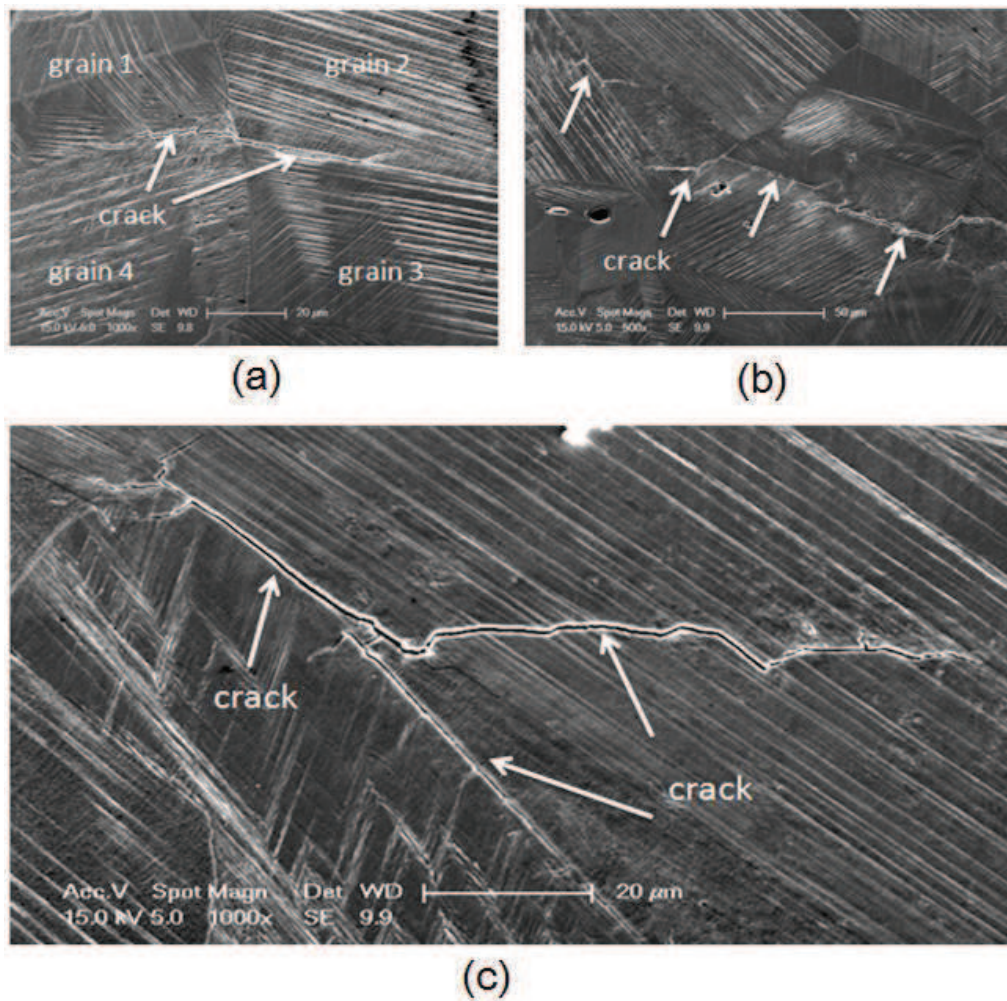


Figure 65 (a) (b) and (c): Cracks initiate on GB after 20000 cycles under stress amplitude of 220 MPa (specimen A3), observed by SEM

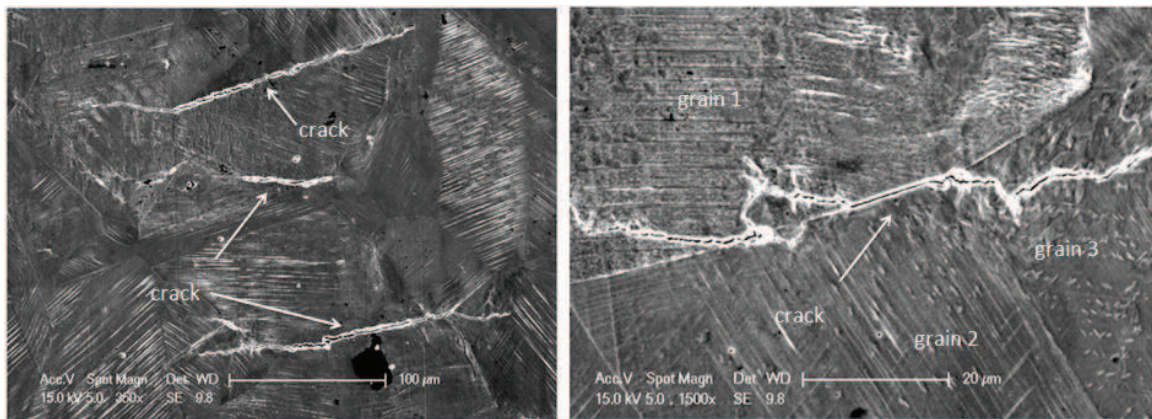


Figure 66 Cracks initiated on GB under stress amplitude of 260 MPa after 5000 cycles (specimen A2), observed by SEM

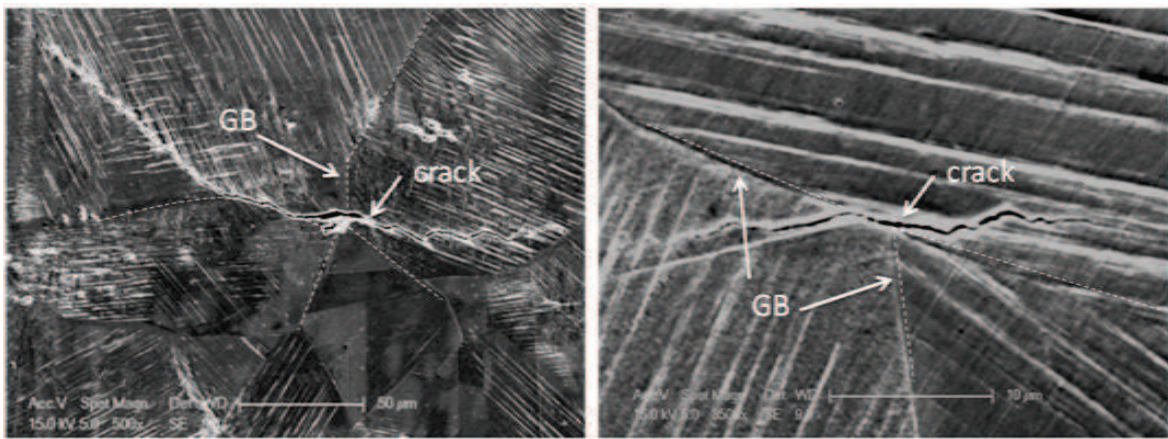


Figure 67 Cracks initiated on GBs and propagated cross or along slip lines the under stress amplitude of 260 MPa after 5000 cycles (specimen A2), observed by SEM

The cracks initiated on GBs were found in all the specimens and account for 38% as shown in Table 10 of all the cracks. In order to study the GB orientation effect on the crack initiation, angle α between cracked GB and the loading axis (as shown in Figure 68) for each crack in this type was measured.

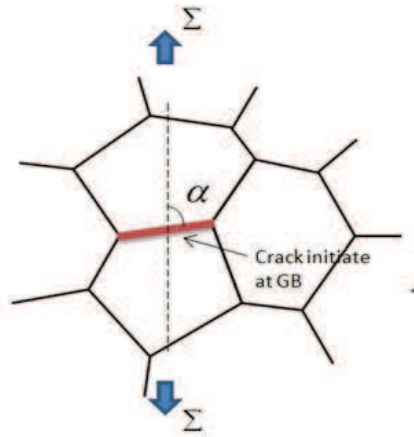


Figure 68 Angle α between cracked GB and the loading axis

According to the observation of the cracks initiated at GBs, the crack direction distribution with the respect to the angle α is summed up and given in Table 11. The angle α varies from 30° to 90° .

Table 11 Distribution of the orientations of cracks initiated in grain boundaries with respect to angle α

Specimen NO.	Loading type	Number of the cracks initiate at GBs with various angle α angle α : between cracked GB and the loading axis					
		30°- 40°	40°-50°	50°- 60°	60°- 70°	70°- 80°	80°- 90°
A1	± 260 MPa		2		2	4	1
A2	± 260 MPa		2		4	9	3
A3	± 220 MPa	1		2	4	1	1
A7	± 220 MPa			1		1	
A4	220-320-220 MPa-CT					1	
A5	220-320-220 MPa-TC					2	
A8	220-320-220 MPa-CC	1			2		1
A9	220-320-220 MPa-TT					1	1

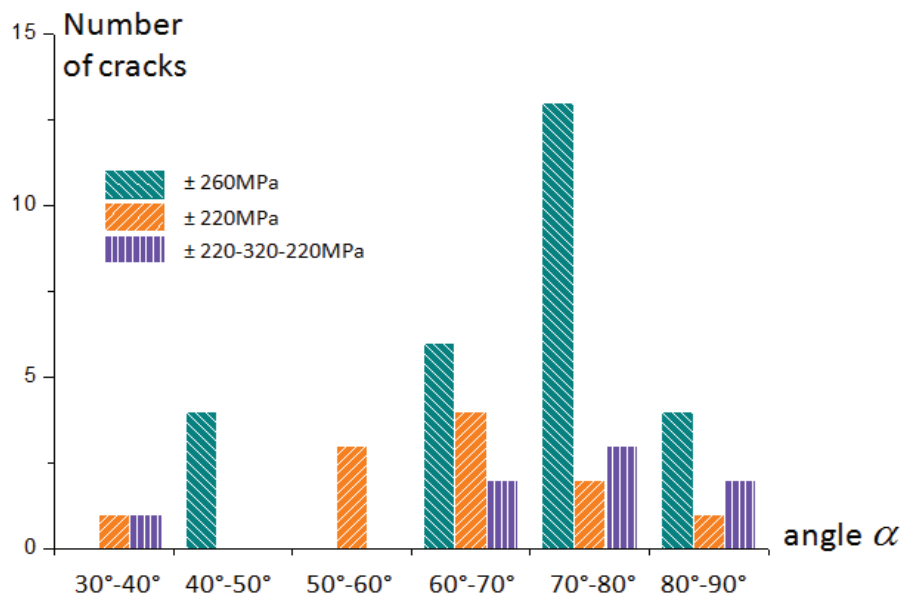


Figure 69 Distribution of the orientations of cracks initiated in grain boundaries with respect to angle α

As seen in Figure 69 and in Table 11, among these cracks, in case of strain amplitude of ± 260 MPa, the cracks initiated on the GBs with angle α varying from 60° to 90° account for more than 80%. Under stress amplitude of ± 220 MPa, the angle α varies distributed predominately from 50° to 80° , which accounts for about 90% of the whole population.

4.2.3 Crack initiation on slip lines (SLs)

It has been demonstrated that even in the case of idealized materials, having no defect, no precipitate and no grain boundary, and being perfectly polished, cyclic deformation will lead sooner or later to crack initiation, provided some infinitesimal amount of localized irreversible plastic slip is present. Dislocations that are transported towards the surface generate a slip step, where fresh metal surface is exposed to oxygen from the environment. Absorption of oxygen impedes complete rewelding of the slip step, which is moved back into the bulk during load reversal. As a consequence, local bonding along the slip band generates crack-initiation sites. Beside the environmental effect, cyclic slip irreversibility can be attributed to mutual interactions between dislocations. The dynamic equilibrium between dislocation multiplication by the Frank-Read mechanism and the annihilation of screw and edge dislocations in persistent slip bands (PSBs) leads to the generation of vacancies, which eventually cause macroscopic roughness along the intersection lines between SLs and originally polished specimen surface [Suresh 1991; Ravichandran, Ritchie and Murakami 1999; Stephens, Fatemi, Stephens and Fuchs 2000; Hull and Bacon 2001; Krupp 2007].

For 304L steel, this kind of crack initiation was also frequently observed. For example, when specimen A7 was subjected under a stress amplitude of 220 MPa, microcracks initiated along slip lines were observed on the surface after 30000 cycles. Furthermore,

microcracks initiated along slip lines were observed in both constant and various stress amplitude fatigue tests. Figure 70 and Figure 71 show some cracks initiate at SLs on the surface of specimens A3 and A7.

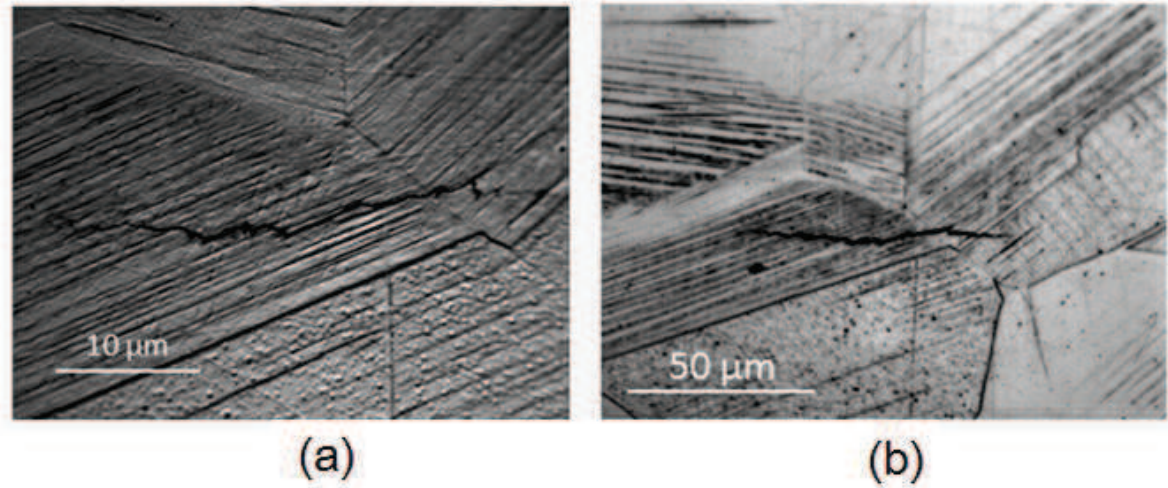


Figure 70 (a) A crack initiated on slip lines, under stress amplitude of 220 MPa after 30000 cycles (specimen A7), observed with an optical microscope LEICA (b) the crack propagates in the lateral direction, this image is taken after 35000 cycles with an optical microscope ALICONA.

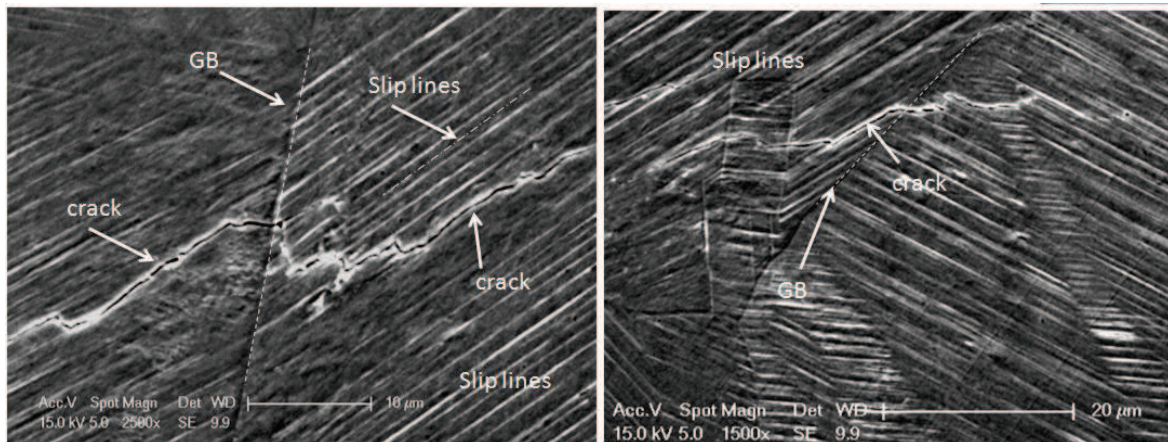


Figure 71 Cracks initiated on slip lines after 20000 cycles under stress amplitude of 220 MPa (specimen A3), observed in the SEM.

In order to study the effect of the orientation of slip line on the crack initiation, angle β between loading axis and the cracked slip line (as shown in Figure 72) was measured. Table 12 and Figure 73 present the distribution of the orientations of cracks initiated on slip lines with respect to angle β from 8 fatigue tests.

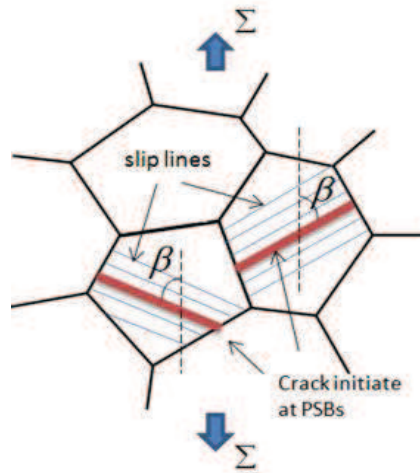


Figure 72 Angle β between cracked slip lines and the loading axis

Table 12 Distribution of the orientations of cracks initiated on slip lines with respect to angle β

Specimen NO.	Loading type	Number of the cracks initiate at SLs with various angle β angle β : between cracked SL and the loading axis				
		40°-50°	50°- 60°	60°- 70°	70°- 80°	80°- 90°
A1	±260 MPa	3	6	2		1
A2	±260 MPa		3	5	1	1
A3	±220 MPa	3	5	1		
A7	±220 MPa			1		
A4	220-320-220 MPa-CT					
A5	220-320-220 MPa-TC					
A8	220-320-220 MPa-CC			2		
A9	220-320-220 MPa-TT		1	1	2	

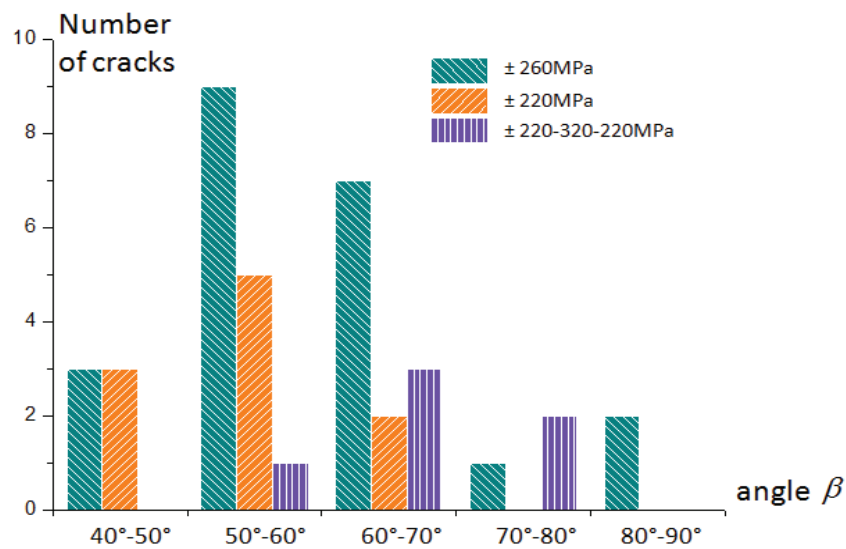


Figure 73 Distribution of the orientations of cracks initiated on slip lines with respect to angle β

It was found that about 85% cracks initiated on the slip lines with an angle β varying from 40° to 70° in case of stress amplitude of ± 260 MPa. When the stress amplitude is ± 220 MPa, all of the angles β measured were in range from 50° to 80° , which accounts for about 90% of the whole population.

4.2.4 Crack Initiation at GB-SLs intersection

In the crack observations, it is also found that cracks initiated preferentially on the GB sites where slip lines were impinged and then propagate along the grain boundaries or impinged slip lines when the cracks are still short (less than about one to two mean grain sizes). In our work, this kind of crack initiation was considered separately from the whole.

As shown in Figure 74, three short cracks are observed at the intersection between the slip lines and the grain boundary in the SEM. It can be seen that these cracks have a common characteristic that they propagate along the grain boundary in one side and along the slip lines in the other side with a “V” shape. The crack is not initiated at triple junctions. From the results of EBSD, the crystallographic orientations around the cracks were observed (Figure 75).

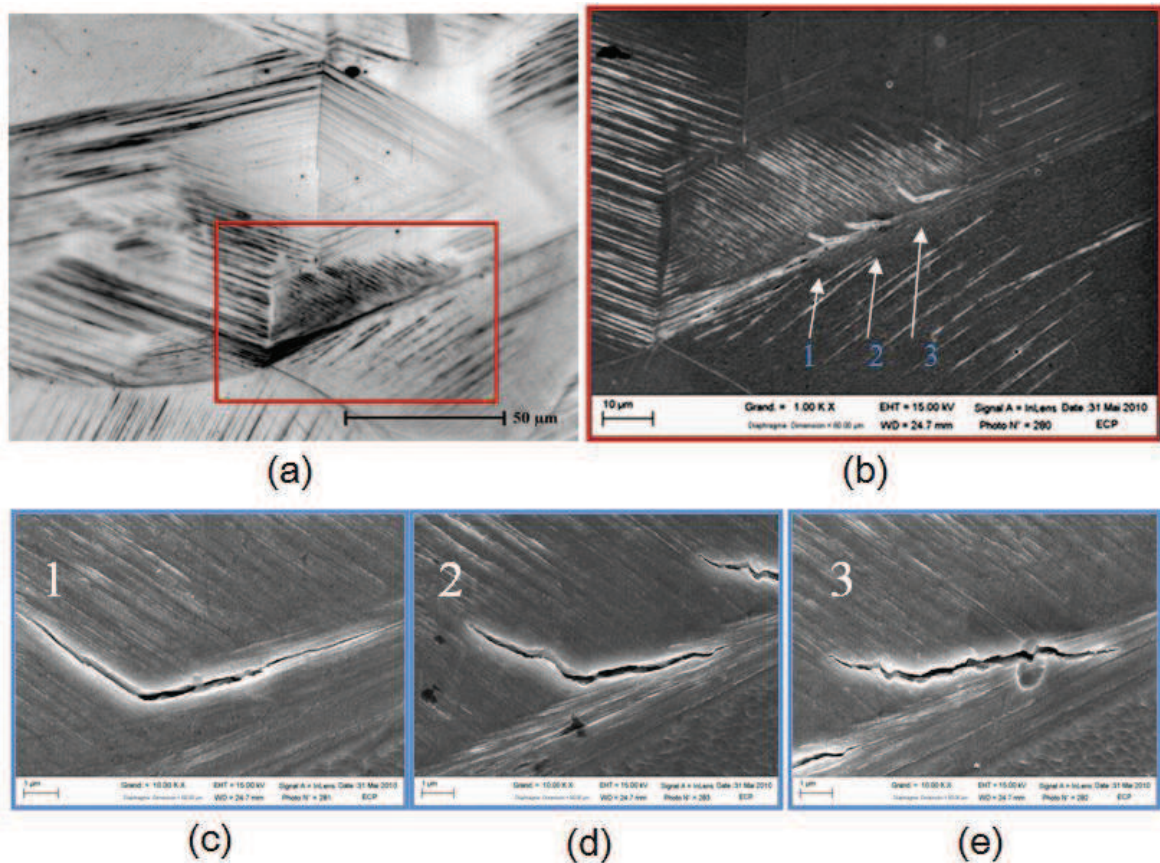


Figure 74 Cracks initiated at intersection of grain boundaries and slip lines, under stress amplitude of 260 MPa after 11500 cycles (specimen A1) (a) observed in an optical microscope Alicona (b) observed in the SEM on same zone of a (c) first crack indicated in b (d) second crack indicated in b (e) third crack indicated in b

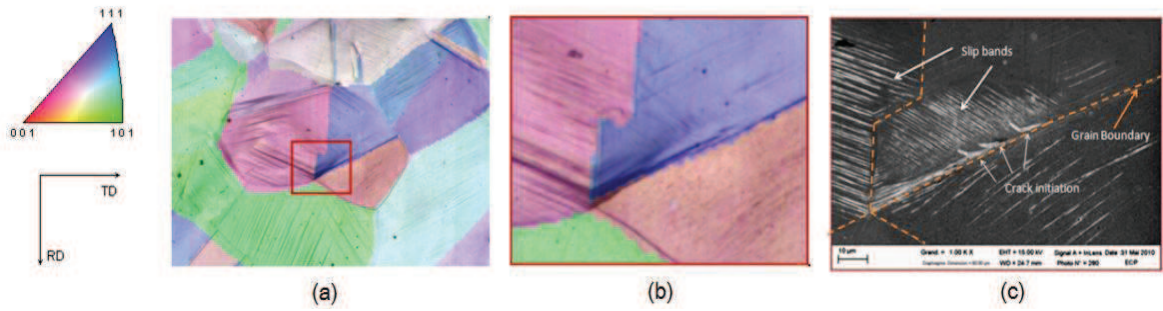


Figure 75 The same crack initiation as shown in Figure 74 (a) and (b) crystallographic orientations obtained from EBSD (c) observed in SEM

The observations also show that GB-SLs crack can initiate on the GB which is almost parallel to the imposed stress axis. This is different with the GBs crack initiations. Those cracks initiated from GB keep propagating along GB to a long length (about 30 to 100 μm) and the minimum value of α observed is 30°. Figure 76 shows the crack initiated at GB-SLs and propagates along the slip lines. In this case, the GB is almost parallel to the imposed loading direction. Active slip lines can be observed clearly in these images.

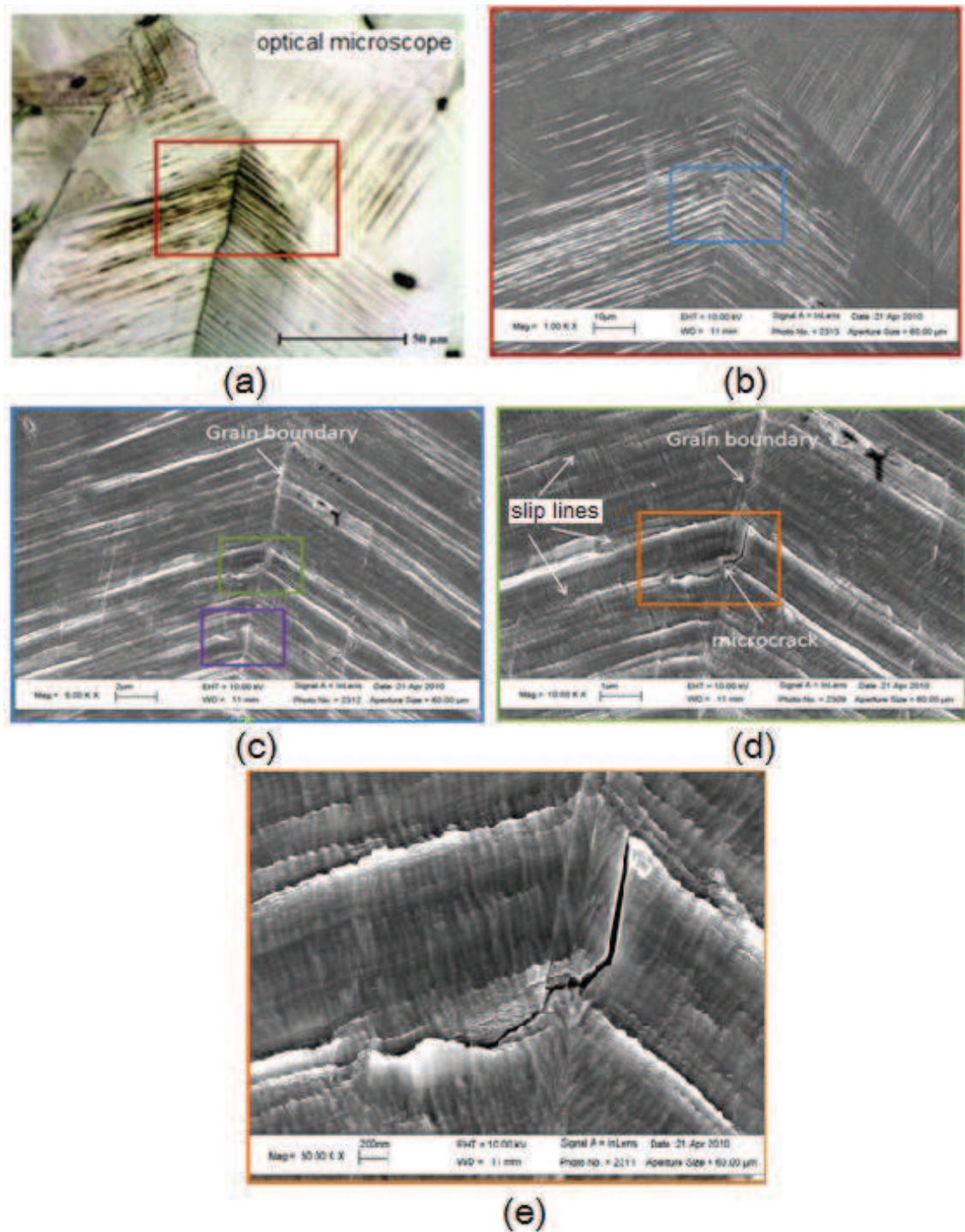


Figure 76 Crack initiation (Specimen A1) observed in SEM after 9500 cycles under stress amplitude of 260 MPa (a) observed by an optical microscope Alicona (b) observed in the SEM at 1000x magnification (c) at 5000x magnification (d) at 10000x magnification (e) at 30000x magnification

Even for the microcrack initiated along the grain boundary, it is still unsuitable to call it as transgranular crack. Because they also may immediately propagate into the neighboring grain by the strong interaction between slip line and grain boundary. Figure

77 gives an example that the crack initiates along a grain boundary. It propagates first along the slip line and then in the lateral direction. In addition, it can be seen that from Figure 77(b) that when the crack length reaches about 150 μm , the right microcrack tip still propagates along the slip line so the microcrack propagation path is still dependent on the microstructure near the crack tip.

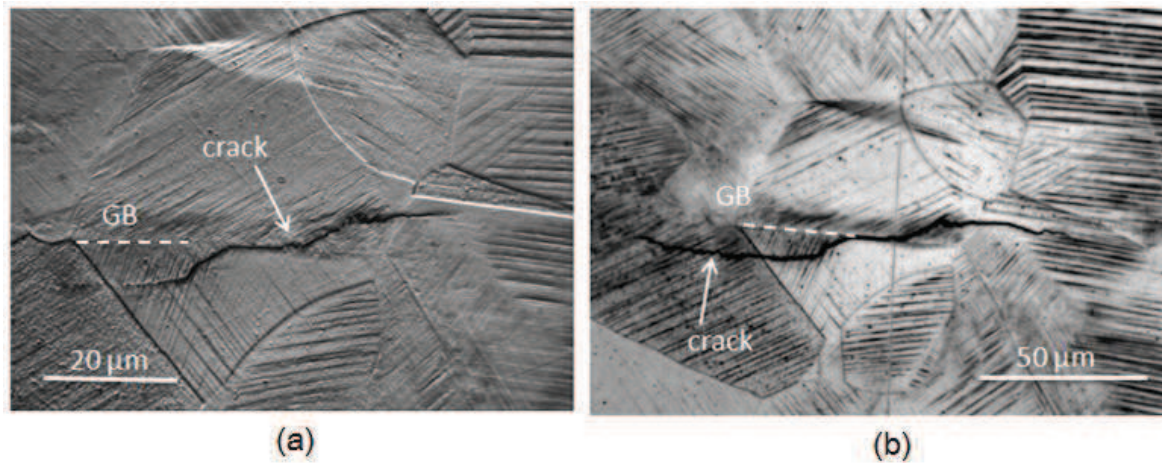


Figure 77 (a) A crack observed with an optical microscope LEICA after 30000cycles under stress amplitude of 220 MPa, the crack initiates along the grain boundary (b) The crack propagates first along the slip line and then in the lateral direction, this image was taken after 35000 cycles with an optical microscope ALICONA.

Table 13 and Table 14 give the statistical data of number of the cracks initiated at GB-SLs with various angle α' and β' . As shown in Figure 79, angle α' is the orientation between cracked GB and the loading axis and angle β' is one between cracked SL and the loading axis.

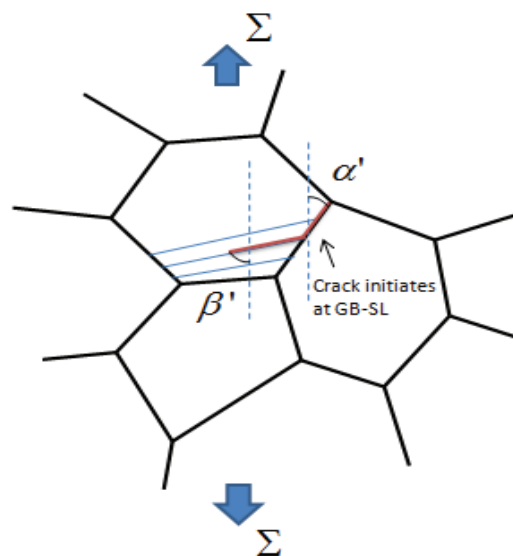


Figure 78 Angle α' between GB and the loading axis; angle β' between corresponding SL and the loading axis for the cracks initiated at GB-SL

Table 13 Distribution of the orientations of cracks initiated GB-SLs with respect to angle α'

Specimen NO.	Loading type	Number of the cracks initiate at GB-SLs with various angle α' angle α' : between cracked GB and the loading axis							
		10°- 20°	20°- 30°	30°- 40°	40°- 50°	50°- 60°	60°- 70°	70°- 80°	80°- 90°
A1	±260 MPa	1		2			3		
A2	±260 MPa			1	3	2		2	2
A3	±220 MPa					1	2	2	2
A7	±220 MPa				1				1
A4	220-320-220 MPa-CT						1		
A5	220-320-220 MPa-TC						2		
A8	220-320-220 MPa-CC			1				1	
A9	220-320-220 MPa-TT						1		

Table 14 Distribution of the orientations of cracks initiated GB-SLs with respect to angle β'

Specimen NO.	Loading type	Number of the cracks initiate at GB-SLs with various angle β' angle β' : between cracked SL and the loading axis								
		0°- 10°	10°- 20°	20°- 30°	30°- 40°	40°- 50°	50°- 60°	60°- 70°	70°- 80°	80°- 90°
A1	±260 MPa						4			2
A2	±260 MPa	2		1			1		5	1
A3	±220 MPa					1		4	1	1
A7	±220 MPa						1	1		
A4	220-320-220 MPa-CT								1	
A5	220-320-220 MPa-TC							2		
A8	220-320-220 MPa-CC							1		1
A9	220-320-220 MPa-TT							1		

From Table 13, it is found that under stress amplitude of ±260 MPa more than 90% of these GB-SLs cracks initiated at SLs or propagated along the SLs with the angle α' varying from 30° to 90°. When stress amplitude is ±220 MPa, angles α' are ranging from 40° to 90°. Moreover, Table 14 shows that these cracks initiated or micro-propagated preferentially at GBs with an angle β' ranging from 50° to 90°. In addition, it is found that

most of these “V” cracks show angles between SL and GB distributed between 110° and 150° , for 90% of all cases.

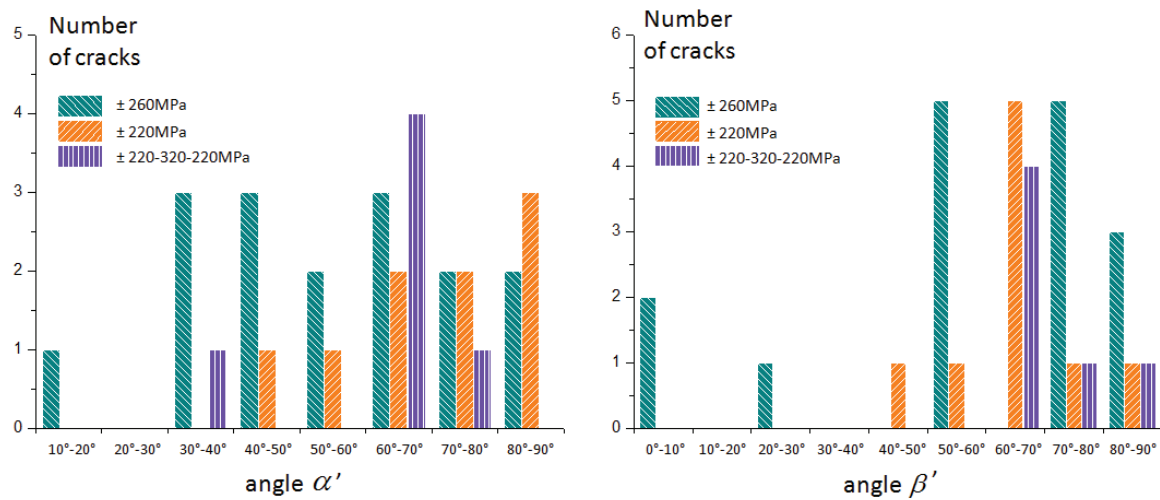


Figure 79 Distribution of crack initiations at GB-SLs with various α' and β' angles observed on the surfaces of eight specimens under different load spectra

This GB-SLs crack initiation can be considered as caused by the interaction between SLs and GBs and also by the elastic and plastic anisotropy between grains. The elastic response of a crystalline material to mechanical loading depends on the direction of loading and also on the crystallographic orientations. However, when the mechanical behavior of a quasi-isotropic polycrystal on the length scale of the grain size is examined closely, the elastic and plastic anisotropy may be a factor determining local deviations from the remote loading. Differences in crystallographic orientation of the grains cause local stress or strain peaks at the grain boundaries and slip lines that may eventually cause fatigue crack initiation.

4.2.5 Summary for crack initiation observation

1. According the crack observations in this work, grain boundaries are the most favorable location for crack initiation under low cyclic fatigue for 304L (under total strain amplitude of 0.3% and 0.5%). Among these cracks, in case of stress amplitude of $\pm 260\text{MPa}$, the cracks initiated on the GBs with angle α from 60° to 90° account for more than 80% of all cases. Under stress amplitude of $\pm 220\text{MPa}$, the angles α obtained were predominately from 50° to 80° , which accounts for about 90% of all cases.

2. Crack initiation on slip lines is also frequently observed under these level stress amplitude fatigue. The orientation difference, angle β between cracked SL and the loading axis for all this kind of cracks were measured from 40° to 80° . About 85% cracks initiated at the slip lines with an angle β from 40° to 70° in case of stress amplitude of $\pm 260\text{MPa}$. When stress amplitude is $\pm 220\text{MPa}$, the angle α was distributed mainly in range 50° to 80° , which accounts for about 90%.

3. shows that these cracks initiated or micro-propagated preferentially at GBs with an angle β' in range 50° to 90° . Most of these “V” cracks show the an angle between SL and GB varying from 110° to 150° , which accounts for about 90% of all cases.

4. Inclusions are not common sites for fatigue crack initiation for 304L. Cracks initiate generally at inclusions located near grain boundaries or among the slip lines especially for the large inclusions with a diameter greater than $5\ \mu\text{m}$. In most cases, the cracks that initiate from inclusions formed earlier than the ones initiated in other locations.

5. Microcrack propagation can be disrupted not only by grain boundaries but also by slip lines. When a crack crosses a grain boundary or a slip line, it may change its propagation direction.

6. The distribution of slip lines within a grain may greatly influence crack initiation and microcrack propagation. Crossing slip lines can be a major deceleration for microcrack propagation, while fine and straight slip lines are favorable for them.

4.3 Prediction of the crack initiation sites

4.3.1 Review of fatigue criteria

Among a large number of fatigue criteria proposed for the prediction of crack initiation in mechanical fatigue, various approaches have been found to be particularly useful for certain categories of materials over specific domains of temperature and cyclic loading. However, no particular approach appears to give invariably better predictions than others, so that the choice of the criterion must be based on validation for the relevant circumstances. As a result, according to different conditions such as different material mechanical qualities, different loading type, the fatigue life are calculated or estimated by the appropriate fatigue criteria. In this section, some classical and recent fatigue criteria based on both macro- and micro-mechanical approaches will be reviewed. Some factors in these fatigue criteria will be used and evaluated in the following section about numerical simulation.

4.3.1.1 Classical macroscopic fatigue criteria

Low-cycle fatigue as a phenomenon has received much attention since the early work of Coffin and Manson in the fifties and the sixties. It became clear that low-cycle fatigue is a problem which is different from high-cycle fatigue. In low-cycle fatigue, macroscopic plastic deformation can occur in every cycle. Under low-cycle fatigue, failure can occur in a small number of cycles, i.e. 1000 cycles or less. Small cracks are usually initiated at the very beginning of the loading. In case of loadings of high amplitude level, crack initiation represents the largest part of the fatigue life.

• **Manson–Coffin criterion**

In 1910, Basquin observed that stress-life data could be modeled using a power relationship, which results in a straight line on a log-log plot. This observation corresponds to an elastic material behavior in the strain-life approach. Basquin's equation can be expressed in terms of true elastic strain amplitude as:

$$\varepsilon_e = \frac{\sigma_a}{E} = \frac{\sigma'_f}{E} (2N_f)^b \quad (33)$$

where ε_e is the elastic component of the cyclic strain amplitude; σ_a is the cyclic stress amplitude; σ'_f is the regression intercept called the fatigue strength coefficient; N_f is the number of cycles to failure; b is the regression slope called the fatigue strength exponent.

In the 1950's, Manson and Coffin [Manson 1954; Coffin 1954] independently found that plastic strain-life data could also be modeled using a power law relationship:

$$\frac{\Delta\varepsilon_p}{2} = \varepsilon'_f (2N_f)^c \quad (34)$$

where $\Delta\varepsilon_p$ is the plastic component of the cyclic strain range, $\frac{\Delta\varepsilon_p}{2}$ the cyclic strain amplitude; ε'_f the regression intercept called the fatigue ductility coefficient; N_f the number of cycles to failure; c the regression slope called the fatigue ductility exponent.

The strain-life curve can be formed by adding the elastic and plastic components:

$$\varepsilon_t = \varepsilon_e + \varepsilon_p \quad (35)$$

$$\varepsilon_t = \frac{\sigma'_f}{E} (2N_f)^b + \varepsilon'_f (2N_f)^c \quad (36)$$

The influence of the elastic and plastic components on the strain-life curve is shown in Figure 80. It is noted that elastic strains have a greater influence on fatigue lives above the transition life. Plastic strains have a greater influence below the transition life. Thus the transition life provides a convenient delineation between low-cycle and high-cycle fatigue regimes.

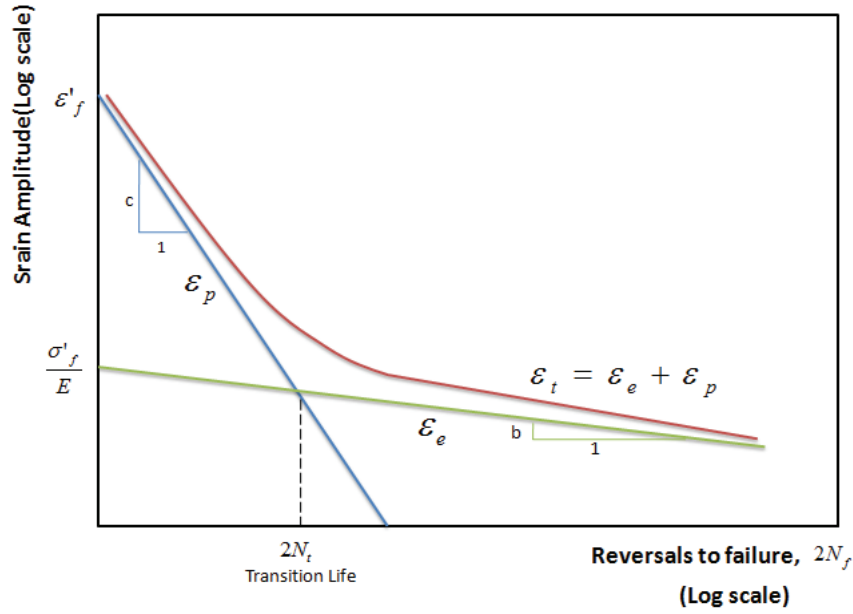


Figure 80 Typical Strain-Life Curve

• **Smith–Watson–Topper criterion**

Most basic S-N fatigue data are generated using a fully-reversed stress cycle. However, actual loading applications usually involve a mean stress on which the oscillatory stress is superimposed [Suresh 1991; Stephens, Fatemi, Stephens and Fuchs 2000; Krupp 2007]. Morrow was the first to propose a modification to the baseline strain-life curve to account for the effect of mean stress [Morrow 1964]. His approach was to alter the value of the fatigue strength coefficient in the elastic component of the stress-strain relationship:

$$\sigma_a = (\sigma'_f - \sigma_0)(2N_f)^b \quad (37)$$

where σ_0 is the mean stress. In this equation, tensile mean stresses are positive ($\sigma_0 > 0$), and compressive mean stresses are negative ($\sigma_0 < 0$). In terms of strain-life relationship, the Morrow Mean Stress Correction can be expressed by:

$$\varepsilon_t = \frac{\sigma'_f - \sigma_0}{E} (2N_f)^b + \varepsilon'_f (2N_f)^c \quad (38)$$

A different method for modifying the strain-life curve to account for mean stress was proposed by Smith, Watson, and Topper [Smith, Watson and Topper 1970]. Their approach uses Basquin's relationship relating the maximum stress σ_{max} of a fully-reversed cycle to fatigue life:

$$\sigma_{max} = \sigma'_f (2N_f)^b \quad (39)$$

Multiplying the strain-life equation by this term gives the Smith-Watson-Topper (SWT) mean stress correction:

$$\sigma_{max} = \frac{\sigma_f'}{2} (2N_f)^{2b} + \sigma_f' \varepsilon_f' (2N_f)^{b+c} \quad (40)$$

The SWT equation predicts that no fatigue damage occurs when the maximum stress is zero or negative (i.e., compressive), which is not always true. Therefore Morrow's correction should be used for loading sequences that are predominantly compressive. In cases of predominantly tensile loading, the SWT approach is more conservative than Morrow's approach and is thus recommended.

• *Walker criterion*

Walker's criterion [Walker 1970] is similar with Smith–Watson–Topper criterion, which also takes into account the effect of mean stress on fatigue life. The equation can be written as:

$$\frac{\sigma_{max}}{E} \left(\frac{\Delta \varepsilon_t E}{\sigma_{max}} \right)^m N_f^\alpha = \beta \quad (41)$$

where α, β are material dependent constants; m is a material parameter characterizing the fatigue behavior.

• *Ostergren criterion*

Ostergren criterion [Ostergren 1976] has a modification to the baseline strain-life curve to account for the effect of mean stress. Ostergren's criterion takes into account the hold time and frequency effects in elevated temperature low cycle fatigue:

$$(\sigma_{max} \Delta \varepsilon_t) v^{b(k-1)} N_f^\alpha = \beta \quad (42)$$

where v is the frequency of the test cycle; α, β are material dependent constants; b, k are material parameters characterizing the fatigue behavior.

4.3.1.2 *Fatigue criteria based on micromechanical approaches*

At the grain scale, a mesoscopic description of fatigue phenomena should improve the robustness of the predictions. At this scale, the heterogeneity is due to the grains, which are intrinsically anisotropic. At the macroscopic scale, the material can be considered as homogeneous, and may be isotropic if the grain crystallographic orientations are randomly distributed. Based on this framework, some fatigue criteria based on microplasticity approaches were proposed and widely used in multiscale fatigue analyses. Only those with well-oriented slip planes, maximizing the shear stress for a given loading path among all grains and possible slip planes can develop plasticity and create localized slip bands inducing crack initiation.

• **Energy dissipation criterion**

In the above fatigue criterion, the values were taken at the maximum extreme points in the cycle. These may present a limitation because the same extreme points can correspond to different families of fatigue loops which have distinctly different shape and area.

For the energy dissipation criteria, let Φ be a functional, which depends on the deformation history including the combination of stress and strain values at all points in the stabilized loop. Following the work of Korsunsky group [Korsunsky, Dini, Dunne and Walsh 2007], the functional Φ may be written as dissipated energy for one stabilized cycle (as shown in Figure 81):

$$\Phi(x) = \Delta W_p(x)_{cycle} = \int_{cycle} \sigma(x, t) \dot{\epsilon}(x, t) dt \quad (43)$$

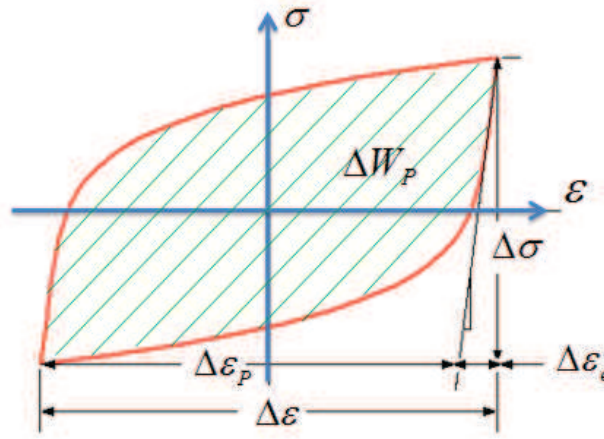


Figure 81 Dissipated energy for one stabilized cycle

where the integral is taken over the stabilized cycle, and x denotes the point at which the field values are considered. In order to find the critical location within the structure, the criterion is written as:

$$\{max \Phi_x(x)\} N_f^b = c \quad (44)$$

The points where significant slip localization takes place are also associated with increased dissipation of energy, and would be expected to become initiation sites for fatigue cracks. In some recently proposed energy-based fatigue criteria [Seweryn, Buczynski and Szusta 2008; Vincent 2008; Fissolo, Gourdin, Ancelet, Amiable, Demassieux, Chapuliot, Haddar, Mermaz, Stelmaszyk, Constantinescu, Vincent and Maillot 2009; Maurel, Rémy, Dahmen and Haddar 2009], dissipated energy as an important metric is taken into account, which depends on the deformation history including the combination of shear stress and shear strain values at all points in the stabilized loop:

$$dW(x)_{cycle} = \sum_T \tau^s \dot{\gamma}^s dt \quad (45)$$

Then

$$W(x)_{cycle} = \sum_T \int_{cycle} \boldsymbol{\tau}^s : \dot{\boldsymbol{\gamma}}^s dt \quad (46)$$

where T is the total number of active slip systems, $\boldsymbol{\tau}^s$ is the current critical resolved shear stress on the s slip system, $\dot{\boldsymbol{\gamma}}^s$ is the shear strain rate, dt is the duration of load increment, and x refers to the location (integration point). The energy dissipated at point x is obtained by integrating the above expression, and numerically by summation over the load increments constituting a complete cycle.

• *LMS criterion*

This criterion was proposed by Amiable [Amiable 2006; Amiable, Chapuliot, Constantinescu and Fissolo 2006], which takes into account the state of stress triaxiality. For this criterion, a term of hydrostatic pressure has been introduced:

$$\Phi(x) = W_{cycle} + \alpha P_{max} \quad (47)$$

Here, α is a material parameter; W_{cycle} is the energy density dissipated in a stabilized cycle, written as:

$$W_{cycle} = \sum_s \int_{cycle} \boldsymbol{\tau}^s : \dot{\boldsymbol{\gamma}}^s dt \quad (48)$$

and P_{max} is the hydrostatic pressure and can be written as:

$$P_{max} = \max_t [P(t)] = \max_t \left[\frac{1}{3} \text{Tr}(\boldsymbol{\sigma}) \right] \quad (49)$$

The effects of average stress are taken into account.

In our case α is set as 0.01 according the work of [Le-Pecheur 2008].

• *Fatemi-Socie criterion*

The Fatemi and Socie critical plane criterion was presented in 1988. Two important factors of maximum plastic shear strain amplitude and normal stress on the corresponding plane are taken into account. The criterion was written as follows [Fatemi and Socie 1988]:

$$\frac{1}{2} \Delta \gamma_{max} (t_1 - t_2) \left(1 + k \frac{\sigma_n}{\sigma_{yeild}} \right) = \frac{\tau'_f}{G} (2 \cdot N_f)^{b\gamma} + \gamma'_f (2 \cdot N_f)^{c\gamma} \quad (50)$$

In this model, $\Delta \gamma_{max}$ is the maximum plastic shear strain amplitude value of 12 slip systems, σ_n is the normal stress on the corresponding plane with maximum plastic shear strain amplitude $\Delta \gamma_{max}$. It is considered in this criterion that shear loading is essential for crack initiation since fatigue cracks initiate on planes of high shear. However, the normal stress is also important. A positive normal stress increases the distance between the

atomic planes in the structure, which facilitates the shear loading to cause damage. The opposite occurs for a negative normal stress.

The left hand side of the equation is denoted as “effective shear strain amplitude” and the right hand side contains the number of cycles to crack initiation, N , and some material dependent constants: τ'_f the shear fatigue strength coefficient; b_f the shear fatigue strength exponent; γ'_f the shear fatigue ductility coefficient; c_f the shear fatigue ductility exponent; G the shear modulus.

The Fatemi-Socie model is widely applied as the shear damage fatigue criterion [Stephens, Fatemi, Stephens and Fuchs 2000]. In order to be used in a micromechanical approach, the elastic yield stress can be replaced by the critical stress for slip system activation. Then the functional form of a micromechanical approach of FS criterion is written as:

$$\Phi = \frac{1}{2} \Delta \gamma_{max} (t_1 - t_2) \left(1 + k \frac{\sigma_n}{\tau_c} \right) \quad (51)$$

where τ_c is the critical stress for slip system activation material and k is a material constant, which can be found by fitting fatigue data from simple uniaxial tests to fatigue data from simple torsion tests which is set to 1 in our case.

• Critical plane criterion

This is an another criterion based on the plane with maximum plastic shear stress which was firstly proposed by Le-Pecheur [Le-Pecheur 2008]. This criterion is similar to that of Fatemi-Socie but simpler to implement. In this criterion, it is considered that the formations of extrusions on the surface are physically driven by slips in the well-oriented plane. The crack may initiate from these extrusions and then it may propagate through the initiated opening. In this criterion, χ , reflecting the effect of stress triaxiality, was taken into account and was considered as a factor controlling initiated opening. The functional form was given as:

$$\Phi = \Delta \gamma_{max} (1 + \chi) \quad (52)$$

$$\chi = \frac{P_{max}}{\sigma_{eq}^{mises}} \quad (53)$$

where P_{max} is hydrostatic pressure, which is written as:

$$P_{max} = \max_t [P(t)] = \max_t \left[\frac{1}{3} \text{Tr}(\boldsymbol{\sigma}) \right] \quad (54)$$

and σ_{eq}^{mises} is equivalent Mises stress:

$$\sigma_{eq}^{mises} = \sqrt{\frac{3}{2} \boldsymbol{\sigma}' : \boldsymbol{\sigma}'} \quad (55)$$

where $\boldsymbol{\sigma}'$ is the derivative part of $\boldsymbol{\sigma}$.

• Depres criterion

The grain size is an important parameter in plasticity, in monotonous tension case, and directly influences the value of the yield stress, or fatigue. Some studies have shown that it had an influence not only on the characteristics of cyclic hardening of material but also on the fatigue life [Hong, Qiao, Liu and Zheng 1998; Song, Lee and Kim 2005; Zhang and Jiang 2006; Basu, Das, Bhattacharjee and Chakraborti 2007]. Depres proposed a criterion taking into account the grain size and mean plastic strain effects, which was determined from simulation in dislocation dynamics [Depres 2004]. This criterion is expressed as:

$$\gamma_{p,irr,cum}^{surf}(N) = k \left(\frac{\tau_{dev}}{\tau_{prim}} \right) \frac{h_g}{D_g} \left(1 + 2 \frac{|\bar{\varepsilon}_p^m|}{\Delta \varepsilon_p^m} \right) \Delta \varepsilon_p^m \sqrt{N} \quad (56)$$

where $\gamma_{p,irr,cum}^{surf}(N)$ is irreversible cumulated deformation on the surface; τ_{dev} and τ_{prim} are the resolved shear stresses on the primary slip system and deviated slip system, respectively; h_g, D_g are the values of depth of the SL and grain size (as shown in Figure 82); $\bar{\varepsilon}_p^m$ and $\Delta \varepsilon_p^m$ are the values of the mean plastic strain and the plastic strain amplitude.

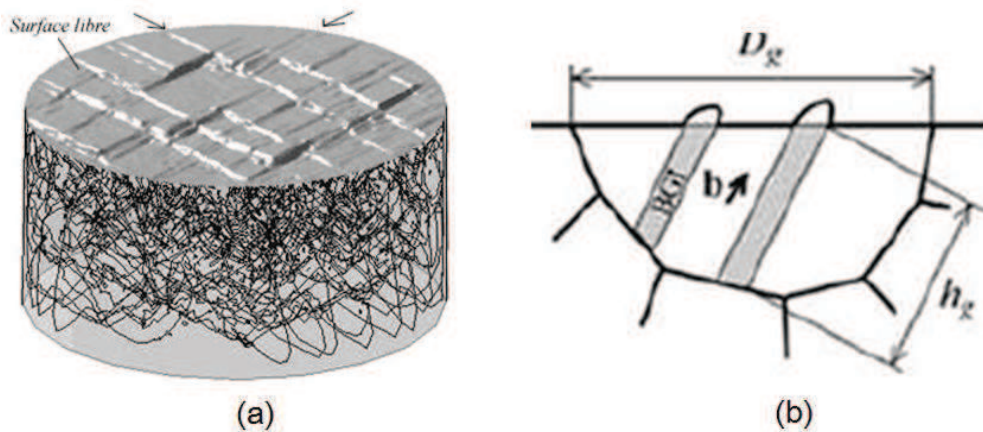


Figure 82 (a) Simulation of extrusions on the surface by dislocation dynamics (b) Depth of the SL h_g and grain size D_g [Depres 2004]

• Dang Van criterion

The Dang Van criterion is based on the Lin–Taylor homogenization assumption in order to relate meso and macroscopic mechanical fields and uses shakedown concepts. It introduces a linear combination of hydrostatic pressure $P_H(t)$ and mesoscopic resolved shear stress amplitude $\tau(t)$.

According to Dang Van, fatigue damage appears in a finite time when the combination of local shear stresses $\tau(t)$ and hydrostatic stress $P_H(t)$ reaches the borders of an admissible fatigue area:

$$\text{Max}[\tau(t) + \kappa P_H(t)] \leq \lambda \quad (57)$$

where the material parameters κ and λ can, in principle, be determined with data from two high cycle fatigue tests: reversed bend (fatigue limit f_{-1}) and reversed torsion (fatigue limit τ_{-1}). $\lambda = \tau_{-1}$ and $\kappa = \frac{3\tau_{-1}}{f_{-1}} - \frac{3}{2}$.

To sum up, the general formulation of a fatigue criterion can be expressed mathematically as a relation between the number of cycles to failure of the structure N_f and a function of the cyclic strain or stress values [Constantinescu, Charkaluk, Lederer and Verger 2004]:

$$\Phi(\varepsilon_t, \varepsilon_p, \varepsilon_{eq}, \sigma, \sigma_{eq}, \Delta\gamma_{max}, \sigma_n \dots) N_f^\alpha = \beta \quad (58)$$

where N_f denotes the number of cycles to failure, α and β are material dependent constants, and $\varepsilon_t, \varepsilon_p, \varepsilon_{eq}, \sigma, \sigma_{eq}, \Delta\gamma, \sigma_n$ are the values of the parameters taken at certain points in a stabilized cycle.

For the Manson–Coffin, Smith–Watson–Topper, Walker and Ostergren, Energy dissipation, LMS, Fatemi-Socie, Critical plan, Depres and Dang Van criteria, the form of function Φ is summarized in Table 15. Here $\Delta\varepsilon_p, \Delta\varepsilon_t, \sigma_{max}$ denote, respectively, the plastic strain range, the total strain range and the maximum tensile stress over a uniaxial cycle; $\Delta\gamma_{max}$ is the maximum slip value of the 12 slip systems; σ_n is the maximum normal stress on that plane; E is the Young's modulus and ν is the frequency of the test cycle; b, k, c, m are material parameters characterizing the fatigue behavior.

Table 15 $\Phi(x)$ fonction in the fatigue criteria

Criterion	$\Phi(x)$	Factors used in this work
Manson-Coffin	$\Delta\varepsilon_p$	ε_{22}
Smith–Watson–Topper	$\sqrt{E\Delta\varepsilon_t\sigma_{max}}$	σ_{max}
Walker	$\frac{\sigma_{max}}{E} \left(\frac{\Delta\varepsilon_t E}{\sigma_{max}} \right)^m$	σ_{max}
Ostergren	$(\sigma_{max} \Delta\varepsilon_t) v^{b(k-1)}$	σ_{max}
Energy dissipation	$W_{cycle} = \sum_s \int_{cycle} \boldsymbol{\tau}^s : \dot{\boldsymbol{\gamma}}^s dt$	Φ
LMS	$W_{cycle} + \alpha P_{max}$	Φ, W_{cycle}
Fatemi-Socie	$\frac{1}{2} \Delta\gamma_{max} (t_1 - t_2) \left(1 + k \frac{\sigma_n}{\tau_c} \right)$	$\Phi, \Delta\gamma_{max}, \sigma_n$
Critical plan	$\Delta\gamma_{max} \left(1 + \frac{P_{max}}{\sigma_{eq}^{mises}} \right)$	$\Delta\gamma_{max}$
Depres criterion	$\left(\frac{\gamma_{p,irr,cum}^{surf}(N) \cdot D_g}{\kappa \left(\frac{\tau_{dev}}{\tau_{prim}} \right) \cdot h_g \cdot \left(1 + 2 \frac{ \overline{\varepsilon_p^m} }{\Delta\varepsilon_p^m} \right) \cdot \Delta\varepsilon_p^m} \right)^2$	
Dang Van criterion	$\tau(t) + \kappa P_H(t)$	

As mentioned in section 4.3.1, many fatigue criteria have been proposed for the prediction of microcrack initiation in both low cycle fatigue (LCF) and high cycle fatigue (HCF). These various macro or micromechanical approaches have proven to be efficient for specific material structures over certain loading conditions. However, making the choice of an appropriate fatigue criterion is in practice difficult because it strongly depends on specificities of the problem to solve.

In the next section, some numerical field results, as shown in Table 15, are presented to evaluate the mechanical factors (indicators in fatigue crack initiation criteria) that

controlled crack initiation at the grain scale and to compare the capabilities of different fatigue criteria.

4.3.2 Simulation procedure

In order to get the numerical mechanical field results to study the microstructure effect on fatigue crack initiation, to predict crack initiation sites on the surface and to evaluate the crack initiation predictive capabilities of some factors in fatigue criteria, three numerical aggregates were built from one fatigue specimen. Three zones of the surface were chosen containing 1 or 2 cracks in each zone as shown in Figure 83. The cracks had a length varying from about 50 μm to 100 μm . In zone 1, there are two cracks with reference number 3 and 4 indicated in Figure 83 and Figure 84. From these images, it can be seen that crack 3 initiated along a slip lines and is located at a grain boundary. Crack 4 is similar to crack 3. Its initiation also occurred along the slip line in one grain in which two active slip systems were active. Its location is also near a grain boundary.

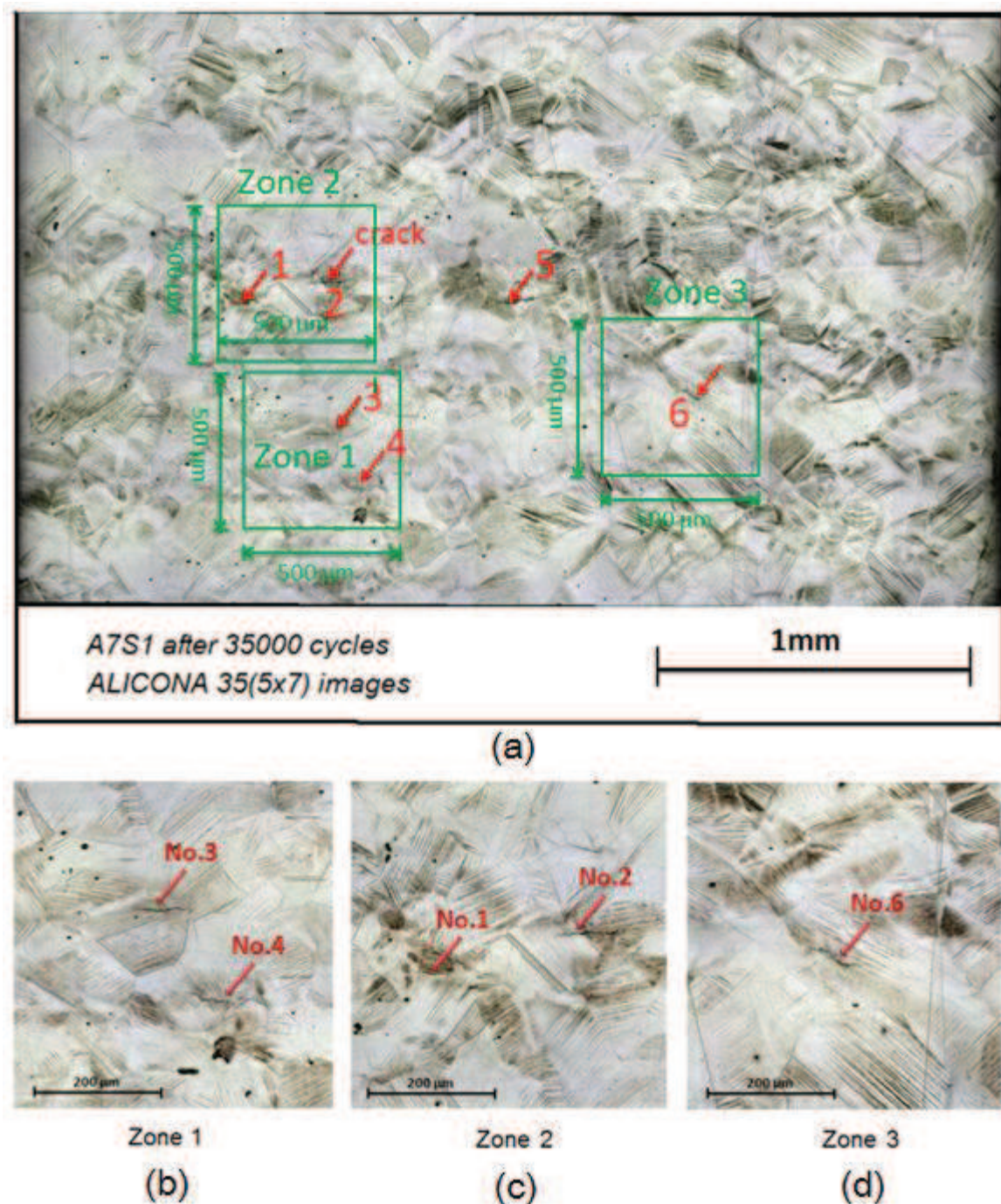


Figure 83 (a) Surface observation with an optical microscope ALICONA after 35000 cycles under 220 MPa stress amplitude (specimen A7); three zones with cracks chosen to make the numerical aggregates (b) zone 1 (c) zone 2 (d) zone 3

In zone 2, crack 1 is formed by two smaller cracks with a length of about 25 µm connected together and propagating along the grain boundary. Crack 2 initiated from an inclusion close to the boundary between a large grain and a quite small grain. Crack 6 in zone 3 is also composed of two shorter cracks that initiated along slip lines near a grain

boundary which is parallel to the slip line direction. For all these five cracks considered in the aggregates, the angle between crack initiation axis and load axis is in the range $[30^\circ$ to $80^\circ]$.

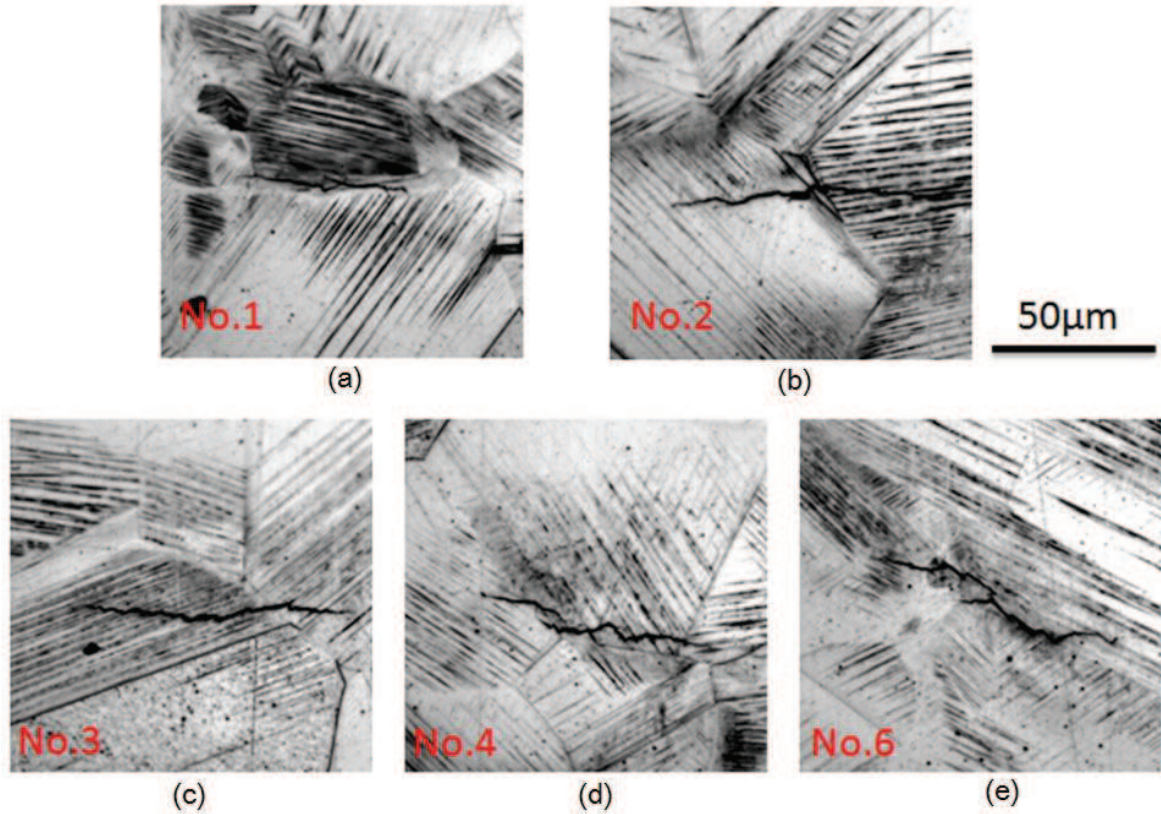


Figure 84 Different kinds of cracks indicated in Figure 83, observed after 35000 cycles under 220 MPa stress amplitude with an optical microscope Alicona (a) Crack No. 1 in zone 2 (b) Crack No. 2 in zone 2 (c) Crack No. 3 in zone1 (d) Crack No. 4 in zone 1 (b) Crack No. 6 in zone 3

Figure 85 gives the surface observations combined with EBSD maps on the three considered zones. The crack locations and their neighboring grains can be seen.

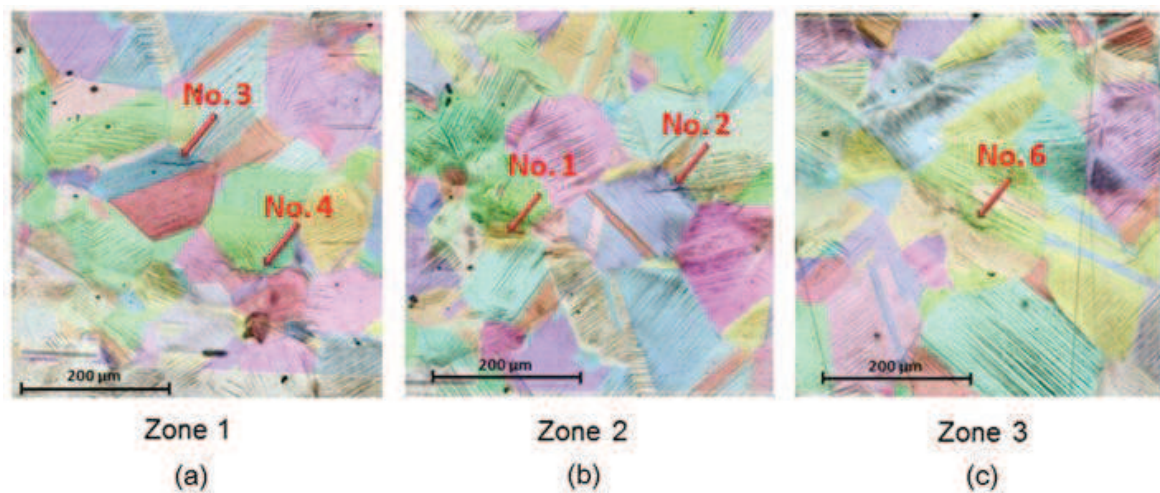


Figure 85 Surface observation combined with EBSD maps on the three considered zones (a) zone 1 (b) zone 2 (c) zone 3 (cracks are indicated with arrows)

The 3D numerical aggregates were constructed from four electron backscattered diffraction (EBSD) maps performed on successive cross-section polishing on the same area as shown in Figure 88. In order to make sure to get the same area for each EBSD measurement, microhardness marks were done as shown in Figure 86. However, it is difficult to measure and to control the distance between two successive layers to a required distance of 27 μm . Because the Vickers diamond pyramid indenter is machined in the form of a squared pyramid with an angle of 136° between faces and the depth of indentation is 1/7 of the diagonal length as shown in Figure 87, we can measure and calculate the polished-out thickness according to the change of d_1 and d_2 at each point. The polished-out thickness is considered as an average value of these four microhardness marks.

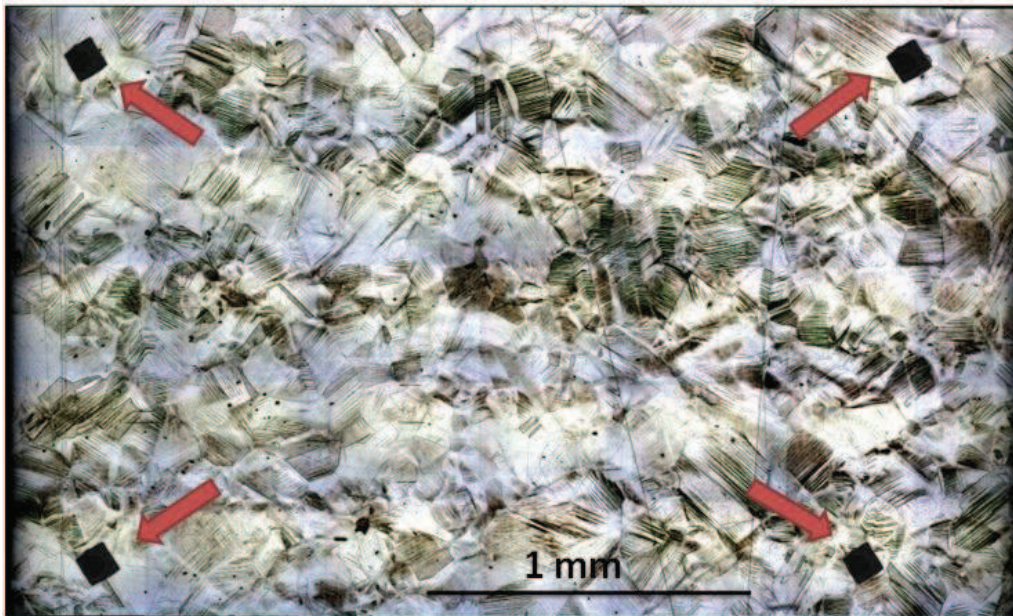


Figure 86 Microhardness marks proformed for location-setting and measuring the polished-out thickness

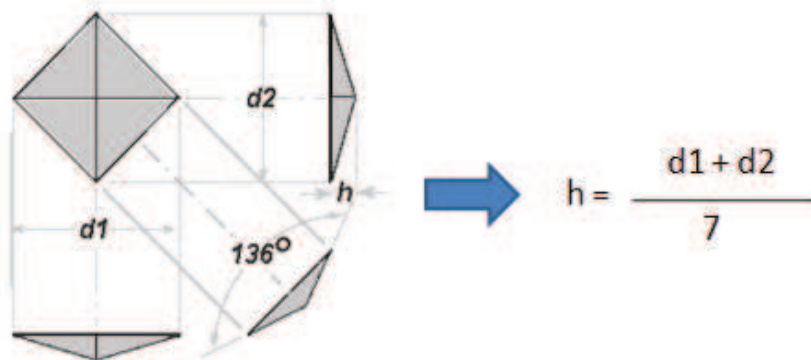


Figure 87 Vickers pyramid diamond indenter indentation

After the EBSD measurements, EBSD maps of the four layers were corrected by a rigid body displacement in order to erase the slight position and orientation errors made when positioning the sample in the SEM. An optimization program was developed in our laboratory [Schwartz 2011], which minimizes the error of position of the center of a given number of grains. Figure 88 gives adjusted EBSD maps on four layers and 3D meshed aggregate which is built up according to the real grain orientation information included in these EBSD maps. The EBSD maps were acquired with a resolution of 2 μm . Because a successful EBSD measurement requires careful sample surface preparation, the first layer of EBSD map was taken before the fatigue test. The last three layers of EBSD were obtained after the fatigue test.

The aggregates were meshed with the method mentioned in the previous section, with eight-node brick elements with reduced integration and respecting the real texture and morphology of the material. The element size used is $4\mu\text{m} \times 4\mu\text{m} \times 9\mu\text{m}$. The surface sizes of these three zones are all $500\mu\text{m}$ by $500\mu\text{m}$. The microstructure of each layer is extruded through the third direction. The distance between two layers is $27\mu\text{m}$. So the numerical aggregate thickness is $108\mu\text{m}$.

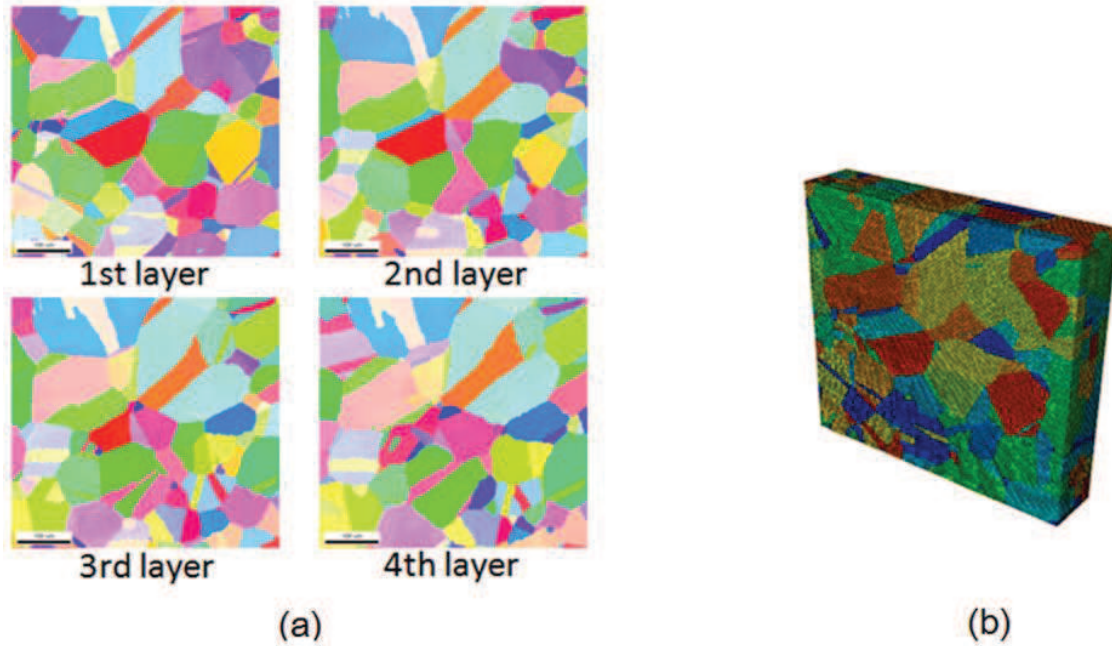


Figure 88 (a) EBSD maps on four successive layers in zone 1 (b) the 3D meshed aggregate

The boundary conditions are chosen the same as that in previous chapter. They are approximated for a small aggregate with a free surface contained in a large specimen. The detailed constraint conditions imposed during the simulation are shown in Figure 89. The displacements of all the nodes on the surface 2 are fixed to zero in direction 2 ($u_2=0$); the displacements of all the nodes on the surface 1 are also fixed to zero in direction 3 ($u_3=0$); the displacements of all the nodes on the surface 3 are fixed to zero in direction 1 ($u_1=0$) and surface 4 is kept parallel to surface 3 during cyclic loading. The remaining two surfaces are the load surface subjected to a stress amplitude of $\pm 220\text{ MPa}$ and a free surface ($\sigma_3 = 0$), respectively.

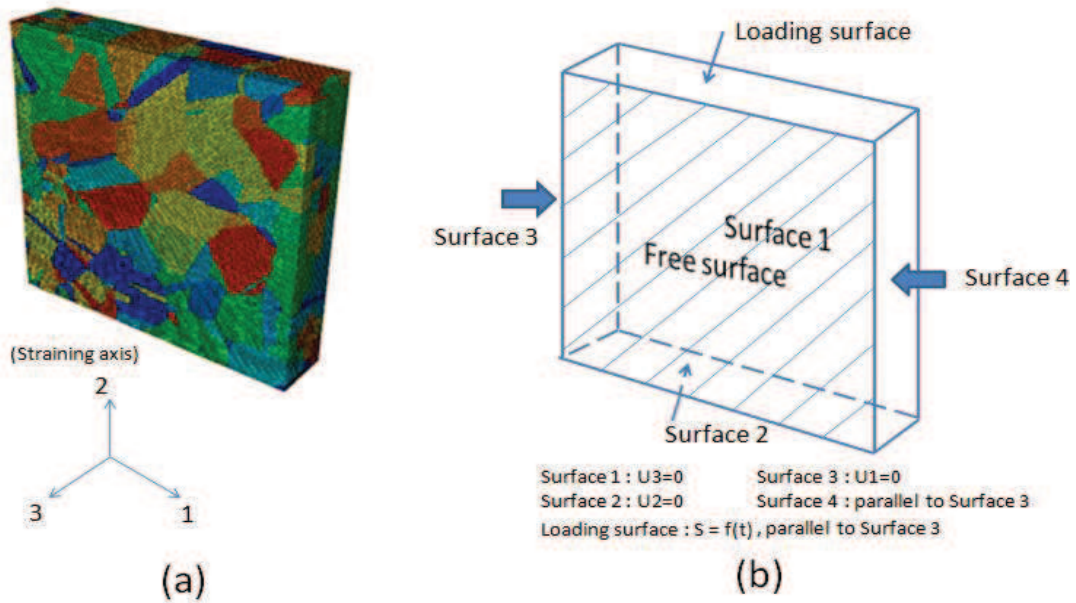


Figure 89 (a) Numerical aggregate of zone 1 performed based on EBSD measurement results (b) boundary conditions applied to the aggregate during the simulation

4.3.3 Simulation results

In this section, some numerical simulation results are presented aiming at comparing with experimental surface observation regarding the predictive capabilities of fatigue crack initiation metrics in fatigue criteria. One of the difficulties arising in this situation is the choice of the “physical” metrics of crack initiation which is not in fact well established.

4.3.3.1 Macroscopic crack initiation indicators

The fatigue criteria presented in section 4.3.1 are based on some conventional indicators. These indicators can be calculated in our model. Based on numerical results on the surface of aggregate, the role that these criteria play on crack initiation can be evaluated by the comparisons with experimental crack initiation observations.

• *Maximum local stress and strain*

As mentioned in section 4.3.1, local stress and strain values are two important factors in classical fatigue criteria, which have a significant influence on fatigue life. Figure 90- Figure 92 show strain ϵ_{22} and the stress σ_{22} field results compared to the experimental surface observations. It is clear that these two indicators from classical fatigue criteria cannot predict the possible location of the crack initiation, especially the local stress.

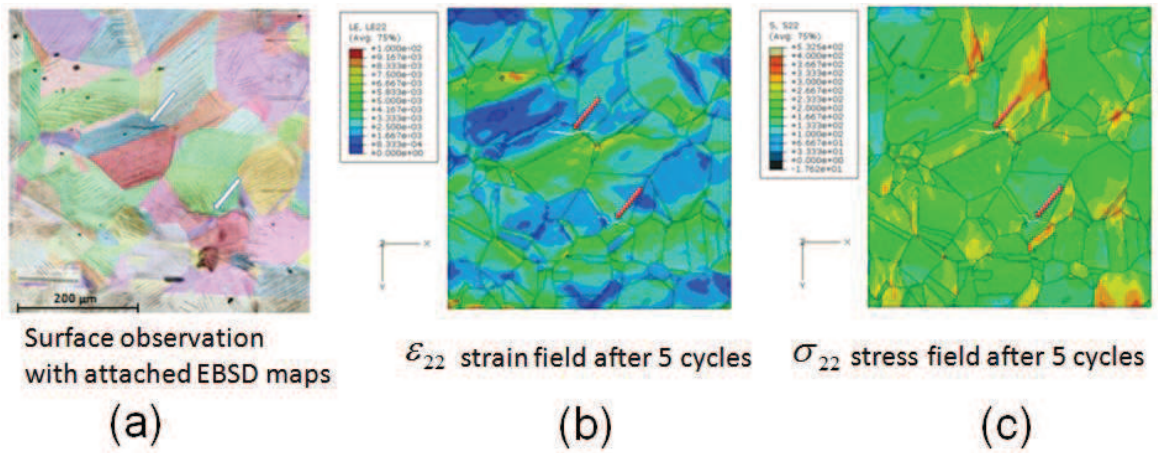


Figure 90 (a) Surface observation combined with EBSD maps of zone 1 with an optical microscopy after 35000 cycles under 220 MPa stress amplitude (b) strain ϵ_{22} field after 5 cycles at strain peak (c) stress σ_{22} field after 5 cycles at strain peak

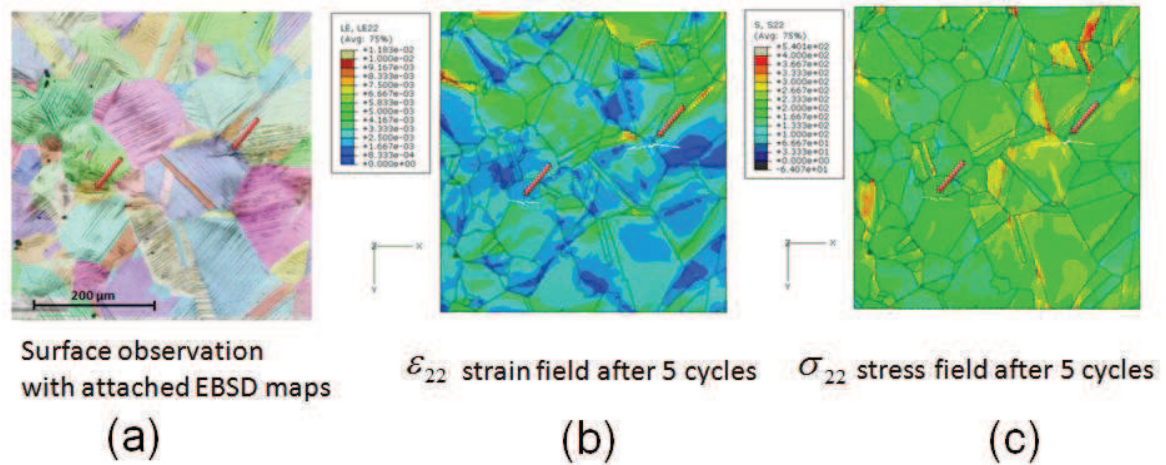


Figure 91 (a) Surface observation combined with EBSD maps of zone 2 with an optical microscopy after 35000 cycles under 220 MPa stress amplitude (b) strain ϵ_{22} field after 5 cycles at strain peak (c) stress σ_{22} field after 5 cycles at strain peak

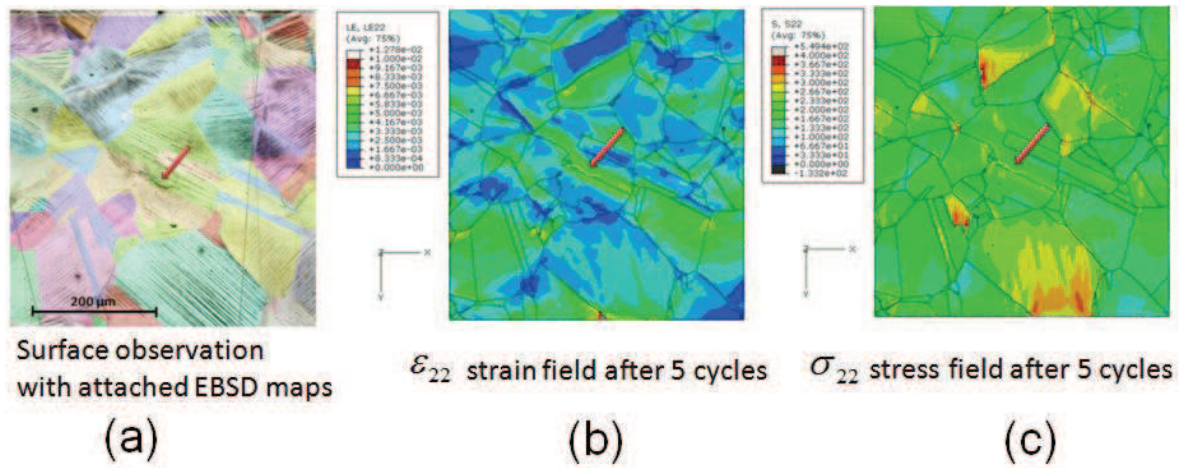


Figure 92 (a) Surface observation combined with EBSD maps of zone 3 with an optical microscopy after 35000 cycles under 220 MPa stress amplitude (b) strain ϵ_{22} field after 5 cycles at strain peak (c) stress σ_{22} field after 5 cycles at strain peak

4.3.3.2 Microscopic crack initiation indicators

• Maximum shear strain amplitude and normal stress

Two indicators, the maximum shear strain amplitude on the 12 slip systems $\Delta\gamma_{\max}$ and the normal stress on the slip plane with maximum shear strain amplitude σ_n are taken into account in Fatemi-Socie's criterion. It is considered that the shear strain amplitude is essential for crack initiation since fatigue cracks usually initiate on planes of high shear strain amplitudes. The normal stress is also important because a positive normal stress increases the distance between atomic planes in the structure, which facilitates shear loading to cause damage. The opposite occurs for a negative normal stress. Figure 93- Figure 95 show the $\Delta\gamma_{\max}$ and σ_n field results compared to the experimental observations. The simulation field results show that some cracks initiated (as shown in Figure 93b and Figure 95b) at sites where significant maximum shear strain amplitude takes place. It means that maximum shear strain amplitude is a good crack initiation indicator and can predict crack initiation sites for the cracks initiated on slip lines. However, it is almost not valid for the cracks initiated from inclusions and GBs. Concerning the field of σ_n , only one crack initiated in a zone where σ_n is significant (see Figure 93c). In the other cases, σ_n has a medium or low value.

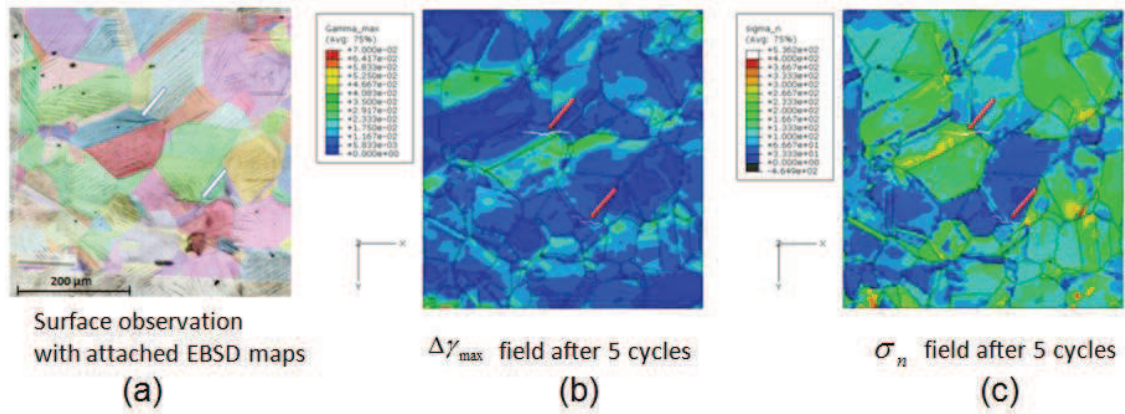


Figure 93 (a) Surface observation of zone 1 with an optical microscopy after 35000 cycles under 220 MPa stress amplitude (b) $\Delta\gamma_{max}$ field after 5 cycles at strain peak (c) σ_n field after 5 cycles at strain peak

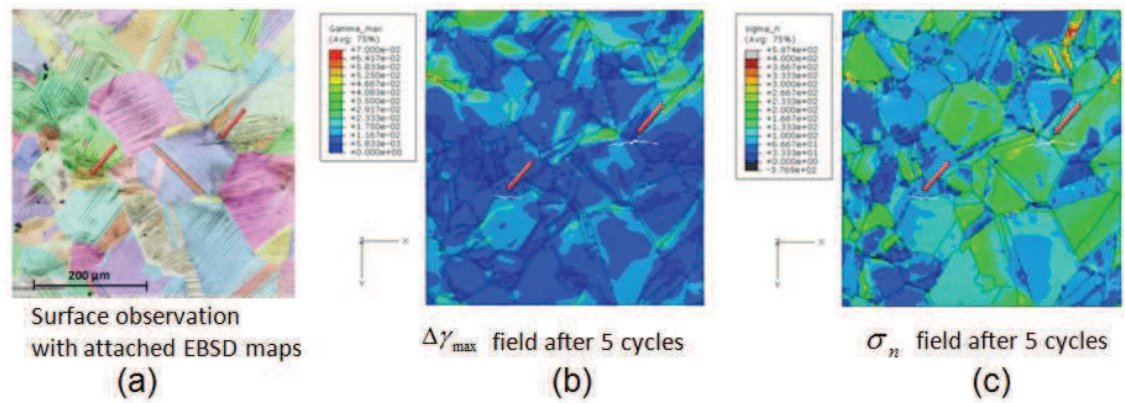


Figure 94 (a) Surface observation of zone 2 with an optical microscopy after 35000 cycles under 220 MPa stress amplitude (b) $\Delta\gamma_{max}$ field after 5 cycles at strain peak (c) σ_n field after 5 cycles at strain peak

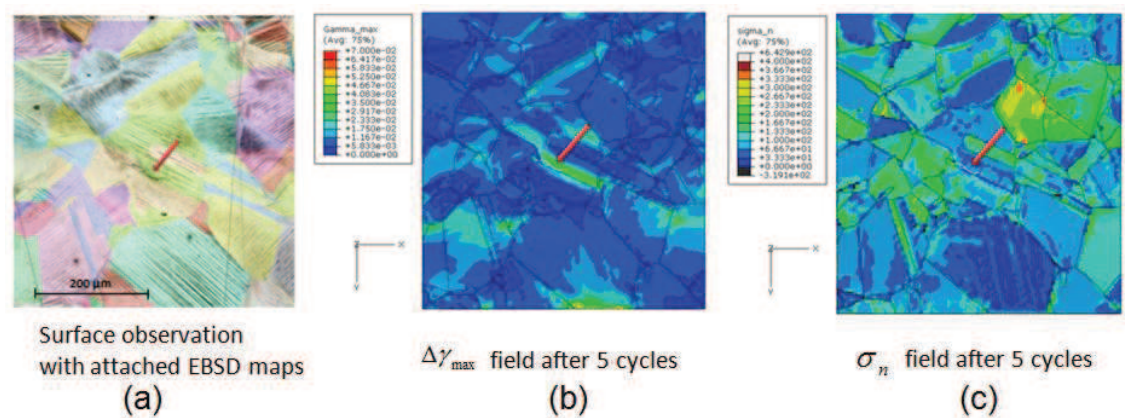


Figure 95 (a) Surface observation of zone 3 with an optical microscopy after 35000 cycles under 220 MPa stress amplitude (b) $\Delta\gamma_{max}$ field after 5 cycles at strain peak (c) σ_n field after 5 cycles at strain peak

• *Fatemi-Socie criterion*

As mentioned in section 4.3.1.2, Fatemi-Socie (FS) criterion is widely applied for shear damage model and it can be used in a micro approach. The function value of the micro approach of FS criterion may be considered as an indicator for crack initiation. Figure 96 shows the simulation function fields (given in equation (51)) of FS criterion for the three considered zones. By comparison with the surface observations (Figure 96d, e and f), it is clear that the points where slip lines crack initiation takes place are significantly associated with the function value of SF criterion (see Figure 96d and f). It can be seen that this slip-based criterion give similar predictive results with the one of maximum shear strain amplitude. Both of them can well indicate the crack initiation location for those initiated on slip lines (see Figure 96d and f). However, they are not valid for the cracks initiated at GBs or inclusions.

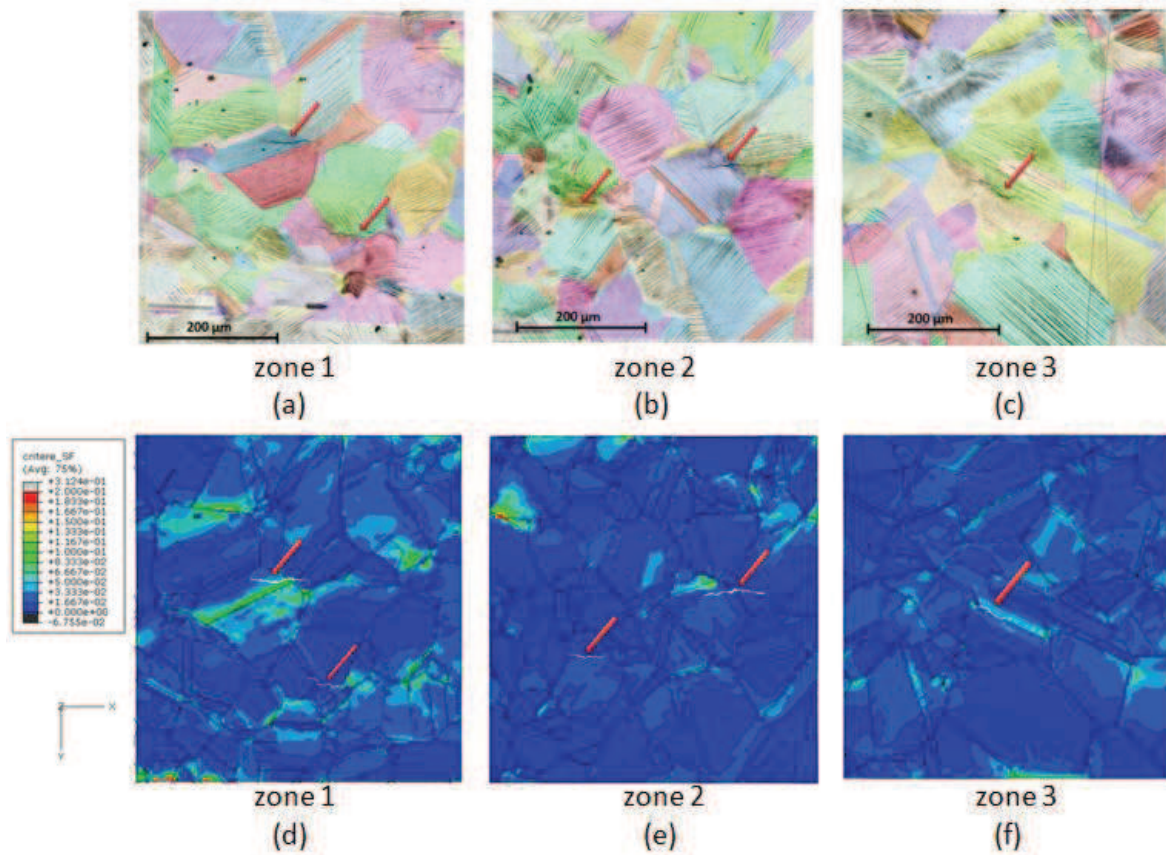


Figure 96 FS criterion function fields compared with the surface crack observation

• **Microscopic dissipated energy**

Figure 97 shows the simulation field results of plastic strain energy (given in equation (46)) in the three considered zones and they are compared with the surface crack observations. The results show that the dissipated energy would also be expected to have good predictive capabilities for crack initiation on slip lines rather than those at inclusion and GBs.

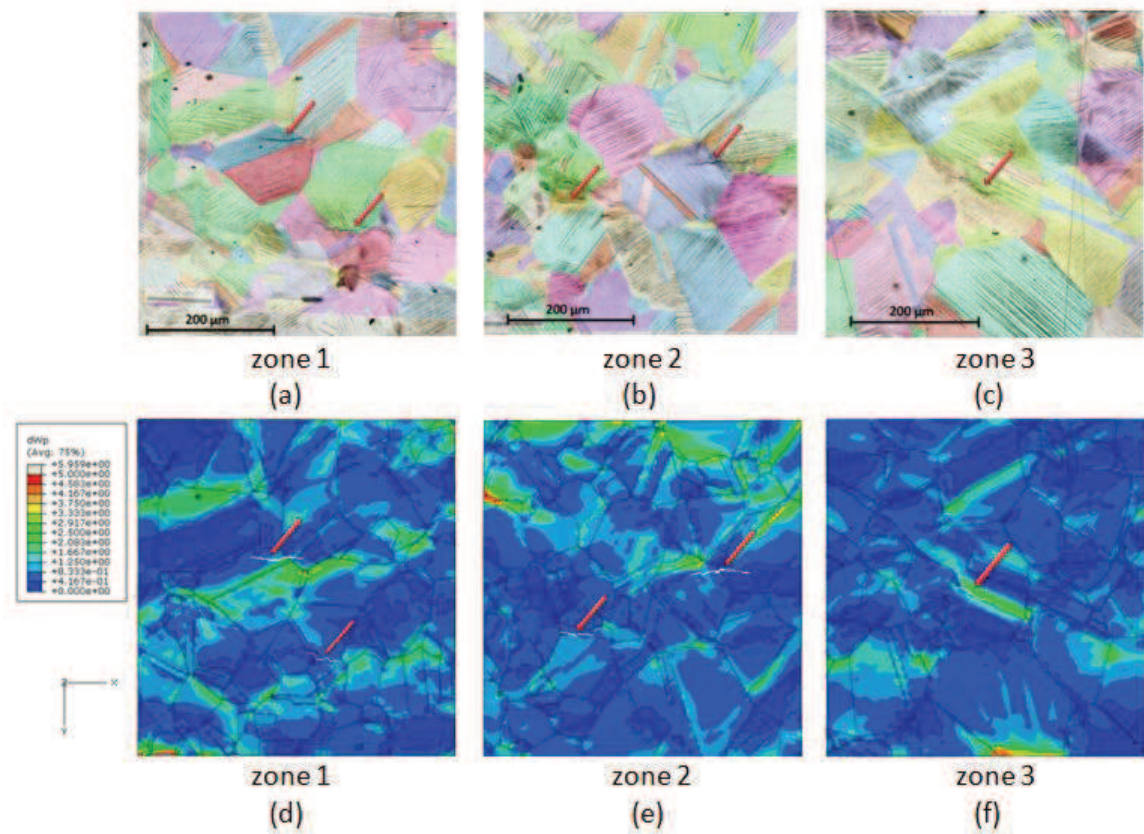


Figure 97 Plastic strain energy fields compared with the surface crack observation

• LMS criterion

As reviewed in section 4.3.1.2, LMS criterion is an energy-based criterion and it takes into account the state of stress triaxiality. Figure 98 gives simulation results of the LMS criterion function fields (shown in equation (47)) compared with the surface crack observations.

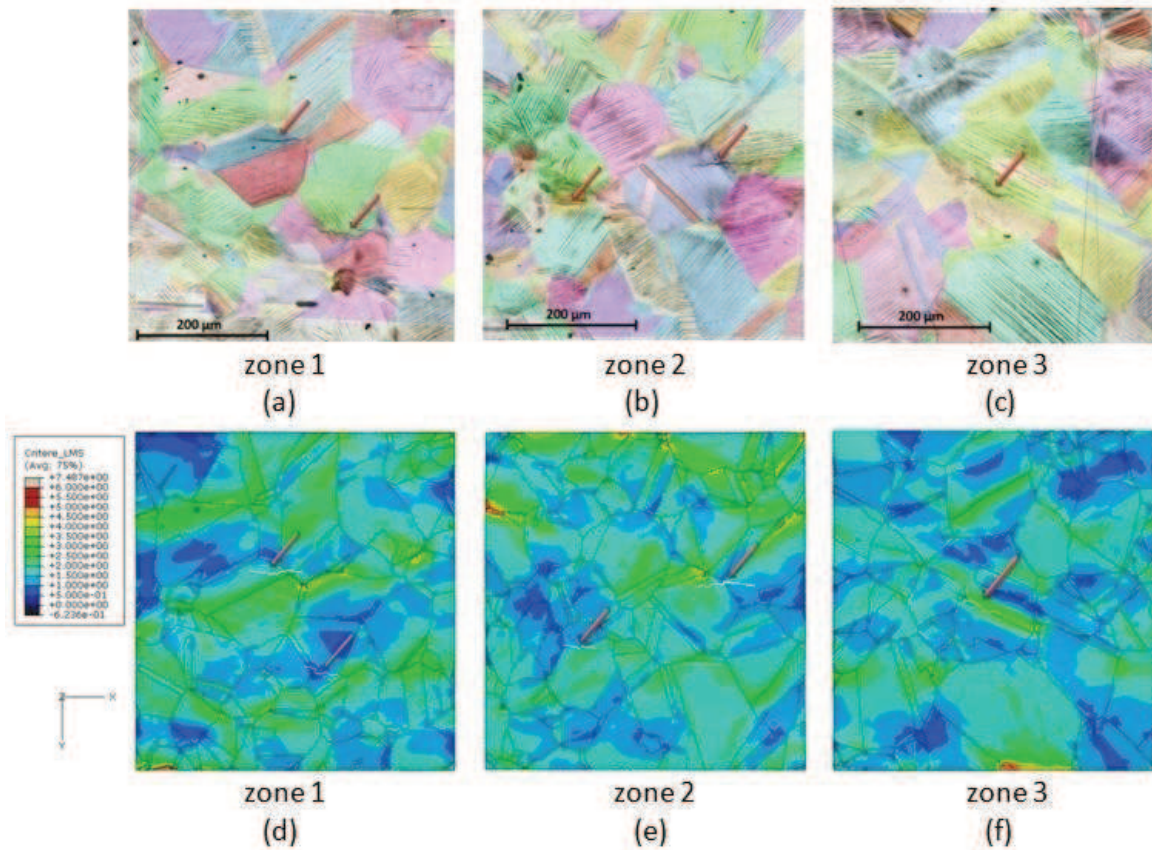


Figure 98 LMS criterion function fields compared with the surface crack observation

It can be seen clearly that distributions of the function value of LMS criterion are more homogeneous with small gradients. The locations where crack initiation takes place are not markedly related with increased function value. By comparisons with the predictions based on dissipated energy, it can be concluded that hydrostatic pressure P_{max} has almost no influence on the crack initiation and function value of LMS criterion cannot be a good indicator for crack initiation.

4.4 Conclusions

According to the optical microscopy and SEM observations on the surfaces of the specimens during fatigue tests, four kinds of crack initiation sites were sorted out: inclusions, grain boundaries (GB), slip lines (SLs) and at the location with the interaction of GB and SLs. Grain boundaries are the most favorable location for crack initiation under low cyclic fatigue for 304L. Among these cracks, the ones that initiate on the GBs with angle α from 60° to 90° account for 80%. Inclusions are not common sites for fatigue crack initiation for 304L. Cracks prefer to initiate at those inclusions that locate near grain boundaries or among the slip lines. In most cases, the cracks that initiate from inclusions formed earlier than the ones initiate in other locations. Crack initiation on slip lines is also frequently observed under stress controlled amplitude fatigue. The orientation difference, angle β between cracked SL and the loading axis for all such cracks were measured varying from 45° to 75° . 90% of GB-SLs type cracks initiated at SLs or propagated along the SLs with an angle α' varying from 30° to 90° . These cracks prefer to initiate on or propagate along GBs with angle β' lying in range 50° to 90° . Most of these cracks show an angle between SL and GB distributed from 110° to 130° , about 90% of all cases. Furthermore, early growth of cracks is obstructed not only by grain boundaries but also by slip lines. When a crack grows across a grain boundary or a slip line, its growth direction is likely to change. The distribution of slip lines within a grain may greatly influence crack initiation and growth. Cross slip lines are major obstructions for crack initiation and growth, while fine and straight slip lines are favorable for them.

As for numerical simulation, first some macro classical low cycle and micro slip-base and energy-based fatigue criteria are reviewed. Three numerical aggregates with realistic microstructures of 304L steel were built from one fatigue specimen and subjected to stress amplitude loading of ± 220 MPa. The field results of maximum local stress and strain, maximum shear strain amplitude, normal stress on the corresponding critical slip plane, Fatemi-Socie criterion function value, dissipated energy and LMS criterion function value are simulated and compared to the experimental surface observation. Under a constant ± 220 MPa stress amplitude, among these simulated micromechanical factors, maximum shear strain amplitude and microscopic dissipated energy were found to provide comparable levels of predictive ability for the cracks initiated on slip lines. The SF criterion also showed good correlation and sensitivity to experimental crack initiation on slip lines. However they are not valid for cracks initiated on inclusions or GBs, for which other specific fatigue criterion should be considered in future. Other factors such as local uniaxial stress, normal stress on critical slip plane, hydrostatic pressure did not show good prediction for the crack initiation at grain scale. Because LMS and Dang Van criteria are based on the hydrostatic pressure, their field simulation also showed less sensitivity to experimental crack initiation site. It should be noted that though these factors cannot predict crack initiation sites and show little correlation with experimental crack initiation sites, they may still have great influence on the microcrack propagation stage because this stage is significantly influenced by microstructure as well.

Chapter 5

Variable amplitude loading effects on cyclic plasticity and microcrack initiation

Table of contents

CHAPTER 5 VARIABLE AMPLITUDE LOADING EFFECTS ON CYCLIC PLASTICITY AND MICROCRACK INITIATION.....	131
5.1 INTRODUCTION	133
5.2 DISTRIBUTION CLOUDS CORRESPONDING TO LOCAL STRESS AND STRAIN	133
5.3 OVERLOAD EFFECTS.....	136
5.3.1 <i>Strain-controlled</i>	136
5.3.1.1 Experiment procedure	137
• Specimen.....	137
• Loading.....	137
• Interruptions for observation	138
• Observation.....	138
5.3.1.2 Experimental results	139
5.3.1.3 Simulation results.....	141
5.3.2 <i>Load-controlled</i>	148
5.3.2.1 Experimental results	148
5.3.2.2 Simulation results.....	149
5.4 CONCLUSIONS.....	159

5.1 Introduction

As mentioned in Chapter 1, the fatigue behavior of metallic materials under variable amplitude loading has been addressed in many papers over the last decades and remains an open problem [Shin and Hsu 1993; Shimojo, Chujo, Higo and Nunomura 1998; Wei, Li and Ke 1998; Hussain, Tauqir, Ul Haq and Khan 1999; Morel 2000; Kelestemur and Chaki 2001; Pommier 2003; Hamam, Pommier and Bumbleler 2007; Daneshpour, Kocak, Langlade and Horstmann 2009]. It is recognized that the occurrence of positive overloads or the alternance of high to low load sequences has a strong effect on the crack propagation behavior leading in most cases to favorable crack growth retardation [Shin and Hsu 1993; Shimojo, Chujo, Higo and Nunomura 1998; Wei, Li and Ke 1998; Hussain, Tauqir, Ul Haq and Khan 1999; Kelestemur and Chaki 2001; Daneshpour, Kocak, Langlade and Horstmann 2009]. However, it is not well understood whether the overload cycles before the initiation of a microcrack are also beneficial for the fatigue crack initiation life.

In this section, the work aims at using a 3D polycrystalline aggregate to simulate the local cyclic mechanical fields within grains on the surface under different loading conditions and then to study the variable amplitude loading effects on cyclic plasticity and microcrack initiation in austenitic steel 304L.

Due to significant cyclic hardening/softening and strong deformation history effects of 304L stainless steel observed in fatigue experiments as discussed in chapter 3, and also found in other works [Turner 1975; Bayoumi and Ellatif 1995], the influence of overload on fatigue life is quite distinct under load or strain controlled tests [Fatemi and Colin 2010]. In this work, both load-controlled and strain-controlled test modes are considered. The simulation results are compared with experimental results to investigate the influence of variable amplitude loading effects on cyclic plasticity and assess the applicability of appropriate fatigue crack initiation prediction parameters under variable amplitude loading conditions.

Load-controlled fatigue tests were conducted under stress amplitude changing from ± 220 MPa to ± 320 MPa (overload) and back to ± 220 MPa. Four different loading paths were considered in which the overload block begins (or ends) either in tension or in compression. Strain-controlled fatigue tests were conducted under ± 0.3 - 0.7 - 0.3% . The stress levels of 220 and 320 MPa used for load-controlled tests correspond to the midlife stress amplitudes of $\pm 0.3\%$ and $\pm 0.7\%$ constant amplitude strain-controlled tests. The simulation results under the load spectrum of ± 0.1 - 0.5 - 0.1% were analyzed and compared with those under ± 0.3 - 0.7 - 0.3% load spectrum which involves more cyclic plasticity.

5.2 Distribution clouds corresponding to local stress and strain

Because in classical fatigue criteria, the maximum stress or strain are considered as the important factors controlling crack initiation, it is necessary to study the distribution of local strain and stress on the specimen surface. The aggregate of 304L steel (the same

aggregate as in chapter 3) was subjected to five different total strain amplitudes including two distinct fatigue regimes: high-cycle fatigue regime ($\pm 0.1\%$) and low-cycle fatigue regimes ($\pm 0.3\%$, $\pm 0.5\%$, $\pm 0.7\%$, and $\pm 1.0\%$).

For each strain amplitude tested, 5 cycles were simulated (H values are adapted to mid-life simulation) on the aggregate to get the stabilized cycle. The distribution cloud of points corresponding to local stress-strain within each element ($4\mu\text{m} \times 4\mu\text{m} \times 8\mu\text{m}$) on the surface of the aggregate is computed. For this simulation, local stress-strain values were obtained within 5625 (75×75) elements on the surface (Element C3D8R only has one integration point located in the middle of the element).

Figure 99a shows simulated stabilized hysteresis loops subjected to fully reversed tension-compression cyclic loading ($R=-1$) with increasing values of total strain amplitude. In order to get the simulated stabilized cycles and accelerate the calculation, different H factors are used and the numbers of cycles in the different cases are listed in Table 16. From Figure 99b, it can be seen that the dispersivity of local strain and stress values on the surface depends on applied strain amplitude: high amplitude gives larger dispersivity in the results (Figure 100). As shown in Table 16, mean stress value of σ_{22} is equal to 137.8 MPa and standard deviation to 22.4 MPa under a strain amplitude of 0.1%. With increasing values of total strain amplitude to 1.0%, they reach respectively 402.1 MPa and 117.7 MPa. Concerning strain fields, the strain standard deviation value changes gradually from 2.45×10^{-4} to 0.00507 when the total strain amplitude increases from 0.1% to 1.0%.

From Figure 100, it is found that the maximum values of local strain are always about 4 times of the mean values when large strain amplitude is imposed (greater than 0.3%). In parallel, the maximum values of local stress are always about 2 to 2.5 times the average under this range of strain amplitudes.

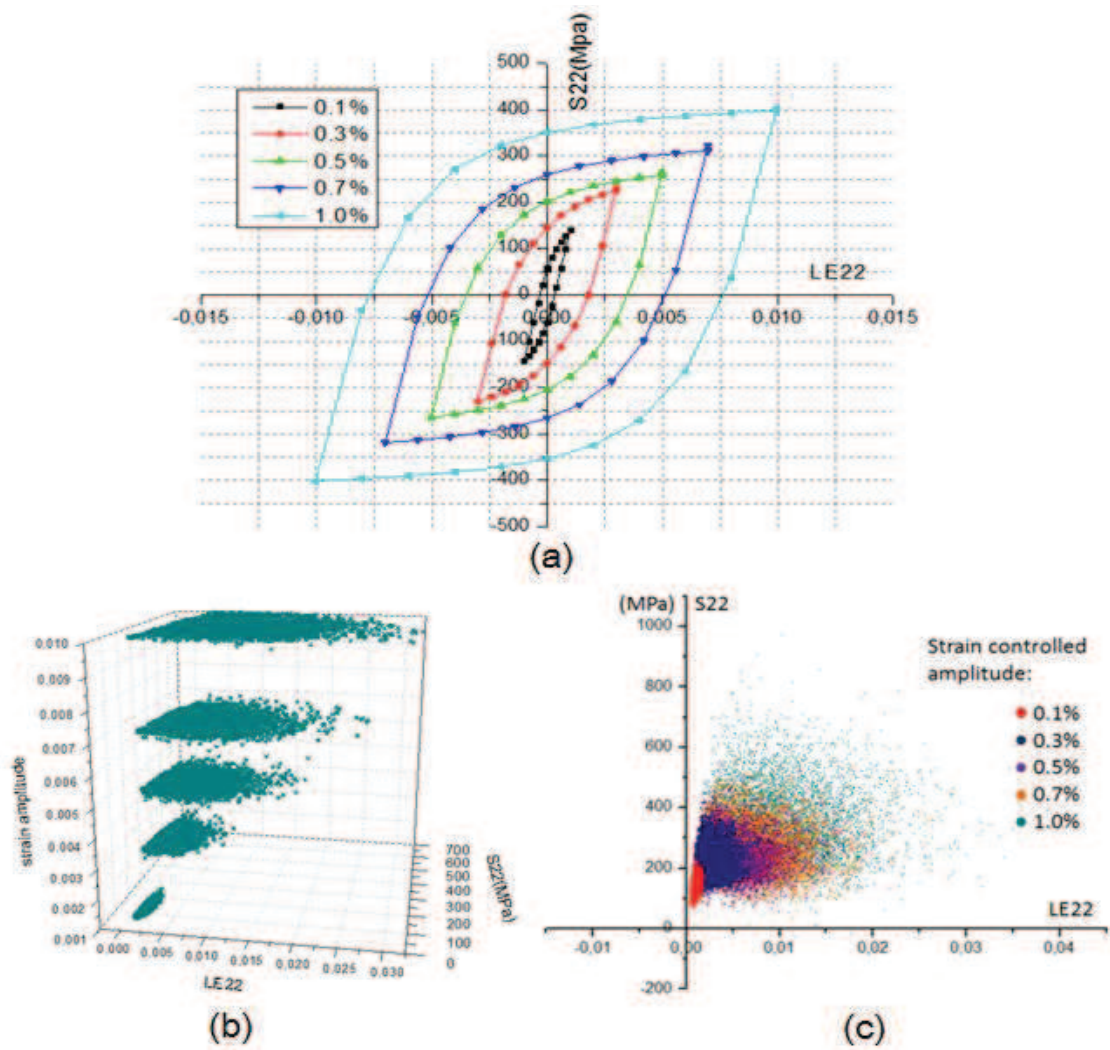


Figure 99 (a) Simulation results of stabilized hysteresis loops subjected to fully reversed tension-compression cyclic deformation ($R = -1$) with increasing values of total strain amplitude at stabilized cycles. (b) and (c) The distribution clouds of points corresponding to local stress-strain within each element on the surface in peak tension.

Table 16 Analysis of distribution clouds in the stabilized state: $\sigma_{22} - \varepsilon_{22}$ in peak tension

Strain amplitude	H factor	Calculated cycles	Stress amplitude (experiment)	Mean value of σ_{22} (simulated)	σ_{22} standard deviation (simulated)	Mean value of ε_{22} (simulated)	ε_{22} standard deviation (simulated)
0.1%	200	5	-	137.8 MPa	24.4 MPa	0.1%	2.45×10^{-4}
0.3%	25	5	220 MPa	221.8 MPa	47.8 MPa	0.3%	0.00116
0.5%	10	5	260 MPa	254.8 MPa	58.0 MPa	0.5%	0.00267
0.7%	4	5	320 MPa	319.2 MPa	75.7 MPa	0.7%	0.00363
1%	1	5	400 MPa	402.1 MPa	117.7 MPa	1.0%	0.00507

Strain amplitude of 0.1% is in the regime of high-cycle fatigue. Local stress is low and deformation in the grains is primarily elastic. It can be found that the distribution cloud of points corresponding to local stress and strain under a strain amplitude of 0.1% is more concentrated than those obtained with the other four strain amplitudes (Figure 99b and c). Under this strain amplitude, the fatigue behavior is almost elastic and the simulated stress-strain cloud thus shows very little heterogeneity. When the imposed strain amplitude increases, the plastic part of the strain increases, and the effect of plastic anisotropy is significant.

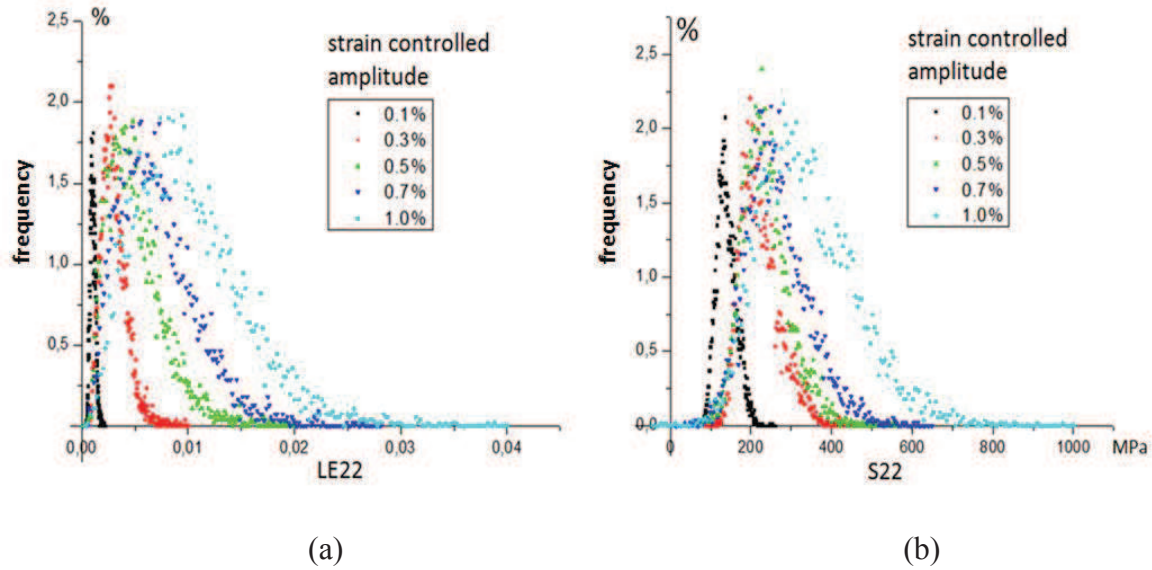


Figure 100 (a) Distribution of the strain ε_{22} of the surface layer at the stabilized cycle; (b) Distribution of the stress σ_{22} of the surface layer at the stabilized cycle.

5.3 Overload effects

In the following part, both load-controlled and strain-controlled modes are considered.

5.3.1 Strain-controlled

In order to study overload effects in different fatigue regimes, two different simple load spectra were considered. In the first case, the total strain amplitude changed from 0.3% to 0.7 % (overload) then back to 0.3%. The strain amplitude of 0.3% is a relatively high value corresponding to the low cycle fatigue regime. In the second case, the strain amplitude changed from 0.1% to 0.5% then back to 0.1% where the strain amplitude of 0.1% is a rather low value corresponding to the high cycle fatigue regime. In these two cases, the overload level was chosen as an increase of 0.4% from the initial strain amplitude.

5.3.1.1 Experimental procedure

Two fatigue tests were performed under strain-controlled fatigue loading in order to get information on crack evolution. One sample was subjected to sinusoidal load spectrum of 0.3-0.7-0.3% and the other one was subjected to sinusoidal loading with constant strain amplitude of 0.3%. The strain rates are 4×10^{-3} /s for these two tests. The mechanical fatigue tests were conducted on the same MTS 810 servo-hydraulic testing machine as mentioned in Section 4.1.1.

• Specimen

Under strain-controlled loading, the specimen geometry is the same as in [Le-Pecheur 2008]. It is shown in Figure 101a. In order to better observe the microcracks with an optical microscope and SEM, two symmetrical cylindrical notches were machined and the detailed shapes are shown in Figure 101b.

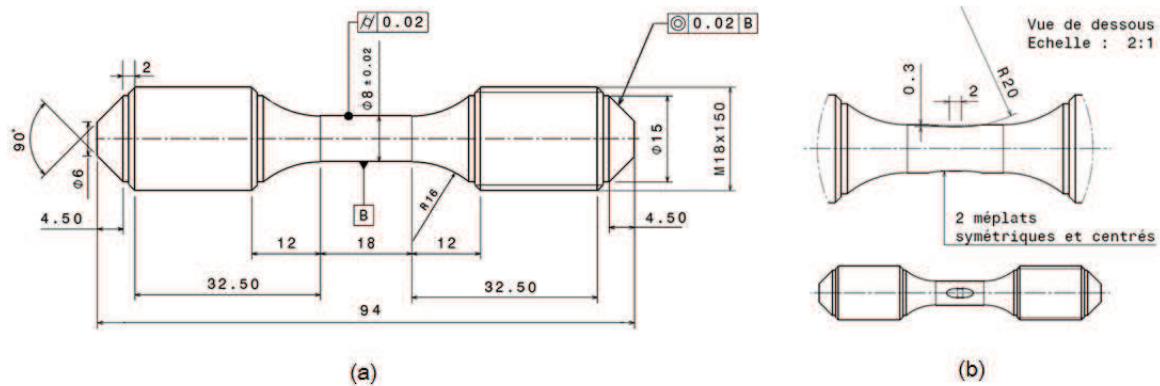


Figure 101 (a) The specimen geometry for fatigue tests under strain control (b) shape of the notches

The surface polishing procedure was the same as that used for flat specimens, which has been introduced in Section 4.1.2. As the surfaces of these specimens were larger than those of flat ones, the time for electro-polishing was increased to 180 seconds to reveal the microstructure and better remove the residual stresses on the surface.

• Loading

One specimen (B2) was subjected to a load spectrum of 0.3-0.7-0.3% and the other one (B1) was subjected to a constant strain amplitude of 0.3% (as shown in Figure 102). The first loading block with the amplitude of 0.3% was performed during 1000 cycles, and the specimen was then subjected to the overloading with amplitude of 0.7% during 20 cycles. After these 1020 cycles, no crack was found on the surface. Then the strain amplitude was back to 0.3% until cracks initiate and propagate enough to leave out the first stage of the crack initiation (greater than 200 μm).

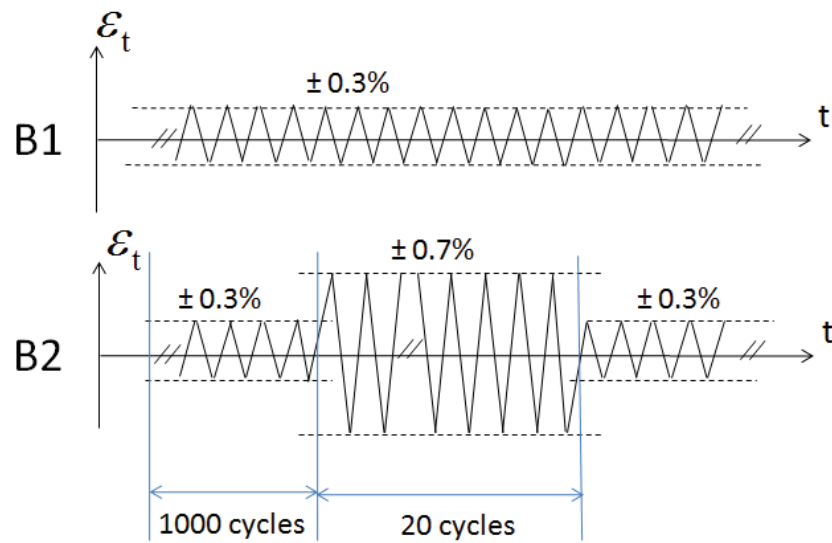


Figure 102 Load spectra for total strain-controlled fatigue tests

• **Interruptions for observation**

These two fatigue tests were all interrupted and unmounted after 2000, 5000, 9000, 12000 and 15000 cycles for surface observation. Then the specimens were carefully remounted and the fatigue test continued to the next interruption. Fatigue tests were terminated when the longest crack was long enough (200 μm in this work). The number of cycles for crack initiation is defined once the longest crack is longer than 200 μm .

• **Observation**

The central zone on the specimen corresponding to an area of about 4 mm^2 (as shown in Figure 103) was observed with an Alicona microscope at every interruption. SEM was used to observe the cracks on the surface at the end of the test after 15000 cycles.

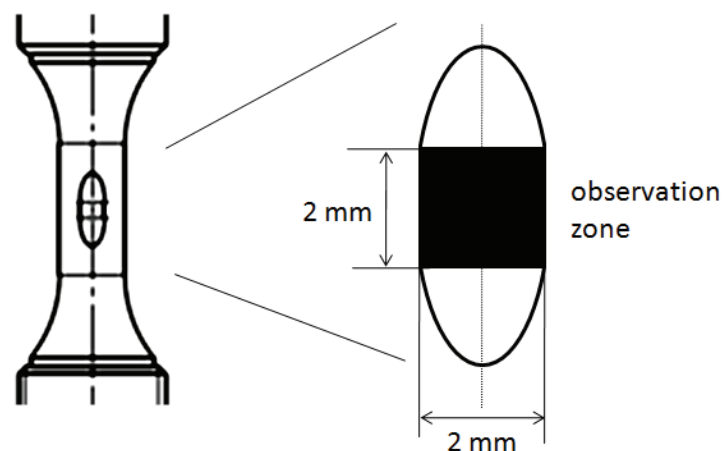


Figure 103 Microscope observation zone (2mm x 2mm) on the surface

5.3.1.2 Experimental results

Figure 104 shows the hardening and softening curves under constant total strain amplitude of $\pm 0.3\%$ and under variable strain amplitudes of $0.3-0.7-0.3\%$, which are compared with uninterrupted fatigue tests under constant total strain amplitude of 0.3% . It is shown that the overload block has not significant effect on the level of stress amplitude at stabilized cycles (the difference is less than 5 MPa). Furthermore, although it can be observed a little step of increase of the stress amplitude after each interruption, this has not influence on the stress amplitudes in the stabilized state.

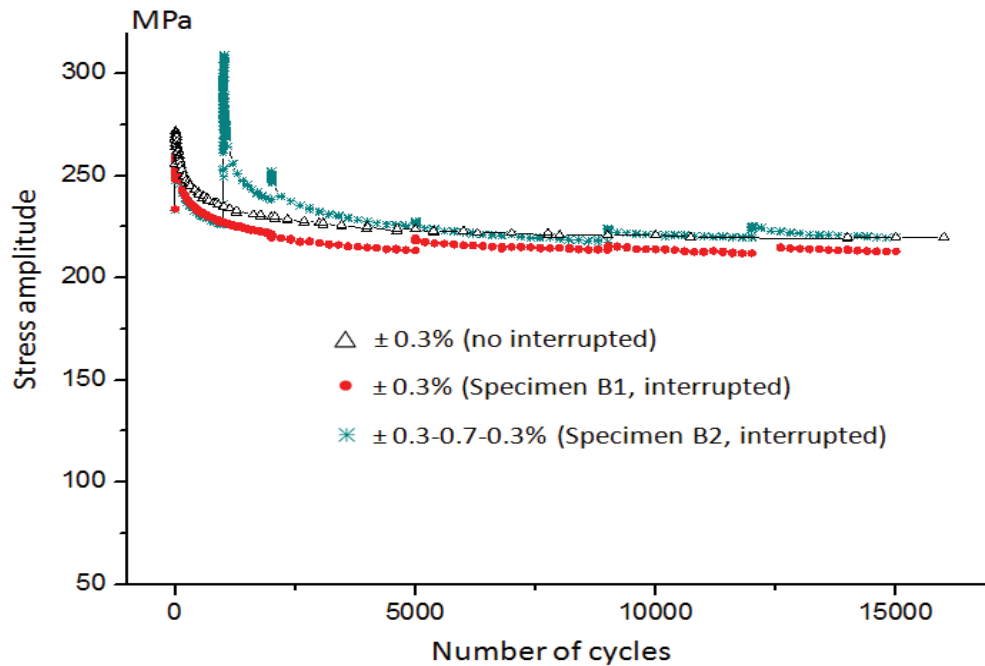


Figure 104 Comparison of hardening and softening curves obtained under constant strain amplitude of 0.3% and under variable strain amplitude of $0.3-0.7-0.3\%$ for 304L steel, the test under strain amplitude of 0.3% without interruption is from [Le-Pecheur 2008] on the same material.

Figure 105 shows the evolutions of stress/strain hysteresis loops during fatigue under constant total strain amplitude of $\pm 0.3\%$ and variable strain amplitude of $0.3-0.7-0.3\%$. From the comparison of these results, it can be clearly seen that the overload block with strain amplitude of 0.7% has little influence on the shape of stress/strain hysteresis loops. As the number of cycles increases, the difference between stress/strain hysteresis loops at 0.3% and $0.3-0.7-0.3\%$ reduces significantly. It means that the influence of the overload vanishes with increasing number of cycles after the overload, from a macroscopic point of view.

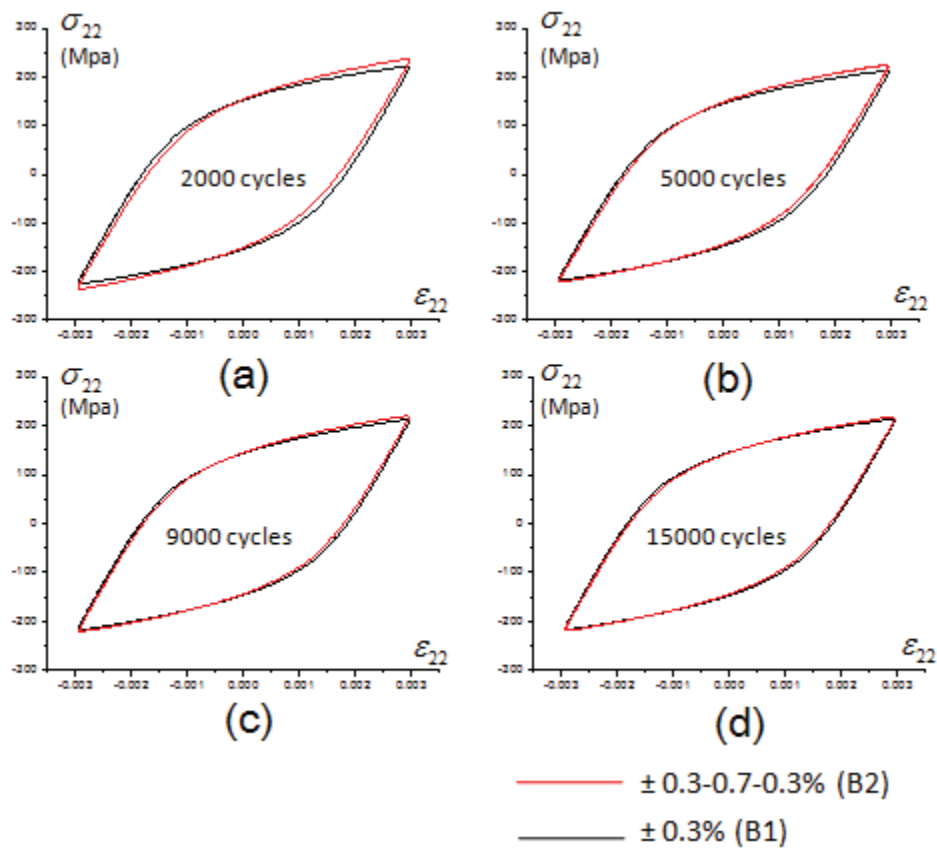


Figure 105 Stress/strain hysteresis loops during fatigue under total strain-controlled loading, comparison between constant total strain amplitude of $\pm 0.3\%$ and variable strain amplitude of $\pm 0.3-0.7-0.3\%$ (a) after 2000 cycles (b) after 5000 cycles (c) after 9000 cycles (d) after 15000 cycles

Figure 106 shows the relationship between the number of cycles and the corresponding number of cracks observed within the 4 mm^2 observation area on the specimen surface. The two fatigue tests were both terminated after 15000 cycles when the longest crack observed was longer than $200 \text{ }\mu\text{m}$. After 15000 cycles, 13 cracks were observed on the observation zone of specimen B1 under constant total strain amplitude of $\pm 0.3\%$ and 12 cracks were observed on B2 under variable strain amplitude loading of $0.3-0.7-0.3\%$. Thus overload effects on crack initiation are not significant under this load spectrum of $0.3-0.7-0.3\%$.

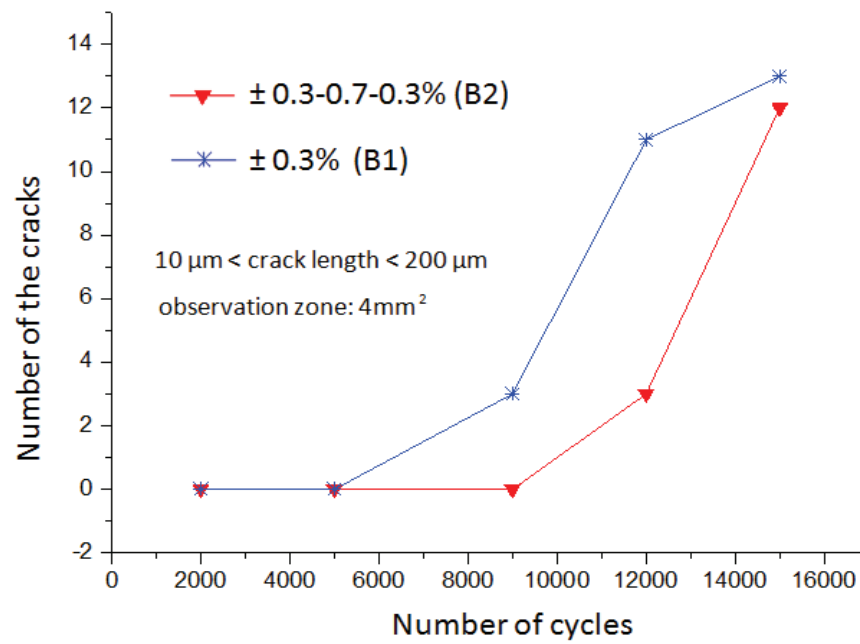


Figure 106 The relationship between the number of cracks on 4 mm^2 observation area of the specimen surface and number of loading cycles under strain-controlled amplitude loading.

5.3.1.3 Simulation results

For each strain level, five cycles were simulated on the aggregate after the change of loading with a rather high value $H=10$ to reach the stabilized cycle. In order to study the overload effect on crack initiation and cyclic plasticity, distribution clouds of points corresponding to local stress-strain within each element ($4\mu\text{m} \times 4\mu\text{m} \times 8\mu\text{m}$) on the free surface of the aggregate were computed. For this simulation, local stress-strain values were obtained within 5625 (75×75) elements located on the free surface of the aggregate (Element C3D8R only have one integration point located in the middle of the element). In the first case ($0.3\%-0.7\%-0.3\%$ loading sequence), it can be seen from Figure 107 that the surface stress-strain distribution clouds after the overload (orange cloud in Figure 107b) are quite similar to that before the overload (orange cloud in Figure 107a). This is due to the fact that plastic strains are still important at total amplitude of 0.3% and make the residual stress and strain fields vanish rapidly after the overload. Because we set the factor H , in equation (29), which controls the channel volumetric fraction evolution, as a large value of 10 in order to accelerate calculation, the rather transient overload effects are not observed. Considering local stress and strain, it was found that as long as the crack initiation (not modeled here) does not occur during overload, there is no strong effect of overload in this load spectrum of $0.3\%-0.7\%-0.3\%$ corresponding to low cycle fatigue. In other words, the influence of the overload effect on the cyclic localized plasticity and further crack initiation is not significant in the low cycle fatigue regime as long as there is no crack initiation on the surface during or just after the overload.

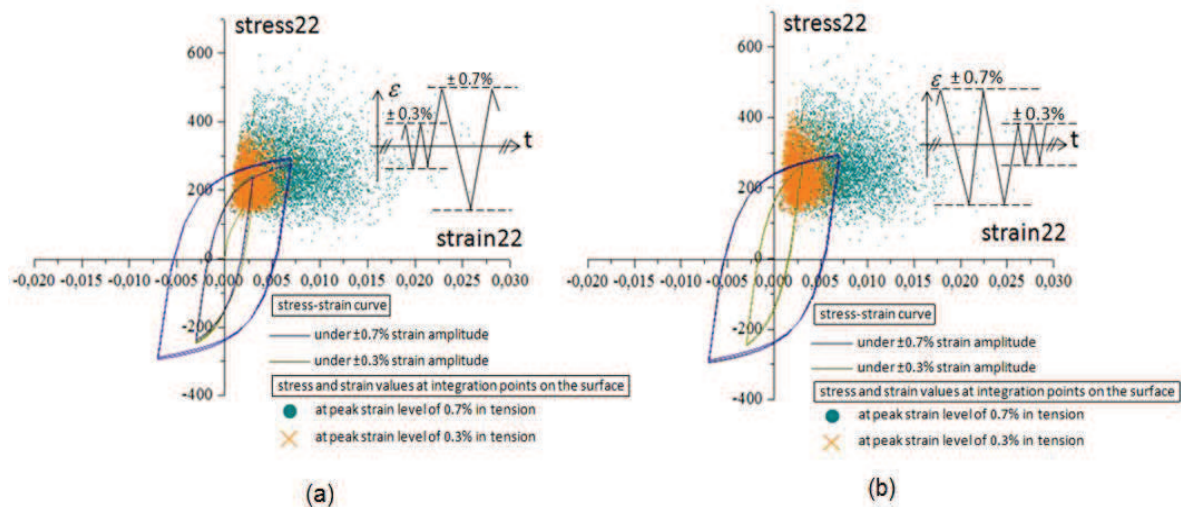


Figure 107 Cyclic stress-strain curves and surface local stress-strain distributions in tension peak under variable amplitude load spectrum, (a) from 0.3% to 0.7%, (b) from 0.7% to 0.3%

Figure 108 gives quantitative distributions of the strain ε_{22} and stress σ_{22} in the surface layer elements before and after the overload when the overload block ends in tension. It can be found that the distributions do not significantly change after the overload.

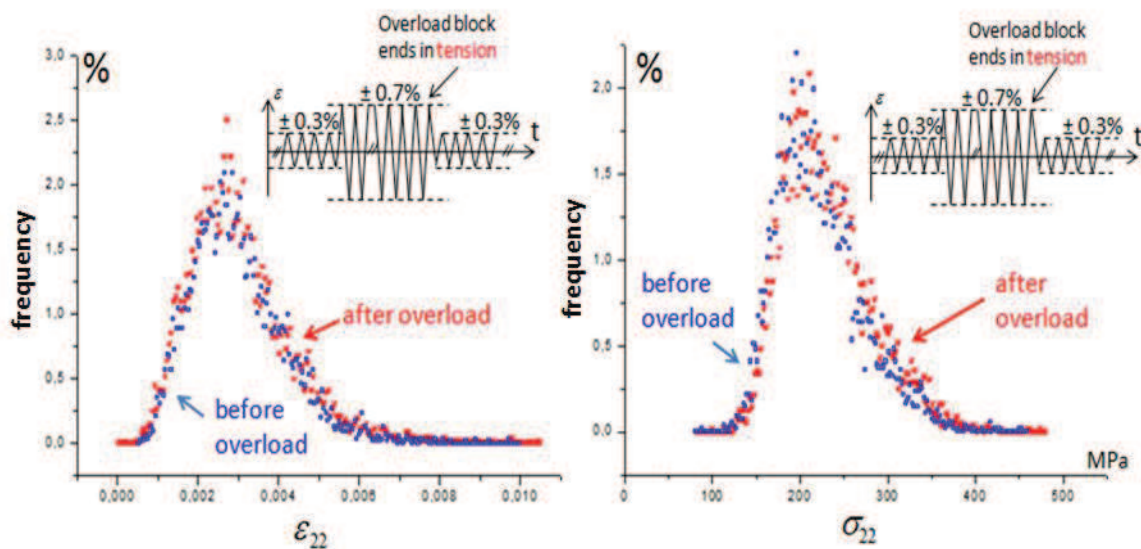


Figure 108 Distributions of the strain ε_{22} and stress σ_{22} in the surface layer elements before and after the overload when the overload block ends in tension

Figure 109 shows two “microscopic” factors, the maximum shear strain amplitude on the 12 slip systems, $\Delta\gamma_{\max}$, and the normal stress on the slip plane with the maximum shear strain amplitude, σ_n , used in SF criterion. There is almost no change on the distribution of maximum shear strain amplitude before and after the overload and the maximum normal stress increases a little.

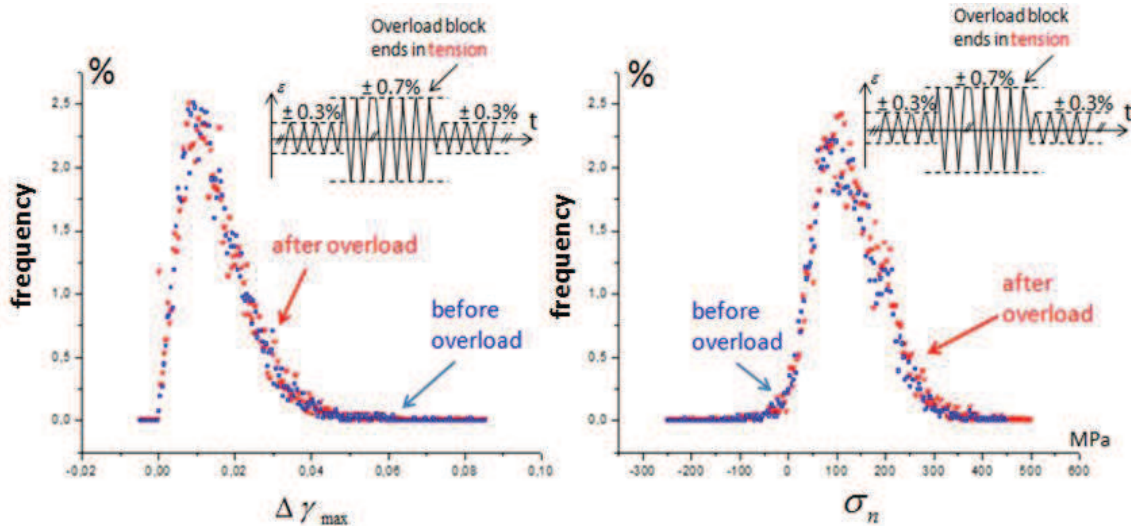


Figure 109 Distributions of the maximum shear strain amplitude on the 12 slip systems and of the normal stress on the slip plane with maximum shear strain amplitude in the surface layer elements before and after the overload when overload block ends in tension

By comparison with the experimental results, $\Delta\gamma_{\max}$ shows good capabilities to predict overload effects under this load spectrum of 0.3-0.7-0.3% rather than the local strain and stress. It is worth noting that when overload block ends in compression, the results obtained are quite similar. So the end sign of the overload block is not important in this loading condition and does not influence the cyclic plasticity after the overload.

Concerning the high cycle fatigue regime, we studied the second load spectrum with a total strain amplitude changing from 0.1% to 0.5% and back to 0.1%. This load spectrum has the same strain amplitude decrease of 0.4% as the load spectrum discussed above, but here the low load level block 0.1% is very low, within the high cycle fatigue regime.

As shown in Figure 110, comparing the stress-strain distribution clouds obtained before and after the overload (the two orange clouds shown in Figure 110a and Figure 110b), it can be found that the range of local stress and strain values after the overload is much larger than that before the overload. Residual mean stresses are observed after the overload. The explanation is that in this case the low loading block is only 0.1% of total strain amplitude within the high-cycle fatigue regime keeping a rather low local cyclic plastic strain. Therefore a long persistent sequence memory effect in the following cycles is observed.

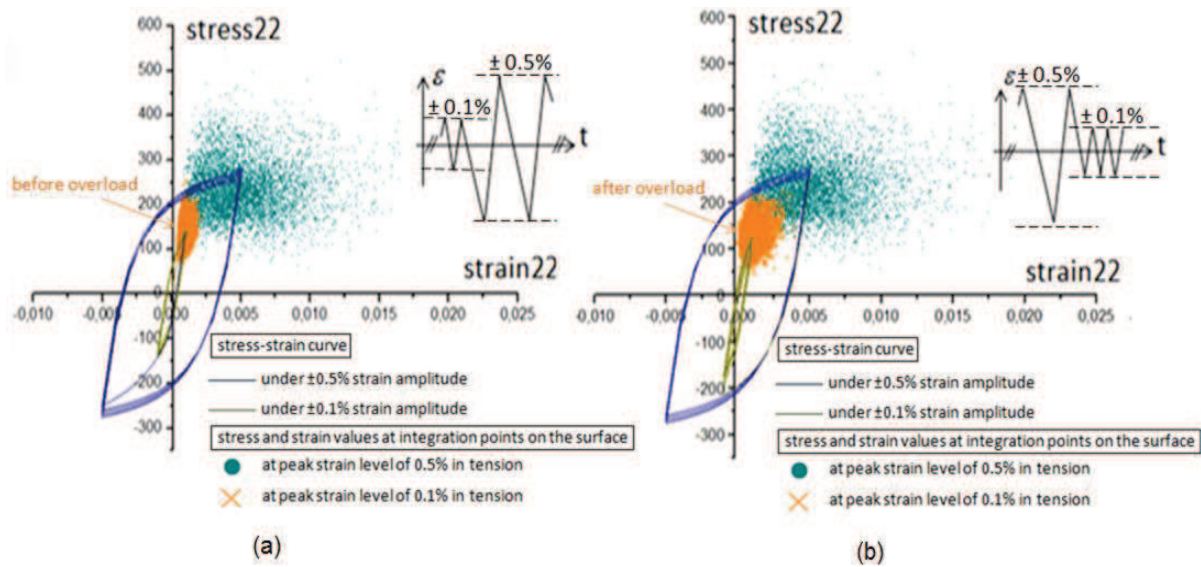


Figure 110 Cyclic stress-strain curves and surface local stress-strain distributions in tension peak under variable amplitude load spectrum, (a) $\Delta\epsilon_t/2$ from 0.1% to 0.5%, (b) $\Delta\epsilon_t/2$ from 0.5% to 0.1%

As residual stresses and memory effects are important in the case of load sequence 0.1%-0.5%-0.1%, the effect of the way of starting and end the overload block was checked. For this purpose, four different loading paths were considered, in which the overload block begins (or ends) either in tension or in compression. The results show that the sign of the first cycle of the overload block has no influence on local stress/strain distribution. However, the sign of the last cycle of the overload block is important. Even with the same loading amplitude, the local stress-strain distribution after the overload end in tension is different from the one end in compression.

This memory effect can also be seen on the hysteresis loops (Figure 111). When the overload block ends in compression, it can be seen in Figure 111b that the following mean stress is positive. On the contrary, a negative mean stress is seen if the overload block ends in tension (Figure 111a).

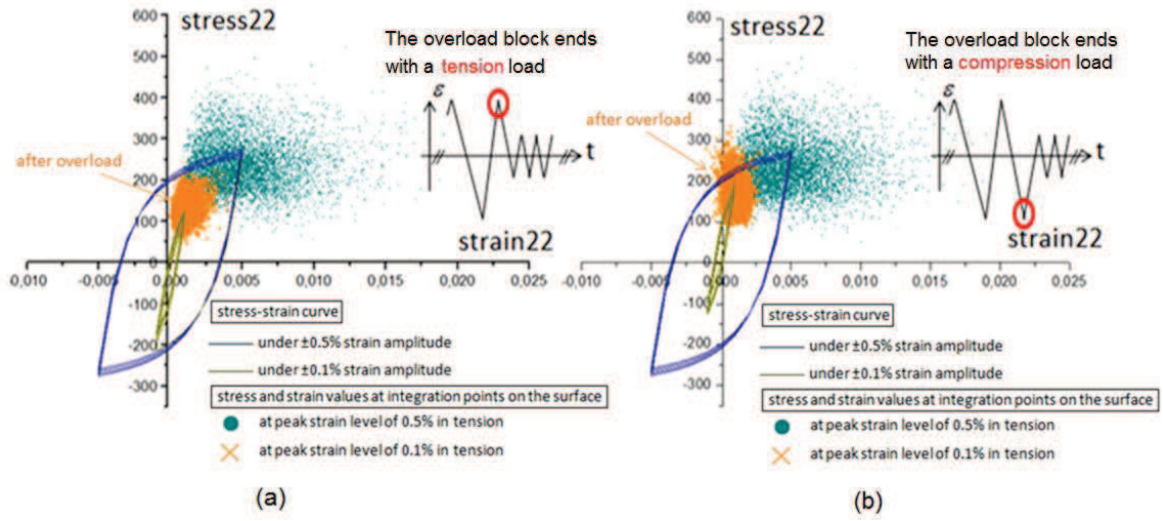


Figure 111 Stress-strain curves and surface local stress-strain distributions in tension peak while loading amplitude changing from 0.5% to 0.1% (a) overload block ends in tension (b) overload block ends in compression

The influence of the loading path can be seen more clearly on the strain and stress distribution as shown in Figure 112. After the overload with various loading paths, the aggregate shows different distributions of strain ϵ_{22} and stress σ_{22} in the surface layer elements.

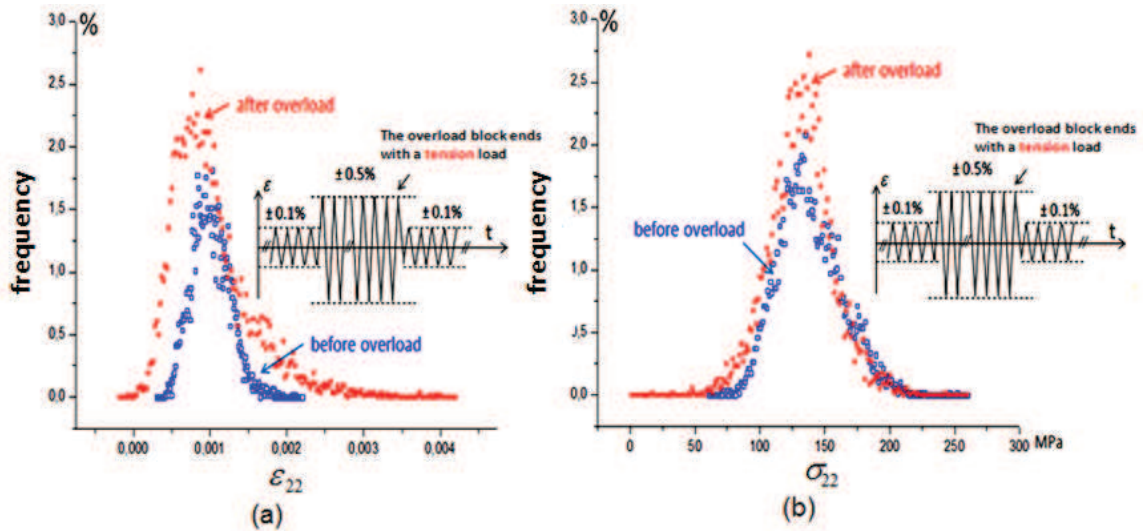


Figure 112 Distributions of local strain ϵ_{22} and stress σ_{22} in the surface layer elements before and after the overload when overload block ends in tension

Furthermore, the distributions of the strain ϵ_{22} are more heterogeneous after the overload than they were before (Figure 112a and Figure 113a). Standard deviation changes from 2.5×10^{-4} before the overload to 5.1×10^{-4} after the overload end in tension; and to 4.6×10^{-4} after the overload end in compression. In particular, it can be especially observed that the number of elements subjected to high strains increases significantly although the

mean stress value decreases as expected if the overload block ends in tension, which may tend to favor crack initiation (Figure 112a).

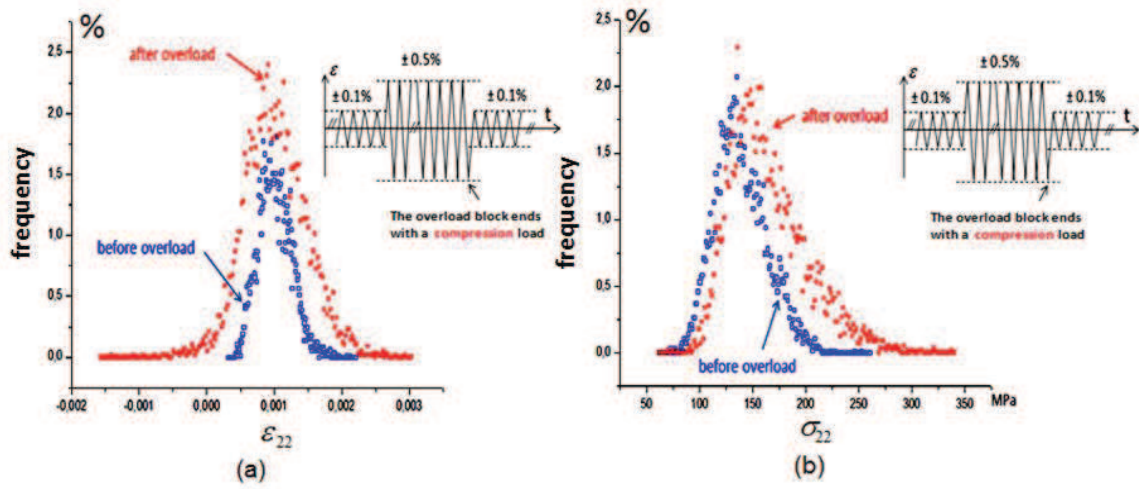


Figure 113 Distribution of local strain ϵ_{22} and stress σ_{22} on the surface layer elements before and after the overload when overload block ends in compression

Concerning the stress field σ_{22} , when the overload block ends in compression, the overload leads to an increase in the mean value of the stress distribution and in the stress heterogeneity (Figure 113b). Before the overload, the mean value of stress σ_{22} is equal to 137.8 MPa and the standard deviation is equal to 20.4 MPa. They reach respectively 162.9 MPa and 35.6 MPa after the overload end in compression. After the overload, the right tail moves to the right. On the contrary, when the overload block ends in tension, as shown in Figure 112b, the overload effect is not significant in terms of stress distribution. The right tail is not modified by the overload. The mean value of the stress and standard deviation after the overload are respectively 131.2 MPa and 24.4 MPa, which are not significantly different from that before the overload.

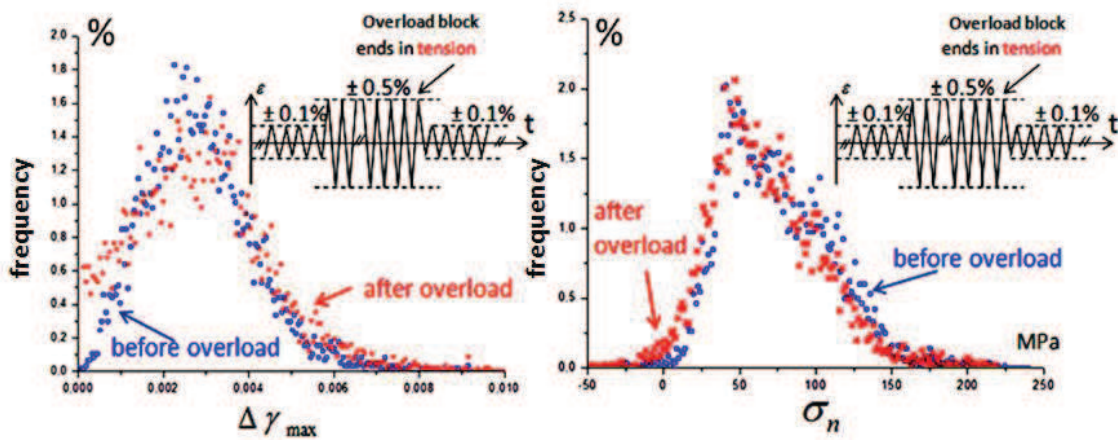


Figure 114 Comparison of the distribution of maximum shear on the 12 slip systems $\Delta\gamma_{max}$ and normal stress on the relevant slip plan σ_n in the surface layer elements before and after an overload when the overload block ends in tension

Furthermore, in agreement with a more “microscopic” point of view, the two factors in SF criterion are also calculated: maximum shear on the 12 slip systems $\Delta\gamma_{max}$ and the normal stress σ_n acting on the corresponding planes. The two cases in which overload block ends in tension and in compression, show that distributions of $\Delta\gamma_{max}$ keep almost the same mean value and standard deviation before and after the overload. From Figure 114 and Figure 115, it is found that the relative frequencies of the elements in which $\Delta\gamma_{max}$ values are greater than 0.005 increases a little after the overload block and the right tail of the $\Delta\gamma_{max}$ distribution moved to the right, which may favor crack initiation. Concerning the normal stress σ_n acting on the corresponding planes distribution, a big difference appears after the overload. When the overload block ends in compression, the mean value increases from 74,2MPa to 90.4MPa after the overload, and standard deviation changes from 35,2 MPa to 51.6 MPa. On the contrary, when the overload block ends in tension, almost no difference is observed after the overload.

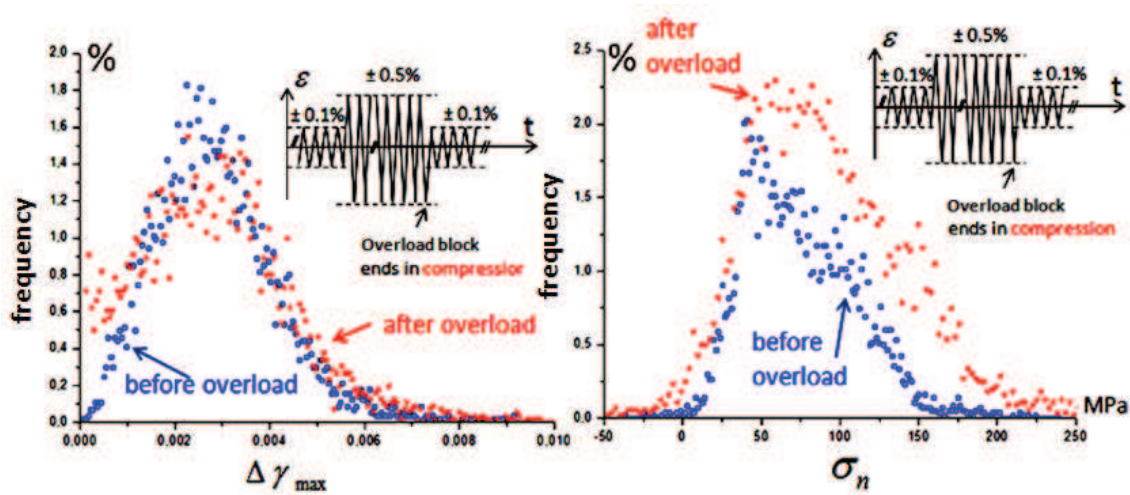


Figure 115 Comparison of the distribution of maximum shear on the 12 slip systems $\Delta\gamma_{max}$ and normal stress on the relevant slip plan σ_n in the surface layer elements before and after an overload when the overload block ends in compression

Function values of SF criterion calculated for the two loading methods and in different loading phases as shown in Figure 116. These values can directly reflect crack initiation. They show that when the overload block ends in compression, after the overload, the microcrack should occur earlier than when overload block ends in tension. And by comparison with the distribution of SF criterion function value before the overload, it can be seen that the overload end in tension is beneficial for the material as it should have a retardation effect on the crack initiation. But in case of overload block end in compression, even though the number of the elements having an SF criterion function value from 0.008 to 0.12 increases significantly compared to the ones before the overload, the maximum value remains almost the same. So it is hard to say if the overload end in compression is deleterious and it is not sure that this kind of overload should accelerate the occurrence of crack initiation.

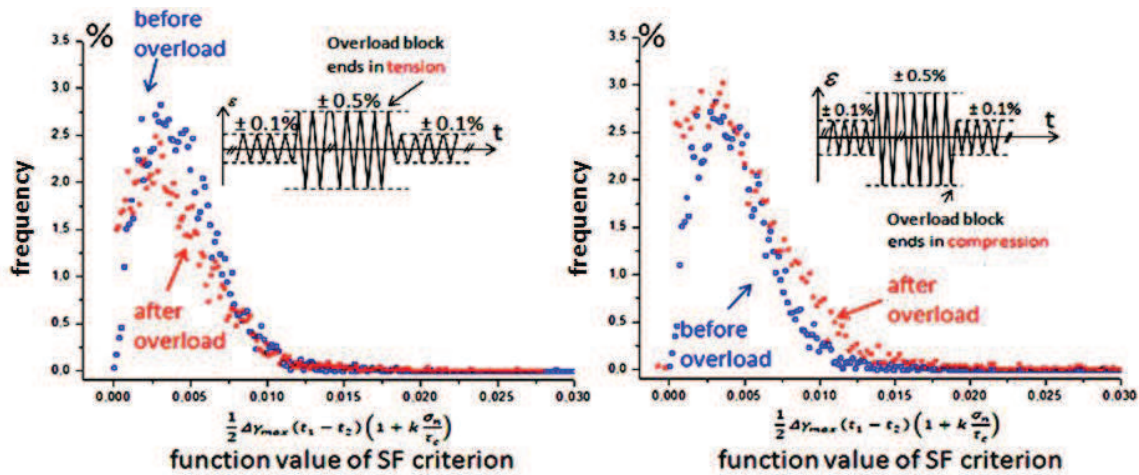


Figure 116 Comparison of distribution of function value of SF criterion in the surface layer elements before and after the overload when overload block ends (a) in tension and (b) in compression

5.3.2 Load-controlled

Because 304L stainless steel shows significant cyclic hardening/softening and strong deformation history effects in fatigue experiments and also found in other works [Turner 1975; Bayoumi and Ellatif 1995], the influence of overload on fatigue life are quite distinct under load or strain controlled tests [Fatemi and Colin 2010]. So the case of load-controlled fatigue will be presented in this section.

Load-controlled fatigue tests were conducted under a stress amplitude changing from ± 220 MPa to ± 320 MPa (overload) and back to ± 220 MPa. These stress levels of 220 and 320 MPa correspond to the midlife stress amplitudes of $\pm 0.3\%$ and $\pm 0.7\%$ of strain controlled test with a constant amplitude. These load-controlled fatigue tests have already been introduced in chapter 4.

5.3.2.1 Experimental results

Figure 117 shows the experimental results which give the relationship between the number of loading cycles and the corresponding number of cracks within the 4.5 mm^2 observation area on the specimen surface.

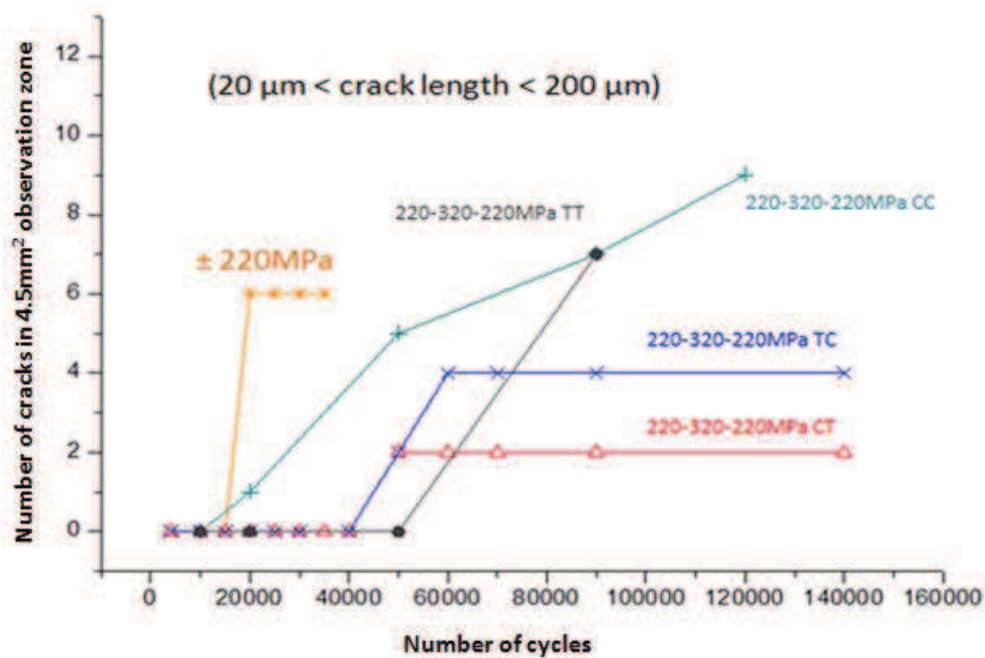


Figure 117 The relationship between the number of cracks on 4.5 mm² observation area of the specimen surface and the number of loading cycles under load-controlled amplitude loading.

It can be seen that overload retardation effects on crack initiation are obvious for all these four loading paths. However, within a dispersivity which remains to be considered, the starting and end signs of the overload block have no significant influence on the crack initiation life under the stress load spectra of 220-320-220 MPa. This is consistent with the fact that for these stress level values, cyclic plasticity after the overload is still large and memory effects should vanish rapidly.

It is worth noting that the test control mode has a strong influence on fatigue crack initiation life. Load-controlled tests presented much longer lives (6 to 9 times) than in strain-controlled tests. It can be explained by lower strain amplitude at the low level after the overload block [Fatemi and Colin 2010], which can also be seen clearly in the following numerical simulation results.

5.3.2.2 Simulation results

In this section, the numerical aggregate was subjected to the load spectra of 220-320-220 MPa. Before the overload block, the aggregate was cycled during 5 cycles under a stress amplitude of 220 MPa to get stabilization. And then the stress amplitude of 320 MPa (overload) is imposed from the 6th to the 8th cycle with four different loading paths as shown in section 4.1.3. Finally, after the overload, the stress amplitude goes back to 220 MPa until the 11th cycle.

From Figure 118, it can be seen that overload effects on the stress/strain curves are strongly dependent on the sign of the beginning and end of the overload block. In terms of

mean strain value after the overload, the third case, in which the overload block starts and ends both in compression, gives the smallest one with a compressive residual strain; the three other cases show a large positive residual strain value. However, the strain amplitudes after the overload are independent of the sign of the beginning and end of the overload block: during overload block, strain amplitude $\Delta\epsilon_{22}/2$ is equal to 0.0045 in all cases; and after the overload, it becomes 0.0015 in the four cases, which is slightly lower than the initial amplitude of 0.002 before the overload.

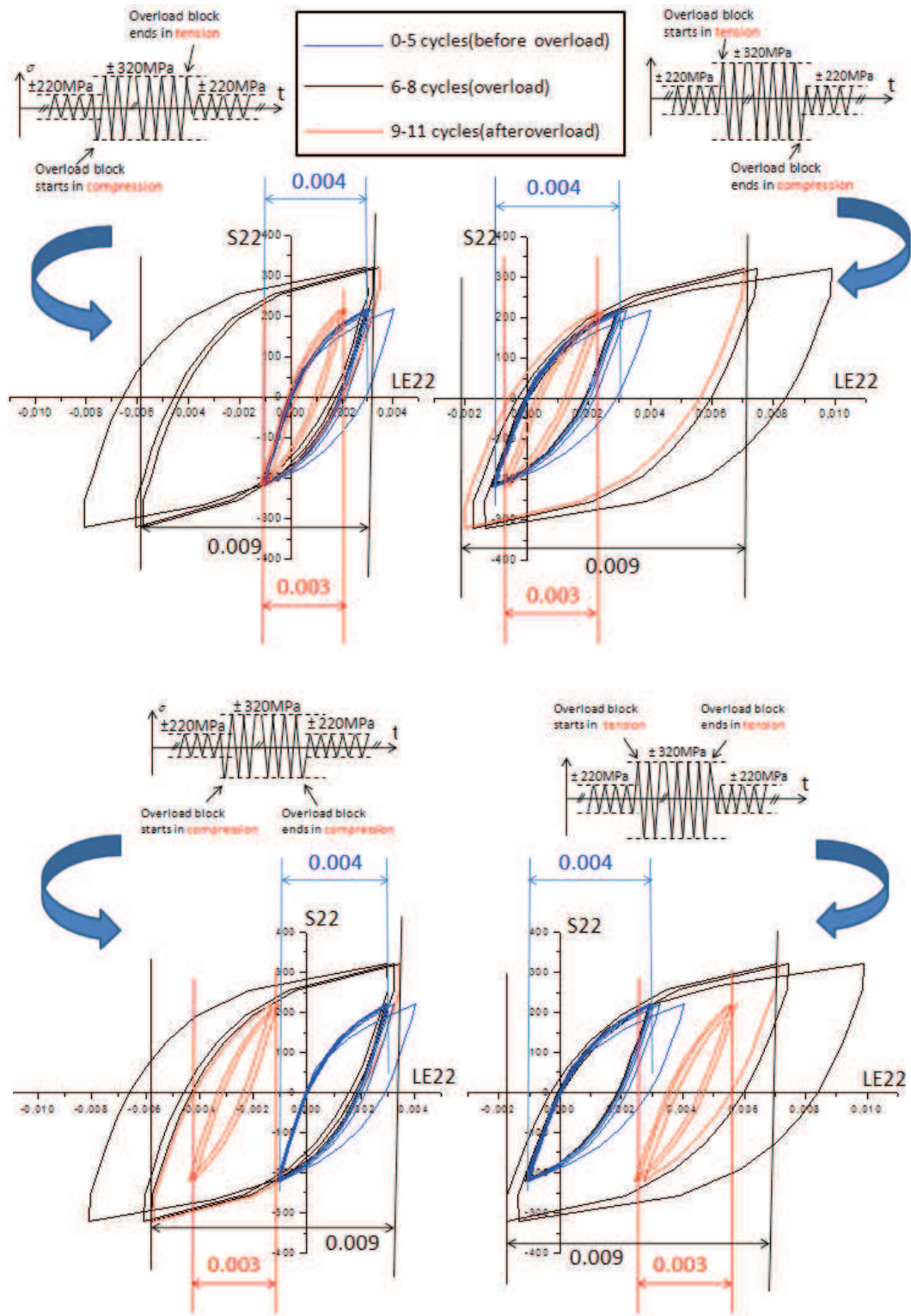


Figure 118 Stress/strain curves simulated under four different loading paths

Figure 119 to Figure 122 give the distributions of strain ϵ_{22} and stress σ_{22} values in the surface layer elements at the peak before and after overload. In all four loading paths, the stress distributions show little changes after the overload. So it can be concluded that, in these load-controlled spectra, the overload block and the sign of the beginning or end of

the overload have little or no influence on stress distribution. As quantitatively shown in Table 17, the mean value and standard deviation of the stress σ_{22} also show little change after the overload.

However, concerning the distributions of strain ε_{22} before and after overload under these four paths as shown in Figure 119 to Figure 122, the overload effect and the path effect are quite significant. First, in terms of standard deviation, it can be found that when the overload block starts and ends with the same sign of load (the beginning and end are both a tension load, or both a compression load), the local strain on the surface is more inhomogeneous after the overload than before (see Figure 121 and Figure 122). On the contrary, the standard deviation keeps almost the same value when the beginning and end of overload block are of opposite signs (see Figure 119 and Figure 120). Second, the mean strain value in all the elements at the free surface is influenced by the loading path. Analogously, the path effects on the mean strain value after the overload are more significant when the overload block starts and ends with the same load sign than when they are of opposite signs. In case 2, where the overload block starts in tension and ends in compression, there are almost no significant overload effect on the local stresses and strains.

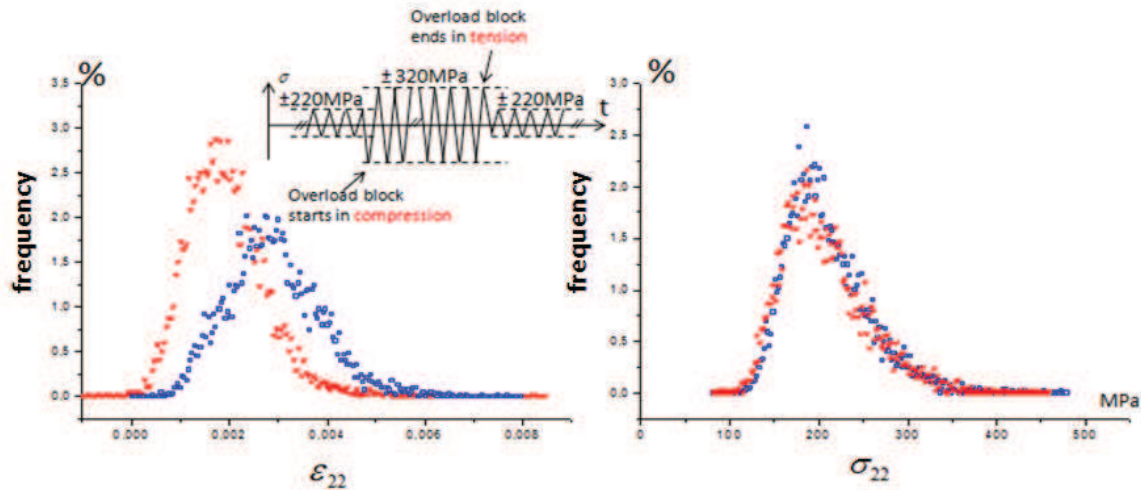


Figure 119 Distributions of strain ε_{22} and stress σ_{22} in the surface layer elements at peaks before and after the overload, loading path 1: overload block starts in compression and ends in tension.

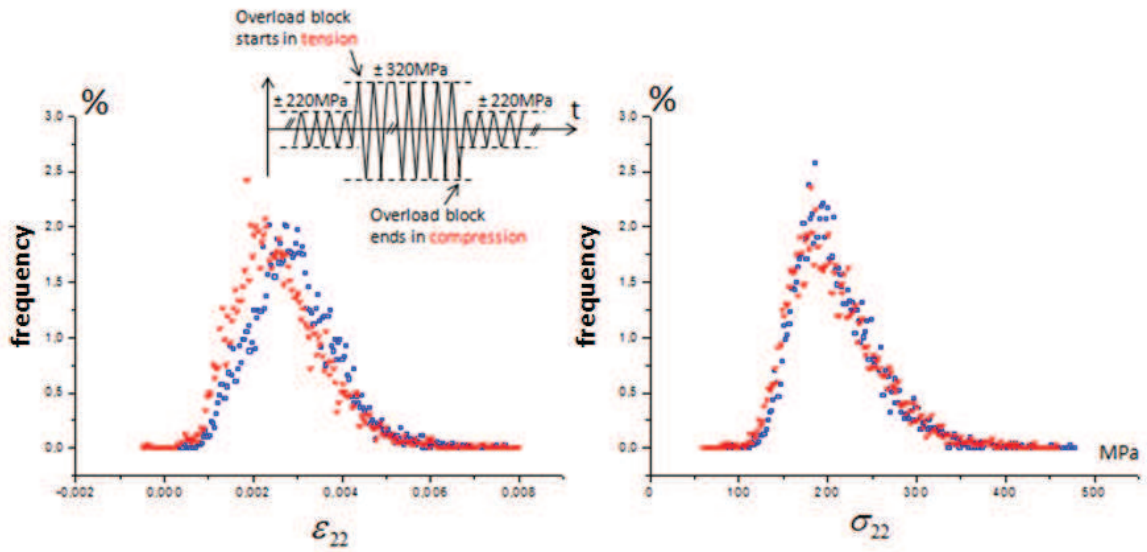


Figure 120 Distributions of strain ε_{22} and stress σ_{22} in the surface layer elements at peaks before and after the overload, loading path 2: overload block starts in tension and ends in compression.

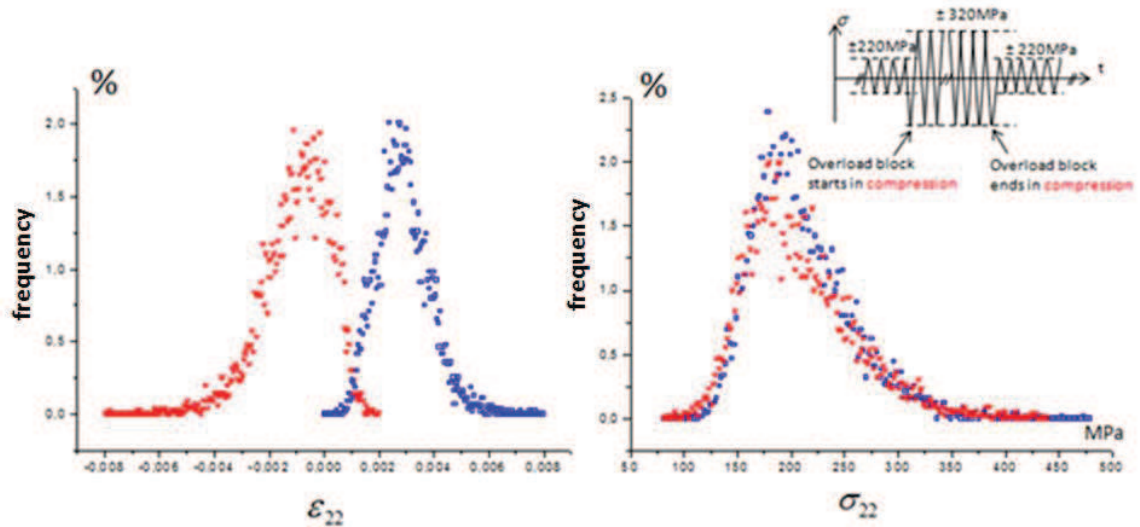


Figure 121 Distributions of strain ε_{22} and stress σ_{22} in the surface layer elements at peaks before and after the overload, loading path 3: overload block starts and ends both in compression.

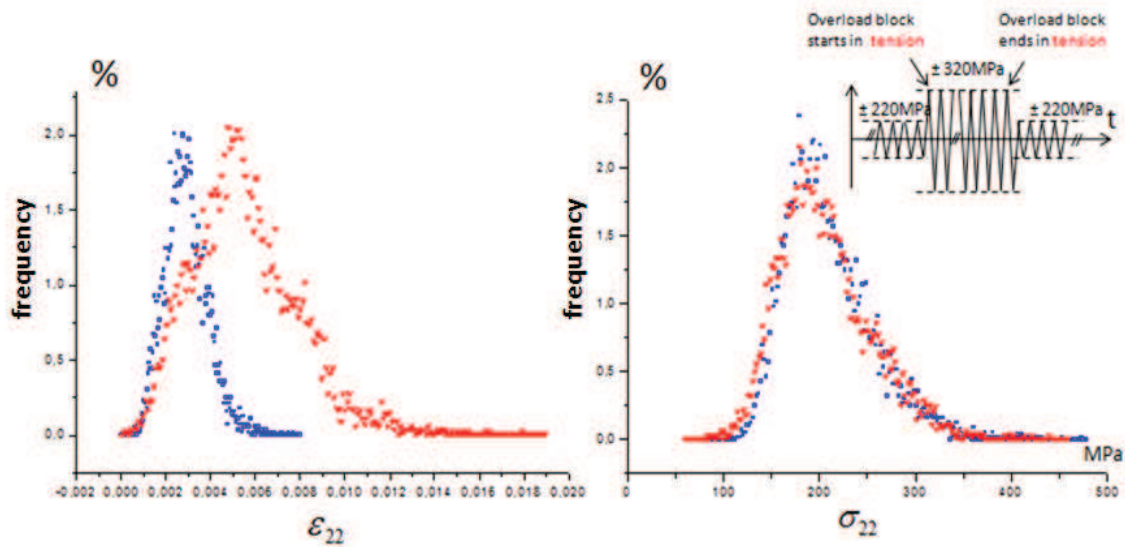


Figure 122 Distributions of strain ε_{22} and stress σ_{22} in the surface layer elements at peaks before and after the overload, loading path 4: overload block starts and ends both in tension.

According to classical fatigue criteria considering maximum strain, in the case of path 3 where the overload block starts and ends in compression, the overload should extend the crack initiation life because it causes a large decrease of the local strain on the surface. On the contrary, when the overload is imposed on the aggregate in the fourth path the tension-tension overload may lead to a shorter crack initiation life.

Table 17 Values of the local stress and strain in all the elements at free surface before and after the overload

	ε_{22}			
	Mean	Standard Deviation	Minimum	Maximum
Before overload	0,00291	9,35065E-4	4,79E-4	0,0077
After overload				
Path 1	0,00193	7,89032E-4	-0,00116	0,00823
Path 2	0,00257	9,73705E-4	-4,42E-4	0,00763
Path 3	-9,82661E-4	0,0012	-0,00783	0,00179
Path 4	0,00551	0,00231	1,73E-4	0,01794
	σ_{22} (MPa)			
	Mean	Standard Deviation	Minimum	Maximum
Before overload	209,12003	44,91816	92,17915	473,72385
After overload				
Path 1	205,69785	47,03383	89,43192	439,54276
Path 2	207,09976	48,98644	81,20264	456,29294
Path 3	207,54334	50,62898	85,03396	435,07297
Path 4	205,07619	46,78134	82,1906	438,75717

Figure 123 and Figure 124 give the results of the local strain and stress field at the free surface before and after the overload with the same color scale. As discussed above, it can be seen that the overload effects on the local strain distribution are significant. The local strain distributions after the overload do not only depend on the overload level but strongly depend on the starting and end of the overload block. For example, when the overload block starts and ends in tension, the level of local strain after the overload increases markedly. It means that the overload block in this path should favor crack initiation and lead to a shorter crack initiation life which is not supported by experimental evidence.

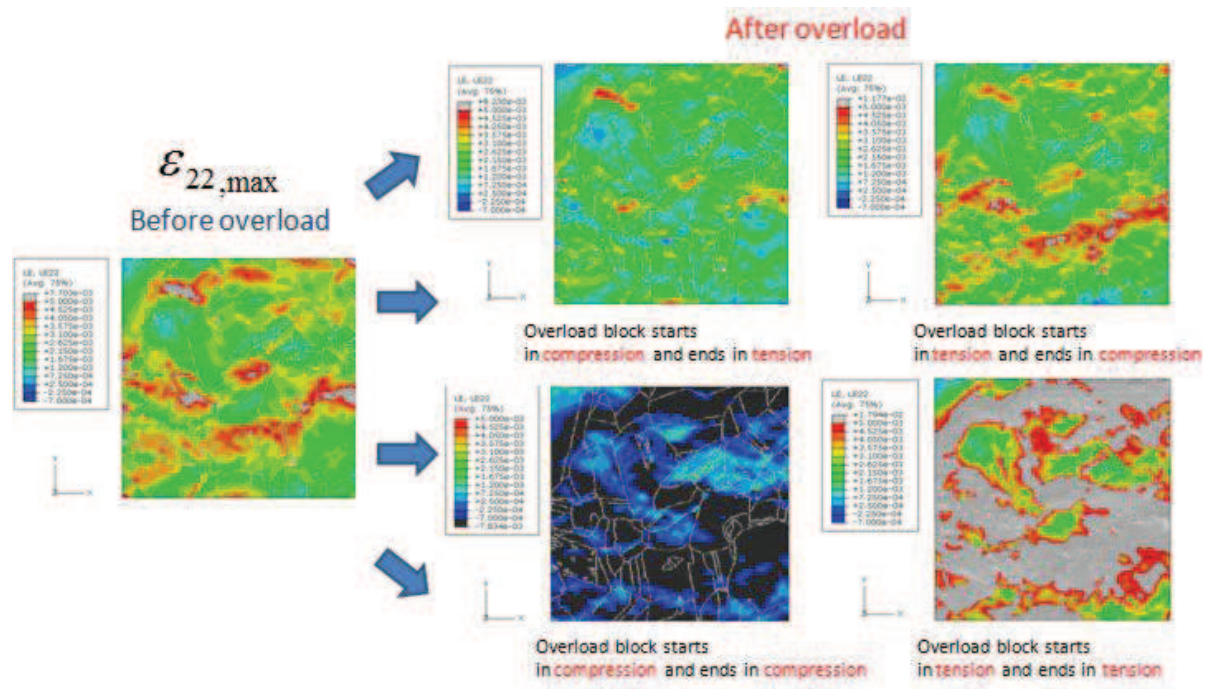


Figure 123 Field results of strain ϵ_{22} in the surface layer elements at peak before and after the overload, analysis of the four loading paths

In terms of local stress as shown in Figure 124, the field results show that the change of its distributions on the surface after the overload is small. So it can be concluded that the local strain and stress along loading axis are not good indicators for fatigue crack initiation criteria under variable stress amplitude at least in this case corresponding to low cycle fatigue.

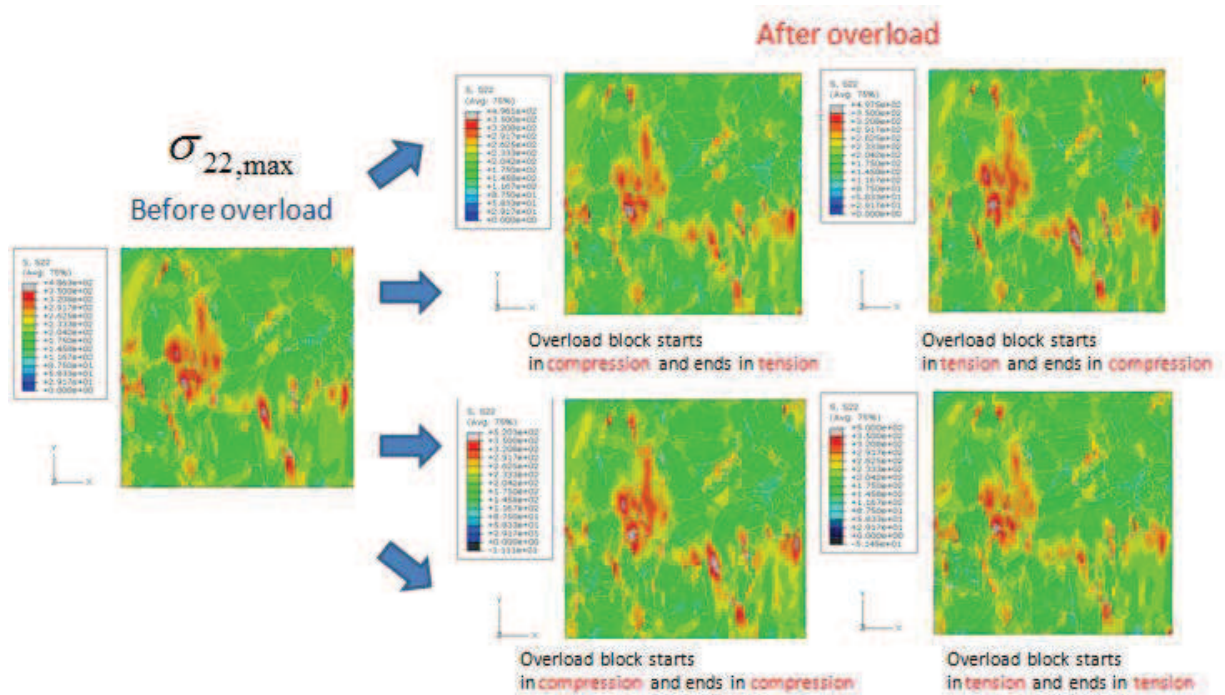


Figure 124 Field results of strain σ_{22} in the surface layer elements at peak before and after the overload, analysis of the four loading paths (same color scale)

Although the local strain is strongly influenced by the sign of the beginning and end of the overload block, the strain amplitudes were almost independent of the sign of the beginning and end of the overload block as shown in Figure 125. It can be seen that after the overload for all four loading paths, the level of strain amplitude of $\Delta\epsilon_{22}/2$ decreases significantly. The signs of the starting and end of overload block have almost no influence on $\Delta\epsilon_{22}/2$ fields after the overload. In means that the signs of the starting and end of overload block only influence the level of the mean strain.

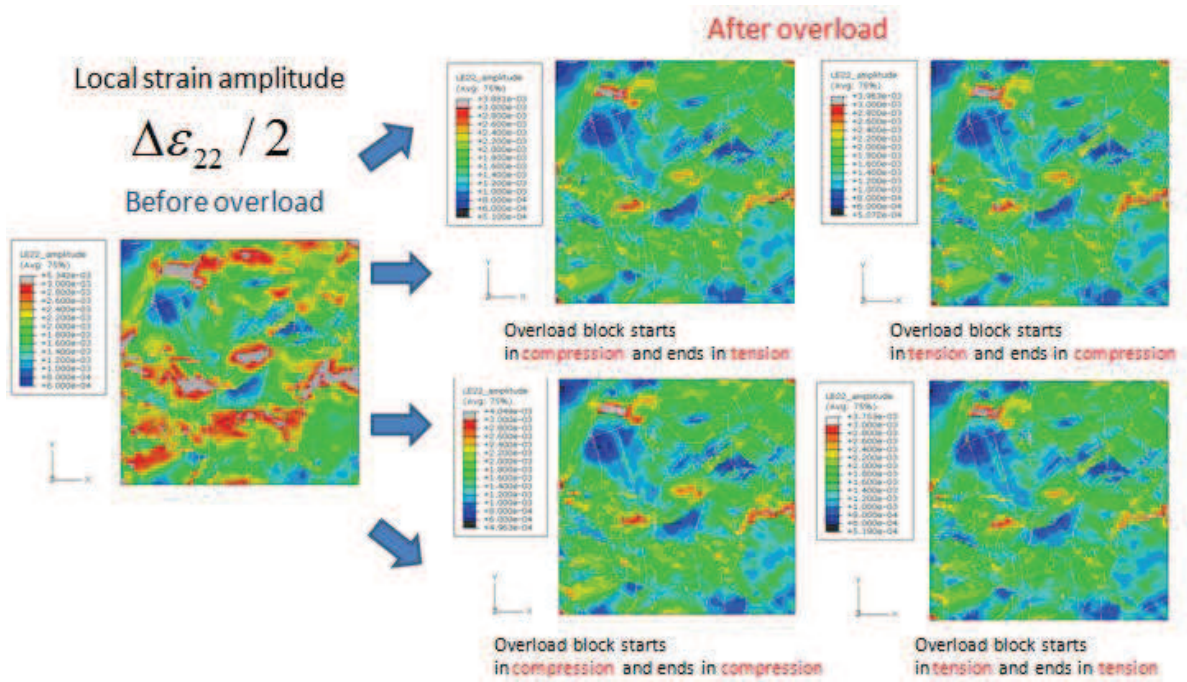


Figure 125 Field results of strain amplitude of $\Delta\epsilon_{22}/2$ in the surface layer elements before and after the overload, analysis of the four loading paths (same color scale)

Figure 126 gives the simulation fields of maximum shear strain amplitude on the 12 slip systems $\Delta\gamma_{\max}$ used in an SF criterion. After overload, the value of $\Delta\gamma_{\max}$ decreased remarkably independently of the signs of beginning and end of the overload block. Moreover, the second factor in an SF criterion, the normal stress on the corresponding plane (Figure 127) shows no difference between that before and after the overload and remains independent of the signs of starting and end load in the overload block. These results mean that the overload block in the load spectra of 220-320-220 MPa can lead to retarded crack initiation whatever the signs of the starting and end of the overload applied in overload block. So the prediction results according to Socie and Fatemi (SF) criterion are in good agreement with experiments (Figure 117).

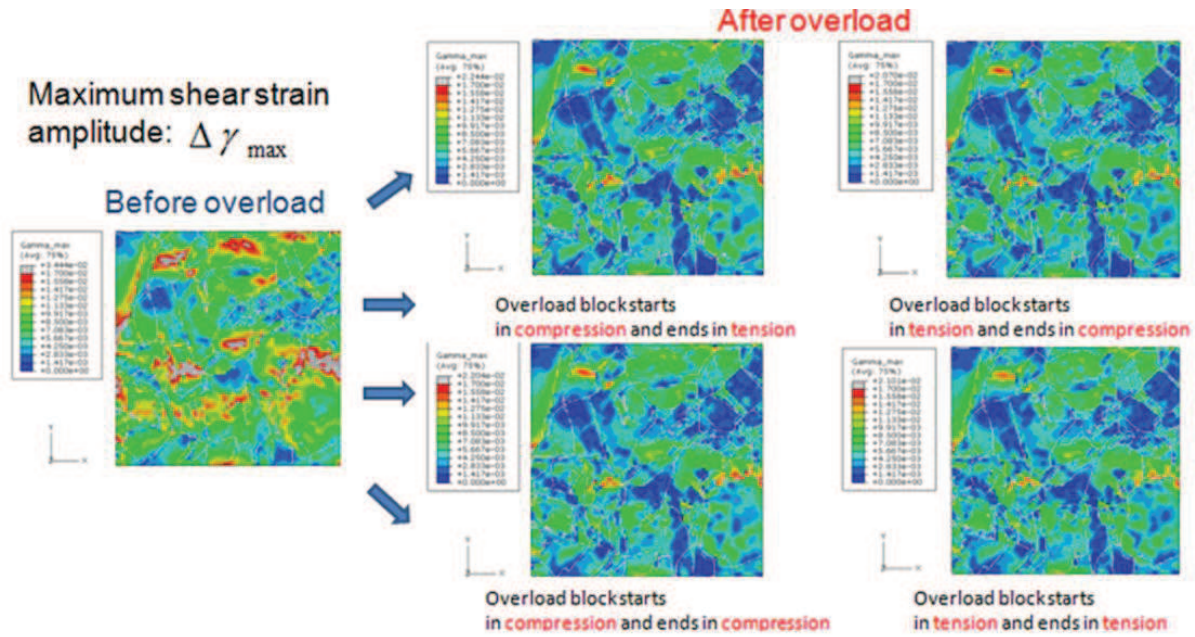


Figure 126 Maximum shear strain amplitude fields before and after the overload with four different loading paths (same color scale)

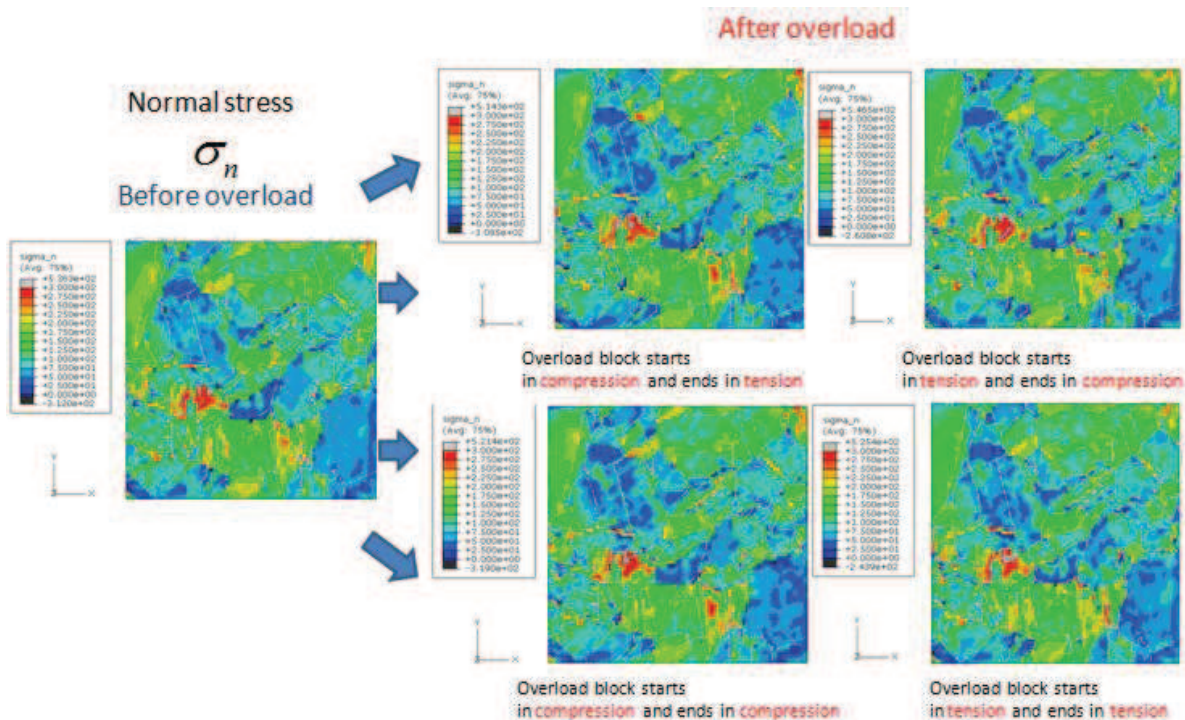


Figure 127 Fields results of normal stress on corresponding plane before and after the overload with four different loading paths (same color scale)

5.4 Conclusions

In this chapter, a finite element model using crystalline plasticity was used under various variable amplitude cyclic load spectra. Both load- and strain-controlled fatigue tests were considered to study the overload effects on cyclic plasticity. The analysis of the simulation results gave the following conclusions:

In the case of strain-controlled fatigue, two loading sequences were studied and compared: $\pm 0.3\%-0.7\%-0.3\%$ and $\pm 0.1\%-0.5\%-0.1\%$. The residual stress and strain maps after the overload were compared to the initial ones. It was found that the memory effect depends on the amplitude level of the low amplitude block. When the strain amplitude changes from $\pm 0.7\%$ to $\pm 0.3\%$, the memory effect is transient and vanishes rapidly because of the high level of plasticity acting at 0.3% . On the contrary, in the case of strain amplitude decreasing from $\pm 0.5\%$ to $\pm 0.1\%$, the residual stresses and strains do not vanish and the memory effect is significant. It depends also on the end sign of the last cycle in the overload block. Two fatigue tests were performed under strain-controlled amplitude. One specimen was subjected to a load spectrum of $\pm 0.3-0.7-0.3\%$ and the other one was subjected to constant strain amplitude of $\pm 0.3\%$. By comparison of simulation with the experimental results which show little difference on crack initiation, only plastic shear strain amplitude $\Delta\gamma_{\max}$ shows good capability to predict overload effects under this load spectrum of $\pm 0.3-0.7-0.3\%$.

In the other case of load-controlled fatigue, the constant amplitude fatigue tests were conducted under stress amplitude of ± 220 MPa and the variable amplitude tests were performed under stress amplitude of $\pm 220-320-220$ MPa with four different loading paths. These stress levels of 220 and 320 MPa correspond to the midlife stress amplitudes of $\pm 0.3\%$ and $\pm 0.7\%$ strain-controlled tests with the constant amplitude. The experimental results show that overload retardation effects on fatigue crack initiation are remarkable and the same for all four loading paths. The starting and end signs of the overload block have no influence on crack initiation. Furthermore, it was found that the test control mode has a significant influence on fatigue crack initiation life. Load-controlled tests presented much longer lives (6 to 9 times) than strain-controlled test due to lower strain amplitude at the low level after the overload block.

In terms of numerical simulations, the field results of the local axial stress and strain, maximum shear strain amplitude on the 12 slip systems and normal stress on the corresponding slip plane were computed and analyzed. Their capabilities to predict overload effect on crack initiation under variable amplitude loading condition were evaluated with regard to experimental results which show a strong retardation effect in all cases. The local axial strain and stress field results show they are not good indicators for fatigue crack initiation criteria under variable stress amplitude of $\pm 220-320-220$ MPa. However, the prediction results based on Socie and Fatemi (SF) are in much better agreement with our experiments. The maximum plastic shear strain amplitude on the 12 slip systems $\Delta\gamma_{\max}$ used in SF criterion in particular shows good capabilities to predict overload effects under variable stress amplitude of $\pm 220-320-220$ MPa.

Conclusions and perspectives

The purpose of this work was to study cyclic plasticity and microcrack initiation in a 304L stainless steel under constant and variable amplitude loading in order to propose a numerical polycrystal simulation method to evaluate the mechanical quantities which can control crack initiation at the grain scale and to study the variable amplitude loading effects on cyclic plasticity and microcrack initiation.

Main points of this work are listed as follows:

1. Modeling of the fatigue cyclic hardening/softening behavior of 304L based on a finite element model of crystal plasticity.
2. Considering a representative volume of 304L steel, with details of realistic grain morphology and crystallographic orientation in order to:
 - simulate of micromechanical behavior of 304L steel;
 - compare with the experimental surface observation;
 - study the microstructure effect on fatigue crack initiation;
 - evaluate the crack initiation predictive capabilities of some mechanical factors in fatigue criteria.
3. This finite element model of crystal plasticity was also used to:
 - study fatigue test mode (strain-controlled, load-controlled) effects on cyclic plasticity and fatigue crack initiation under variable amplitude loading conditions;
 - study loading history effects on cyclic plasticity and fatigue crack initiation under different fatigue regime (low or high cycle fatigue).

For this purpose, some experimental studies have been done:

4. Experimental study of the cyclic behavior of 304L under constant and variable amplitude loading;
5. Experimental observation and analysis of the crack initiation sites at grain scale;
6. Experimental analysis of the influence of the different fatigue loading conditions on the crack initiation.

In the first chapter, some important points of fatigue studies in literature were reviewed in particular for 304L, such as its macroscopic cyclic stress- strain response and evolution of dislocation microstructure during cyclic loading. It was noted that stage I microcrack propagation is observed in 304L both in high cycle fatigue and in low cycle fatigue. Crack initiation and stage I crack propagation are strongly affected by microstructures and environments that tend to concentrate slip and affect slip reversibility. Last, the research status of an open problem, fatigue behavior under variable amplitude loading was reviewed and discussed.

In order to predict cyclic plasticity and mechanical factors affecting fatigue crack initiation and fatigue life, such as plastic cyclic shear strain amplitude more accurately through numerical simulation, the fatigue cyclic hardening and softening behavior of

materials had to be studied and the cyclic microstructure evolution must be implemented in the code. In the third chapter, CristalECP was enriched in order to describe the cyclic hardening/softening on the basis of slip lines formation and the evolution of dislocation densities on slip systems. The simulation results of cyclic hardening/softening curves are in good agreement with experiments under two strain amplitude loadings of $\pm 0.3\%$ and $\pm 0.5\%$. The results show that it is possible to simulate the fatigue cyclic hardening/softening behavior based on a finite element model of crystal plasticity. Through the comparison with results obtained not considering cyclic softening, it shows that although the model not considering cyclic hardening/softening behavior can give good predictive results of macroscopic stress-strain loops at stabilized cycle, the peak mechanical values within certain grains cannot be simulated correctly, which will give nonconservative predictive results for crack initiation. It can be concluded that it is of importance to take into account the real stress-strain history for accurately predicting local strain heterogeneities and strain life.

In terms of fatigue experiments, both load-controlled and strain-controlled test modes were considered. Load-controlled fatigue tests were conducted under constant amplitude loadings of ± 220 MPa and ± 260 MPa as well as under variable amplitude loading of ± 220 -320(overload)-220 MPa. Four different loading paths were considered in variable amplitude tests, with differing signs of beginning and end of the overload block (CT, TC, CC and TT). Total strain-controlled fatigue tests were conducted under variable amplitude load spectrum of ± 0.3 -0.7-(overload)-0.3%, which were compared to constant amplitude loading of $\pm 0.3\%$. These stress levels of 220 and 320 MPa used here correspond to the midlife stress amplitudes of $\pm 0.3\%$ and $\pm 0.7\%$ constant amplitude strain-controlled tests. The microscopic sites of fatigue crack initiation at grain size scale were observed. Under these loading conditions, four kinds of crack initiation sites were sorted out: inclusions, grain boundaries (GB), slip lines (SLs) and at locations where the GB and SLs (GB-SLs) interact.

Concerning numerical simulations, in the fourth chapter, three 3D numerical aggregates with realistic crystallographic orientations issued from successive EBSD maps in 304L steel were constructed and used to simulate micromechanical behavior of 304L steel and to study the microstructure effect on fatigue crack initiation. The simulation results were compared to experimental observations to evaluate the crack initiation predictive capabilities of the main mechanical factors used in fatigue criteria. Under constant ± 220 MPa stress amplitude, among these micromechanical factors, maximum shear strain amplitude and microscopic dissipated energy were found to provide comparable levels of predictive ability. The Socie-Fatemi criterion also showed good correlation and sensitivity to experimental crack initiation sites.

In the fifth chapter, the numerical polycrystalline aggregate was used to simulate the local cyclic mechanical fields under various loading conditions to study the variable amplitude loading effects on cyclic plasticity and microcrack initiation in 304L austenitic stainless steel. Both load- and strain-controlled fatigue tests were considered in this work. In the case of strain-controlled fatigue, two loading sequences were studied and compared: $\pm 0.3\%$ -0.7%-0.3% and $\pm 0.1\%$ -0.5%-0.1%. It is found from numerical results that the

memory effects are different under these two load spectra and they depend on the amplitude level of the low amplitude block. In the case when the strain amplitude changes from 0.7% to 0.3% which is still a high level, the memory effect is transient and vanishes rapidly. On the contrary, when the strain amplitude decreases from 0.5% to 0.1%, the residual stress and strain do not vanish and the memory effect is significant. This effect is also dependent on the sign of the last cycle in the overload block. Under a load spectrum of ± 0.3 -0.7-0.3%, through comparison of the simulation with the experimental results which show little difference on crack initiation, only plastic shear strain amplitude $\Delta\gamma_{\max}$ shows good capability to predict overload effects rather than local uniaxial strain and stress value at top of the cycle.

In the case of load-controlled fatigue, under load spectra of ± 220 -320-220 MPa, the experimental results show that overload retardation effects on fatigue crack initiation are remarkable and the same for all four loading paths but differ with signs of beginning and end of the overload block (CT, TC, CC and TT). The beginning and end signs of the overload block seem to have no significant influence on crack initiation. Furthermore, it was also found that the test control mode has a significant influence on fatigue crack initiation. Load-controlled tests presented much longer lives (6 to 9 times) than strain-controlled tests due to lower strain amplitude at the low level after the overload block. Simulation results show that the maximum plastic shear strain amplitude on the 12 slip systems $\Delta\gamma_{\max}$ used in Socie-Fatemi criterion shows especially good capabilities to predict overload effects under variable stress amplitude loading of ± 220 -320-220 MPa.

Perspectives

In this study, the process of numerical modeling and the results were mainly used to understand the microstructural effects on cyclic plasticity and crack initiation, and to try to find a methodology to assess which kind of “macroscopic” or microscopic” criterion can be the most representative for the given material and specific loading conditions (e.g. periodic, test control mode...). In the future, there are also several studies that can be proposed to continue along the current one:

Concerning 3D aggregate:

First, as mentioned in chapter 1, stage I microcrack propagation is strongly influenced by microstructure. Its propagation mechanism is still not well understood because it is influenced by the local stress/strain, grain orientation or slip lines orientation and so on. The microcracks observed in the actual specimen could be taken into account in the numerical aggregate to better study crystallographic orientation effect on microcrack propagation. For this purpose, a microcrack propagation law has therefore to be considered.

Second, in order to obtain the spatial distribution of the microstructure in the RVE, a serial sectioning method was used in our work, and the microstructure of the aggregate was simply extruded from layer to layer through the third direction leading to a “rough” description of grain boundary geometry. In future works, an improved meshing method should be developed to better describe 3D microstructure as well as, if needed, to involve

particular elements to take into account imperfect grain boundaries, which are not considered in this current work. Such an improved aggregate could be used to study chemical segregation, grain boundary crack initiation and propagation, 3D microcrack modelling and so on. Moreover, inclusions could also be taken into account with their specific properties of elasticity and critical fracture stress.

Concerning CristalECP code:

In this work, a nonlinear kinematic hardening rule has been chosen in the usual classic form initially proposed by Armstrong and Frederick [Armstrong and Frederick 1966] in which only two material parameters were considered. In future work, the kinematic back stress could be better described based on dislocation theory and dislocation dynamics simulations, for example, based on the work of [Manole, Depres and Tabourot 2009; Manole, Depres and Tabourot 2009].

According to Mughrabi [Mughrabi 1978; Mughrabi 1983], cyclic softening was described on the basis of the evolution of dislocation densities in walls and channels on the 12 slip systems with different dislocation hardening laws. In future work, it could be also possible to consider cyclic softening due to the evolution of the distance of dislocation annihilation within channels during cyclic loading.

Concerning loading conditions:

Due to the long duration of the experiments, it is not easy to investigate more variable amplitude loadings. However, it could be interesting to conduct fatigue tests under other loading conditions for enriching the fatigue crack initiation data base, especially for load spectrum of 0.1-0.5-0.1% for which simulation shows significant overload memory effect. Then the experimental results could be compared with simulation results presented in this work. However, the large scatter of high cycle experiments will have to be taken into account.

Furthermore, multiaxial non-proportional fatigue is also a difficult problem due to the complex stress states, loading histories and different possible orientations of the initial crack in the components. Therefore, multiaxial fatigue is still an open problem in the material and mechanics field. Considering the difficulties of multiaxial experiments [Rupil, Raka, Vincent, Desmorat, Le-roux, Courtin and HILD 2011], numerical modeling method could be applied to study multiaxial cyclic plasticity and crack initiation under constant or variable amplitude loading within 3D numerical aggregates.

Concerning crack initiation life prediction:

Some of the crack initiation sites were observed at GBs and inclusions, for which most of local fatigue criteria are not adequate and cannot be applied. It could be interesting to develop a specific criterion or adapt from an existing criterion on the basis of comparison between simulated local mechanical field values (such as normal stress on GB) and observed crack initiation life.

Furthermore, the distribution of local mechanical fields of factors and functional values of fatigue criteria obtained from this model could be used to calculate and analyze the scatter of fatigue crack initiation life [Doudard, Hild and Calloch 2007; Malésys, Vincent and Hild 2009; Rupil, Vincent, Roux and Hild 2011] in order to implement statistical crack initiation laws in fatigue modeling of short and long cracks.

References

- Abdul-Latif, A. (2004). "A comparison of two self-consistent models to predict the cyclic behavior of polycrystals." *Journal of Engineering Materials and Technology-Transactions of the Asme* 126: 62-69.
- Ahmadi, A. and H. Zenner (2006). "Lifetime simulation under multiaxial random loading with regard to the microcrack growth." *International Journal of Fatigue* 28(9): 954-962.
- Akahori, T., M. Niinomi and A. Ozeki (1998). "Effect of microstructure on small fatigue crack initiation and propagation characteristics of Ti-6Al-7Nb alloy." *Journal of the Japan Institute of Metals* 62(10): 952-960.
- Alain, R., P. Violan and J. Mendez (1997). "Low cycle fatigue behavior in vacuum of a 316L type austenitic stainless steel between 20 and 600 degrees C .1. fatigue resistance and cyclic behavior." *Materials Science and Engineering a-Structural Materials Properties Microstructure and Processing* 229(1-2): 87-94.
- Amiable (2006). "Prédiction de durée de vie de structures sous chargement de fatigue thermique." Thèse de doctorat de l'Université de Versailles.
- Amiable, S., S. Chapuliot, A. Constantinescu and A. Fissolo (2006). "A comparison of lifetime prediction methods for a thermal fatigue experiment." *International Journal of Fatigue* 28(7): 692-706.
- Armas, A. F., C. Petersen, R. Schmitt, M. Avalos and I. Alvarez-Armas (2002). "Mechanical and microstructural behaviour of isothermally and thermally fatigued ferritic/martensitic steels." *Journal of Nuclear Materials* 307-311(Part 1): 509-513.
- Armstrong, P. J. and C. O. Frederick (1966). A mathematical representation of the multiaxial baushinger effect. Berkeley, Nuclear Laboratories.
- Babout, L., T. J. Marrow, D. Engelberg and P. J. Withers (2006). "X-ray microtomographic observation of intergranular stress corrosion cracking in sensitised austenitic stainless steel." *Materials Science and Technology* 22(9): 1068-1075.
- Baffie, N., J. Stolarz and T. Magin (2000). "Influence of strain-induced martensitic transformation on fatigue short crack behaviour in an austenitic stainless steel." *Matériaux et Techniques* 5-6: 57-64.
- Barbe, F., L. Decker, D. Jeulin and G. Cailletaud (2001). "Intergranular and intragranular behavior of polycrystalline aggregates. Part 1: FE model." *International Journal of Plasticity* 17(4): 513-536.

- Barbe, F., S. Forest and G. Cailletaud (2001). "Intergranular and intragranular behavior of polycrystalline aggregates. Part 2: Results." *International Journal of Plasticity* 17(4): 537-563.
- Basu, K., M. Das, D. Bhattacharjee and P. C. Chakraborti (2007). "Effect of grain size on austenite stability and room temperature low cycle fatigue behaviour of solution annealed AISI 316LN austenitic stainless steel." *Materials Science and Technology* 23(11): 1278-1284.
- Bayoumi, M. R. and A. K. A. Ellatif (1995). "Characterization of Cyclic Plastic Pending of Austenitic Aisi-304 Stainless-Steel." *Engineering Fracture Mechanics* 51(6): 1049-1058.
- Bjerken, C. and S. Melin (2003). "A tool to model short crack fatigue growth using a discrete dislocation formulation." *International Journal of Fatigue* 25(6): 559-566.
- Bjerken, C. and S. Melin (2004). "A study of the influence of grain boundaries on short crack growth during varying load using a dislocation technique." *Engineering Fracture Mechanics* 71(15): 2215-2227.
- Blom, A. E., A. Hedlund, W. Zhao, A. Fathalla, B. Weiss and R. Stickler (1985). "Short fatigue crack growth in Al 2024 and Al 7475. Behaviour of Short Fatigue Cracks, Symp., Sheffield. EGF 1, MEP (1986)."
- Bodelot, L., L. Sabatier and E. Charkaluk (2009). "Experimental setup for fully coupled kinematic and thermal measurements at the microstructure scale of an AISI 316L steel." *Materials Science and Engineering: A* 501(1-2): 52-60.
- Breedis, J. F. and W. D. Robertson (1962). "The martensitic transformation in single crystals of ironchromium-nickel alloys " *Acta Metallurgica* 10: 1077-1088.
- Brinckman, S. and E. Van der Giessen (2007). "A fatigue crack initiation model incorporating discrete dislocation plasticity and surface roughness." *International Journal of Fracture* 148(2): 155-167.
- Broom, T. and R. K. Ham (1957). "The Hardening and Softening of Metals by Cyclic Stressing." *Proceedings of the Royal Society of London Series a-Mathematical and Physical Sciences* 242(1229): 166-179.
- Bullen, W. P., A. K. Head and W. A. Wood (1953). "Structural changes during the fatigue of metals." *Proc. Roy. Soc A* 216.
- Cailletaud, G. (1992). "A Micromechanical Approach to Inelastic Behavior of Metals." *International Journal of Plasticity* 8(1): 55-73.
- Cedat, D., M. Libert, M. L. Flem, O. Fandeur, C. Rey, M. Clavel and J.-H. Schmitt (2009). "Experimental characterization and mechanical behaviour modelling of molybdenum-titanium carbide composite for high temperature applications." *International Journal of Refractory Metals and Hard Materials* 27(2): 267-273.

-
- Chevalier, L., S. Calloch, F. Hild and Y. Marco (2001). "Digital image correlation used to analyze the multiaxial behavior of rubber-like materials." *European Journal of Mechanics a-Solids* 20(2): 169-187.
- Choe, B. H. and H. C. Lee (1995). "Cyclic Softening and Hardening Behavior of a Nickel-Base Superalloy." *Scripta Metallurgica Et Materialia* 32(8): 1283-1287.
- Coffin, L. F. (1954). "A Study of the Effects of Cyclic Thermal Stresses on a Ductile Metal." *Transactions of ASME*.
- Constantinescu, A., E. Charkaluk, G. Lederer and L. Verger (2004). "A computational approach to thermomechanical fatigue." *International Journal of Fatigue* 26(8): 805-818.
- Cunat, P.-J. (2003). "Aciers Inoxydables : critères de choix et structure." *Les techniques de l'ingénieur M 4 540*.
- Curtit, F. (2007). "Description and evaluation of fatigue criteria under random multiaxial stress." EDF report 67.
- Daneshpour, S., M. Kocak, S. Langlade and M. Horstmann (2009). "Effect of overload on fatigue crack retardation of aerospace Al-alloy laser welds using crack-tip plasticity analysis." *International Journal of Fatigue* 31(10): 1603-1612.
- Demulsant, X. and J. Mendez (1995). "Microstructural effects on small fatigue crack initiation and growth in Ti6Al4V alloys." *Fatigue & Fracture of Engineering Materials & Structures* 18(12): 1483-1497.
- Depres, C. (2004). *Modelisation physique des stades precursurs de l'endommagement en fatigue dans l'acier inoxydable austenitique 316L*. Thèse de doctorat. Grenoble, Institut Polytechnique de Grenoble.
- Depres, C., M. Fivel and L. Tabourot (2008). "A dislocation-based model for low-amplitude fatigue behaviour of face-centred cubic single crystals." *Scripta Materialia* 58(12): 1086-1089.
- Depres, C., C. F. Robertson and M. C. Fivel (2004). "Crack initiation in fatigue: experiments and three-dimensional dislocation simulations." *Materials Science and Engineering a-Structural Materials Properties Microstructure and Processing* 387-89: 288-291.
- Deshpande, V. S., A. Needleman and E. Van-Der-Giessen (2003). "Discrete dislocation plasticity modeling of short cracks in single crystals." *Acta Materialia* 51: 1-15.
- Devincere, B., L. Kubin and T. Hoc (2006). "Physical analyses of crystal plasticity by DD simulations." *Scripta Materialia* 54(5): 741-746.
- Devincere, B. and L. P. Kubin (1997). "Mesoscopic simulations of dislocations and plasticity." *Material Science and Engineering* 234-236: 8-14.

- Dobrich, K. M., C. Rau and C. E. Krill (2004). "Quantitative characterization of the three-dimensional microstructure of polycrystalline Al-Sn using X-ray microtomography." *Metallurgical and Materials Transactions a-Physical Metallurgy and Materials Science* 35A(7): 1953-1961.
- Doudard, C., F. Hild and S. Calloch (2007). "A probabilistic model for multiaxial high cycle fatigue." *Fatigue & Fracture of Engineering Materials & Structures* 30(2): 107-114.
- Drugan, W. J. and J. R. Willis (1996). "A micromechanics-based nonlocal constitutive equation and estimates of representative volume element size for elastic composites." *Journal of the Mechanics and Physics of Solids* 44(4): 497-524.
- Efstathiou, C., H. Sehitoglu and J. Lambros (2010). "Multiscale strain measurements of plastically deforming polycrystalline titanium: Role of deformation heterogeneities." *International Journal of Plasticity* 26(1): 93-106.
- El Bartali, A., V. Aubin and S. Degallaix (2008). "Fatigue damage analysis in a duplex stainless steel by digital image correlation technique." *Fatigue & Fracture of Engineering Materials & Structures* 31(2): 137-151.
- Elber, W. (1970). "Fatigue crack closure under cyclic tension." *Engineering Fracture Mechanics* 2(2): 37-45.
- Erieau, P. and C. Rey (2004). "Modeling of deformation and rotation bands and of deformation induced grain boundaries in IF steel aggregate during large plane strain compression." *International Journal of Plasticity* 20(10): 1763-1788.
- Estrin, Y., Tóth, L.S., Molinari, A., Bréchet, Y. (1998). "A dislocation-based model for all hardening stages in large strain deformation." *Acta Materialia* 46: 5509-5522.
- Evers, L. P., D. M. Parks, W. A. M. Brekelmans and M. G. D. Geers (2002). "Crystal plasticity model with enhanced hardening by geometrically necessary dislocation accumulation." *Journal of the Mechanics and Physics of Solids* 50(11): 2403-2424.
- Evrard, P., I. Alvarez-Armas, V. Aubin and S. Degallaix (2010). "Polycrystalline modeling of the cyclic hardening/softening behavior of an austenitic-ferritic stainless steel." *Mechanics of Materials* 42(4): 395-404.
- Evrard, P., V. Aubin, S. Degallaix and D. Kondo (2008). "Formulation of a new single crystal law for modeling the cyclic softening." *Mechanics Research Communications* 35(8): 589-594.
- Ewing, J. A. and J. W. C. Humfrey (1903). "The Fracture of Metals under Repeated Alternations of Stress." *Philos. Trans. R. SOC.* 200: 241-253.
- Farahmand, B., G. Bockrath and J. Glassco (1997). "Fatigue and fracture mechanics of high risk parts: application of LEFM & FMDM theory." Kluwer Academic Pub.

- Fatemi, A. and J. Colin (2010). "Variable amplitude cyclic deformation and fatigue behaviour of stainless steel 304L including step, periodic, and random loadings." *Fatigue & Fracture of Engineering Materials & Structures* 33(4): 205-220.
- Fatemi, A. and D. Socie (1988). "A critical plane approach to multiaxial fatigue damage including out-of-phase loading." *Fat. and Fract. of Eng. Mat. and Structures* 11(3): 149-165.
- Ferrie, E., J. Y. Buffiere and W. Ludwig (2005). "3D characterisation of the nucleation of a short fatigue crack at a pore in a cast Al alloy using high resolution synchrotron microtomography." *International Journal of Fatigue* 27(10-12): 1215-1220.
- Ferrie, E., J. Y. Buffiere, W. Ludwig, A. Gravouil and L. Edwards (2006). "Fatigue crack propagation: In situ visualization using X-ray microtomography and 3D simulation using the extended finite element method." *Acta Materialia* 54(4): 1111-1122.
- Fissolo, A., C. Gourdin, O. Ancelet, S. Amiable, A. Demassieux, S. Chapuliot, N. Haddar, F. Mermaz, J. M. Stelmaszyk, A. Constantinescu, L. Vincent and V. Maillot (2009). "Crack initiation under thermal fatigue: An overview of CEA experience Part II (of II): Application of various criteria to biaxial thermal fatigue tests and a first proposal to improve the estimation of the thermal fatigue damage." *International Journal of Fatigue* 31(7): 1196-1210.
- Fomichev, P. A. (2008). "Method for the Evaluation of the Service Life under Random Loading Based on the Energy Criterion of Fatigue Fracture." *Strength of Materials* 40(2): 224-235.
- Forsyth, P. and C. Stubbington (1955). "The slip band extrusion effect observed in some aluminum alloys subjected to cyclic stresses." *Journal Institute of Metals* 3(395).
- Garcia, C. (2006). "Caractérisation microstructurale d'aciers inoxydables austénitiques (304L) sollicités en fatigue." Note EDF H-T27-2006-03851-FR.
- Gerland, M., R. Alain, B. A. Saadi and J. Mendez (1997). "Low cycle fatigue behaviour in vacuum of a 316L-type austenitic stainless steel between 20 and 600 degrees C .2. dislocation structure evolution and correlation with cyclic behaviour." *Materials Science and Engineering a-Structural Materials Properties Microstructure and Processing* 229(1-2): 68-86.
- Goudeau, P., P. Villain, N. Tamura and H. A. Padmore (2003). "Mesoscale x-ray diffraction measurement of stress relaxation associated with buckling in compressed thin films." *Applied Physics Letters* 83(1): 51-53.
- Haddar, N. (2003). "Fatigue thermique d'un acier inoxydable austénitique 304L: simulation de l'amorçage et de la croissance des fissures courtes en fatigue isotherme et anisotherme." PHD thesis, ENSMP.

References

- Hamam, R., S. Pommier and F. Bumbieler (2007). "Variable amplitude fatigue crack growth, experimental results and modeling." *International Journal of Fatigue* 29(9-11): 1634-1646.
- Hamam, R., S. Pommier and F. Bumbleler (2007). "Variable amplitude fatigue crack growth, experimental results and modeling." *International Journal of Fatigue* 29(9-11): 1634-1646.
- Harmain, G. A. (2009). "A model for predicting the retardation effect following a single overload." *Theoretical and Applied Fracture Mechanics* 53(1): 80-88.
- Heino, S. and B. Karlsson (2001). "Cyclic deformation and fatigue behaviour of 7Mo-0.5N superaustenitic stainless steel-slip characteristics and development of dislocation structures." *Acta Materialia* 49(2): 353-363.
- Helgeland, O. (1965). "Cyclic Hardenins and. Fatigue of Copper Single Crystals." *Journal of the Institute of Metals* 93: 570-575.
- Hennessy, D., G. Steckel and C. Altstetter (1976). "Phase transformation of stainless steel during fatigue." *Metallurgical Transactions a-Physical Metallurgy and Materials Science* 7: 415-424.
- Herbig, M., A. King, P. Reischig, H. Proudhon, E. M. Lauridsen, J. Marrow, J. Y. Buffiere and W. Ludwig (2011). "3-D growth of a short fatigue crack within a polycrystalline microstructure studied using combined diffraction and phase-contrast X-ray tomography." *Acta Materialia* 59(2): 590-601.
- Heripre, E., M. Dexet, J. Crepin, L. Gelebart, A. Roos, M. Bornert and D. Caldemaison (2007). "Coupling between experimental measurements and polycrystal finite element calculations for micromechanical study of metallic materials." *International Journal of Plasticity* 23(9): 1512-1539.
- Hong, Y., Y. Qiao, N. Liu and X. Zheng (1998). "Effect of grain size on collective damage of short cracks and fatigue life estimation for a stainless steel." *Fatigue & Fracture of Engineering Materials & Structures* 21(11): 1317-1325.
- Huang, H. L. (2003). "A study of dislocation evolution in polycrystalline copper during low cycle fatigue at low strain amplitudes." *Materials Science and Engineering a-Structural Materials Properties Microstructure and Processing* 342(1-2): 38-43.
- Huang, H. L. and N. J. Ho (2000). "The study of fatigue in polycrystalline copper under various strain amplitude at stage I: crack initiation and propagation." *Materials Science and Engineering a-Structural Materials Properties Microstructure and Processing* 293(1-2): 7-14.
- Hull, D. and D. J. Bacon (1965). "Introduction to Dislocations, Fourth Edition." Butterworth-Heinemann.
- Hull, D. and D. J. Bacon (2001). *Introduction to Dislocations*, Butterworth-Heinemann.

- Huntington, H. B. (1958). The elastic constants of crystals, in: F. Seitz, D. Turnbull (Eds.). New York, Academic Press Incorporation Publishers.
- Hussain, K., A. Tauqir, A. Ul Haq and A. Q. Khan (1999). "Overload effect on fatigue crack propagation in 2024-Al alloy." Fatigue '99: Proceedings of the Seventh International Fatigue Congress, Vols 1-4: 1021-1026.
- Jia, W. P. and J. V. Fernandes (2003). "Mechanical behaviour and the evolution of the dislocation structure of copper polycrystal deformed under fatigue-tension and tension-fatigue sequential strain paths." Materials Science and Engineering a-Structural Materials Properties Microstructure and Processing 348(1-2): 133-144.
- Kelestemur, M. H. and T. K. Chaki (2001). "The effect of overload on the fatigue crack growth behaviour of 304 stainless steel in hydrogen." Fatigue & Fracture of Engineering Materials & Structures 24(1): 15-22.
- Kim, S. T., D. Tadjiev and H. T. Yang (2006). "Fatigue life prediction under random loading conditions in 7475-T7351 aluminum alloy using the RMS model." International Journal of Damage Mechanics 15(1): 89-102.
- King, A., M. Herbig, W. Ludwig, P. Reischig, E. M. Lauridsen and T. Marrow (2009). "Non-destructive analysis of micro texture and grain boundary character from X-ray diffraction contrast tomography." Nuclear Instruments and Methods in Physics Research Section B: Beam Interactions with Materials and Atoms 268(3-4): 291-296.
- Kitagawa, H. and S. Takahashi (1976). "Applicability of fracture mechanics to very small cracks or cracks in the early stage." Proceedings of the 2nd International Conference on the Behaviour of Materials: 627-631.
- Kobayashi, K., K. Yamaguchi, M. Hayakawa and M. Kimura (2005). "Grain size. effect on high-temperature fatigue properties of alloy718." Materials Letters 59(2-3): 383-386.
- Komano, K., S. Ishihara, A. J. McEvily and H. Shibata (2007). "Effect of microstructure on small fatigue crack initiation and propagation behavior of Ti-6Al-4V alloy." Progresses in Fracture and Strength of Materials and Structures, 1-4 353-358: 1215-1218.
- Korsunsky, A. M., D. Dini, F. P. E. Dunne and M. J. Walsh (2007). "Comparative assessment of dissipated energy and other fatigue criteria." International Journal of Fatigue 29(9-11): 1990-1995.
- Krupp, U. (2007). Fatigue Crack Propagation in Metals and Alloys-Microstructural Aspects and Modelling Concepts, Wiley-VCH.
- Kunkler, B., O. Duber, P. Koster, U. Krupp, C. P. Fritzen and H. J. Christ (2008). "Modelling of short crack propagation - Transition from stage I to stage II." Engineering Fracture Mechanics 75(3-4): 715-725.

- Lacombe, P., B. Baroux and G. Béranger (1990). "Les aciers inoxydables." Editions de Physique.
- Lagoda, T. (2001). "Energy models for fatigue life estimation under uniaxial random loading. Part I: The model elaboration." *International Journal of Fatigue* 23(6): 467-480.
- Lagoda, T. (2001). "Energy models for fatigue life estimation under uniaxial random loading. Part II: Verification of the model." *International Journal of Fatigue* 23(6): 481-489.
- Le-Pecheur, A. (2008). *Fatigue thermique d'un acier inoxydable austénitique :influence de l'état de surface par une approche multi-échelles.* PhD Thesis. Ecole Centrale Paris.
- Le Pecheur, A., M. Clavel, F. Curtit, C. Rey, J.-M. Stephan and P. Bompard (2011). "Influence of surface conditions on fatigue strength through the numerical simulation of microstructure." *Rev. Metall.* 107(10-11): 477-489.
- Lebedev and Kosarchuk (2000). "Influence of phase transformations on the mechanical properties of austenitic stainless steel." *International Journal of Plasticity* 16: 749-767.
- Lecroisey, F. and A. Pineau (1972). "Martensitic transformations induced by plastic deformation in the Fe-Ni-Cr-C system " *Metallurgical and Materials Transactions B* 3: 391-400.
- Lehericy, Y. and J. Mendez (2006). "Effect of low cycle fatigue damage on the residual fatigue strength of 304L austenitic stainless steel." 9th International Fatigue Congress Atlanta, GA.
- Lehericy, Y. and J. Mendez (2006). "Effect of low cycle fatigue damage on the residual fatigue strength of 304l austenitic stainless steel." 9th International Fatigue Congress, Atlanta , GA
- Lemaitre, J. and R. Desmorat (2005). *Engineering Damage Mechanics* New York Springer Berlin Heidelberg New York
- Li, X. D. (1996). "Micromechanical model of stage I to stage II crack growth transition for aluminium alloys." *Theoretical and Applied Fracture Mechanics* 24(3): 217-231.
- Li, Y., V. Aubin, C. Rey and P. Bompard (2011). "Polycrystalline numerical simulation of variable amplitude loading effects on cyclic plasticity and microcrack initiation in austenitic steel 304L." *International Journal of Fatigue* In Press, Corrected Proof.
- Li, Y. and C. Laird (1994). "Cyclic response and dislocation structures of AISI 316L stainless steel. Part 1: single crystals fatigued at intermediate strain amplitude." *Materials Science and Engineering: A* 186(1-2): 65-86.

- Li, Y. and C. Laird (1994). "Cyclic response and dislocation structures of AISI 316L stainless steel. Part 2: polycrystals fatigued at intermediate strain amplitude." *Materials Science and Engineering: A* 186(1-2): 87-103.
- Limodin, N., J. Rethore, J. Y. Buffiere, F. Hild, W. Ludwig, J. Rannou and S. Roux (2011). "3D X-ray Microtomography Volume Correlation to Study Fatigue Crack Growth." *Advanced Engineering Materials* 13(3): 186-193.
- Lin, T. H., H. Q. Liu and N. G. Liang (2003). "A micromechanical theory of fatigue crack initiation of an aluminum single crystal." *International Journal of Fatigue* 25(9-11): 871-876.
- Mailliot, V., G. Degallaix, S. Degallaix and A. Fissolo (2006). "Biaxial thermomechanical fatigue on a 304 L-type austenitic stainless steel." *Materialprüfung* 48(1-2): 44-49.
- Malésys, N., L. Vincent and F. Hild (2009). "A probabilistic model to predict the formation and propagation of crack networks in thermal fatigue." *International Journal of Fatigue* 31(3): 565-574.
- Manole, C., C. Depres and L. Tabourot (2009). "Development of a dislocation-based constitutive law for fcc crystals on a wide range of deformation amplitude." 15th International Conference on the Strength of Materials Dresden August 16 – 21.
- Manole, C., C. Depres and L. Tabourot (2009). "Development of a dislocation-based constitutive law for fcc crystals on a wide range of deformation amplitude." X International Conference on Computational Plasticity Barcelona.
- Manson, S. S. (1954). *Behaviour of Materials under Conditions of Thermal Stress*, NACA Report. .
- Marmy, P. and T. Kruml (2008). "Low cycle fatigue of Eurofer 97." *Journal of Nuclear Materials* 377(1): 52-58.
- Marrow, T. J., J. Y. Buffiere, P. J. Withers, G. Johnson and D. Engelberg (2004). "High resolution X-ray tomography of short fatigue crack nucleation in austempered ductile cast iron." *International Journal of Fatigue* 26(7): 717-725.
- Mastorakos, I. N. and H. M. Zbib (2008). "Dislocation-cracks interaction during fatigue: A discrete dislocation dynamics simulation." *Jom* 60(4): 59-63.
- Maurel, V., L. Rémy, F. Dahmen and N. Haddar (2009). "An engineering model for low cycle fatigue life based on a partition of energy and micro-crack growth." *International Journal of Fatigue* 31(5): 952-961.
- Maxwell, P. C., A. Goldberg and J. C. Shyne (1974). "Stress assisted and strain induced martensite in Fe-Ni-Cr alloys. ." *Metallurgical and Materials Transactions B* 5: 1395-1318.
- Mayama, T. and K. Sasaki (2006). "Investigation of subsequent viscoplastic deformation of austenitic stainless steel subjected to cyclic preloading." *International Journal of Plasticity* 22(2): 374-390.

References

- McDowell, D. L. (1996). "Basic issues in the mechanics of high cycle metal fatigue." *International Journal of Fracture* 80(2-3): 103-145.
- McDowell, D. L. and F. P. E. Dunne (2010). "Microstructure-sensitive computational modeling of fatigue crack formation." *International Journal of Fatigue* 32(9): 1521-1542.
- McEvily, A. J., J. L. Gonzalez and J. M. Hallen (1996). "Dislocation substructures at fatigue crack tips of 304 stainless steel cycled in air or vacuum." *Scripta Materialia* 35(6): 761-765.
- Mcguire, M. (2008). "Stainless steels for design engineers." ASM International Materials Park, Ohio 44073-0002.
- Miner, M. A. (1945). "Cumulative damage in fatigue, ." *J. Appl. Mech.* Vol. 12, Trans. ASME, Vol. 67.
- Mochizuki, M., M. Hayashi and T. Hattori (2000). "Numerical analysis of welding residual stress and its verification using neutron diffraction measurement." *Journal of Engineering Materials and Technology-Transactions of the Asme* 122(1): 98-103.
- Morel, F. (2000). "A critical plane approach for life prediction of high cycle fatigue under multiaxial variable amplitude loading." *International Journal of Fatigue* 22(2): 101-119.
- Moreno, B., J. Zapatero and J. Dominguez (2003). "An experimental analysis of fatigue crack growth under random loading." *International Journal of Fatigue* 25(7): 597-608.
- Morrow, J. (1964). "Fatigue properties of metals." *Proceedings of the division 4 of the SAE iron and steel technical committee vol. Nov. 4(Warrendale (PA))*.
- Mughrabi, H. (1978). "Cyclic Hardening and Saturation Behavior of Copper Single-Crystals." *Materials Science and Engineering* 33(2): 207-223.
- Mughrabi, H. (1983). "Dislocation wall and cell structures and long range internal stresses in deformed metals crystals." *Acta Materiala* 31: 1367-1379.
- Mutoh, Y., T. Moriya, S. J. Zhu and Y. Mizuhara (1998). "Initiation and growth of small fatigue crack in TiAl intermetallics at elevated and room temperatures." *Materials Science Research International* 4(1): 19-25.
- Obrtlík, K., T. Kruml and J. Polak (1994). "Dislocation structures in 316L stainless steel cycled with plastic strain amplitudes over a wide interval." *Materials Science and Engineering: A* 187(1): 1-9.
- Ostash, O. P., V. V. Panasyuk and E. M. Kostyk (1998). "Unified model of nucleation and growth of fatigue cracks. Part 1. Use of force parameters of fracture mechanics of materials in the stage of crack nucleation." *Materials Science* 34(1): 1-18.

- Ostergren, W. J. (1976). "A Damage Function and Associated Failure Equations for Predicting Hold Time and Frequency Effects in Elevated Temperature Low Cycle Fatigue " *Journal of Testing and Evaluation* 4(5): 327-337.
- Osterstock, S. (2008). Vers la prédiction de l'apparition de réseaux de fissures : influence des paramètres microstructuraux sur la dispersion à l'amorçage. Thèse de doctorat, Ecole Centrale Lille.
- Palmgren, A. (1924). "The Service Life of Ball Bearings." *Zetschrift des Vereines Deutscher Ingenieure*, Vol. 68, No. 14.
- Paris, P. C. (1965). "The fracture mechanics approach to fatigue." In *Proceedings of the Tenth Sagamore Conference*, Syracuse University Press, New York.
- Peralta, P., C. Laird, U. Ramamurty, S. Suresh, G. H. Campbell, W. E. King and T. E. Mitchell (1999). "Fatigue crack nucleation in metallic materials." *Small Fatigue Cracks: Mechanics, Mechanisms, and Applications*: 17-28.
- Pickering, F. P. (1984). "Physical metallurgical development of stainless steel." *Proceeding of the conference stainless steel prime*, Göteborg.
- Polak, J., S. Degallaix and G. Degallaix (1993). "The Role of Cyclic Slip Localization in Fatigue Damage of Materials." *Journal De Physique Iv* 3(C7): 679-684.
- Polak, J., K. Obrtlík and M. Hajek (1994). "Cyclic Plasticity in Type 316L Austenitic Stainless-Steel." *Fatigue & Fracture of Engineering Materials & Structures* 17(7): 773-782.
- Pommier, S. (2003). "Cyclic plasticity and variable amplitude fatigue." *International Journal of Fatigue* 25(9-11): 983-997.
- Quey, R., P. R. Dawson and F. Barbe (2011). "Large-scale 3D random polycrystals for the finite element method: Generation, meshing and remeshing." *Computer Methods in Applied Mechanics and Engineering* 200(17-20): 1729-1745.
- Raman, S. G. S. and K. A. Padmanabhan (1995). "A Comparison of the Room-Temperature Behavior of Aisi 304L Stainless-Steel and Nimonic-90 under Strain Cycling." *International Journal of Fatigue* 17(4): 271-277.
- Rao, K. B. S., M. Valsan, R. Sandhya, S. L. Mannan and P. Rodriguez (1991). "Synergistic Interactions during High-Temperature Fatigue of Type-304 Stainless Steel-Grain Size Dependence." *Transactions of the Indian Institute of Metals* 44(3): 255-270.
- Ravichandran, S., R. O. Ritchie and Y. Murakami (1999). *Small Fatigue Cracks: Mechanics, Mechanisms and Applications*, ELSEVIER.
- Reed, R. P. (1962). "The Spontaneous Martensitic Transformations in 18 pct Cr, 8 pct Ni Steels." *Acta Metallurgica* 10,: 865-877.

- Robertson, C., M. C. Fivel and A. Fissolo (2001). "Dislocation substructure in 316L stainless steel under thermal fatigue up to 650 K." *Materials Science and Engineering a-Structural Materials Properties Microstructure and Processing* 315(1-2): 47-57.
- Rousseau, P. (1973). "Aciers inoxydables à haute caractéristiques." *Aciers spéciaux* 24: 6-10.
- Rupil, J., L. Vincent, S. Roux and F. Hild (2011). "Identification and probabilistic modeling of mesocrack initiations in 304L stainless steel." *International Journal for Multiscale Computational Engineering* 9(4): 445-458.
- Rupil, J. P., M. , B. Raka, L. Vincent , R. Desmorat, J. C. Le-roux, S. Courtin and F. HILD (2011). "Essais de fatigue équibiaxiale à grand nombre de cycles d'un acier 304L : mesure de l'amplitude de déformation et suivi d'endommagement." 20e Congrès Français de Mécanique -CFM
- Saai, A., H. Louche, L. Tabourot and H. J. Chang (2010). "Experimental and numerical study of the thermo-mechanical behavior of Al bi-crystal in tension using full field measurements and micromechanical modeling." *Mechanics of Materials* 42(3): 275-292.
- Sandor, B. I. (1972). *Fundamentals of Cyclic Stress and Strain*, Univ of Wisconsin Press.
- Sauzay, M. (2006). "Effet de l'anisotropie élastique cristalline sur la distribution des facteurs de Schmid à la surface des polycristaux." *Comptes Rendus Mecanique* 334(6): 353-361.
- Schijve, J. (2009). *Fatigue of Structures and Materials*. Netherlands, Springer Science+Business Media, B.V.
- Schmid, E. and W. Boas (1935). "Kristall plastizität." Springer Verlag.
- Schwartz, J. (2011). *Approche non locale en plasticité cristalline : application à l'étude du comportement mécanique de l'acier AISI 316LN en fatigue oligocyclique*. PHD thesis. Paris, Ecole Centrale Paris.
- Schwartz, J., O. Fandeur and C. Rey (2010). "Fatigue crack initiation modeling of 316LN steel based on non local plasticity theory." *Procedia Engineering* 2(1): 1353-1362.
- Seweryn, A., A. Buczynski and J. Szusta (2008). "Damage accumulation model for low cycle fatigue." *International Journal of Fatigue* 30(4): 756-765.
- Shimojo, M., M. Chujo, Y. Higo and S. Nunomura (1998). "Mechanism of the two stage plastic deformation following an overload in fatigue crack growth." *International Journal of Fatigue* 20(5): 365-371.
- Shin, C. S. and S. H. Hsu (1993). "On the mechanisms and behaviour of overload retardation in AISI 304 stainless steel." *International Journal of Fatigue* 15(3): 181-192.

- Shiozawa, K., S. Nishino, T. Ohtani and S. Mizuno (1999). "Subsurface fatigue-crack initiation and growth of plasma-assisted duplex surface-treated tool steel." *Small Fatigue Cracks: Mechanics, Mechanisms, and Applications*: 39-47.
- Shiozawa, K., Y. Tohda and S. M. Sun (1997). "Crack initiation and small fatigue crack growth behaviour of squeeze-cast Al-Si aluminium alloys." *Fatigue & Fracture of Engineering Materials & Structures* 20(2): 237-247.
- Smith, K. N., P. Watson and T. H. Topper (1970). "A stress-strain function for the fatigue of metals." *Journal of materials* 5: 767-778.
- Song, Y. S., M. R. Lee and J. T. Kim (2005). "Effect of grain size for the tensile strength and the low cycle fatigue at elevated temperature of alloy 718 cogged by open die forging press." *Superalloys 718, 625, 706 and Derivatives, Proceedings*: 539-549.
- Stephens, R., A. Fatemi, R. Stephens and H. Fuchs (2000). *Metal fatigue in engineering*, Willy Interscience Publication.
- Suresh, S. (1991). *Fatigue of Materials* (Cambridge Solid State Science Series), Cambridge University Press.
- Swenson, D. O. (1969). "Transition between Stage-I and Stage-2 Modes of Fatigue Crack Growth." *Journal of Applied Physics* 40(9): 3467-&.
- Takago, S., H. Yasui, K. Awazu, T. Sasaki, Y. Hirose and K. Sakurai (2006). "Application of in-plane X-ray diffraction technique for residual stress measurement of TiN film/WC-Co alloy." *Bunseki Kagaku* 55(6): 405-410.
- Takaya, S. and K. Miya (2005). "Application of magnetic phenomena to analysis of stress corrosion cracking in welded part of stainless steel." *Journal of Materials Processing Technology* 161(1-2): 66-74.
- Takaya, S., T. Suzuki, Y. Matsumoto, K. Demachi and M. Uesaka (2004). "Estimation of stress corrosion cracking sensitivity of type 304 stainless steel by magnetic force microscope." *Journal of Nuclear Materials* 327(1): 19-26.
- Tanguy, D., M. Razafindrazaka and D. Delafosse (2008). "Multiscale simulation of crack tip shielding by a dislocation." *Acta Materialia* 56(11): 2441-2449.
- Tewari, A., A. M. Gokhale, J. E. Spowart and D. B. Miracle (2004). "Quantitative characterization of spatial clustering in three-dimensional microstructures using two-point correlation functions." *Acta Materialia* 52(2): 307-319.
- Thompson, N., N. Wadsworth and N. Louat (1956). "The origin of fatigue fracture in copper." *Philosophical Magazine* 1(2): 113-126.
- Turner, A. P. L. (1975). "Cyclic Hardening and Softening of Stainless-Steel." *Jom-Journal of Metals* 27(12): A49-A50.

- Van der Giessen, E., V. S. Deshpande, H. H. M. Cleveringa and A. Needleman (2001). "Discrete dislocation plasticity and crack tip fields in single crystals." *Journal of the Mechanics and Physics of Solids* 49(9): 2133-2153.
- Vincent, L. (2008). "On the ability of some cyclic plasticity models to predict the evolution of stored energy in a type 304L stainless steel submitted to high cycle fatigue." *European Journal of Mechanics a-Solids* 27(2): 161-180.
- Walker, K. (1970). "The Effect of Stress Ratio During Crack Propagation and Fatigue for 2024-T3 and 7075-T6 Aluminum, Effects of Environment and Complex Load History on Fatigue Life." ASTM STP 462, Am. Soc. for Testing and Materials West Conshohocken, PA.
- Walther, F. and D. Elfler (2007). "Fatigue life calculation of SAE 1050 and SAE 1065 steel under random loading." *International Journal of Fatigue* 29(9-11): 1885-1892.
- Weertman, J. (2007). "Dislocation crack tip shielding and the Paris exponent." *Materials Science and Engineering a-Structural Materials Properties Microstructure and Processing* 468: 59-63.
- Wei, L. W., E. R. de los Rios and M. N. James (2002). "Experimental study and modelling of short fatigue crack growth in aluminium alloy Al7010-T7451 under random loading." *International Journal of Fatigue* 24(9): 963-975.
- Wei, X. J., J. Li and W. Ke (1998). "Crack growth retardation of single overload for A537 steel in a 3.5% NaCl solution under cathodic potential and free corrosion condition." *International Journal of Fatigue* 20(3): 225-231.
- Williford, R. E., C. F. Windisch Jr and R. H. Jones (2000). "In situ observations of the early stages of localized corrosion in Type 304 SS using the electrochemical atomic force microscope." *Materials Science and Engineering: A* 288(1): 54-60.
- Woo, W., Z. L. Feng, X. L. Wang, K. An, C. R. Hubbard, S. A. David and H. Choo (2006). "In situ neutron diffraction measurement of transient temperature and stress fields in a thin plate." *Applied Physics Letters* 88(26): -.
- Yang, J. H., Y. Li, S. X. Li, C. X. Ma and G. Y. Li (2001). "Simulation and observation of dislocation pattern evolution in the early stages of fatigue in a copper single crystal." *Materials Science and Engineering a-Structural Materials Properties Microstructure and Processing* 299(1-2): 51-58.
- Yokoyama, H., O. Umezawa, K. Nagai, T. Suzuki and K. Kokubo (2000). "Cyclic deformation, dislocation structure, and internal fatigue crack generation in a Ti-Fe-O alloy at liquid nitrogen temperature." *Metallurgical and Materials Transactions a-Physical Metallurgy and Materials Science* 31(11): 2793-2805.
- Zapatero, J., B. Moreno, A. Gonzalez-Herrera and J. Dominguez (2005). "Numerical and experimental analysis of fatigue crack growth under random loading." *International Journal of Fatigue* 27(8): 878-890.

- Zeghad, A., S. Forest, A. F. Gourgues and O. Bouaziz (2007). "Ensemble averaging stress-strain fields in polycrystalline aggregates with a constrained surface microstructure - Part 2: crystal plasticity." *Philosophical Magazine* 87(8-9): 1425-1446.
- Zeghad, A., F. N'Guyen, S. Forest, A. F. Gourgues and O. Bouaziz (2007). "Ensemble averaging stress-strain fields in polycrystalline aggregates with a constrained surface microstructure - Part 1: anisotropic elastic behaviour." *Philosophical Magazine* 87(8-9): 1401-1424.
- Zhang, J. X. and Y. Y. Jiang (2006). "Fatigue of polycrystalline copper with different grain sizes and texture." *International Journal of Plasticity* 22(3): 536-556.

Amorçage de fissures en fatigue dans un acier 304L: influence de la microstructure et d'un chargement d'amplitude variable

Résumé: L'amorçage et la propagation de microfissures dans les matériaux à haute résistance représente une part importante de la durée de vie en fatigue, en particulier dans le cas d'un chargement à faible amplitude. Ces phénomènes, d'un grand intérêt scientifique, ont été de plus en plus étudiés au cours des dernières années. L'orientation cristallographique et les hétérogénéités de déformation induites influent sur l'amorçage et le comportement des microfissures de fatigue tant que leur taille caractéristique est inférieure ou de l'ordre de grandeur de la taille de grains. L'objectif principal de cette étude est de caractériser l'influence de la microstructure et d'un chargement cyclique à amplitude variable sur la plasticité cristalline et plus précisément sur l'amorçage de microfissures dans un acier inoxydable 304L. La première partie de cette étude consiste à l'amélioration de la loi de comportement cristalline CristalECP codée dans le logiciel éléments finis ABAQUS afin de mieux prendre en compte la distribution et l'évolution de la densité de dislocation sur les systèmes de glissement. Ce travail permet également de décrire la formation des bandes persistantes de glissement qui sont responsables du durcissement et de l'adoucissement cyclique. La seconde partie de cette étude concerne l'évaluation de l'influence de la microstructure sur les valeurs locales des paramètres mécaniques utilisés pour les critères de fatigue aussi bien macroscopiques que microscopiques, et relier ces valeurs à l'amorçage de microfissures à l'échelle cristalline. Pour ceci, une comparaison est réalisée entre les résultats expérimentaux d'observation de surfaces et les simulations numériques d'agrégats 3D présentant les orientations cristallines réelles de ces éprouvettes. La simulation de la plasticité cristalline peut apporter une contribution utile pour la prédiction de la localisation et de l'intensité de l'amorçage de microfissures de fatigue, mais également aider à choisir un critère d'amorçage de microfissures basé sur des considérations mécaniques. La dernière partie de ce manuscrit porte sur les effets d'un chargement d'amplitude variable (séquence de surcharge) sur la plasticité cristalline et l'amorçage de microfissures. Deux modes de chargement ont été considérés pour les essais de fatigue : contrainte contrôlée et déformation contrôlée. Les essais avec surcharge en contrainte contrôlée présentent une durée de vie plus importante (six à neuf fois) que les essais avec surcharge en déformation contrôlée, ce qui est lié au durcissement cyclique important du 304L. De plus, les simulations montrent que sous chargement à déformation contrôlée, l'effet mémoire de la surcharge est dépendant du niveau du chargement qui suit la surcharge : cet effet mémoire est plus important dans le cas d'un chargement à faible amplitude (fatigue à grand nombre de cycles) qu'en fatigue oligocyclique à forte amplitude.

Fatigue crack initiation (in 304L steel): influence of the microstructure and variable amplitude loading

Abstract: Because fatigue crack initiation and propagation of microstructurally short cracks represent most of the fatigue life in high-strength materials, especially under low amplitude loading, the study of crack initiation is of significant importance and attracted increasing attention recently. As long as the microcrack size is comparable with the grain size, the microcrack initiation is strongly influenced by the crystallographic microstructure. The main purpose of this work is to study the influence of the microstructure and variable amplitude loading on cyclic plasticity and microcrack initiation in stainless steel 304L. The first part of this work aims at enriching the crystal plasticity code CristalECP to better simulate the evolution of dislocation densities on slip systems and formation of PSBs which are responsible for the fatigue cyclic hardening/softening behavior. The second part concerns the evaluation of the influence of local values of mechanical factors, issued from both macroscopic and microscopic fatigue criteria, on crack initiation in the grains through the comparison between experimental surface observations and numerical simulations of 3D aggregates with realistic crystallographic orientations. It is shown that the crystal plasticity simulation can give useful contributions to predict the crack initiation sites and severity, and help to select fatigue crack initiation criterion based on mechanical parameters which actually control the crack initiation. The last part studies the effects of the variable amplitude loading (high-low sequence) on cyclic plasticity and crack initiation. Both load- and strain-controlled fatigue tests were considered. Load-controlled tests present much longer lives (6 to 9 times) than in strain-controlled tests due to strain hardening. Furthermore, simulations show that under strain-controlled loading, memory effect of overload is dependent on the amplitude level of the low amplitude block, which is more significant in high cycle fatigue than in low cycle fatigue.

Key words: crack initiation, cyclic plasticity, fatigue, crystal plasticity, polycrystalline aggregate, finite elements analysis, 304L austenitic stainless steel